



HAL
open science

Nouveau cadre de modélisation de la capture d'interface et de l'ébullition pour le refroidissement industriel

Ali-Malek Boubaya

► **To cite this version:**

Ali-Malek Boubaya. Nouveau cadre de modélisation de la capture d'interface et de l'ébullition pour le refroidissement industriel. Mécanique des fluides [physics.class-ph]. Université Paris sciences et lettres, 2022. Français. NNT : 2022UPSLM026 . tel-03951688

HAL Id: tel-03951688

<https://pastel.hal.science/tel-03951688>

Submitted on 23 Jan 2023

HAL is a multi-disciplinary open access archive for the deposit and dissemination of scientific research documents, whether they are published or not. The documents may come from teaching and research institutions in France or abroad, or from public or private research centers.

L'archive ouverte pluridisciplinaire **HAL**, est destinée au dépôt et à la diffusion de documents scientifiques de niveau recherche, publiés ou non, émanant des établissements d'enseignement et de recherche français ou étrangers, des laboratoires publics ou privés.



THÈSE DE DOCTORAT
DE L'UNIVERSITÉ PSL

Préparée à MINES Paris - PSL

**New interface capturing and boiling framework modeling
for industrial cooling**

Nouveau cadre de modélisation de la capture d'interface et de
l'ébullition pour le refroidissement industriel

Soutenue par

Ali-Malek BOUBAYA

Le 05 Juillet 2022

École doctorale n°364

**Sciences Fondamentales et
Appliquées**

Spécialité

**Mathématiques Numériques,
Calcul Intensif et Données**

Composition du jury :

Pr. Médéric ARGENTINA
Université Côte d'Azur

Président

Pr. Stefanie ELGETI
Technischen Universität Wien

Rapporteur

Pr. Franck BOYER
Université de Toulouse

Rapporteur

Dr. Aurélien LARCHER
Mines Paris

Co-encadrant de thèse

Pr. Elie HACHEM
Mines Paris

Directeur de thèse

*À l'âme de mon cher oncle Mohamed,
À mes chers grand-parents,
À mon cher Papa,
À ma chère Maman.*

Contents

| | |
|---|-----------|
| Contents | i |
| List of Figures | v |
| List of Tables | ix |
| General introduction | 1 |
| Industrial motivations | 3 |
| Interface capturing methods | 4 |
| Volume-of-Fluid method | 5 |
| Level-set method | 8 |
| Diffuse-interface method | 10 |
| Objectives of the thesis | 14 |
| Numerical framework | 15 |
| Layout of the thesis | 15 |
| Bibliography | 16 |
| 1 Cahn–Hilliard as an interface capturing method | 21 |
| 1.1 Introduction | 23 |
| 1.2 Cahn–Hilliard origins | 23 |
| 1.3 The governing equations | 25 |
| 1.4 Mathematical properties | 29 |
| 1.5 Space and time discretization for the Cahn–Hilliard equations | 35 |
| 1.5.1 Mixed finite element framework | 35 |
| 1.5.2 Time discretized scheme and linearization | 37 |
| 1.6 Numerical properties | 40 |
| 1.7 Simulation of an interface transport | 44 |
| 1.7.1 Numerical convergence analysis | 45 |
| 1.7.2 Pulse rotation | 48 |
| 1.7.3 Single Vortex | 50 |
| 1.7.4 Zalesak’s Disk | 52 |

| | | |
|----------|--|------------|
| 1.8 | Conclusion | 55 |
| | Bibliography | 56 |
| 2 | Multiphase flow and coupling | 59 |
| 2.1 | Introduction | 61 |
| 2.2 | Balance equations | 61 |
| 2.3 | Korteweg’s capillarity theory | 65 |
| 2.4 | The governing coupled equations | 67 |
| 2.5 | Mathematical properties of the coupled equations | 68 |
| 2.6 | Space and time discretization | 74 |
| 2.6.1 | Finite element discretization | 74 |
| 2.6.2 | Time discretization | 78 |
| 2.7 | Two-phase flow simulation with interface capturing | 80 |
| 2.7.1 | Dam-break 2D | 80 |
| 2.7.2 | Rising bubble 2D | 83 |
| 2.7.3 | Rayleigh–Taylor instability 2D | 89 |
| 2.8 | Conclusion | 93 |
| | Bibliography | 93 |
| 3 | Anisotropic mesh adaptation for phase-field methods | 97 |
| 3.1 | Introduction | 99 |
| 3.2 | Edge-based metric | 100 |
| 3.2.1 | Length distribution tensor | 100 |
| 3.2.2 | Edge based error estimation | 101 |
| 3.2.3 | Gradient recovery procedure | 101 |
| 3.2.4 | Metric construction | 102 |
| 3.2.5 | Mesh adaptation criteria | 103 |
| 3.3 | Numerical experiments | 104 |
| 3.3.1 | Dam-break 2D | 104 |
| 3.3.2 | Rising bubble 2D | 107 |
| 3.3.3 | Rayleigh–Taylor instability 2D | 112 |
| 3.3.4 | Dam-break 3D | 117 |
| 3.3.5 | Rising bubble 3D benchmark | 120 |
| 3.3.6 | Rayleigh–Taylor instability 3D | 122 |
| 3.4 | Conclusion | 124 |
| | Bibliography | 125 |
| 4 | Applications to boiling | 127 |
| 4.1 | Introduction | 130 |
| 4.2 | Liquid-to-vapor phase change and heat transfer | 130 |
| 4.3 | Convection-diffusion-reaction for cooling | 140 |

| | | |
|----------|--|------------|
| 4.4 | Numerical simulation | 142 |
| 4.4.1 | Stefan problem | 142 |
| 4.4.2 | Boiling case | 143 |
| 4.5 | Industrial applications | 148 |
| 4.5.1 | 3D quenching of a solid | 149 |
| 4.5.2 | 3D quenching of two identical solids | 154 |
| 4.5.3 | 3D queching of a large solid with a complex geometry | 159 |
| 4.6 | Conclusion | 163 |
| | Bibliography | 163 |
| 5 | Conclusions and Perspectives | 165 |
| 5.1 | Conclusion | 167 |
| 5.2 | Perspectives | 167 |
| | Bibliography | 168 |

List of Figures

| | | |
|------|--|----|
| 1 | Industrial quenching (from heattreatmentsservices.com) | 3 |
| 2 | Multiphysics phenomena (pictures from conmecheng.com and heat-treatmart.com) | 4 |
| 3 | ANR industrial chair: INFINITY | 4 |
| 4 | Level-set function α for a two-fluid flow | 9 |
| 5 | Diffuse-interface for a bi-fluid system | 11 |
| 1.1 | Order parameter identifying the phases | 24 |
| 1.2 | Two-phase system within the phase-field Cahn–Hilliard approach | 24 |
| 1.3 | Homogeneous free energy | 25 |
| 1.4 | Initial step for benchmarks | 44 |
| 1.5 | Spatial convergence analysis at constant CFL ≈ 0.1 (log scale) | 47 |
| 1.6 | Phase-field solution at $t=0, 314, 628, 942,$ and 1256 | 49 |
| 1.7 | Phase-field solution at $t=0, 1, 2, 3,$ and 4 | 51 |
| 1.8 | Zalesak disk benchmark | 52 |
| 1.9 | Phase-field solution of the Zalesak disk at $t=0, 314,$ and 628 | 53 |
| 1.9 | Phase-field solution of the Zalesak disk at $t= 942$ and 1256 | 54 |
| 1.10 | Evolution of the order parameter at the neighborhood of the interface diffuse | 55 |
| 2.1 | Two-fluid flow with the phase-field Cahn–Hilliard approach | 62 |
| 2.2 | Capillary action | 65 |
| 2.3 | Dam-break benchmark | 80 |
| 2.4 | Phase-field solution at $t=0, 0.2, 0.4, 0.6, 1,$ and 2 of the dam-break evolution | 81 |
| 2.5 | Non-dimensional evolution of the front position and the height column | 82 |
| 2.6 | Rising bubble benchmark | 83 |
| 2.7 | Phase-field solution of the bubble evolution at $t=0, 1,$ and 2 with $\sigma=1.96$ | 84 |
| 2.7 | Phase-field solution of the bubble evolution at $t=3, 4,$ and 5 with $\sigma=1.96$ | 84 |
| 2.8 | Position and velocity evolution of the bubble mass center for $\sigma=1.96$ | 85 |

| | | |
|------|---|-----|
| 2.9 | Phase-field solution of the bubble evolution at $t=0, 1,$ and 2 with $\sigma=24.5$ | 86 |
| 2.9 | Phase-field solution of the bubble evolution at $t=3, 4,$ and 5 with $\sigma=24.5$ | 86 |
| 2.10 | Position and velocity evolution of the bubble mass center for $\sigma=24.5$ | 87 |
| 2.11 | Phase field solution of the rising bubble evolution at $t_f=5$ with scaled (left) and unscaled (right) values of φ | 88 |
| 2.12 | Rayleigh–Taylor instability | 89 |
| 2.13 | Phase-field solution of the Rayleigh–Taylor instability at $t=0.75, 1,$ $1.25, 1.5,$ and 1.75 | 91 |
| 2.14 | Phase field solution of the Rayleigh–Taylor instability evolution at $t=1.75$ with scaled (left) and unscaled (right) values of φ | 92 |
| 3.1 | Phase-field solution at $t=0$ and 0.2 of the dam-break evolution with mesh adaptation | 105 |
| 3.1 | Phase-field solution at $t=0.4, 0.6, 1, 2, 4,$ and 10 of the dam-break evolution with mesh adaptation | 106 |
| 3.2 | Non-dimensional evolution of the front position and the height column within the mesh adaptation framework | 107 |
| 3.3 | Phase-field solution and adapted mesh of the bubble evolution at $t=0, 1,$ and 2 with $\sigma=1.96$ | 108 |
| 3.3 | Phase-field solution and adapted mesh of the bubble evolution at $t=3, 4,$ and 5 with $\sigma=1.96$ | 109 |
| 3.4 | Position and velocity evolution of the bubble mass center for $\sigma=1.96$ with mesh adaptation | 109 |
| 3.5 | Phase-field solution and adapted mesh of the bubble evolution at $t=0, 1, 2, 3, 4,$ and 5 with $\sigma=24.5$ | 110 |
| 3.6 | Position and velocity evolution of the bubble mass center for $\sigma=24.5$ with mesh adaptation | 111 |
| 3.7 | Phase-field solution and adapted mesh of the Rayleigh–Taylor instability at $t=1.5$ and 1.75 | 114 |
| 3.8 | Phase-field solution of the Rayleigh–Taylor instability at $t=115$ for the uniform mesh and the adapted mesh | 115 |
| 3.9 | Volume loss evolution over time of the lighter fluid for the uniform and adapted mesh | 116 |
| 3.10 | Dam-break benchmark 3D | 117 |
| 3.12 | Non-dimensional evolution of the front position and the height of the dam-break in 3D | 119 |
| 3.13 | Rising bubble benchmark 3D | 120 |
| 3.14 | Interface evolution at $t=0, 1, 2,$ and 3 of the rising bubble in 3D | 121 |
| 3.15 | Rayleigh–Taylor instability 3D | 122 |

| | | |
|------|--|-----|
| 3.16 | Interface evolution at $t=0$, 0.25, and 0.5 of the Rayleigh–Taylor instability in 3D | 123 |
| 3.16 | Interface evolution at $t=0.75$, 1, and 1.25 of the Rayleigh–Taylor instability in 3D | 124 |
| 4.1 | Level-set and phase-field hybrid interfaces | 139 |
| 4.2 | Volume that has vaporized between t and $t + \Delta t$ | 140 |
| 4.3 | Initial setup of the Stefan problem | 142 |
| 4.4 | Evolution of the interface position for the Stefan problem | 143 |
| 4.5 | Solid immersed in a water/vapor environment | 144 |
| 4.6 | Dynamics (left) and temperature (right) evolution during the quenching duration (contin.) | 146 |
| 4.7 | Evolution of the temperature at different region of the solid | 147 |
| 4.8 | Quenching of a piece | 149 |
| 4.9 | Dynamics, mesh, and temperature evolution during the quenching of a solid (contin.) | 151 |
| 4.10 | Evolution of the temperature at the solid interface and the dynamics of the interface separating water and vapor with a view from above (left) and below (right) at different time of the quenching of a solid (cont.) | 153 |
| 4.11 | Quenching of 2 pieces | 154 |
| 4.12 | Dynamics, mesh, and temperature evolution during the quenching of two identical solids (contin.) | 156 |
| 4.13 | Evolution of the temperature at the solid interface and the dynamics of the interface separating water and vapor with a view from above (left) and below (right) at different time of the quenching of two identical solids (cont.) | 158 |
| 4.14 | Quenching of a large solid with a complex geometry | 159 |
| 4.15 | Evolution of the temperature at the solid interface and the dynamics of the interface separating water and vapor with a view from above (left) and below (right) at different time of the quenching of a complex geometrical solid (cont.) | 161 |
| 4.15 | Evolution of the temperature at the solid interface and the dynamics of the interface separating water and vapor with a view from above (left) and below (right) at different time of the quenching of a complex geometrical solid (cont.) | 162 |

List of Tables

| | | |
|-----|--|-----|
| 1.1 | Pulse rotation: comparison of the volume loss by number of elements | 50 |
| 1.2 | Single Vortex: comparison of the volume loss by number of elements | 52 |
| 1.3 | Zalesak Disk: comparison of the volume loss by number of elements | 54 |
| 2.1 | Parameters of the dam-break test case | 80 |
| 2.2 | Parameters of the rising bubble test case | 83 |
| 2.3 | Parameters of the Rayleigh–Taylor instability test case | 90 |
| 3.1 | Parameters of the 2D dam-break test case with mesh adaptation | 105 |
| 3.2 | Parameters of the rising bubble test case with anisotropic mesh adaptation | 108 |
| 3.3 | Parameters of the Rayleigh–Taylor instability test case with anisotropic mesh adaptation | 112 |
| 3.4 | Parameters for the simulation of the dam-break test case in 3D | 117 |
| 3.5 | Parameters for the simulation of the dam-break test case in 3D | 120 |
| 3.6 | Parameters for the simulation of the 3D test case of Rayleigh–Taylor instability | 123 |
| 4.1 | Physical properties for the vapor and the water | 143 |
| 4.2 | Parameters of the boiling case | 144 |
| 4.3 | Fixed parameters of the 3D quenching test cases | 149 |

General introduction

Contents

| | |
|--|-----------|
| Industrial motivations | 3 |
| Interface capturing methods | 4 |
| Volume-of-Fluid method | 5 |
| Level-set method | 8 |
| Diffuse-interface method | 10 |
| Objectives of the thesis | 14 |
| Numerical framework | 15 |
| Layout of the thesis | 15 |
| Bibliography | 16 |

Résumé en Français

Ce chapitre présente le contexte général de la thèse où les motivations industrielles ont mené à l'initiation d'un projet académo-industriel dans lequel cette thèse s'inscrit : la chaire ANR INFINITY. Cette chaire a pour but de développer un outil de simulation numérique pour la trempe industrielle permettant ainsi aux divers industriels partenaires de la chaire de considérablement améliorer leurs fabrications industrielles nécessitant un procédé de trempe. Ce procédé industriel met en jeu une multitude phénomènes physiques (échanges thermiques, dynamique des fluides, mouillage, tension de surface,...) pour permettre le refroidissement d'un solide, initialement à haute température, au sein d'un fluide (liquide ou gaz) de plus basse température.

Lors de la trempe d'un solide au sein d'un liquide comme l'eau, la température du liquide proche du solide se met à augmenter pour atteindre la température de saturation ce qui provoque la création d'une fine couche de vapeur enrobant le solide. Cette couche de vapeur possède donc une température plus élevée que celle du liquide qui n'est plus au contact du solide. Ainsi, le solide se refroidit plus lentement ce qui amène une perte de qualité. En effet, plus le refroidissement de la pièce industrielle est rapide, meilleure sera la qualité de cette pièce.

Comprendre les échanges thermiques ayant lieu dans tout l'environnement de la pièce est donc de la plus haute importance pour espérer améliorer la qualité du matériau. À travers toute cette thèse, un intérêt particulier sera établi numériquement sur les échanges ayant lieu dans le mélange liquide/vapeur. Pour cela, il est nécessaire d'adopter une méthode de capture d'interface permettant d'apporter des informations sur la physique du système ainsi qu'une robustesse numérique. Un bref descriptif des principales méthodes de capture d'interface a été établi dans ce chapitre et une de ces méthodes répondant aux critères d'adoption a été choisie pour être implémentée au sein de la bibliothèque numérique existante CIMLIB-CFD développée par l'équipe académique à travers la méthode des éléments finis \mathbb{P}_1 .

La librairie CIMLIB-CFD est à la base du développement du futur logiciel de simulation numérique issu de la chaire permettant ainsi de traiter des cas de trempe industriels avancés. Après avoir défini les objectifs de cette thèse, une vue globale de sa composition est présentée et sera détaillée dans les chapitres suivants.

Industrial motivations

To meet the challenges of competitiveness and technological innovation in the energy, automotive, air, and space transport sectors, manufacturers are placing a strong demand on obtaining quality material for their production. This demand varies according to the structure of the material and its geometry due to the diversity of applications such as the production of cars, airplanes or power plants, aircraft or energy plants. Today, to improve the quality of the material, the industrialists use a metallurgical process, called the quenching process.

The quenching process is a heat treatment operation consisting of heating a material at a high temperature for a certain time and then cooling suddenly by immersing it in a liquid (water, polymer, etc.) at a lower temperature to give a certain micro-structure to the metal to obtain desired mechanical properties (Figure 1).



Figure 1: Industrial quenching (from heattreatmentsservices.com)

Heating a material in a furnace allows the diffusion of specific atoms (e.g., carbon atoms). To prevent segregation of these atoms during the cooling phase and therefore inhomogeneity of the microstructure, the cooling must be sudden. Consequently, the control of the cooling rate is of the utmost importance in quenching.

When in contact with the liquid, the high-temperature difference leads to boiling, producing then a film of vapor enveloping the material. This film of vapor acts as a thermal mantle which decreases the cooling rate of the material. Controlling the cooling during the quenching process is, therefore, a major issue. The approach currently followed by the industrialists to study the cooling of the material relies on models based on averaged semi-empirical parameters, called exchange coefficients. These are limited to particular scenarios and for a specific geometrical evolution of the flow. They are determined experimentally and multiplying these experiments

is not an economically viable strategy because of the cost of this process. Thus, physical modeling of the system coupled with numerical simulation is a promising alternative since Computational Fluid Dynamics (CFD) offers powerful numerical tools thanks to the increase in computational performance. Although numerical simulation is beginning to be used in the metallurgy industry, there is no software available today that can reliably simulate a quenching process because of the complexity of the physical phenomena involved (Figure 2).



Figure 2: Multiphysics phenomena (pictures from conmecheng.com and heattreatmart.com)

To develop this new numerical tool, the ANR industrial chair *INFINITY* (Figure 3), a 4-year project gathering academic and industrial partners has been initiated. This software will allow industrialists to accelerate the decision support to obtain a high-quality material, without cracks and with the desired properties.



Figure 3: ANR industrial chair: *INFINITY*

However, a clear understanding of the physical phenomena is required and remains today a major challenge for both the industrial and academic sectors. For example, modeling the liquid/vapor phase change as well as studying the heat exchange between the liquid and the vapor occurring during boiling due to temperature differences are one of the many challenges to be addressed. To achieve this modeling, it is necessary to describe the evolution of the liquid/vapor interface in a precise way.

Interface capturing methods

Accurate computing of the interface evolution remains a challenge. Interface capturing methods are widely used in the computation of flow problems with moving boundaries and interfaces [1]. This category of problems includes free-surface [2, 3] and interfacial flows referring to multiphase flow problems [4] that involve several immiscible fluids, like liquid-gas or liquid-liquid systems separated by time-evolving sharp interfaces. Flow problems with moving interfaces are also involved in fluid-structure interaction problems [5] combining fluid flow and solid mechanics to capture the interaction between the solid and the fluid.

Interface capturing methods are then crucial to understanding heat transfer for a liquid/gas flow [6]; however, interface moving problems offer many computational challenges like precision, computational cost, or robustness. The particularity of the interface capturing methods is that they can locate the interface within the Eulerian framework by capturing the interface. Concretely, an appropriate field is introduced for keeping track of its evolution. This is different from tracking the interface within the Lagrangian framework by following marking points located on the interface [7, 8]. Different interface capture methods exist and for each one of these methods, the appropriate field describing the interface is named differently like volume-fraction function, level-set function, or phase-indicator function. More references to these methods will be given below in each dedicated subsection.

In all the following, Ω denotes a domain of \mathbb{R}^d , where d is the geometric dimension, with a smooth enough boundary $\partial\Omega$. \mathbf{n} represents the unit exterior normal to the boundary. Coordinates of Ω and $\partial\Omega$ are respectively denoted by \mathbf{x} and s , and accordingly $d\mathbf{x}$ and ds stand for the d -dimensional and $(d-1)$ -dimensional Lebesgue measure. $t_f > 0$ denotes the final time. The velocity field of the flow is denoted by \mathbf{u} . A computational cell is denoted by K and its volume by $|K|$.

Volume-of-Fluid method

In the class of interface capturing methods, an approach consists in approximating the localization of the interface and assigning properly the fluid properties by defining a volume-fraction function. This approach is called the Volume-of-Fluid (VoF) method [9–11]. One considers two non-miscible and incompressible fluids occupying a domain Ω . The region $\Omega_{ref} \subset \Omega$ occupied by the reference fluid at a given instant t is defined by a phase indicator function $H : \Omega \times [0, t_f] \rightarrow \{0, 1\}$ as follows:

$$H(\mathbf{x}, t) = \begin{cases} 1 & \text{if } \mathbf{x} \in \Omega_{ref}, \\ 0 & \text{if } \mathbf{x} \in \Omega_{ref}^c. \end{cases} \quad (1)$$

In the absence of phase change, each fluid parcel retains its phase indicator value during its motion. Therefore, the material derivative of H is zero, i.e.

$$\frac{DH}{Dt} = \partial_t H + (\mathbf{u} \cdot \nabla)H = 0 \quad (2)$$

The volume-fraction function C_K is defined, in each computational cell K , as the spatial average of the phase indicator function H :

$$C_K(t) := \frac{1}{|K|} \int_K H(\mathbf{x}, t) \, d\mathbf{x} \quad (3)$$

Cells in which $C_K = 1$ are full of reference fluid, those where $C_K = 0$ are full of the other fluid, while those for which $0 < C_K < 1$ contain a part of the interface. By integrating Equation (2) over K and by using the definition introduced in (3), it comes

$$|K| \partial_t C_K(t) + \int_{\partial\Omega} (\mathbf{u} \cdot \mathbf{n}) H(s, t) \, ds = \int_{\Omega} H \nabla \cdot \mathbf{u} \, d\mathbf{x} \quad (4)$$

Since $\nabla \cdot \mathbf{u} = 0$ for incompressible flows, the term in the right-hand side of (4) should be vanished. However, the approximation may not enforce the divergence-free constraint at the discrete level. Two main categories of VoF methods exist in the literature: geometric VoF and algebraic VoF methods. In geometric VoF methods an approximation to H is found geometrically (e.g. by a plane), whereas in algebraic VoF [9] methods H is represented by a function (e.g. polynomial or trigonometric function).

Geometric VoF method

Geometric VoF methods proceed in two steps. First, the interface is reconstructed in each computational cell knowing the volume fraction field. Second, the reconstructed interface is advected by computing the fluxed volume across each computational cell using geometric methods. For the first task, the most widely used method is the Piecewise Linear Interface Calculation (PLIC) scheme [12]. In this approach, the interface is approximated in each interfacial cell as a line in two dimensions or a plane in three dimensions as

$$\mathbf{n} \cdot \mathbf{x} + \alpha = 0 \quad (5)$$

where α is the constant in the plane equation that is selected to enforce that the volume cut by the interface is equal to C_K in the computational cell. The main choice left to the user is how to compute the interface normal \mathbf{n} [13]. Once the normal \mathbf{n} has been calculated, the next step is to compute α [11]. For the second task, the interface is advected by integrating (4) in time. The main decision left to the user is on how the volume fluxes of the reference fluid are calculated. Two classes of

advection algorithms have emerged: (i) split methods that rely on operator-splitting to perform a series of one-dimensional advections in each spatial dimension and (ii) unsplit methods, which advect the interface in one step.

Split methods are algorithmically straightforward to implement compared to multidimensional (unsplit) schemes. Unsplit schemes involve the computation of polyhedral complex flux in computational cells containing the interface. These computations are expensive and can lead to significant parallel load imbalance if left untreated [14]. On the other hand, unsplit methods have the advantage to require only one advection and reconstruction step. This category of methods is then more amenable for general three-dimensional unstructured meshes. Split advection schemes use operator-splitting to decompose (4) into a series of one-dimensional advection. Because spatial derivative terms are generally non-zero, the right-hand side in (4) is retained. This is in contrast to unsplit schemes which omit the last term due to incompressibility constraint $\nabla \cdot \mathbf{u} = 0$. Unsplit VoF advection methods compute and transport the fluxed volume in one step. In two dimensions, the first split advection scheme to satisfy the boundedness condition, $0 \leq C_K \leq 1$, and mass conservation in incompressible flow is known as the Eulerian implicit – Lagrangian explicit scheme [8].

It is important to note that in VoF advection schemes, discrete mass conservation is only guaranteed if $\nabla \cdot \mathbf{u} = 0$ is satisfied discretely in every grid cell. In practice, the condition $\nabla \cdot \mathbf{u} = 0$ is typically only satisfied up to some user-specified tolerance through the iterative solution of the Poisson equation for pressure [15].

Algebraic VoF methods

Algebraic VoF methods are probably one of the oldest classes of interface capturing methods and the first of the VoF-type methods [9]. In these methods, the volume fraction C_K is obtained via Equation (4) with a numerical approximation (volume-averaged, polynomial or hyperbolic-tangent representation) for the phase indicator function H . These methods compute the fluxes algebraically without the need for geometric reconstruction of the interface. Algebraic VoF methods can be classified into two categories based on an approach used to compute the fluxes: compressive class and THINC class (tangent of hyperbola for interface capturing).

Compressive schemes use the information of the orientation of the interface (interface normal) with respect to the cell face and compute the face flux for the VoF function. The precision of the compressive algebraic VoF method is generally found to be about an order of magnitude lower than geometric VoF methods. An artificial interface sharpening term is typically added to the right-hand side of Equation (4)

to avoid the diffusion of the interface when the interface gets deformed within flows with high strain rates.

THINC schemes [16] are a group of relatively new methods within algebraic VoF where a hyperbolic-tangent profile is assumed for the phase indicator function H within the cell containing the interface, and the fluxes are computed algebraically according to this assumption from Equation (4). The accuracy of these methods can be close to the geometric VoF method at a lesser cost. Unlike the compressive scheme, these methods do not require artificial compression.

To summarize the VoF method, each cell is represented by its liquid volume fraction, and the interface is marked by a volume-fraction function. The VoF method is conservative and can deal with extensive topological changes in the interface. Despite its good mass conservation properties, the interface reconstruction can involve considerable computational effort, especially for three-dimensional problems. Another drawback is that it is difficult to compute accurate interface normal and curvature because of the discontinuity of the color function which can make the simulation of an evolving interface very challenging. In particular, authors in [17] argue that the VoF method is inherently limited by the second-order accuracy of schemes used for advection in this context. However, it is still one of the most popular techniques in front capturing due to its good conservation properties.

Level-set method

An alternative to the VoF method in capturing fronts is the level-set method. This method was introduced by Osher & Sethian (1999) [18, 19]. Due to its simplicity and ability to capture interfaces, it has been widely applied in a variety of fields, such as incompressible fluid dynamics, combustion, image processing, etc. This method considers the zero isocontour of a function α which implicitly defines the interface Γ of two-phase flows:

$$\Gamma := \{\mathbf{x} \in \Omega \text{ such that } \alpha(\mathbf{x}, t) = 0, \forall t \in [0, t_f]\}$$

This function α is chosen as a signed distance function $\alpha : \Omega \times [0, t_f] \rightarrow \mathbb{R}$ called level-set function, that represents the Euclidean distance d_{eucl} to the interface Γ of a position $\mathbf{x} \in \Omega = \Omega_1 \sqcup \Gamma \sqcup \Omega_2$ at an instant $t \in [0, t_f]$:

$$\alpha(\mathbf{x}, t) := \pm \min_{\mathbf{x}_\Gamma \in \Gamma} d_{eucl}(\mathbf{x}, \mathbf{x}_\Gamma) \begin{cases} > 0 \text{ if } \mathbf{x} \in \Omega_1, \\ = 0 \text{ if } \mathbf{x} \in \Gamma, \\ < 0 \text{ if } \mathbf{x} \in \Omega_2, \end{cases} \quad (6)$$

Ω_i denotes the region occupied by the fluid $i \in 1, 2$. The sign of α is defined as positive on one side of the interface and negative on the other. This function allows to identify the location of the interface (Figure 4).

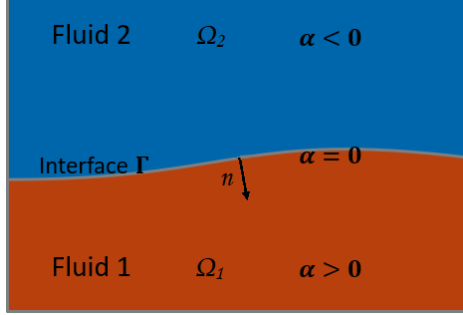


Figure 4: Level-set function α for a two-fluid flow

In the case of two incompressible fluids separated by the interface Γ within a domain Ω , the level-set function is advected by the fluid velocity field \mathbf{u} :

$$\partial_t \alpha + (\mathbf{u} \cdot \nabla) \alpha = 0 \quad (7)$$

This equation describes the evolution of α in Ω over time.

In order to capture the interface accurately, the level-set function must be a distance function, that is,

$$|\nabla \alpha| = 1.$$

However, since the velocity field is not a simple uniform one, α loses its signed distance property after the advection step, and hence needs to be reinitialized by solving a Hamilton–Jacobi equation. This equation reconstructs the level-set with the exact zero isovalue of α . By introducing a virtual time τ , one searches ψ that has the same zero values as α such that:

$$\frac{\partial \psi}{\partial \tau} + S(\alpha)(|\nabla \psi| - 1) = 0, \quad (8)$$

$$\psi(\mathbf{x}, \tau = 0) = \alpha(\mathbf{x}, t), \quad (9)$$

where the sign function $S(\alpha)$ is defined as:

$$S(\alpha) := \begin{cases} 1 & \text{if } \alpha > 0 \\ 0 & \text{if } \alpha = 0 \\ -1 & \text{if } \alpha < 0 \end{cases} \quad (10)$$

Equation (8)-(9) can be rewritten as an advection equation:

$$\frac{\partial \psi}{\partial \tau} + \mathbf{U} \cdot \nabla \psi = S(\alpha), \quad (11)$$

$$\psi(\mathbf{x}, \tau = 0) = \alpha(\mathbf{x}, t), \quad (12)$$

with the velocity \mathbf{U} computed as:

$$\mathbf{U} = S(\alpha) \frac{\nabla \psi}{|\nabla \psi|} \quad (13)$$

The level-set method offers many advantages over other methods such as:

1. accurate computation of normal and curvature which are naturally defined from α by

$$\mathbf{n} := \frac{\nabla \alpha}{|\nabla \alpha|} \quad (14)$$

and

$$\kappa := \nabla \cdot (\mathbf{n}), \quad (15)$$

due to the smoothness of the α field.

2. straightforward extensions to Cartesian adaptive mesh refinement.

This method can handle the merging and breaking of interfaces automatically, so the interface never has to be explicitly reconstructed as with the VoF method. However, the biggest disadvantage of this method is the fact that the mass of each phase is not conserved, a crucial requirement for numerical modeling of realistic two-phase flows because of a nonphysical loss/gain of the fluid at each time step. As time evolves, even a negligibly small error can be accumulated to a sufficiently large magnitude and may finally lead to the solution breaking down [17]. this kind of mass loss/gain mainly comes from two aspects. Firstly, the discretization of the level set equation can lead to numerical dissipation which requires remedying using a higher-order and conservative discretization scheme. Secondly, a mass loss/gain can occur from the reinitialization process necessary to keep the level-set function as a signed distance function. Another disadvantage of this method is the choice of the reinitialization frequency because of the more frequent the reinitialization, the longer the computation time.

To summarize, the level-set method is an interface capturing method which distributes the physical properties of each phase and captures the evolution of the interface. Its ability to deal with complex topology changes of the interface and the ease to compute from the level-set function quantities such as the curvature of the interface or the normal field to the interface makes it very useful in our context: heat transfer simulation and particularly in phase change.

Diffuse-interface method

In contrast to the VoF and level-set methods in which the interface separating two fluids is sharp, diffuse-interface models represent the interfacial region by continuous variations of an order parameter φ , such as concentration or density. These variations give the interface a non-zero thickness (*i.e.* it is diffuse) and an internal structure (Figure 5). Moreover, the order parameter is described smoothly through the interfacial region which is identified by a range of constant contours. This means that interface tracking is unnecessary. Originally, the diffuse-interface model is based on the Van der Waals model of capillarity [20]. It consists of describing an interface separating a liquid and a vapor phase of a pure fluid with a thermodynamic model. Specifically, the internal structure of an interface is mostly at equilibrium and only perturbed by dynamic effects. Moreover, in the thermodynamic model of Van der Waals, the energy of the fluid allows recovering of surface tension considered as energy concentrated at the interface. When the interface thickness approaches zero, the diffuse-interface model tends to be identical to a sharp interface, like in the level-set formulation.

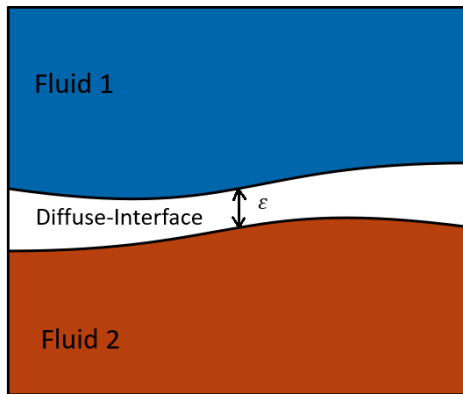


Figure 5: Diffuse-interface for a bi-fluid system

Since then, the diffuse-interface theories have been used in modeling physical phenomena such as superconductivity [21], spinodal decomposition [22, 23], ordering transition in alloys [24, 25], and hydrodynamic [26]. It also has been used in critical phenomena [27], and phase transitions - like dendritic growth [28, 29] -, and solidification [30, 31]. With the development of computers, the diffuse-interface method has recently gained popularity for numerical simulations of two-phase flow problems. This kind of problem is very challenging to numerically simulate, especially in three dimensions, because it is a moving boundary problem. It needs a particular numerical treatment to apply the boundary conditions at the moving interfaces, which is difficult [32]. This difficulty can be overcome with the help of diffuse-interface methods. These numerically attractive methods can remove the

difficult problem of the treatment of the boundary conditions at the interfaces by describing the moving of an entire two-phase system, even within interfacial regions with a continuous transition.

These are the main advantages to consider a thickness for the interface. Despite these advantages, it is important to note that when equations are numerically solved, they need to be discretized in time and space. In spatial discretization, the interface must be captured by the mesh, which means that the mesh size must be smaller than the interface thickness. Remember that interface models have been derived based on physical arguments, especially that the interfacial internal structure is physical and therefore, the interface thickness too. In this case, the scale of the interface thickness is of the order of 10^{-9} m. Thus, the mesh size should be $h \leq 10^{-9}$ m, which is extremely small for many applications and especially industrial applications because they are at a macroscopic scale. Too many mesh cells would be necessary only to capture the interfacial regions. This leads to a very important computation cost which is a big challenge. A way to manage this major issue is to develop an adaptive mesh refinement technique for capturing the interfacial regions. Indeed, because many physical phenomena happen near the interface, a fine spatial discretization is necessary to capture them. But for mesoscopic scale problems, like the size of bubbles or droplets, or macroscopic scale problems, like industrial processes, all the physical phenomena of interest occur at a similar scale. Thus, a scale separation with the interface thickness can be justified. This means that the thickness must be adapted so that a reasonable mesh size can be used to capture the interface structure. The interface thickness should then be a free parameter whose value can be arbitrarily considered.

Although in realistic immiscible two-phase flow applications, the physical thickness of the interface is practically impossible to resolve numerically, this method offers some desirable properties which have attracted the interest of two-phase flow modelers in recent years. For instance, authors in [26] developed a tool for two-phase flows of Newtonian fluids based on the diffuse-interface model. In [33, 34], a diffuse-interface model, based on the so-called *Model H* [27, 35, 36], has been used to simulate Rayleigh–Taylor instability, capillary waves, and contact line dynamics. Simulation of phase separation under shear has been done in [37]. In [38], authors showed comparable results between those obtained by analyzing the flow near a moving contact line based on the *Model H* and those from the association of Navier–Stokes equations with a sharp interface.

For these applications, the diffuse-interface method, also called the phase-field method, is either based on Cahn–Hilliard or Allen–Cahn equations, which are two important gradient flows of the Ginzburg–Landau–Wilson free energy functional

[21]. In a bounded physical domain given by Ω this energy functional is defined on the $H^1(\Omega)$ space in the form

$$\begin{aligned} \mathcal{E} &: H^1(\Omega) \longrightarrow [0, \infty] \\ \varphi &\longmapsto \mathcal{E}(\varphi) = \int_{\Omega} \left(F(\varphi) + \frac{\epsilon^2}{2} |\nabla\varphi|^2 \right) d\mathbf{x} \end{aligned} \quad (16)$$

where φ is the so-called order parameter or phase-field function, ϵ is the interface thickness and F is the free energy of the system. The Allen–Cahn phase-field model [24, 25] consists of a nonlinear convection–diffusion–reaction equation. Different well-established numerical methods could be implemented for solving such equations. This easy-to-implement second order PDE is widely used in material science applications where the phase change occurs. This equation is in fact the $L^2(\Omega)$ gradient flow of the energy functional defined in (16),

$$\partial_t \varphi + \nabla \cdot (\varphi \mathbf{u}) = \frac{\delta \mathcal{E}}{\delta \varphi}(\varphi) \quad (17)$$

This equation is in non-conservative form. The inherent lack of conservation of φ in the Allen–Cahn equation is a major limitation for immiscible two-phase flows. In the computational studies of the Allen–Cahn equation, one of the major challenges is to effectively resolve the thin interfacial layer. Variational discretization based on the Galerkin finite element method of the equation leads to spurious oscillations in the solution when the convection or reaction effects are dominant [39]. Although linear stabilization methods such as Streamline–Upwind–Petrov–Galerkin (SUPG) [40] and Galerkin/Least-Squares (GLS) can reduce spurious oscillations, the solution has oscillatory behavior near the region of high gradients. The solution thus obtained can affect the physical results and lead to the wrong prediction of the underlying phenomenon being studied. Regarding phase-field modeling of two-phase flows, the interface between the two fluids is represented by the order parameter φ which is solved by the Allen–Cahn equation. The variable φ is also used to define the physical properties of the fluid phases such as density and viscosity, which should always be positive. Oscillations in φ can lead to unbounded values which can cause the density or viscosity to be negative, thus producing unstable or nonphysical results. Despite many existing investigations, there is still a lack of complete understanding today on how the spatial mesh size h and time-step size Δt should be chosen in connection to the value of the small parameter ϵ .

The Cahn–Hilliard equation [41] introduced to describe the initial stage of spinodal decomposition [22] is a more popular option because it conserves total mass. This equation is given by,

$$\partial_t \varphi + \nabla \cdot (\varphi \mathbf{u}) = \nabla \cdot \left(\frac{\delta \mathcal{E}}{\delta \varphi}(\varphi) \right) \quad (18)$$

is the $H^{-1}(\Omega)$ gradient flow of the energy functional defined in (16). The density, viscosity, and other physical quantities are characterized by the order parameter φ which evolution is governed by (18). Because φ allows for a smooth transition between the liquid phase and the vapor phase, the physical properties are changing across the interface. However, the phase-field function φ changes quickly near the interface and, hence, must be well resolved. In other words, a relatively large number of grid points near the interface are needed. An appropriate choice of the measure of interface thickness value noted ϵ is important for accurate calculations. Taking too large ϵ may give rise to nonphysical solutions, while too small ϵ to numerical difficulties. The Cahn–Hilliard model, like the other diffuse-interface models can be viewed as a physically motivated level-set method. This model is therefore a promising way to describe the transition between the liquid phase and its vapor. Consequently, fluid interactions and phase change can be solved in the whole domain.

Objectives of the thesis

This thesis is part of the desire to have a numerical framework dealing with complex industrial cases. For this reason, it is necessary to develop new solvers that enrich the library of methods currently used in the team. This desire relies on the will to consider a new approach of interface capturing enabling the obtaining of new information about the physics of the system and bringing numerical robustness. The phase-field method is based on an energetic approach of the interface separating the phases that which is not the case for the currently used interface capturing method. Furthermore, the method owns good properties to model the capillary action - involved in the wetting - and considers contact angles. Directed by a perspective of industrial applications, this interface capturing aims to be unified with other physical models for a multiphysics characteristic and multiple applications to the industrial numerical simulation.

This thesis consists of a first entrance of the phase-field method in the research work of the team. The purpose is to develop a numerical tool implementing this method with a \mathbb{P}_1 finite element method in the CIMLIB-CFD library. This involves a presentation and a theoretical study of the considered interface capturing method as well as a numerical study. For an application on physical systems involving fluid movement, an understanding of the way to consider the interface capturing in the framework of the fluid dynamics is required. Therefore, a theoretical study about the coupling with fluid dynamics must be done. With the will to perform CFD simulations, a numerical study can be considered as well. In the framework of the INFINITY project, simulations of the quenching process are aimed. This implies extending the model studied and developed in this thesis to the consideration of the

temperature evolution within the systems. With this accomplishment, a challenging multiphysics and unified solver can be designed in the proposed work, which is a real breakthrough and innovation allowing us to robustly deal with realistic industrial conditions of the quenching process in the future.

Numerical framework

The numerical experiments that we will consider in this thesis are all implemented with CIMLIB-CFD, a finite element library for automated finite element-based scientific computing that provides high-level capabilities in advanced computing in material forming and computational fluid dynamics. It offers access to high-performance linear algebra, including a parallelization based on MPI, supported through the incorporation of open-source libraries such as PETSc. This scientific library has been developed by the Computing & Fluid (CFL) team at the Center for Material forming (CEMEF), a research laboratory of Mines Paris - PSL Research University. It represents an object-oriented program, written in C++, and gathers the numerical development of the team members (Ph.D. students, researchers, and associate professors...). CIMLIB-CFD aims at providing a set of tools that can be gathered to perform numerical simulations of industrial processes, like the quenching process, in collaboration with industrial partners.

Layout of the thesis

After the present introduction chapter about the motivations of this thesis and an overview of the main interface capturing methods, the thesis is divided into four chapters. Chapter 1 is an introduction to the Cahn–Hilliard equations considered as an interface capturing method. Chapter 2 is dedicated to the coupling of the Cahn–Hilliard equations with the dynamics governing multiphase flows. For these two chapters, mathematical and numerical models will be presented as well as a series of numerical simulations for a numerical verification and validation of the method. In Chapter 3, different approaches to improve the numerical method are used to perform industrial type simulation. A first approach for modeling the phase change at the interface with the phase-field function within a multiphase flow is detailed in Chapter 4. Numerical multiphysics simulations for the quenching process will be presented. Finally, a conclusion chapter will explore the limits and the possible extensions of the present work to include more features in future contributions.

Bibliography

- [1] S. Mirjalili, S. S. Mirjalili, and M. S. Sundar, Dodd. Interface-capturing methods for two-phase flows: An overview and recent developments. *Center for Turbulence Research - Annual Research Briefs 2017*, pages 117–135, 2017. [5](#)
- [2] R. A. Cairncross, P. R. Schunk, T. A. Baer, R. R. Rao, and P. A. Sackinger. A finite element method for free surface flows of incompressible fluids in three dimensions. Part I. Boundary fitted mesh motion. *International Journal for Numerical Methods in Fluids*, 33(3):375–403, 2000. [5](#)
- [3] S. N. Elgeti, H. Sauerland, L. H. Pauli, and M. Behr. On the Usage of NURBS as Interface Representation in Free-Surface Flows. *International journal for numerical methods in fluids*, 69(1):73–87, 2012. [5](#)
- [4] J. H. Ferziger and M. Perić. *Computational Methods for Fluid Dynamics*. Springer, Berlin, 3rd edition, 2002. [5](#)
- [5] Y. Bazilevs, K. Takizawa, and T. E. Tezduyar. *Computational Fluid-Structure Interaction: Methods and Applications*. Wiley Series in Computational Mechanics. Wiley, 2013. [5](#)
- [6] T. L. Bergman, A. S. Lavine, F.P. Incropera, and D. P. Dewitt. *Fundamentals of Heat and Mass Transfer*. John Wiley & Sons, 8th edition edition, 2017. [5](#)
- [7] S. McKee, M. F. Tomé, V. G. Ferreira, J. A. Cuminato, A. Castelo, F. S. Sousa, and N. Mangiavacchi. The MAC method. *Computers & Fluids*, 37(8):907–930, 2008. [5](#)
- [8] G. Tryggvason, R. Scardovelli, and S. Zaleski. *Direct numerical simulations of gas-liquid multiphase flows*. Cambridge University Press, 2011. [5](#), [7](#)
- [9] C. W. Hirt and B. D. Nichols. Volume of Fluid (VOF) method for the dynamics of free boundaries. *Journal of Computational Physics*, 39(1):201–225, 1981. [5](#), [6](#), [7](#)
- [10] D. Gueyffier, J. Li, A. Nadim, R. Scardovelli, and S. Zaleski. Volume-of-Fluid Interface Tracking with Smoothed Surface Stress Methods for Three-Dimensional Flows. *Journal of Computational Physics*, 152(2):423–456, jul 1999.
- [11] R. Scardovelli and S. Zaleski. Direct numerical simulation of free-surface and interfacial flow. *Annual Review of Fluid Mechanics*, 31(1):567–603, 1999. [5](#), [6](#)

-
- [12] R. B. DeBar. Fundamentals of the KRAKEN code. Eulerian hydrodynamics code for compressible nonviscous flow of several fluids in two-dimensional (axially symmetric) region. Technical report, California Univ., Livermore (USA). Lawrence Livermore Lab, 1974. [6](#)
- [13] D. L. Youngs. Time-dependent multi-material flow with large fluid distortion. *Numerical Methods for Fluid Dynamics*, 1982. [6](#)
- [14] L. Jofre, R. Borrell, O. Lehmkuhl, and A. Oliva. Parallel load balancing strategy for volume-of-fluid methods on 3-d unstructured meshes. *Journal of Computational Physics*, 282(C):269–288, 2015. [7](#)
- [15] J.-L. Guermond and A. J. Salgado. A splitting method for incompressible flows with variable density based on a pressure poisson equation. *Journal of Computational Physics*, 228:2834–2846, 2009. [7](#)
- [16] F. Xiao, Y. Honma, and T. Kono. A simple algebraic interface capturing scheme using hyperbolic tangent function. *International Journal for Numerical Methods in Fluids*, 48(9):1023–1040, 2005. [8](#)
- [17] T. W. H. Sheu, C. H. Yu, and P. H. Chiu. Development of level set method with good area preservation to predict interface in two-phase flows. *International Journal for Numerical Methods in Fluids*, 67(1):109–134, 2011. [8](#), [10](#)
- [18] S. Osher and J. A. Sethian. Fronts propagating with curvature-dependent speed: Algorithms based on Hamilton–Jacobi formulations. *Journal of Computational Physics*, 79(1):12–49, 1988. [8](#)
- [19] J. A. Sethian. *Level Set Methods and Fast Marching Methods: Evolving Interfaces in Computational Geometry, Fluid Mechanics, Computer Vision, and Materials Science*. Cambridge University Press, 1999. ISBN 978-0-521-64557-7. [8](#)
- [20] J. D. Van Der Waals. The thermodynamic theory of capillarity under the hypothesis of a continuous variation of density. *Journal of Statistical Physics*, 20(2):200–244, 1894. [11](#)
- [21] V. L. Ginzburg and L. D. Landau. On the theory of superconductivity. *Sov. Phys. JETP*, 20:1064, 1950. [11](#), [13](#)
- [22] J. W. Cahn and J. E. Hilliard. Free Energy of a Nonuniform System. I. Interfacial Free Energy. *Journal of Chemical Physics*, 28(2):258–267, 1958. [11](#), [13](#)

- [23] J. W. Cahn. On spinodal decomposition. *Acta Metallurgica*, 9(9):795–801, 1961. [11](#)
- [24] J. W. Cahn and S. M. Allen. A microscopic theory for domain wall motion and its experimental verification in Fe-Al alloy domain growth kinetics. *J. Phys. Colloques*, 38(C7):C7–51–C7–54, 1977. [11](#), [13](#)
- [25] S. Allen and J. W. Cahn. A microscopic theory for antiphase domain boundary motion and its application to antiphase domain coarsening. *Acta Metallurgica*, 27:1085–1095, 1979. [11](#), [13](#)
- [26] D. M. Anderson, G. B. McFadden, and A. A. Wheeler. Diffuse-interface in fluid mechanics. *Annual Review of Fluid Mechanics*, 30(1):139–165, 1998. [11](#), [12](#)
- [27] P. C. Hohenberg and B. I. Halperin. Theory of dynamic critical phenomena. *Reviews of Modern Physics*, 49(3):435–479, 1977. Publisher: American Physical Society. [11](#), [12](#)
- [28] R. Kobayashi. Modeling and numerical simulations of dendritic crystal growth. *Physica D: Nonlinear Phenomena*, 63(3):410–423, March 1993. [11](#)
- [29] A. Karma and W. J. Rappel. Quantitative phase-field modeling of dendritic growth in two and three dimensions. *Physical Review E*, 57:4323–4349, Apr 1998. [11](#)
- [30] A. Karma. Phase-field formulation for quantitative modeling of alloy solidification. *Phys. Rev. Lett.*, 87:115701, Aug 2001. [11](#)
- [31] B. Nestler, H. Garcke, and B. Stinner. Multicomponent alloy solidification: phase-field modeling and simulations. *Phys. Rev. E*, 71:041609, Apr 2005. [11](#)
- [32] D. Jamet, D. Torres, and J. U. Brackbill. On the Theory and Computation of Surface Tension: The Elimination of Parasitic Currents through Energy Conservation in the Second-Gradient Method. *Journal of Computational Physics*, 182(1):262–276, oct 2002. [11](#)
- [33] D. Jacqmin. Calculation of Two-Phase Navier–Stokes Flows Using Phase-Field Modeling. *Journal of Computational Physics*, 155(1):96–127, 1999. [12](#)
- [34] D. Jacqmin. Contact-line dynamics of a diffuse fluid interface. *Journal of Fluid Mechanics*, 402(1):57–88, 2000. [12](#)
- [35] V. Starovoitov. Model of the motion of a two-component liquid with allowance of capillary forces. *Journal of Applied Mechanics and Technical Physics*, 35:891–897, 1994. [12](#)

- [36] M. E. Gurtin. Generalized Ginzburg-Landau and Cahn-Hilliard equations based on a microforce balance. *Physica D: Nonlinear Phenomena*, 92(3):178–192, 1996. [12](#)
- [37] V. E. Badalassi, H. D. Cenicerros, and S. Banerjee. Computation of multiphase systems with phase field models. *Journal of Computational Physics*, 190(2):371 – 397, 2003. [12](#)
- [38] H. Ding, P. D. M. Spelt, and C. Shu. Diffuse interface model for incompressible two-phase flows with large density ratios. *Journal of Computational Physics*, 226(2):2078 – 2095, 2007. [12](#)
- [39] V. Joshi and R. K. Jaiman. A positivity preserving and conservative variational scheme for phase-field modeling of two-phase flows. *Journal of Computational Physics*, May 2018. [13](#)
- [40] R. Sevilla, O. Hassan, and K. Morgan. An analysis of the performance of a high-order stabilised finite element method for simulating compressible flows. *Computer Methods in Applied Mechanics and Engineering*, 253:15–27, 2013. [13](#)
- [41] J. W Cahn and J. E Hilliard. Spinodal decomposition: A reprise. *Acta Metallurgica*, 19(2):151–161, 1971. [13](#)

BIBLIOGRAPHY

Chapter 1

Cahn–Hilliard as an interface capturing method

Contents

| | | |
|------------|--|-----------|
| 1.1 | Introduction | 23 |
| 1.2 | Cahn–Hilliard origins | 23 |
| 1.3 | The governing equations | 25 |
| 1.4 | Mathematical properties | 29 |
| 1.5 | Space and time discretization for the Cahn–Hilliard equations | 35 |
| 1.5.1 | Mixed finite element framework | 35 |
| 1.5.2 | Time discretized scheme and linearization | 37 |
| 1.6 | Numerical properties | 40 |
| 1.7 | Simulation of an interface transport | 44 |
| 1.7.1 | Numerical convergence analysis | 45 |
| 1.7.2 | Pulse rotation | 48 |
| 1.7.3 | Single Vortex | 50 |
| 1.7.4 | Zalesak’s Disk | 52 |
| 1.8 | Conclusion | 55 |
| | Bibliography | 56 |

Résumé en Français

Ce chapitre présente la méthode phase-field permettant de capturer l'interface d'un mélange liquide/vapeur. Cette méthode modélise une interface diffuse, c'est-à-dire avec une certaine épaisseur séparant les phases liquide et vapeur. La méthode phase-field est basée sur les équations de Cahn–Hilliard qui prennent leurs origines dans la transformation de phase et la décomposition spinodale. Ces équations correspondent à une équation de continuité par rapport à une certaine variable, appelée paramètre d'ordre permettant d'identifier les phases pures (liquide et vapeur) et l'interface, et une équation dérivée d'une énergie dépendante du paramètre d'ordre, appelée énergie libre qui n'est nulle que dans les phases pures.

Pour mieux appréhender et comprendre ces équations, une étude mathématique et numérique les concernant est requise. Pour initier cette étude, quelques rappels de propriétés mathématiques de ces équations, accompagnés d'éléments de preuve sont présentés dans ce chapitre. En particulier, sont abordées la propriété de conservation de la masse des équations de Cahn–Hilliard sous l'hypothèse d'une vitesse d'advection à divergence nulle, la propriété de dissipation de l'énergie libre et la propriété d'estimation d'énergie des équations de Cahn–Hilliard.

Afin d'implémenter numériquement cette méthode de capture d'interface, il est nécessaire de procéder à une discrétisation spatiale et temporelle de ces équations pour en obtenir une formulation matricielle correspondante au système à résoudre. La discrétisation spatiale est formulée dans un cadre élément fini mixte. Pour la discrétisation temporelle, une linéarisation du terme non-linéaire est requise. Une fois la forme discrète des équations de Cahn–Hilliard obtenues, un rappel de la propriété d'estimation d'énergie discrète des équations est proposé, accompagnée d'éléments de preuve. En particulier, sont déduits les espaces d'énergie auxquelles appartiennent les solutions des équations de Cahn–Hilliard.

Pour tester le solveur de ces équations, une étape de vérification consistant en l'étude de convergence du solveur est réalisée. Elle permet de déduire l'ordre de convergence des solutions des équations selon le schéma numérique utilisé. Vient ensuite une étape de validation dans laquelle sont simulés des cas de transport d'interface pure pour une comparaison des performances avec celles obtenues par une autre méthode de capture d'interface déjà utilisée par CIMLIB : la méthode level-set.

1.1 Introduction

This chapter presents the framework of the interface capturing based on the phase-field method. It is the first step to simulating a liquid/vapor interaction within the quenching process. The origins of the phase-field method in the Cahn & Hilliard theory will first be investigated. The obtained governing equations will then be explained. In the next section, a study of some mathematical properties of these equations is proposed. To get a solver allowing the interface capturing, a full space and time discretization of these equations will be established. Then, some numerical properties of the discretized equations will be described. Finally, a series of numerical simulations will be performed to have a first glimpse of the solver's abilities.

1.2 Cahn–Hilliard origins

The origins of the Cahn–Hilliard equations come from phase transformations [1] and spinodal decomposition [2]. Phase transformations happen when a region in a material can decrease its free energy by modifying its structure, composition, or anything characterizing a phase within this material. These processes occur in many physical phenomena like melting, solidification, condensation, or evaporation for instance. Transformations from an unstable to a stable phase do not happen simultaneously within all the material but start in a part of the material due to spontaneous fluctuation in the material [3]. Spinodal decomposition is an example of phase transformation for which composition variations increase over time in a phase until two distinguished phases are created whose concentrations are determined by the equilibrium conditions. During this process, phases move from regions of low chemical potential to high chemical potential. That diffusion occurs to diminish the composition variations and to get a spatially uniform distribution of the chemical potential. The Cahn–Hilliard theory [4, 5] is based on a continuum equation for the kinetics of spinodal decomposition. In this theory, the free energy is a function of the concentration which has a spatial dependence. This concentration, called order parameter and denoted by φ , allows to identify two phases (Figure 1.1).

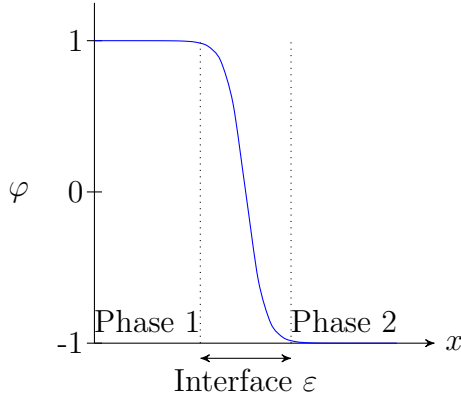


Figure 1.1: Order parameter identifying the phases

It should be understood as being a volume fraction or a mass fraction. With the volume (or mass) fraction meaning, the order parameter is the volume (or mass) fraction per unit volume (or mass) of one phase, in a system having two phases. It takes the value +1 in the first phase and -1 in the second one with a thin, smooth transition region of width ε between the two phases (Figure 1.2). Consequently the interface in which these two phases coexist is described by the zero isocontour of the order parameter φ : $\Gamma_t := \{\mathbf{x} \in \Omega \text{ such that } \varphi(\mathbf{x}, t) = 0\}$, $\forall t \in [0, t_f]$.

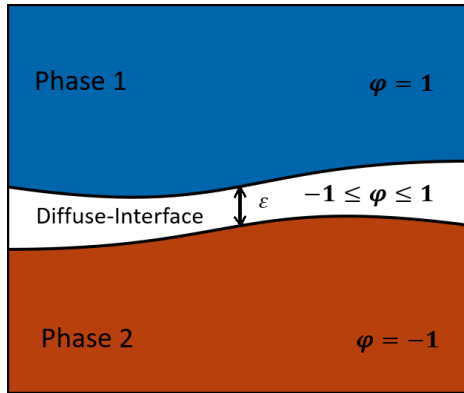


Figure 1.2: Two-phase system within the phase-field Cahn–Hilliard approach

The free energy must increase if φ varies. Specifically, the free energy is minimized for a constant φ , therefore in the pure phases when $\varphi = \pm 1$. By considering the gradient of the order parameter as a measure of spatial variations in the concentration, the Ginzburg–Landau free energy functional [6] is defined as follows:

$$\mathcal{E}(\varphi) := \int_{\Omega} F(\varphi) + \frac{\varepsilon^2}{2} |\nabla \varphi|^2 \, d\mathbf{x} \quad (1.1)$$

where ϵ is the interface thickness and F is the homogeneous free energy. This energy describes the entropy of mixing and takes into account the interaction between the two components. The second term of the integral is the energy used to form the interface separating the two phases. It penalizes large gradients and was introduced in the theory of phase transitions to model capillary effects. Some expressions for the free energy have been developed [4, 7–9]. One of the common expressions of the homogeneous free energy function is the quartic polynomial in the order parameter φ with a double-well potential form:

$$F(\varphi) = \frac{1}{4}(\varphi^2 - 1)^2 \quad (1.2)$$

for which two minima are reached for $\varphi = -1$ and $\varphi = +1$ corresponding to the two pure phases as represented in Figure 1.3.

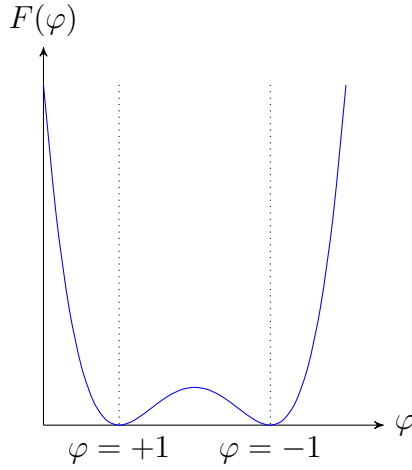


Figure 1.3: Homogeneous free energy

The double-well form is a fundamental physical assumption for the free energy F in the phase separation framework. A logarithmic expression of F can also be found in the literature [10–12]. However, because of its simplicity in the numerical framework, the usual form in the numerical literature is the polynomial expression (1.2). In the following, this expression of free energy is adopted, which is easier to work with.

1.3 The governing equations

The Cahn–Hilliard equation can be derived from the total free energy functional which can be rewritten as

$$\mathcal{E}[\varphi] = \mathcal{F}[\varphi] + \mathcal{G}[\varphi]$$

where,

$$\mathcal{F}[\varphi] = \int_{\Omega} F(\varphi) \, d\mathbf{x} \quad \text{and} \quad \mathcal{G}[\varphi] = \int_{\Omega} \frac{\varepsilon^2}{2} |\nabla \varphi|^2 \, d\mathbf{x}$$

In the following, boundary conditions on φ are assumed to be as follows:

$$\nabla \varphi \cdot \mathbf{n} = 0 \text{ on } \partial\Omega.$$

Definition 1.3.1. Let φ be a real function, the **directional derivative** of a functional $F[\varphi(x)]$ is defined by

$$\mathbf{D}_{[\lambda(x)]} F[\varphi(x)] := \lim_{\mu \rightarrow 0} \frac{F[\varphi(x) + \mu \lambda(x)] - F[\varphi(x)]}{\mu}$$

and is a linear functional of $\lambda(x)$ and admits $\int \alpha(x') \lambda(x') dx'$ as its representation, where

$$\alpha(x) := \frac{\delta F[\varphi(x)]}{\delta \varphi(x)} = \int \alpha(x') \delta(x' - x) dx'$$

Definition 1.3.2. One defines the *chemical potential* ω as the first derivative of the free energy functional \mathcal{E} with respect to the order parameter φ :

$$\omega := \frac{\delta \mathcal{E}}{\delta \varphi}$$

Proposition 1.3.3. *The chemical potential ω is related to the order parameter φ by the following relation:*

$$\omega = -\varepsilon^2 \Delta \varphi + F'(\varphi) \tag{1.3}$$

where $F'(\varphi) = \varphi(\varphi^2 - 1)$.

Proof. The directional derivative of $\mathcal{E}(\varphi)$ on ψ is

$$\mathbf{D}_{[\psi]} \mathcal{E}[\varphi] = \int_{\Omega} \psi \frac{\delta \mathcal{E}[\varphi]}{\delta \varphi} \, d\mathbf{x}$$

therefore

$$\frac{\delta \mathcal{E}[\varphi]}{\delta \varphi} = \frac{\delta \mathcal{F}[\varphi]}{\delta \varphi} + \frac{\delta \mathcal{G}[\varphi]}{\delta \varphi}$$

Lemma 1.3.4. *If*

$$F[\varphi] = \int f(\varphi(x)) dx$$

then,

$$\mathbf{D}_{[\lambda(x)]} F[\varphi(x)] = \int \lambda(x) \frac{\partial}{\partial \varphi} f(\varphi(x)) dx$$

whence

$$\frac{\delta F[\varphi(x)]}{\delta \varphi(x)} = \frac{\partial}{\partial \varphi} f(\varphi(x))$$

By **Lemma 1.3.4**,

$$\frac{\delta \mathcal{F}[\varphi]}{\delta \varphi} = \frac{\partial}{\partial \varphi} F(\varphi) = \varphi(\varphi^2 - 1)$$

Let $\lambda \in \mathbb{R}$ and $\psi \in H^1(\Omega)$, then

$$\begin{aligned} \mathcal{G}[\varphi + \lambda\psi] &= \int_{\Omega} \frac{\varepsilon^2}{2} |\nabla(\varphi + \lambda\psi)|^2 d\mathbf{x} \\ &= \int_{\Omega} \frac{\varepsilon^2}{2} |\nabla\varphi + \lambda\nabla\psi|^2 d\mathbf{x} \\ &= \int_{\Omega} \frac{\varepsilon^2}{2} (|\nabla\varphi|^2 + 2\lambda\nabla\varphi \cdot \nabla\psi + \lambda^2|\nabla\psi|^2) d\mathbf{x} \\ &= \int_{\Omega} \frac{\varepsilon^2}{2} |\nabla\varphi|^2 d\mathbf{x} + \int_{\Omega} \frac{\varepsilon^2}{2} 2\lambda\nabla\varphi \cdot \nabla\psi d\mathbf{x} + \int_{\Omega} \frac{\varepsilon^2}{2} \lambda^2 |\nabla\psi|^2 d\mathbf{x} \\ \mathcal{G}[\varphi + \lambda\psi] &= \mathcal{G}[\varphi] + \lambda\varepsilon^2 \left(\int_{\partial\Omega} \underbrace{\psi \nabla\varphi \cdot \mathbf{n}}_0 d\sigma - \int_{\Omega} \psi \Delta\varphi d\mathbf{x} \right) + \lambda^2 \int_{\Omega} \frac{\varepsilon^2}{2} |\nabla\psi|^2 d\mathbf{x} \end{aligned}$$

Therefore,

$$\frac{\mathcal{G}[\varphi + \lambda\psi] - \mathcal{G}[\varphi]}{\lambda} = - \int_{\Omega} \psi(\varepsilon^2 \Delta\varphi) d\mathbf{x} + \lambda \int_{\Omega} \frac{\varepsilon^2}{2} |\nabla\psi|^2 d\mathbf{x}$$

Thus,

$$\mathbf{D}_{[\psi]} \mathcal{G}[\varphi] = \lim_{\lambda \rightarrow 0} \frac{\mathcal{G}[\varphi + \lambda\psi] - \mathcal{G}[\varphi]}{\lambda} = \int_{\Omega} \psi \cdot \underbrace{(-\varepsilon^2 \Delta\varphi)}_{\frac{\delta \mathcal{G}[\varphi]}{\delta \varphi}} d\mathbf{x}$$

It comes that

$$\omega := \frac{\delta \mathcal{E}[\varphi]}{\delta \varphi} = \varphi(\varphi^2 - 1) - \varepsilon^2 \Delta\varphi$$

□

Since the order parameter $\varphi(\mathbf{x}, t)$ must be conserved within the domain Ω in the absence of sources and sinks, this quantity satisfies to the continuity equation:

$$\frac{d\varphi}{dt} + \nabla \cdot \mathbf{J} = 0 \quad (1.4)$$

where \mathbf{J} representing the mass flux is determined by the Fick’s first law as

$$\mathbf{J} = -D\nabla\varphi \quad (1.5)$$

where D is the diffusion coefficient, which means that the mass flux points in the direction of decreasing concentration. Note that the usual uniform quantity in equilibrium is not the concentration φ but the chemical potential ω which is a thermodynamic quantity, unlike φ . A more general form of this driving force for diffusion is obtained by considering the chemical potential $\omega(\mathbf{x}, t)$. For the i -th pure phase in the domain, \mathbf{J}_i is induced by the gradient of the chemical potential:

$$\mathbf{J}_i = -c_i m_i \frac{\omega_i}{\partial \mathbf{x}} \quad (1.6)$$

where c_i and m_i are respectively the concentration and the mobility of the i -th pure phase. Thus, the generalized statement of the Fick’s first law is given by:

$$\mathbf{J} = -M(\varphi)\nabla\omega \quad (1.7)$$

where $M(\varphi)$ is the mobility coefficient [13]. The diffusion within the system is always down the gradient of the chemical potential, *i.e.* from areas of high chemical potential to areas of low chemical potential. By combining this law with the continuity equation, it comes

$$\frac{d\varphi}{dt} + \nabla \cdot (-M(\varphi)\nabla\omega) = 0. \quad (1.8)$$

With Equations (1.3) and (1.8), the Cahn–Hilliard equations are written as the following mixed formulation of a non-linear fourth-order diffusion equation for the order parameter φ :

$$\frac{d\varphi}{dt} - \nabla \cdot (M(\varphi)\nabla\omega) = 0 \quad (1.9)$$

$$\omega + \varepsilon^2 \Delta\varphi - F'(\varphi) = 0 \quad (1.10)$$

Nowadays, this model is applied in diverse scientific fields, such as multiphase fluid flows, tumor growth, image processing, and population dynamics.

In order to capture the interface and transport it with a flow velocity \mathbf{u} in the fluid dynamics framework, the **Cahn–Hilliard equations** become:

$$\frac{\partial \varphi}{\partial t} + \nabla \cdot (\varphi \mathbf{u}) - \nabla \cdot (M(\varphi) \nabla \omega) = 0 \quad \text{in } \Omega, \quad (1.11)$$

$$\omega + \varepsilon^2 \Delta \varphi - F'(\varphi) = 0 \quad \text{in } \Omega. \quad (1.12)$$

with the following initial and boundary conditions:

$$\varphi(\cdot, 0) = \varphi_0 \quad \text{in } \Omega, \quad (1.13)$$

$$\frac{\partial \varphi}{\partial \mathbf{n}} = \frac{\partial \omega}{\partial \mathbf{n}} = 0 \quad \text{on } \partial \Omega \times [0, t_f]. \quad (1.14)$$

The degeneracy of the mobility $M(\varphi)$ involves difficulties in the study of the Cahn–Hilliard equations. The mobility $M(\varphi) = M$ is therefore assumed as constant and positive [14, 15]. However, in the literature [8, 16, 17], different forms of the mobility, constant or depending on φ , are suggested. Thus, the Cahn–Hilliard equations are equivalent to a convection-diffusion equation, with non-linear diffusion. The convection is given by the velocity field \mathbf{u} which is assumed fixed, known, and with enough regularity (at least $\mathbf{u} \in \mathcal{C}^1$), in all the present chapter. φ and ω are the two solution fields of these equations, which are consequently written under a mixed formulation. There is no exact solutions for $d \geq 2$. Numerical methods must be used to determine the solutions and study their evolution. Before tackling the numerical framework, one introduces some mathematical properties of these equations.

1.4 Mathematical properties

The role of mathematics is to enable the theoretical and numerical validation of the models and approximations. Three components are in permanent interaction:

1. **Modeling:** to identify the phenomena to model, to identify the scales and the pertinent parameters for the phenomenon to model, to propose mechanisms explaining these phenomena, to propose simplified systems for which the mathematical study is possible, etc...
2. **Theoretical analysis:** proof of the "well-posedness" characteristic of the models (existence and uniqueness of solutions), asymptotic analysis of the models (when the parameters tend toward zero), stability analysis of the stationary solutions (equilibrium points of the system), compactness study, etc...
3. **Numerical analysis:** proof of results justifying the relevance of the numerical approximation, effective calculation of the models approximated solutions,

predicting the unstable behaviors, parameter dependency analysis, developing more robust and faster codes based on the mathematical analysis of the system, etc...

In all the theoretical results introduced in the present chapter, the order parameter φ is assumed respecting the maximum principle. One notes that it is a strong hypothesis since it is the biggest difficulty in the mathematical analysis of the Cahn–Hilliard equations [18]

The present section will focus on a brief review of the mathematical results of the model (1.11)-(1.14) introduced previously. These governing equations describe the time-space evolution of the macroscopic quantities involved in the mixture composition, *i.e.* the order parameter φ and the chemical potential ω . The Equations (1.11)-(1.12) associated to the boundary conditions (1.13)-(1.14) verify the following property, also called **mass conservation of the Cahn–Hilliard equations**.

Definition 1.4.1. The mass m of the order parameter φ in the domain Ω is defined by:

$$m(\varphi) := \int_{\Omega} \varphi(\mathbf{x}, t) \, d\mathbf{x}$$

Proposition 1.4.2. For all solution φ of (1.11)-(1.12) verifying the conditions (1.13)-(1.14) with a regular enough velocity field \mathbf{u} verifying the divergence-free condition $\nabla \cdot (\mathbf{u}) = 0$ in Ω ,

$$\frac{d}{dt} m(\varphi) = 0$$

which implies

$$m(\varphi(t)) = m(\varphi_0)$$

Proof. Let φ a solution of (1.11)-(1.12) verifying (1.13)-(1.14) and \mathbf{u} regular enough verifying $\nabla \cdot (\mathbf{u}) = 0$ in Ω , then

$$\begin{aligned} \frac{d}{dt} m(\varphi(t)) &= \frac{d}{dt} \int_{\Omega} \varphi(\mathbf{x}, t) \, d\mathbf{x} \\ &= \int_{\Omega} \frac{d}{dt} \varphi(\mathbf{x}, t) \, d\mathbf{x} \\ &= \int_{\Omega} \nabla \cdot (M(\varphi) \nabla \omega) - \underbrace{\varphi \nabla \cdot (\mathbf{u})}_0 \, d\mathbf{x} \end{aligned}$$

$$\begin{aligned}
 &= \int_{\partial\Omega} M(\varphi) \underbrace{\nabla\omega \cdot \mathbf{n}}_{0 \text{ on } \partial\Omega} \, ds \\
 \frac{d}{dt} m(\varphi(t)) &= 0.
 \end{aligned}$$

It comes that $m(\varphi(t))$ is constant with respect to the time t :

$$m(\varphi(t)) = m(\varphi_0)$$

□

Another property of the model (1.11)-(1.14) is **the dissipation of the free energy functional** (16) relying on this model.

Proposition 1.4.3. *For all solution φ of (1.11)-(1.12) verifying the conditions (1.13)-(1.14),*

$$\frac{d}{dt} \mathcal{E}(\varphi) \leq 0$$

Proof. Let φ a solution of (1.11)-(1.12) verifying (1.13)-(1.14), then

$$\begin{aligned}
 \frac{d}{dt} \mathcal{E}(\varphi) &= \frac{d}{dt} \int_{\Omega} (F(\varphi) + \frac{\varepsilon^2}{2} |\nabla\varphi|^2) \, d\mathbf{x} \\
 &= \int_{\Omega} (\frac{d}{dt} F(\varphi) + \frac{\varepsilon^2}{2} \frac{d}{dt} |\nabla\varphi|^2) \, d\mathbf{x} \\
 &= \int_{\Omega} (f(\varphi) \frac{d\varphi}{dt} + \frac{\varepsilon^2}{2} 2 \nabla\varphi \cdot \underbrace{\frac{d}{dt} \nabla\varphi}_{\nabla(\frac{d\varphi}{dt})}) \, d\mathbf{x} \\
 &= \int_{\Omega} (f(\varphi) - \varepsilon^2 \Delta\varphi) \frac{d\varphi}{dt} \, d\mathbf{x} + \int_{\partial\Omega} \varepsilon^2 \frac{d\varphi}{dt} \underbrace{\nabla\varphi \cdot \mathbf{n}}_{0 \text{ on } \partial\Omega} \, ds \\
 &= \int_{\Omega} \omega \nabla \cdot (M(\varphi) \nabla\omega) \, d\mathbf{x} \\
 &= \int_{\partial\Omega} \omega M(\varphi) \underbrace{\nabla\omega \cdot \mathbf{n}}_{0 \text{ on } \partial\Omega} \, ds - \int_{\Omega} \nabla\omega \cdot (M(\varphi) \nabla\omega) \, d\mathbf{x} \\
 &= - \int_{\Omega} M(\varphi) |\nabla\omega|^2 \, d\mathbf{x} \quad \text{where } M(\varphi) \text{ is positive} \\
 \frac{d}{dt} \mathcal{E}(\varphi) &\leq 0
 \end{aligned}$$

□

The mathematical study usually relies on different fundamental questions. First, the question of the existence and uniqueness of solutions allows to state the well-posedness of the problem (1.11)-(1.14). It is often very difficult to answer this question in the framework of strong solutions. They require strong regularities, they are in complex spaces, and they are not necessarily unique. The framework of the weak solutions is a bit easier because they require weak regularities. They are found in the energy spaces and before looking into their existence, one usually looks for these energy spaces, by establishing the **energy estimate** similarly to [19].

Theorem 1.4.4. *If the solutions φ and ω of (1.11)-(1.12) with the conditions (1.13)-(1.14) exist in the weak sense where the velocity field \mathbf{u} is regular enough and verifies $\mathbf{u} \cdot \mathbf{n} = 0$ on $\partial\Omega$, then*

$$\begin{aligned}\varphi &\in L^\infty([0, t_f]; H^1(\Omega)) \cap L^2([0, t_f]; H^2(\Omega)) \\ \omega &\in L^2([0, t_f]; H^1(\Omega))\end{aligned}$$

and the following energy estimate is obtained for a certain $c_1, c_2, c_3 > 0$:

$$\begin{aligned}&c_1 \int_0^t \|\nabla\omega(s)\|_{L^2(\Omega)}^2 ds + c_2 \int_0^t \|\mathbf{u}(s)\|_{L^2(\Omega)}^2 ds \\ &+ c_3 \|\nabla\varphi(t)\|_{L^2(\Omega)}^2 + \left\| \frac{\varphi^2(t) - 1}{2} \right\|_{L^2(\Omega)}^2 \\ &\leq c_3 \|\nabla\varphi_0\|_{L^2(\Omega)}^2 + \left\| \frac{\varphi_0^2 - 1}{2} \right\|_{L^2(\Omega)}^2\end{aligned}\tag{1.15}$$

The sketch of the proof is established here for the sake of completeness.

Proof. Let φ and ω weak solutions of (1.11)-(1.12) with the conditions (1.13)-(1.14) where the velocity field \mathbf{u} is regular enough and verifies $\mathbf{u} \cdot \mathbf{n} = 0$ on $\partial\Omega$. One multiplies Equation (1.11) by ω and integrates it on Ω . Then, Equation (1.12) is multiplied by $-\partial_t\varphi$ and integrated on Ω . Finally, these both equations are summed. By dealing with each term:

1. $\int_\Omega \omega \partial_t \varphi \, d\mathbf{x}$.
2. $\int_\Omega \omega \nabla \varphi \cdot \mathbf{u} \, d\mathbf{x}$.
3. $\int_\Omega \omega \varphi \nabla \cdot \mathbf{u} \, d\mathbf{x}$

$$4. - \int_{\Omega} \nabla \cdot (M(\varphi) \nabla \omega) \omega \, d\mathbf{x} = - \underbrace{\int_{\Omega} \nabla \cdot (M(\varphi) \omega \nabla \omega) \, d\mathbf{x}}_{\int_{\partial\Omega} M(\varphi) \omega \nabla \omega \cdot \mathbf{n} \, ds = 0} + \int_{\Omega} M(\varphi) |\nabla \omega|^2 \, d\mathbf{x}$$

Therefore $-\int_{\Omega} \nabla \cdot (M(\varphi) \nabla \omega) \omega \, d\mathbf{x} = \int_{\Omega} M(\varphi) |\nabla \omega|^2 \, d\mathbf{x}$ (because of (1.14)).

$$5. - \int_{\Omega} \omega \partial_t \varphi \, d\mathbf{x}.$$

$$6. - \int_{\Omega} \varepsilon^2 \Delta \varphi \partial_t \varphi \, d\mathbf{x} = - \int_{\partial\Omega} \varepsilon^2 \partial_t \varphi \nabla \varphi \cdot \mathbf{n} \, ds + \int_{\Omega} \varepsilon^2 \nabla \cdot (\partial_t \varphi) \cdot \nabla \varphi \, d\mathbf{x}$$

Therefore $-\int_{\Omega} \varepsilon^2 \Delta \varphi \partial_t \varphi \, d\mathbf{x} = \int_{\Omega} \partial_t \left(\frac{\varepsilon^2}{2} |\nabla \varphi|^2 \right) \, d\mathbf{x}$.

$$7. - \int_{\Omega} f(\varphi) \times (-\partial_t \varphi) \, d\mathbf{x} = \int_{\Omega} \partial_t \varphi f(\varphi) \, d\mathbf{x} = \int_{\Omega} \partial_t (F(\varphi)) \, d\mathbf{x} = \partial_t \left(\int_{\Omega} F(\varphi) \, d\mathbf{x} \right).$$

and summing them, it comes

$$\begin{aligned} & \int_{\Omega} \omega \partial_t \varphi \, d\mathbf{x} + \int_{\Omega} \omega \mathbf{u} \cdot \nabla \varphi \, d\mathbf{x} + \int_{\Omega} \omega \varphi \nabla \cdot \mathbf{u} \, d\mathbf{x} + \int_{\Omega} M(\varphi) |\nabla \omega|^2 \, d\mathbf{x} \\ & - \int_{\Omega} \omega \partial_t \varphi \, d\mathbf{x} + \partial_t \left(\int_{\Omega} \frac{\varepsilon^2}{2} |\nabla \varphi|^2 \, d\mathbf{x} \right) + \partial_t \left(\int_{\Omega} F(\varphi) \, d\mathbf{x} \right) = 0 \end{aligned}$$

However, because $\mathbf{u} \cdot \mathbf{n} = 0$ in $\partial\Omega$,

$$\begin{aligned} \int_{\Omega} \omega \mathbf{u} \cdot \nabla \varphi \, d\mathbf{x} + \int_{\Omega} \omega \varphi \nabla \cdot \mathbf{u} \, d\mathbf{x} &= \int_{\Omega} \omega \nabla \cdot (\varphi \mathbf{u}) \, d\mathbf{x} \\ &= \int_{\Omega} \nabla \cdot (\omega \varphi \mathbf{u}) \, d\mathbf{x} - \int_{\Omega} \varphi \mathbf{u} \cdot \nabla \omega \, d\mathbf{x} \\ &= \int_{\partial\Omega} \omega \varphi \underbrace{\mathbf{u} \cdot \mathbf{n}}_0 \, ds - \int_{\Omega} \varphi \mathbf{u} \cdot \nabla \omega \, d\mathbf{x} \\ \int_{\Omega} \omega \mathbf{u} \cdot \nabla \varphi \, d\mathbf{x} + \int_{\Omega} \omega \varphi \nabla \cdot \mathbf{u} \, d\mathbf{x} &= - \int_{\Omega} \varphi \mathbf{u} \cdot \nabla \omega \, d\mathbf{x} \end{aligned}$$

Thus,

$$- \int_{\Omega} \varphi \mathbf{u} \cdot \nabla \omega \, d\mathbf{x} + \int_{\Omega} M(\varphi) |\nabla \omega|^2 \, d\mathbf{x} + \partial_t \left(\int_{\Omega} \frac{\varepsilon^2}{2} |\nabla \varphi|^2 \, d\mathbf{x} + \int_{\Omega} F(\varphi) \, d\mathbf{x} \right) = 0$$

Furthermore,

$$\int_{\Omega} \varphi \mathbf{u} \cdot \nabla \omega \, d\mathbf{x} \leq \|\varphi\|_{L^\infty(\Omega)} \int_{\Omega} \mathbf{u} \cdot \nabla \omega \, d\mathbf{x} \quad \text{because } \varphi \text{ is bounded in } \Omega \times [0, t_f]$$

$$\begin{aligned} &\leq \|\varphi\|_{L^\infty(\Omega)} \|\nabla\omega\|_{L^2(\Omega)} \|\mathbf{u}\|_{L^2(\Omega)} \quad \text{by Cauchy–Schwarz’s inequality} \\ \int_{\Omega} \varphi \mathbf{u} \cdot \nabla\omega \, d\mathbf{x} &\leq \|\varphi\|_{L^\infty(\Omega)} \left(\frac{\alpha}{2} \|\nabla\omega\|_{L^2(\Omega)}^2 + \frac{1}{2\alpha} \|\mathbf{u}\|_{L^2(\Omega)}^2 \right) \end{aligned}$$

by Young’s inequality for a certain $\alpha > 0$.

Thus,

$$- \int_{\Omega} \varphi \mathbf{u} \cdot \nabla\omega \, d\mathbf{x} \geq -\|\varphi\|_{L^\infty(\Omega)} \left(\frac{\alpha}{2} \|\nabla\omega\|_{L^2(\Omega)}^2 + \frac{1}{2\alpha} \|\mathbf{u}\|_{L^2(\Omega)}^2 \right)$$

which means,

$$\begin{aligned} &-\|\varphi\|_{L^\infty(\Omega)} \left(\frac{\alpha}{2} \|\nabla\omega\|_{L^2(\Omega)}^2 + \frac{1}{2\alpha} \|\mathbf{u}\|_{L^2(\Omega)}^2 \right) + \int_{\Omega} M(\varphi) |\nabla\omega|^2 \, d\mathbf{x} \\ &+ \partial_t \left(\int_{\Omega} \frac{\varepsilon^2}{2} \|\nabla\varphi\|^2 \, d\mathbf{x} \right) + \partial_t \left(\int_{\Omega} F(\varphi) \, d\mathbf{x} \right) \leq 0 \end{aligned}$$

Because the mobility is assumed as constant and positive : $M(\varphi) = M > 0$, $F(\varphi) = \left(\frac{\varphi^2-1}{2}\right)^2$, and by integrating w.r.t the time t ,

$$\begin{aligned} &-\|\varphi\|_{L^\infty(\Omega)} \frac{\alpha}{2} \int_0^t \|\nabla\omega(s)\|_{L^2(\Omega)}^2 \, ds + \frac{1}{2\alpha} \int_0^t \|\mathbf{u}(s)\|_{L^2(\Omega)}^2 \, ds \\ &+ M \int_0^t \|\nabla\omega(s)\|_{L^2(\Omega)}^2 \, ds + \frac{\varepsilon^2}{2} \|\nabla\varphi(t)\|_{L^2(\Omega)}^2 - \frac{\varepsilon^2}{2} \|\nabla\varphi_0\|_{L^2(\Omega)}^2 \\ &+ \left\| \frac{\varphi^2(t) - 1}{2} \right\|_{L^2(\Omega)}^2 - \left\| \frac{\varphi_0^2 - 1}{2} \right\|_{L^2(\Omega)}^2 \leq 0 \end{aligned}$$

For $\alpha > 0$ such that $M - \frac{\alpha}{2} \|\varphi\|_{L^\infty(\Omega)} > 0$,

$$\begin{aligned} &\left(M - \|\varphi\|_{L^\infty(\Omega)} \frac{\alpha}{2} \right) \int_0^t \|\nabla\omega(s)\|_{L^2(\Omega)}^2 \, ds + \frac{1}{2\alpha} \int_0^t \|\mathbf{u}(s)\|_{L^2(\Omega)}^2 \, ds \\ &+ \frac{\varepsilon^2}{2} \|\nabla\varphi(t)\|_{L^2(\Omega)}^2 + \left\| \frac{\varphi^2(t) - 1}{2} \right\|_{L^2(\Omega)}^2 \\ &\leq \frac{\varepsilon^2}{2} \|\nabla\varphi_0\|_{L^2(\Omega)}^2 + \left\| \frac{\varphi_0^2 - 1}{2} \right\|_{L^2(\Omega)}^2 \end{aligned}$$

This energy estimate gives a control of the solutions by the initial data. From this estimate, one deduces that

$$\begin{aligned} \varphi &\in L^\infty([0, t_f]; H^1(\Omega)) \cap L^2([0, t_f]; H^2(\Omega)) \\ \omega &\in L^2([0, t_f]; H^1(\Omega)) \end{aligned}$$

□

Once the energy spaces are known, it is usually in the mathematical study to prove the existence and uniqueness of these solutions. In [20], under certain assumptions like periodicity on φ , the existence of global weak solutions of the model (1.11)-(1.14) is proved.

Another fundamental question concerns the order parameter φ which has its physical values between -1 and 1 in the Cahn–Hilliard model. It is then necessary to ensure that the continuous and discrete solutions of the equations verify this property [21, 22]. The main difficulty is the non-existence of the maximum principle for the bilaplacian operator and for the 4th-order elliptic operators [18]. For constant mobility and polynomial free energy such as (1.2), the L^∞ estimation of the maximum principle is not verified. However, as shown in [20], it is at least necessary to have degenerate mobility $M(\varphi)$ for $\varphi = \pm 1$ or free energy with a logarithmic form to satisfy the estimate.

1.5 Space and time discretization for the Cahn–Hilliard equations

Like many other models the Cahn–Hilliard model cannot be solved analytically and needs to be dealt with alternatively. Especially because of its high non-linearity, numerical solving of the equations is necessary. The numerical approach will not allow getting the exact solution(s) of the equations but will help to compute an approximation of the solution. Furthermore, the solutions can be visualized through numerical simulation. In order to do that, the Equations (1.11)-(1.12) need to be discretized in space and time. In this section, the discretization of these equations will be established to get the Cahn–Hilliard solver to implement.

1.5.1 Mixed finite element framework

In this section, a weak formulation of the Cahn–Hilliard model (1.11)-(1.14) similar to [15, 21] is presented. The space discretization will be established with the continuous Galerkin CG1 method in the finite element framework. Let $L^p(\Omega)$ denotes the space of p integrable functions with norm denoted by $\|\cdot\|_{0,p}$, where for simplicity of notation one sets $\|\cdot\|_{0,2} = \|\cdot\|$. Let $H^m(\Omega)$, $m \in \{-1, 1, 2\}$, the usual Sobolev space with norm $\|\cdot\|_m$ and let $(H^1(\Omega))'$ denote the dual space of $H^1(\Omega)$. One defines the following spaces:

$$V = \{v \in H^1(\Omega) \text{ such that } (v, 1) = 0\}, \quad (1.16)$$

$$H_E^m(\Omega) = \{v \in H^m(\Omega) \text{ such that } \partial_{\mathbf{n}} v = 0 \text{ on } \partial\Omega\}, \quad (1.17)$$

where (\cdot, \cdot) denotes the L^2 inner product.

The mixed weak formulation of (1.11)-(1.14) is defined as follows: for $t_f > 0$, find $(\varphi, \partial_t \varphi, \omega) \in L^\infty(0, t_f; H_E^4(\Omega) \cap V) \cap H^1(0, t_f; L^2(\Omega)) \times L^2(0, t_f; (H^1(\Omega))') \times L^\infty(0, t_f; H_E^2(\Omega))$ such that for all $(\psi, \chi) \in H^1(\Omega) \times H^1(\Omega)$

$$(\partial_t \varphi, \psi) + ((\mathbf{u} \cdot \nabla) \varphi, \psi) + (\varphi \nabla \cdot (\mathbf{u}), \psi) + M(\nabla \omega, \nabla \psi) = 0, \quad (1.18)$$

$$(\omega, \chi) - \varepsilon^2(\nabla \varphi, \nabla \chi) - (\varphi(\varphi^2 - 1), \chi) = 0, \quad (1.19)$$

$$\varphi(\cdot, 0) = \varphi_0, \quad (1.20)$$

where $\varphi_0 \in H^1(\Omega)$.

Let the triangulation \mathcal{T}_h of Ω be a family of disjoint elements K so that

$$\Omega = \bigsqcup_{K \in \mathcal{T}_h} K$$

and $\mathcal{V}_h \subset H^1(\Omega)$ the finite element space associated to \mathcal{T}_h defined by

$$\mathcal{V}_h = \{v_h \in \mathcal{C}^0(\bar{\Omega}) \text{ such that } v_h|_K \in \mathbb{P}_1, K \in \mathcal{T}_h\} \quad (1.21)$$

where \mathbb{P}_1 denotes the set of polynomials of degree less or equal to 1. Thus (1.18)-(1.20) can be written under the following \mathbb{P}_1 finite element formulation by the Galerkin approximation : for $t_f > 0$, find $(\varphi_h, \omega_h) \in \mathcal{V}_h \times \mathcal{V}_h$ such that for all $(\psi_h, \chi_h) \in \mathcal{V}_h \times \mathcal{V}_h$

$$(\partial_t \varphi_h, \psi_h) + ((\mathbf{u} \cdot \nabla) \varphi_h, \psi_h) + (\varphi_h \nabla \cdot (\mathbf{u}), \psi_h) + M(\nabla \omega_h, \nabla \psi_h) = 0, \quad (1.22)$$

$$(\omega_h, \chi_h) - \varepsilon^2(\nabla \varphi_h, \nabla \chi_h) - (\varphi_h(\varphi_h^2 - 1), \chi_h) = 0, \quad (1.23)$$

$$\varphi_h(\cdot, 0) = \varphi_{0_h} \quad (1.24)$$

where $\varphi_{0_h} \in \mathcal{V}_h$.

Before having the matrix linear system allowing the numerical solving of the Cahn–Hilliard equations, a time discretization and linearization step is necessary.

1.5.2 Time discretized scheme and linearization

In order to solve the Cahn–Hilliard equations (1.22)–(1.24) with \mathbb{P}_1 finite elements method, the equation is discretized as a system and solved at each time step in $[0, t_f]$, $t_f > 0$, with an implicit time discretization using backward differentiation formula for the time derivative of φ with order p .

$$\begin{aligned}
 t^0 = 0, \quad t^n = n\Delta t \quad \text{and} \quad t^N = t_f, \\
 \mathbf{u}(\cdot, t^{n+1}) &= \mathbf{u}^{n+1} \text{ is known,} \\
 \varphi(\cdot, t^{n+1}) &\approx \varphi^{n+1}, \\
 \frac{\partial \varphi}{\partial t}(\cdot, t^{n+1}) &\approx \frac{\alpha_0 \varphi^{n+1} - \sum_{k=0}^{p-1} \beta_k \varphi^{n-k}}{\Delta t}, \\
 \nabla \varphi(\cdot, t^{n+1}) &\approx \nabla \varphi^{n+1}, \\
 \omega(\cdot, t^{n+1}) &\approx \omega^{n+1}, \\
 \Delta \varphi(\cdot, t^{n+1}) &\approx \Delta \varphi^{n+1}, \\
 \varphi(\varphi^2 - 1)(\cdot, t^{n+1}) &= (\varphi^3 - \varphi)(\cdot, t^{n+1}) \approx (\varphi^3 - \varphi)^{n+1}.
 \end{aligned}$$

Therefore, the space-time discretized Cahn–Hilliard equation with the finite element framework is given by

$$\begin{aligned}
 & \left(\frac{\alpha_0 \varphi_h^{n+1} - \sum_{k=0}^{p-1} \beta_k \varphi_h^{n-k}}{\Delta t}, \psi_h \right) + ((\mathbf{u}^{n+1} \cdot \nabla) \varphi_h^{n+1}, \psi_h) \\
 & + (\varphi_h^{n+1} \nabla \cdot (\mathbf{u}^{n+1}), \psi_h) + M(\nabla \omega_h^{n+1}, \nabla \psi_h) = 0,
 \end{aligned} \tag{1.25}$$

$$(\omega_h^{n+1}, \chi_h) - \varepsilon^2 (\nabla \varphi_h^{n+1}, \nabla \chi_h) - ((\varphi^3 - \varphi)_h^{n+1}, \chi_h) = 0, \tag{1.26}$$

for $\varphi_h^n, \omega_h^n, \psi_h, \chi_h \in \mathcal{V}_h$ and a known \mathbf{u}^{n+1} .

The BDF-1 Cahn–Hilliard equation is considered here. Therefore, with $\alpha_0 = 1$ and $\beta_0 = 1$, it comes the following discretization

$$\frac{\alpha_0 \varphi_h^{n+1} - \sum_{k=0}^{p-1} \beta_k \varphi_h^{n-k}}{\Delta t} = \frac{\varphi_h^{n+1} - \varphi_h^n}{\Delta t} \tag{1.27}$$

Consequently, the space-time discretized Cahn–Hilliard equations become: find $(\varphi_h^{n+1}, \omega_h^{n+1}) \in \mathcal{V}_h \times \mathcal{V}_h$ such that for all $(\psi_h, \chi_h) \in \mathcal{V}_h \times \mathcal{V}_h$,

$$\begin{aligned}
 & \left(\frac{\varphi_h^{n+1}}{\Delta t}, \psi_h \right) + ((\mathbf{u}^{n+1} \cdot \nabla) \varphi_h^{n+1}, \psi_h) \\
 & + (\varphi_h^{n+1} \nabla \cdot (\mathbf{u}^{n+1}), \psi_h) + M(\nabla \omega_h^{n+1}, \nabla \psi_h) = \left(\frac{\varphi_h^n}{\Delta t}, \psi_h \right),
 \end{aligned} \tag{1.28}$$

$$(\omega_h^{n+1}, \chi_h) - \varepsilon^2(\nabla \varphi_h^{n+1}, \nabla \chi_h) - ((\varphi^3 - \varphi)_h^{n+1}, \chi_h) = 0, \quad (1.29)$$

and by considering an element K_p of the triangulation \mathcal{T}_h of $\Omega \subset \mathbb{R}^d$ and denoting by φ_p^{n+1} and ω_p^{n+1} the unknowns solutions in the element K_p at the instant $n+1$, the formulation on each element K_p is written as follows: find $(\varphi_p^{n+1}, \omega_p^{n+1}) \in \mathcal{V}_h \times \mathcal{V}_h$ such that for all $(\psi_h, \chi_h) \in \mathcal{V}_h \times \mathcal{V}_h$,

$$\begin{aligned} & \left(\frac{\varphi_p^{n+1}}{\Delta t}, \psi_h\right)_{K_p} + ((\mathbf{u}^{n+1} \cdot \nabla) \varphi_p^{n+1}, \psi_h)_{K_p} \\ & + (\varphi_p^{n+1} \nabla \cdot (\mathbf{u}^{n+1}), \psi_h)_{K_p} + M(\nabla \omega_p^{n+1}, \nabla \psi_h)_{K_p} = \left(\frac{\varphi_p^n}{\Delta t}, \psi_h\right)_{K_p}, \end{aligned} \quad (1.30)$$

$$(\omega_h^{n+1}, \chi_h)_{K_p} - \varepsilon_{K_p}^2(\nabla \varphi_h^{n+1}, \nabla \chi_h)_{K_p} - ((\varphi^3 - \varphi)_p^{n+1}, \chi_h)_{K_p} = 0, \quad (1.31)$$

where $(\cdot, \cdot)_{K_p}$ denotes the L^2 -inner product on the element K_p .

One introduces the following elementary bilinear forms:

$$\begin{aligned} m_p(\cdot, \cdot) &: H^1(\Omega) \times H^1(\Omega) \rightarrow \mathbb{R} \\ &(u, v) \mapsto \int_{K_p} uv \, dx \\ a_p(\cdot, \cdot) &: H^1(\Omega) \times H^1(\Omega) \rightarrow \mathbb{R} \\ &(u, v) \mapsto \int_{K_p} \nabla u \cdot \nabla v \, dx \\ b_p(\cdot, \cdot) &: H^1(\Omega) \times H^1(\Omega) \rightarrow \mathbb{R} \\ &(u, v) \mapsto \int_{K_p} \varepsilon_{K_p} \nabla u \cdot \nabla v \, dx \\ d_p(\cdot, \cdot) &: H^1(\Omega) \times H^1(\Omega) \rightarrow \mathbb{R} \\ &(u, v) \mapsto \int_{K_p} (\mathbf{u}^{n+1} \cdot \nabla u)v \, dx + \int_{K_p} \nabla \cdot (\mathbf{u}^{n+1})uv \, dx \end{aligned}$$

and denotes

$$\varphi_p^{n+1} = \sum_{j=1}^{d+1} \varphi_j^{n+1} \psi_j^p \quad \text{and} \quad \omega_p^{n+1} = \sum_{j=1}^{d+1} \omega_j^{n+1} \psi_j^p$$

where $(\psi_j^p)_{1 \leq j \leq d+1}$ are the local shape functions associated to the element K_p .

Having a matrix formulation depends on how the non-linear term $(\varphi^3 - \varphi)_p^{n+1}$ in the equation for the chemical potential (1.31) is treated. To deal with this non-linear term, three different discretized linear schemes are proposed for this term:

- A classical linear scheme:

$$(\varphi(\varphi^2 - 1))_p^{n+1} \approx ((\varphi^n)^2 - 1) \varphi_p^{n+1} \quad (1.32)$$

This linear scheme gives the following discrete problem: find $(\varphi_j^{n+1}, \omega_j^{n+1})$, $j \in \{1, \dots, d+1\}$ such that

$$\begin{aligned} & \sum_{i=1}^{d+1} \sum_{j=1}^{d+1} \left(\frac{\varphi_j^{n+1}}{\Delta t} \psi_j^p, \psi_i^p \right)_{K_p} + \sum_{i=1}^{d+1} \sum_{j=1}^{d+1} \left(\varphi_j^{n+1} (\mathbf{u}^{n+1} \cdot \nabla) \psi_j^p, \psi_i^p \right)_{K_p} \\ & + \sum_{i=1}^{d+1} \sum_{j=1}^{d+1} \left(\nabla \cdot (\mathbf{u}^{n+1}) \varphi_j^{n+1} \psi_j^p, \psi_i^p \right)_{K_p} + M \sum_{i=1}^{d+1} \sum_{j=1}^{d+1} \left(\omega_j^{n+1} \nabla \psi_j^p, \nabla \psi_i^p \right)_{K_p} \\ & = \sum_{i=1}^{d+1} \sum_{j=1}^{d+1} \left(\frac{\varphi_j^n}{\Delta t} \psi_j^p, \psi_i^p \right)_{K_p}, \\ & \sum_{i=1}^{d+1} \sum_{j=1}^{d+1} \left(\omega_j^{n+1} \psi_j^p, \psi_i^p \right)_{K_p} - \sum_{i=1}^{d+1} \sum_{j=1}^{d+1} \left(\varepsilon_{K_p}^2 \varphi_j^{n+1} \nabla \psi_j^p, \nabla \psi_i^p \right)_{K_p} \\ & - \sum_{i=1}^{d+1} \sum_{j=1}^{d+1} \left(((\varphi^n)^2 - 1) \varphi_j^{n+1} \psi_j^p, \psi_i^p \right)_{K_p} = 0, \end{aligned}$$

Let Φ_p^{n+1} and \mathbf{X}_p^{n+1} respectively represent the fields φ_p^{n+1} and ω_p^{n+1} in the local basis of the element K_p . The elementary matrix formulation is then written as following

$$\begin{pmatrix} \frac{1}{\Delta t} \mathbf{M}_p^e + \mathbf{D}_p^e(\mathbf{U}^{n+1}) & M \mathbf{K}_p^e \\ -\mathbf{B}_p^e - \mathbf{M}_p^e((\Phi^n)^2 - \mathbf{1}) & \mathbf{M}_p^e \end{pmatrix} \begin{pmatrix} \Phi_p^{n+1} \\ \mathbf{X}_p^{n+1} \end{pmatrix} = \begin{pmatrix} \frac{1}{\Delta t} \mathbf{M}_p^e(\Phi^n) \\ 0 \end{pmatrix} \quad (1.33)$$

where

$$\begin{aligned} [\mathbf{M}_p^e]_{i,j} &= m_p(\psi_j^p, \psi_i^p), \quad \text{for } i, j \in \{1, \dots, d+1\}, \\ [\mathbf{K}_p^e]_{i,j} &= a_p(\psi_j^p, \psi_i^p), \quad \text{for } i, j \in \{1, \dots, d+1\}, \\ [\mathbf{B}_p^e]_{i,j} &= b_p(\psi_j^p, \psi_i^p), \quad \text{for } i, j \in \{1, \dots, d+1\}, \\ [\mathbf{D}_p^e]_{i,j} &= d_p(\psi_j^p, \psi_i^p), \quad \text{for } i, j \in \{1, \dots, d+1\}. \end{aligned}$$

- The Eyre linear scheme for $\beta = 1$ [23]:

$$(\varphi(\varphi^2 - 1))_p^{n+1} \approx \beta \varphi_p^{n+1} + (\varphi^n)^3 - (\beta + 1) \varphi^n = \varphi_p^{n+1} + (\varphi^n)^3 - 2\varphi^n \quad (1.34)$$

By following the same way as above, the matrix formulation is then,

$$\begin{pmatrix} \frac{1}{\Delta t} \mathbf{M}_p^e + \mathbf{D}_p^e(\mathbf{U}^{n+1}) & M \mathbf{K}_p^e \\ -\mathbf{B}_p^e - \mathbf{M}_p^e & \mathbf{M}_p^e \end{pmatrix} \begin{pmatrix} \Phi_p^{n+1} \\ \mathbf{X}_p^{n+1} \end{pmatrix} = \begin{pmatrix} \frac{1}{\Delta t} \mathbf{M}_p^e(\Phi^n) \\ \mathbf{M}_p^e((\Phi^n)^2 - 2\Phi^n) \end{pmatrix} \quad (1.35)$$

- The optimal dissipation scheme [24]:

$$(\varphi(\varphi^2 - 1))_p^{n+1} \approx \frac{1}{2} (3(\varphi^n)^2 - 1) \varphi_p^{n+1} - \frac{1}{2} ((\varphi^n)^3 + \varphi^n) \quad (1.36)$$

which involves the following matrix formulation:

$$\begin{pmatrix} \frac{1}{\Delta t} \mathbf{M}_p^e + \mathbf{D}_p^e(\mathbf{U}^{n+1}) & M \mathbf{K}_p^e \\ -\mathbf{B}_p^e - \mathbf{M}_p^e \left(\frac{3(\Phi^n)^2 - 1}{2} \right) & \mathbf{M}_p^e \end{pmatrix} \begin{pmatrix} \Phi_p^{n+1} \\ \mathbf{X}_p^{n+1} \end{pmatrix} = \begin{pmatrix} \frac{1}{\Delta t} \mathbf{M}_p^e(\Phi^n) \\ -\mathbf{M}_p^e \left(\frac{(\Phi^n)^3 + \Phi^n}{2} \right) \end{pmatrix} \quad (1.37)$$

1.6 Numerical properties

This section is dedicated to the study of the numerical scheme of the Cahn–Hilliard model presented in the previous section. In the numerical study, it is usual to look for the *a priori* estimates by determining beforehand the energy estimate associated with the model. Then, the existence of approximated solutions is deduced. Finally, their convergence is obtained by using compactness results. These two last points will not be treated in the present work.

By starting from the Cahn–Hilliard equations with non-degenerate and constant mobility:

$$\frac{\partial \varphi}{\partial t} + (\mathbf{u} \cdot \nabla) \varphi + \varphi \nabla \cdot (\mathbf{u}) - M \Delta \omega = 0 \quad \text{in } \Omega, \quad (1.38)$$

$$\omega + \varepsilon^2 \Delta \varphi - F'(\varphi) = 0 \quad \text{in } \Omega. \quad (1.39)$$

completed with the initial and boundary conditions given by (1.13)-(1.14), one proposes the following time semi-discretization:

$$\frac{\varphi^{n+1} - \varphi^n}{\Delta t} + (\mathbf{u}^{n+1} \cdot \nabla) \varphi^{n+1} + \varphi^{n+1} \nabla \cdot \mathbf{u}^{n+1} - M \Delta \omega^{n+1} = 0 \quad \text{in } \Omega, \quad (1.40)$$

$$\omega^{n+1} + \varepsilon^2 \Delta \varphi^{n+1} - F'(\varphi)^{n+1} = 0 \quad \text{in } \Omega, \quad (1.41)$$

It is important to note that if the velocity is divergence-free $\nabla \cdot \mathbf{u} = 0$, the approximation may not enforce this constraint at the discrete level. The corresponding discretized term must be kept in the numerical scheme.

Just like Section 1.4, there exists an energy estimate result at the discrete level:

Theorem 1.6.1. *If the solutions φ^n and ω^n of (1.40)-(1.41) exist in the weak sense, then*

$$\begin{aligned}\varphi^n &\in L^\infty(0, t_f; H^1(\Omega)) \cap L^2(0, t_f; H^2(\Omega)) \\ \omega^n &\in L^2(0, t_f; H^1(\Omega))\end{aligned}$$

and for all $N \in \mathbb{N}$ there exists a, b , and $c(\Delta t) > 0$ such that

$$a\|\nabla\varphi^N\|_{L^2(\Omega)}^2 + b(F(\varphi)^N, 1) + c(\Delta t) \sum_{n=0}^{N-1} \|\nabla\omega^{n+1}\|_{L^2(\Omega)}^2 < +\infty \quad (1.42)$$

Proof. Let φ^n and ω^n weak solutions of (1.40)-(1.41). By multiplying Equation (1.40) by $\Delta t\omega^{n+1}$ and Equation (1.41) by $-(\varphi^{n+1} - \varphi^n)$, then by integrating and summing, it comes

$$\begin{aligned}& \cancel{(\varphi^{n+1} - \varphi^n, \omega^{n+1})} + \Delta t ((\mathbf{u}^{n+1} \cdot \nabla)\varphi^{n+1}, \omega^{n+1}) \\ & + \Delta t (\varphi^{n+1} \nabla \cdot \mathbf{u}^{n+1}, \omega^{n+1}) - M\Delta t (\Delta\omega^{n+1}, \omega^{n+1}) \\ & - \cancel{(\varphi^{n+1} - \varphi^n, \omega^{n+1})} - \varepsilon^2 (\Delta\varphi^{n+1}, \varphi^{n+1} - \varphi^n) + (F'(\varphi^n), \varphi^{n+1} - \varphi^n) = 0\end{aligned}$$

Therefore by integrating by parts and using the Neumann boundary conditions on φ^n and ω^n for all $n \in \mathbb{N}$,

$$\begin{aligned}& \Delta t (\nabla \cdot (\varphi^{n+1} \mathbf{u}^{n+1}), \omega^{n+1}) + M\Delta t (\nabla\omega^{n+1}, \nabla\omega^{n+1}) \\ & + (F'(\varphi^n), \varphi^{n+1} - \varphi^n) + \varepsilon^2 \underbrace{(\nabla\varphi^{n+1}, \nabla\varphi^{n+1} - \nabla\varphi^n)}_{\frac{1}{2}(\|\nabla\varphi^{n+1}\|_{L^2(\Omega)}^2 - \|\nabla\varphi^n\|_{L^2(\Omega)}^2 + \|\nabla\varphi^{n+1} - \nabla\varphi^n\|_{L^2(\Omega)}^2)} = 0\end{aligned}$$

Thus,

$$\begin{aligned}& - \Delta t (\varphi^{n+1} \mathbf{u}^{n+1}, \nabla\omega^{n+1}) + M\Delta t \|\nabla\omega^{n+1}\|_{L^2(\Omega)}^2 + (F'(\varphi)^{n+1}, \varphi^{n+1} - \varphi^n) \\ & + \frac{\varepsilon^2}{2} (\|\nabla\varphi^{n+1}\|_{L^2(\Omega)}^2 - \|\nabla\varphi^n\|_{L^2(\Omega)}^2 + \|\nabla\varphi^{n+1} - \nabla\varphi^n\|_{L^2(\Omega)}^2) = 0\end{aligned}$$

Since $\inf_{\mathbb{R}} F'' = -1$, then

$$F(\varphi)^{n+1} - F(\varphi)^n \leq F'(\varphi)^{n+1}(\varphi^{n+1} - \varphi^n) + \frac{(\varphi^{n+1} - \varphi^n)^2}{2}$$

Therefore $(F(\varphi)^{n+1} - F(\varphi)^n, 1) \leq (F'(\varphi)^{n+1}, \varphi^{n+1} - \varphi^n) + \frac{\|\varphi^{n+1} - \varphi^n\|_{L^2(\Omega)}^2}{2}$ and by the Poincaré's inequality, there exists $C_P(h) > 0$ such that

$$(F(\varphi)^{n+1} - F(\varphi)^n, 1) \leq (F'(\varphi)^{n+1}, \varphi^{n+1} - \varphi^n) + C_P \frac{\|\nabla\varphi^{n+1} - \nabla\varphi^n\|_{L^2(\Omega)}^2}{2}$$

In the semi-discrete energy estimate, the expression

$$(F'(\varphi)^{n+1}, \varphi^{n+1} - \varphi^n) + \frac{\varepsilon^2 \|\nabla \varphi^{n+1} - \nabla \varphi^n\|_{L^2(\Omega)}^2}{2}$$

is true for all ε , then by choosing it such that $\varepsilon^2 = C_P$,

$$\begin{aligned} & - \Delta t (\varphi^{n+1} \mathbf{u}^{n+1}, \nabla \omega^{n+1}) + M \Delta t \|\nabla \omega^{n+1}\|_{L^2(\Omega)}^2 + (F'(\varphi)^{n+1}, \varphi^{n+1} - \varphi^n) \\ & + \frac{C_P}{2} (\|\nabla \varphi^{n+1}\|_{L^2(\Omega)}^2 - \|\nabla \varphi^n\|_{L^2(\Omega)}^2 + \|\nabla \varphi^{n+1} - \nabla \varphi^n\|_{L^2(\Omega)}^2) = 0 \end{aligned}$$

Furthermore, respectively because φ is bounded, the Cauchy–Schwarz inequality, and Young’s inequality, it comes

$$\begin{aligned} \Delta t (\varphi^{n+1} \mathbf{u}^{n+1}, \nabla \omega^{n+1}) & \leq \Delta t \|\varphi^{n+1}\|_{L^\infty(\Omega)} (\nabla \omega^{n+1}, \mathbf{u}^{n+1}) \\ & \leq \Delta t \|\varphi^{n+1}\|_{L^\infty(\Omega)} \|\nabla \omega^{n+1}\|_{L^2(\Omega)} \|\mathbf{u}^{n+1}\|_{L^2(\Omega)} \\ \Delta t (\varphi^{n+1} \mathbf{u}^{n+1}, \nabla \omega^{n+1}) & \leq \Delta t \|\varphi^{n+1}\|_{L^\infty(\Omega)} \left(\frac{\theta}{2} \|\nabla \omega^{n+1}\|_{L^2(\Omega)}^2 + \frac{1}{2\theta} \|\mathbf{u}^{n+1}\|_{L^2(\Omega)}^2 \right) \end{aligned}$$

Consequently,

$$-\Delta t (\varphi^{n+1} \mathbf{u}^{n+1}, \nabla \omega^{n+1}) \geq -\Delta t \|\varphi^{n+1}\|_{L^\infty(\Omega)} \left(\frac{\theta}{2} \|\nabla \omega^{n+1}\|_{L^2(\Omega)}^2 + \frac{1}{2\theta} \|\mathbf{u}^{n+1}\|_{L^2(\Omega)}^2 \right)$$

Whence

$$\begin{aligned} & - \Delta t \|\varphi^{n+1}\|_{L^\infty(\Omega)} \left(\frac{\theta}{2} \|\nabla \omega^{n+1}\|_{L^2(\Omega)}^2 + \frac{1}{2\theta} \|\mathbf{u}^{n+1}\|_{L^2(\Omega)}^2 \right) + M \Delta t \|\nabla \omega^{n+1}\|_{L^2(\Omega)}^2 \\ & + (F(\varphi^{n+1}) - F(\varphi^n), 1) + \frac{C_P}{2} (\|\nabla \varphi^{n+1}\|_{L^2(\Omega)}^2 - \|\nabla \varphi^n\|_{L^2(\Omega)}^2) \leq 0 \end{aligned}$$

By choosing $\theta > 0$ such that $\theta < \frac{2M}{\|\varphi^{n+1}\|_{L^\infty(\Omega)}}$,

$$\begin{aligned} & \Delta t \left(M - \|\varphi^{n+1}\|_{L^\infty(\Omega)} \frac{\theta}{2} \right) \|\nabla \omega^{n+1}\|_{L^2(\Omega)}^2 - \frac{\Delta t \|\varphi^{n+1}\|_{L^\infty(\Omega)}}{2\theta} \|\mathbf{u}^{n+1}\|_{L^2(\Omega)}^2 \\ & + (F(\varphi^{n+1}) - F(\varphi^n), 1) + \frac{C_P}{2} (\|\nabla \varphi^{n+1}\|_{L^2(\Omega)}^2 - \|\nabla \varphi^n\|_{L^2(\Omega)}^2) \leq 0 \end{aligned}$$

Since the known data \mathbf{u}^n is assumed in $\mathbf{L}^2(\Omega)$, then \mathbf{u}^n is bounded for all $n \in \{0, 1, \dots, N-1\}$: there exists $\mathbf{u} \in \mathbf{L}^2(\Omega)$ such that

$$\forall n \in \{0, 1, \dots, N-1\}, \|\mathbf{u}^{n+1}\|_{L^2(\Omega)}^2 \leq \|\mathbf{u}\|_{L^2(\Omega)}^2$$

It comes

$$\begin{aligned} & \Delta t \left(M - \|\varphi^{n+1}\|_{L^\infty(\Omega)} \frac{\theta}{2} \right) \|\nabla \omega^{n+1}\|_{L^2(\Omega)}^2 + (F(\varphi^{n+1}) - F(\varphi^n), 1) \\ & + \frac{C_P}{2} (\|\nabla \varphi^{n+1}\|_{L^2(\Omega)}^2 - \|\nabla \varphi^n\|_{L^2(\Omega)}^2) \leq \frac{\Delta t \|\varphi^{n+1}\|_{L^\infty(\Omega)}}{2\theta} \|\mathbf{u}\|_{L^2(\Omega)}^2 \end{aligned}$$

By summing in time for n from 0 to $N-1$, for all $N \in \mathbb{N}$,

$$\begin{aligned} & \Delta t \sum_{n=0}^{N-1} \left(M - \|\varphi^{n+1}\|_{L^\infty(\Omega)} \frac{\theta}{2} \right) \|\nabla \omega^{n+1}\|_{L^2(\Omega)}^2 + \sum_{n=0}^{N-1} (F(\varphi)^{n+1} - F(\varphi)^n, 1) \\ & + \frac{C_P}{2} \sum_{n=0}^{N-1} (\|\nabla \varphi^{n+1}\|_{L^2(\Omega)}^2 - \|\nabla \varphi^n\|_{L^2(\Omega)}^2) \leq \sum_{n=0}^{N-1} \frac{\Delta t \|\varphi^{n+1}\|_{L^\infty(\Omega)}}{2\theta} \|\mathbf{u}\|_{L^2(\Omega)}^2 \end{aligned}$$

Because $\|\varphi^{n+1}\|_{L^\infty(\Omega)} < +\infty$, there exists $C_0 > 0$ such that $\|\varphi^{n+1}\|_{L^\infty(\Omega)} \leq C_0$. Hence

$$\begin{aligned} & \Delta t \left(M - C_0 \frac{\theta}{2} \right) \sum_{n=0}^{N-1} (\|\nabla \omega^{n+1}\|_{L^2(\Omega)}^2) + (F(\varphi)^N, 1) - (F(\varphi)^0, 1) \\ & + \frac{C_P}{2} (\|\nabla \varphi^N\|_{L^2(\Omega)}^2 - \|\nabla \varphi^0\|_{L^2(\Omega)}^2) \leq \frac{\Delta t C_0}{2\theta} \|\mathbf{u}\|_{L^2(\Omega)}^2 \sum_{n=0}^{N-1} 1 \end{aligned}$$

Thus for all $N \in \mathbb{N}$,

$$\begin{aligned} & \Delta t \left(M - C_0 \frac{\theta}{2} \right) \sum_{n=0}^{N-1} (\|\nabla \omega^{n+1}\|_{L^2(\Omega)}^2) + (F(\varphi)^N, 1) + \frac{C_P}{2} \|\nabla \varphi^N\|_{L^2(\Omega)}^2 \\ & \leq \frac{C_P}{2} \|\nabla \varphi^0\|_{L^2(\Omega)}^2 + (F(\varphi)^0, 1) + \frac{\Delta t C_0}{2\theta} \|\mathbf{u}\|_{L^2(\Omega)}^2 \frac{N(N-1)}{2} < +\infty \end{aligned}$$

where φ^0 , $F(\varphi)^0$, and \mathbf{u} are known initial data.

From this estimate and by using the fact that $\Delta \varphi^n$ is in the expression of ω^n , one deduces that for all $n \in \mathbb{N}$

$$\begin{aligned} \varphi^n & \in L^\infty(0, t_f; H^1(\Omega)) \cap L^2(0, t_f; H^2(\Omega)), \\ \omega^n & \in L^2(0, t_f; H^1(\Omega)). \end{aligned}$$

□

The proved relation shows the decay along time of the energy associated with the system (1.40)-(1.41). Moreover, as mentioned previously, the energy estimate (1.6.1) provide also very useful *a priori* estimations allowing to proof the existence of approximated solutions and a convergence towards weak solutions of (1.40)-(1.41). The proof of existence and convergence towards weak solutions has been done in [25] for discretized equations slightly different from those studied in the present work.

A key point of the existence theorem is that the bounds can depend on the time step Δt and the mesh size h , which is a dependence of the Poincaré constant $C_P(h)$, whereas it is crucial that the *a priori* estimates are independent of Δt and h to prove the convergence theorem.

1.7 Simulation of an interface transport

This section is dedicated to the simulation of test cases for interface transport by the Cahn–Hilliard equations and the numerical method previously presented. This is to investigate the efficiency and applicability of this method in two-dimensional space. First, a convergence analysis is performed to assess the numerical solver. Manufactured solutions similar to [26] will be used in the study for the different linearized schemes. Then a series of test cases are performed including a pulse rotation, a single vortex - both of them initially represented in Figure 1.4 below -, and the Zalesak disk benchmark as defined in [27].

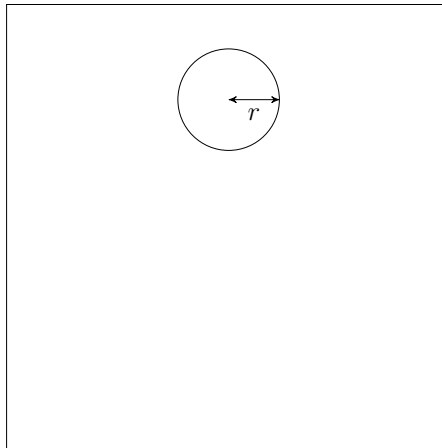


Figure 1.4: Initial step for benchmarks

In the different test cases, the mesh is considered uniform and the mesh size is at the most $h \simeq \frac{\varepsilon}{4}$ so that the bi-Laplacian of the Cahn–Hilliard equations is well approximated. In all the following simulations, the GMRes solver preconditioned by Jacobi ILU is used for the solving of Cahn–Hilliard systems. Furthermore, the phase-field function is initialized from the level-set function which has been regularized and normalized to get a diffuse interface of thickness ε with an order parameter $\varphi \in [-1, 1]$. In this way, the zero isovalues of the level-set and phase-field functions are initially the same.

1.7.1 Numerical convergence analysis

In scientific computing, the aim of code verification is to ensure that the code is a faithful representation of the underlying mathematical model. This model generally consists of partial differential equations (PDEs) with initial and boundary conditions, and possibly other constraints. Code verification therefore considers both the correctness of the numerical algorithms chosen and that of the implementation of these algorithms in the source code [28]. Stern & al. [29] describe a set of procedures for verification, validation and certification methodologies for numerical simulations.

The method of manufactured solutions is a very powerful and general approach to create exact solutions for a system of PDEs. Rather than trying to find an exact solution of the system of PDEs with initial and boundary conditions, the goal is to "manufacture" an exact solution for a system of PDEs slightly modified. For code verification, it is not necessary for the manufactured solution to be related to a realistic physical problem: the verification is only concerned with the mathematics of a given problem. The method of manufactured solutions requires the solution of an inverse problem: given a set of equations and a chosen solution, find a set of modified equations that satisfy this solution.

To study the convergence of our numerical solvers, a body source term is enforced in the Cahn–Hilliard equations to impose an exact solution. The problem is considered in a two-dimensional domain with $(x, y) \in [0, 1]^2$. According to [30], a manufactured Cahn–Hilliard solution is given by

$$\varphi(x, y; t) = \cos(\pi x) \cos(\pi y) \cos(t). \quad (1.43)$$

Using the definition of the chemical potential, the manufactured solution ω is then

$$\omega(x, y; t) = \varphi(\varphi^2 - 1 + 2\pi^2\varepsilon^2) \text{ because } \Delta\varphi = -2\pi^2\varphi, \quad (1.44)$$

with φ given by (1.45).

The velocity is chosen as follows

$$\mathbf{u}(x, y; t) = \begin{pmatrix} \sin(\pi x) \cos(\pi y) \sin(t) \\ -\cos(\pi x) \sin(\pi y) \sin(t) \end{pmatrix}. \quad (1.45)$$

The velocity is divergence-free: $\nabla \cdot \mathbf{u} = 0$. As previously said, this is unfortunately not necessarily verified numerically. Therefore, the velocity divergence term is kept in the discretization. The following initial conditions are deduced:

$$\mathbf{u}(\cdot, 0) = \begin{pmatrix} 0 \\ 0 \end{pmatrix}, \quad \varphi(\cdot, 0) = \varphi_0(x, y) = \cos(\pi x) \cos(\pi y).$$

By injecting the expressions given by (1.43), (1.44), and (1.45) in the Cahn–Hilliard equations (1.38)–(1.39), the different terms are calculated as follows:

- $\partial_t \varphi(x, y; t) = -\cos(\pi x) \cos(\pi y) \sin(t)$
- $\mathbf{u} \cdot \nabla \varphi = \begin{pmatrix} \sin(\pi x) \cos(\pi y) \sin(t) \\ -\cos(\pi x) \sin(\pi y) \sin(t) \end{pmatrix} \cdot \begin{pmatrix} -\pi \sin(\pi x) \cos(\pi y) \cos(t) \\ -\pi \cos(\pi x) \sin(\pi y) \cos(t) \end{pmatrix}$
- $\mathbf{u} \cdot \nabla \varphi = \pi \cos(t) \sin(t) (\cos^2(\pi x) \sin^2(\pi y) - \sin^2(\pi x) \cos^2(\pi y))$
- $\mathbf{u} \cdot \nabla \varphi = \pi \cos(t) \sin(t) \left(\left(\frac{\cos(2\pi x)+1}{2} \right) \left(\frac{1-\cos(2\pi y)}{2} \right) - \left(\frac{1-\cos(2\pi x)}{2} \right) \left(\frac{\cos(2\pi y)+1}{2} \right) \right)$
- $\mathbf{u} \cdot \nabla \varphi = \frac{\pi \cos(t) \sin(t)}{4} (\cos(2\pi x) + 1 - \cos(2\pi y) - \cos(2\pi x) \cos(2\pi y) - [\cos(2\pi y) - \cos(2\pi x) \cos(2\pi y) - \cos(2\pi x) + 1])$
- $\mathbf{u} \cdot \nabla \varphi = \frac{\pi \cos(t) \sin(t)}{4} (2 \cos(2\pi x) - 2 \cos(2\pi y))$
- $\mathbf{u} \cdot \nabla \varphi = \frac{\pi \cos(t) \sin(t)}{2} [\cos(2\pi x) - \cos(2\pi y)]$
- $\Delta \omega = \Delta(\varphi^3) - \Delta \varphi + 2\pi^2 \varepsilon^2 \Delta \varphi = \Delta(\varphi^3) + 2\pi^2 \varphi (1 - 2\pi^2 \varepsilon^2)$ because $\Delta \varphi = -2\pi^2 \varphi$
- $\Delta(\varphi^3) = 6\pi^2 \varphi \cos^3(t) [\cos^2(\pi x) \sin^2(\pi y) + \sin^2(\pi x) \cos^2(\pi y) - \cos^2(\pi x) \cos^2(\pi y)]$

Thus,

$$\begin{aligned} \partial_t \varphi + \mathbf{u} \cdot \nabla \varphi - M \Delta \omega = & -\cos(\pi x) \cos(\pi y) \sin(t) \\ & + \frac{\pi \cos(t) \sin(t)}{2} [\cos(2\pi x) - \cos(2\pi y)] \\ & - M [2\pi^2 \varphi (1 - 2\pi^2 \varepsilon^2) + 6\pi^2 \varphi \cos^3(t) [\cos^2(\pi x) \sin^2(\pi y) \\ & + \sin^2(\pi x) \cos^2(\pi y) - \cos^2(\pi x) \cos^2(\pi y)]] \end{aligned}$$

The source term which must be added to the right-hand side of Equation (1.40) is given by

$$\begin{aligned} \mathbf{f}_{CH} = & - \cos(\pi x) \cos(\pi y) \sin(t) + \frac{\pi \cos(t) \sin(t)}{2} [\cos(2\pi x) - \cos(2\pi y)] \\ & - M[2\pi^2 \varphi(1 - 2\pi^2 \varepsilon^2) + 6\pi^2 \varphi \cos^2(t) [\cos^2(\pi x) \sin^2(\pi y) \\ & + \sin^2(\pi x) \cos^2(\pi y) - \cos^2(\pi x) \cos^2(\pi y)]] \end{aligned}$$

The parameters $M=10^{-5}$, $\varepsilon=10^{-2}$, and $t_f=0.4096$ are fixed for the convergence analysis. The boundary conditions are fixed such that: $\varphi^n = \varphi(\cdot, t^n)$ and $\omega^n = \omega(\cdot, t^n)$ on $\partial\Omega$. The analysis is performed with the three linearizations (1.31), (1.34), and (1.37) at constant CFL (lower than $\frac{\sqrt{2}}{2}$ because of the expression of the analytical velocity) with the following choice of time step Δt and mesh size h :

| Δt | h | $h^{1/2}$ | h^2 |
|-----------------------|-----------------------|----------------------------|--------------------------|
| $3.125 \cdot 10^{-4}$ | $3.125 \cdot 10^{-3}$ | $5.5901699 \cdot 10^{-2}$ | $9.765625 \cdot 10^{-6}$ |
| $6.25 \cdot 10^{-4}$ | $6.25 \cdot 10^{-3}$ | $7.9056941 \cdot 10^{-2}$ | $3.90625 \cdot 10^{-5}$ |
| $1.25 \cdot 10^{-3}$ | $1.25 \cdot 10^{-2}$ | $1.11803399 \cdot 10^{-1}$ | $1.5625 \cdot 10^{-4}$ |

The convergence rate is determined by computing the L^2 -norm and H^1 -norm for φ and ω .

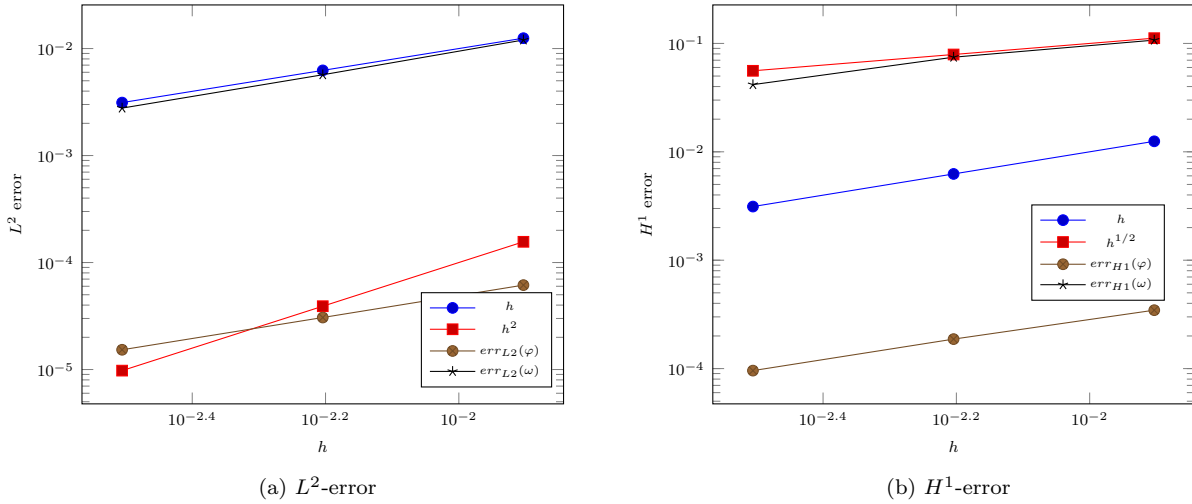


Figure 1.5: Spatial convergence analysis at constant CFL ≈ 0.1 (log scale)

Figure 1.5a depicts the logarithm of L^2 -errors both for φ and ω as a function of the logarithm of h , while Figure 1.5b depicts the logarithm of H^1 -errors. The results are the same for all the linearizations. From the convergence analysis represented in Figure 1.5, one deduces with the slopes that the L^2 order convergences of φ and ω are equal to 1, and the H^1 order convergences are respectively 1 and $\frac{1}{2}$.

1.7.2 Pulse rotation

A unity square domain $[0, 1]^2$ and a disk of radius 0.15 centered in $(0.5, 0.75)$ are here considered as shown in Figure 1.4. The domain is composed of 650,000 elements with a mesh size of $h=0.002$. This disk is transported by the Cahn–Hilliard equations with the following divergence-free velocity field:

$$\mathbf{u}(x, y) = \frac{\pi}{314} \begin{pmatrix} 0.5 - y \\ x - 0.5 \end{pmatrix}. \quad (1.46)$$

The interface thickness is fixed at $\varepsilon=0.008$, the mobility at $M=10^{-6}$, the time step at $\Delta t=0.1$, and the final time at $t_f=1280$ which means a bit more than two revolutions. Figure 1.6 shows the phase-field solution at $t=0$, $t=314$, $t=628$, $t=942$, and $t=1256$.

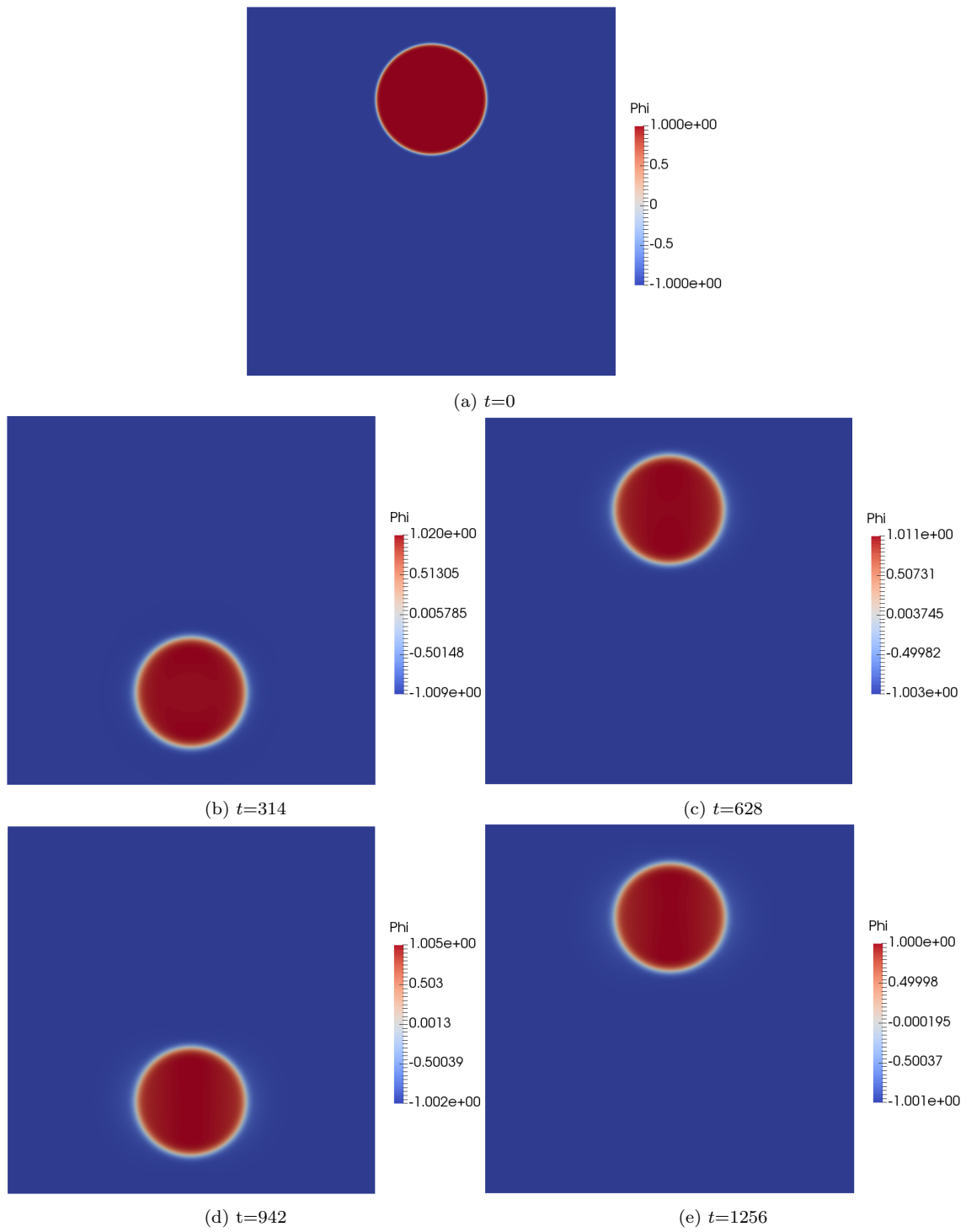


Figure 1.6: Phase-field solution at $t=0, 314, 628, 942,$ and 1256

The volume loss of the positive region of the order parameter φ is computed using the following relation approximated at a first-order accurate error measure:

$$\frac{|\int_{\Omega} H(\varphi(\mathbf{x}, 0)) \, d\mathbf{x} - \int_{\Omega} H(\varphi(\mathbf{x}, t_n)) \, d\mathbf{x}|}{\int_{\Omega} H(\varphi(\mathbf{x}, 0)) \, d\mathbf{x}} \quad (1.47)$$

where $H(\varphi)$ is the indicator function for $\varphi \geq 0$; i.e., $H(\varphi) = 1$ if $\varphi \geq 0$ and $H(\varphi) = 0$ otherwise. The same process can be done for the volume loss computation of the positive region of the level-set function α by only replacing φ by α .

By determining the percentage of volume loss from the relation (1.47), the results given by the phase-field method (PF) and the level-set method (LS) for different mesh sizes h are summarized in Table 1.1.

| $N_{elements}$ | h | ε | % Volume Loss - PF | % Volume Loss - LS |
|----------------|-------------------|--------------------|--------------------|--------------------|
| 648,000 | $2 \cdot 10^{-3}$ | $8 \cdot 10^{-3}$ | 2.07 | 1.59 |
| 152,000 | $4 \cdot 10^{-3}$ | $16 \cdot 10^{-3}$ | 3.47 | 3.92 |
| 67,500 | $6 \cdot 10^{-3}$ | $24 \cdot 10^{-3}$ | 4.89 | 9.34 |
| 38,000 | $8 \cdot 10^{-3}$ | $32 \cdot 10^{-3}$ | 6.26 | 19.20 |

Table 1.1: Pulse rotation: comparison of the volume loss by number of elements

From this Table 1.1, the results show that for the most refined mesh, the volume loss is a bit lesser with the level-set method (LS) than with the phase-field method (PF). However, the coarser is the mesh, the bigger is the volume loss for both methods and especially for LS which is considerably higher than PF.

1.7.3 Single Vortex

As the previous test case, a unity square domain $[0, 1]^2$ and a disk of radius 0.15 centered in (0.5, 0.75) is considered as shown in Figure 1.4. The domain is composed of 650,000 elements with a mesh size of $h=0.002$. This disk is transported by the Cahn–Hilliard equations with the following divergence-free velocity field:

$$\mathbf{u}(x, y) = 2 \begin{pmatrix} -\sin(\pi y) \cos(\pi y) \sin^2(\pi x) \\ \sin(\pi x) \cos(\pi x) \sin^2(\pi y) \end{pmatrix}. \quad (1.48)$$

The interface thickness ε varies with the mesh size h according to Table 1.2, the mobility is fixed at $M=10^{-6}$, the time step at $\Delta t=0.0002$, and the final time at $t_f=4$. All along with the movement, the disk deforms and becomes a single vortex revolving around the center. This problem has been introduced by [31] to test the accuracy of resolving thin filaments on the scale of the mesh size when stretching or tearing flows occur. Figure 1.7 shows the phase-field solution at $t=0$, $t=1$, $t=2$, $t=3$, and $t=4$ after performing the simulation in parallel with 4 cores.

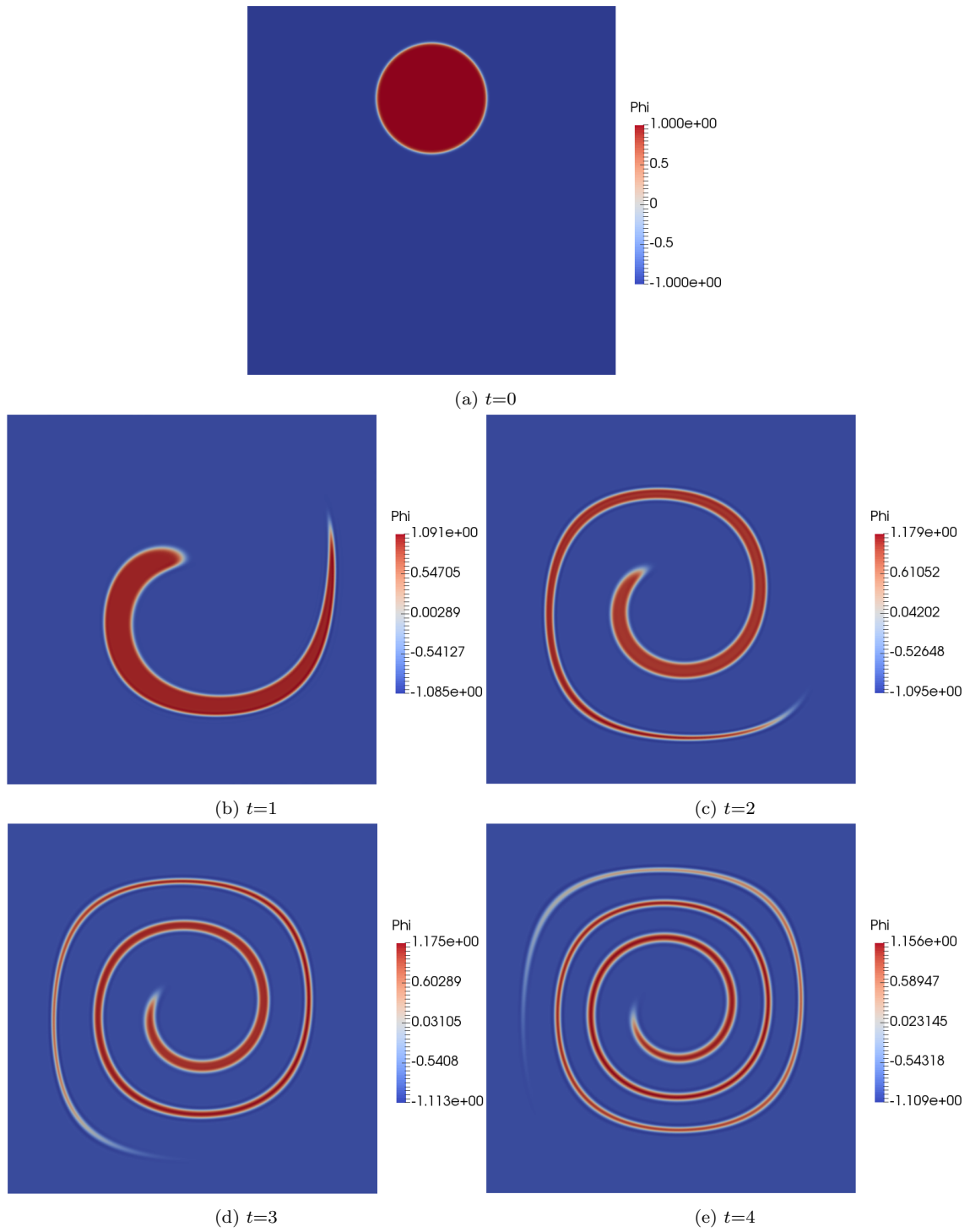


Figure 1.7: Phase-field solution at $t=0, 1, 2, 3,$ and 4

For a simulations performed for different number of elements in parallel with 4 cores, Table 1.2 gives the volume loss computed by the relation (1.47) with the phase-field method (PF) and with the level-set method (LS) at the final time. There is no diffuse interface with thickness ε for the level-set method.

| $Nb_{elements}$ | h | ε | % Volume Loss - PF | % Volume Loss - LS |
|-----------------|------|---------------|--------------------|--------------------|
| 648,000 | 2e-3 | 8e-3 | 0.45 | 1.15 |
| 152,000 | 4e-3 | 16e-3 | 2.04 | 2.77 |
| 67,500 | 6e-3 | 24e-3 | 5.18 | 11.46 |
| 38,000 | 8e-3 | 32e-3 | 11.81 | 31.82 |

Table 1.2: Single Vortex: comparison of the volume loss by number of elements

From Table 1.2, the results show that for the same mesh size the phase-field method losses less volume than the level-set method. From one mesh size to another the gap between the losses is more important for the level-set method than the phase-field method.

1.7.4 Zalesak’s Disk

In interface capturing methods, the Zalesak disk benchmark is a good indicator of diffusion errors. Initially, a slotted disk centered at (0.5,0.75) with a radius of 0.15 in a unity square domain is considered. The slot has a width of 0.05 and a length of 0.25. It is represented in the figure 1.8.

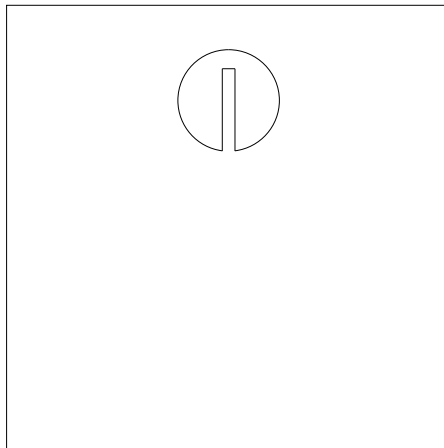


Figure 1.8: Zalesak disk benchmark

The test case consists of a rotation of the disk [32] in the constant velocity field (1.48) which is divergence-free. The domain is composed of 650,000 elements with a mesh size of $2 \cdot 10^{-3}$. The interface thickness is fixed at $\varepsilon=0.008$, the mobility at $M=10^{-6}$, the time step at $\Delta t=0.1$, and the final time at $t_f=1280$ which means a bit more than two revolutions. Figure 1.9 shows the phase-field solution at $t=0$, $t=314$, $t=628$, $t=942$, and $t=1256$ after performing the simulation in parallel with 4 cores.

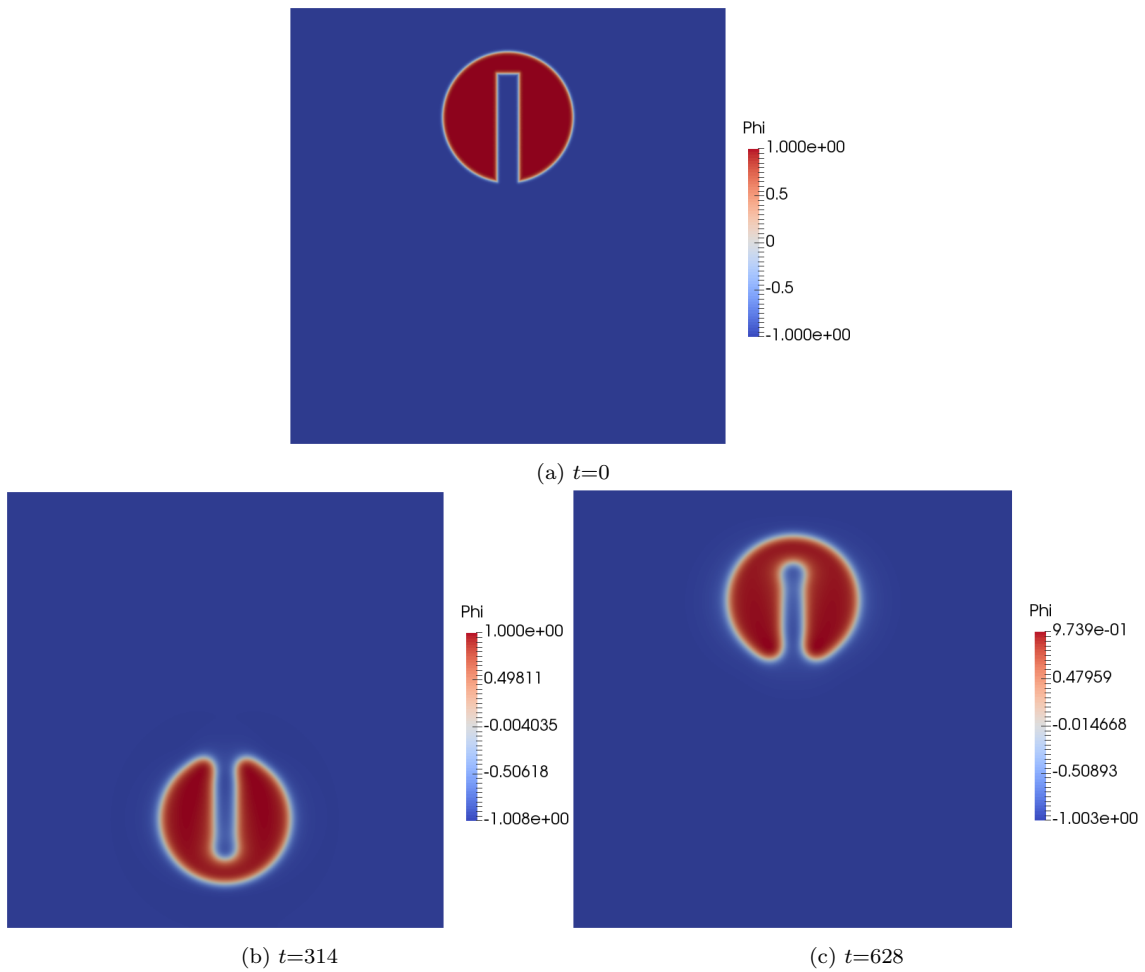


Figure 1.9: Phase-field solution of the Zalesak disk at $t=0$, 314, and 628

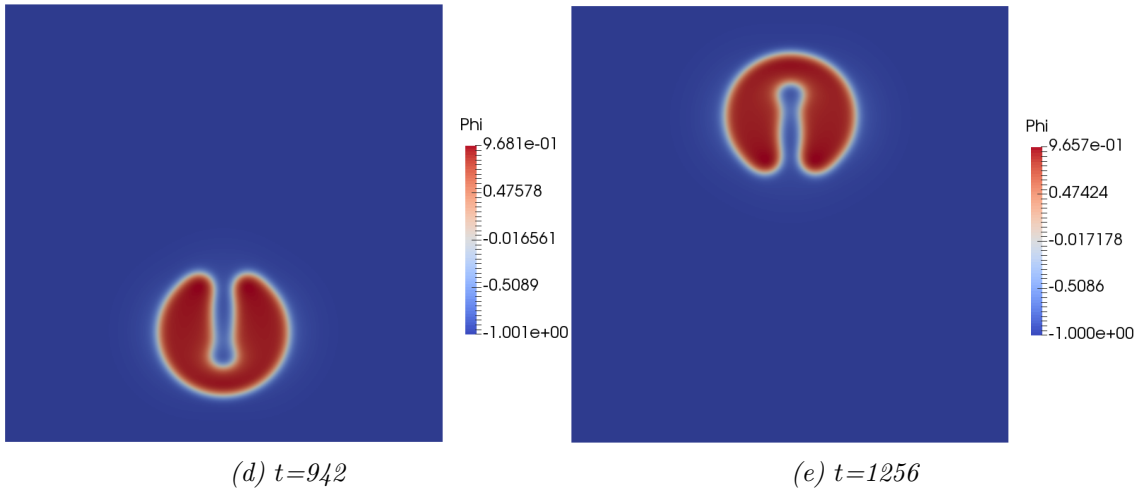


Figure 1.9: Phase-field solution of the Zalesak disk at $t = 942$ and 1256

As for the pulse rotation case, the simulation is performed in parallel with 4 cores and the volume loss is determined from the relation (1.47). The results given by the phase-field method (PF) and the level-set method (LS) for different mesh sizes h are summarized in Table 1.3.

| $Nb_{elements}$ | h | ε | % Volume Loss - PF | % Volume Loss - LS |
|-----------------|------|---------------|--------------------|--------------------|
| 648,000 | 2e-3 | 8e-3 | 0.19 | 7.08 |
| 152,000 | 4e-3 | 16e-3 | 1.73 | 31.63 |
| 67,500 | 6e-3 | 24e-3 | 3.38 | 75.61 |
| 38,000 | 8e-3 | 32e-3 | 4.66 | 100 |

Table 1.3: Zalesak Disk: comparison of the volume loss by number of elements

From this Table 1.3, the results show that for any considered mesh size, the volume loss of the slotted disk for LS is much bigger than for PF and this difference is increasing considerably as the mesh size is decreasing.

1.8 Conclusion

In the present chapter, an interface capturing method based on the Cahn–Hilliard equations has been introduced. Some properties of these equations have been presented and proved in the continuous and discrete framework. Then, a series of test cases have been simulated to investigate the numerical ability of the solver which enables to capture of the evolution of a diffuse interface separating two domains. It is important to note that numerical diffusion is observed in the simulation results. Oscillations of φ characterized by overshoot and undershoot observed on the plot of φ through an axis at the neighborhood of the diffuse interface of thickness ε , in Figure 1.10.

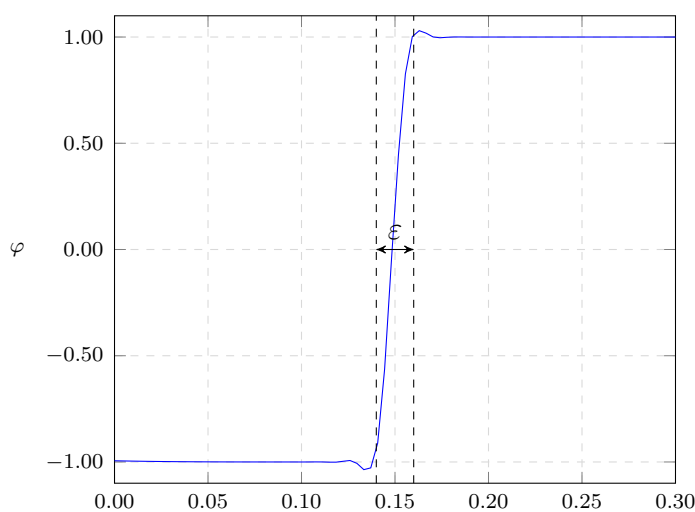


Figure 1.10: Evolution of the order parameter at the neighborhood of the interface diffuse

This is due to the advection operator in the Cahn–Hilliard model and could be boosted by the presence of the bilaplacian which enforces the diffusion. A solution allowing to deal with this drawback will be proposed in the conclusion chapter. Before that, the current model will be coupled to the multiphase flow framework in the next chapter.

Bibliography

- [1] P.G. Shewmon. *Transformations in Metals*. Materials Science and Engineering Series. McGraw-Hill, 1969. [23](#)
- [2] J. W. Cahn. Spinodal decomposition. *Trans. Met. Soc. AIME*, 242:168, 1968. [23](#)
- [3] J. W. Gibbs. *Scientific Papers of J. Willard Gibbs, 2 vols.* Bumstead, H. A., and Van Name. 2 vols. Bumstead, H. A., and Van Name. R. G., eds, 1961. [23](#)
- [4] J. W. Cahn and J. E. Hilliard. Free Energy of a Nonuniform System. I. Interfacial Free Energy. *Journal of Chemical Physics*, 28(2):258–267, 1958. [23](#), [25](#)
- [5] J. W. Cahn and J. E. Hilliard. Spinodal decomposition: A reprise. *Acta Metallurgica*, 19(2):151–161, 1971. [23](#)
- [6] V.L. Ginzburg and L.D. Landau. On the theory of superconductivity. *Sov. Phys. JETP*, 20:1064, 1950. [24](#)
- [7] Amy Novick-Cohen and Lee A. Segel. Nonlinear aspects of the Cahn–Hilliard equation. *Physica D: Nonlinear Phenomena*, 10(3):277–298, 1984. [25](#)
- [8] C. M. Elliott and H. Garcke. On the Cahn–Hilliard Equation with Degenerate Mobility. *SIAM Journal on Mathematical Analysis*, 27(2):404–423, 1996. [29](#)
- [9] J. F. Blowey and C. M. Elliott. The Cahn–Hilliard Gradient theory for phase separation with non-smooth free energy Part I: Mathematical analysis. *European Journal of Applied Mathematics*, 2(3):233–280, 1991. Publisher: Cambridge University Press. [25](#)
- [10] J.D Gunton, M. San Miguel, and P.S. Sahni. Dynamics of domains and textures. *Phase Transitiona and Critical Phenomena*, 8:269–446, 1983. [25](#)
- [11] R. Chella and J. Viñals. Mixing of a two-phase fluid by cavity flow. *Phys. Rev. E*, 53:3832–3840, Apr 1996.
- [12] M. Doi. Dynamics of domains and textures. *Theoretical Challenges in the Dynamics of Complex Fluids*, pages 293–314, 1997. [25](#)
- [13] D.A. Porter and K.E. Easterling. *Phase Transformations in Metals and Alloys, Third Edition (Revised Reprint)*. Taylor & Francis, 1992. [28](#)

-
- [14] A. Novick-Cohen. The Cahn–Hilliard equation: Mathematical and modelling perspectives. *Adv. Math. Sci. Appl.*, 8(3):965–985, 1998. [29](#)
- [15] C. M. Elliott. The Cahn–Hilliard model for the kinetics of phase separation. In José Francisco Rodrigues, editor, *Mathematical Models for Phase Change Problems*, pages 35–73. Birkhäuser Basel, 1989. [29](#), [35](#)
- [16] J. W. Cahn, C. M. Elliott, and A. Novick-Cohen. The Cahn–Hilliard equation with a concentration dependent mobility: motion by minus the laplacian of the mean curvature. *European Journal of Applied Mathematics*, 7(3):287–301, 1996. Publisher: Cambridge University Press. [29](#)
- [17] Y. Jingxue. On the existence of nonnegative continuous solutions of the Cahn–Hilliard equation. *Journal of Differential Equations*, 97(2):310–327, 1992. [29](#)
- [18] R. Dal Passo, H. Garcke, and G. Grün. On a fourth-order degenerate parabolic equation: Global entropy estimates, existence, and qualitative behaviour of solutions. *SIAM J. Math. Anal.*, 29:321–342, 1998. [30](#), [35](#)
- [19] M. A. Khanwale, A. D. Lofquist, H. Sundar, J. A. Rossmannith, and B. Ganapathysubramanian. Simulating two-phase flows with thermodynamically consistent energy stable Cahn–Hilliard Navier-Stokes equations on parallel adaptive octree based meshes. *Journal of Computational Physics*, 419(109674):293–317, 2020. [32](#)
- [20] F. Boyer. Mathematical study of multiphase flow under shear through order parameter formulation. *Asymptotic Analysis*, 20(2):175–212, 1999. [35](#)
- [21] John Barrett and James Blowey. Finite element approximation of the Cahn–Hilliard equation with concentration dependent mobility. *Math. Comp.*, 68, 1996. [35](#)
- [22] A. Debussche and L. Dettori. On the Cahn–Hilliard equation with a logarithmic free energy. *Nonlinear Analysis: Theory, Methods & Applications*, 24(10):1491–1514, 1995. [35](#)
- [23] DJ Eyre. An unconditionally stable one-step scheme for gradient systems. *IEEE Transactions on Image Processing*, 1998. [39](#)
- [24] F. Guillén-González and G. Tierra. On linear schemes for a Cahn–Hilliard diffuse interface model. *Journal of Computational Physics*, 234:140–171, Feb 2013. [40](#)

- [25] H. Abels, D. Depner, and H. Garcke. Existence of Weak Solutions for a Diffuse Interface Model for Two-Phase Flows of Incompressible Fluids with Different Densities. *Journal of Mathematical Fluid Mechanics*, 15:453–480, 2013. [44](#)
- [26] F Pigeonneau, P Samarito, and E Hachem. Discontinuous Galerkin finite element method applied to the coupled unsteady Stokes/Cahn–Hilliard equations. *International Journal for Numerical Methods in Fluids*, 90(6):267–295, 2019. [44](#)
- [27] PH Chiu and YT Lin. A conservative phase field method for solving incompressible two-phase flows. *Journal of Computational Physics*, 230(1):185–204, 2011. [44](#)
- [28] P. Knupp and K. Salari. *Verification of Computer Codes in Computational Science and Engineering*. Chapman and Hall/CRC, 1 edition, 2002. [45](#)
- [29] F. Stern, R. Wilson, and J. Shao. Quantitative V&V of CFD simulations and certification of CFD codes. *International Journal for Numerical Methods in Fluids*, 50(11):1335–1355, 2006. [45](#)
- [30] S Dong and J Shen. A time-stepping scheme involving constant coefficient matrices for phase-field simulations of two-phase incompressible flows with large density ratios. *Journal of Computational Physics*, 231(17):5788–5804, 2012. [45](#)
- [31] J. B. Bell, P. Colella, and H. M Glaz. A second-order projection method for the incompressible Navier–Stokes equations. *Journal of Computational Physics*, 85(2):257–283, 1989. [50](#)
- [32] Steven T Zalesak. Fully multidimensional flux-corrected transport algorithms for fluids. *Journal of Computational Physics*, 31(3):335–362, 1979. [53](#)

Chapter 2

Multiphase flow and coupling

Contents

| | | |
|------------|---|-----------|
| 2.1 | Introduction | 61 |
| 2.2 | Balance equations | 61 |
| 2.3 | Korteweg’s capillarity theory | 65 |
| 2.4 | The governing coupled equations | 67 |
| 2.5 | Mathematical properties of the coupled equations | 68 |
| 2.6 | Space and time discretization | 74 |
| 2.6.1 | Finite element discretization | 74 |
| 2.6.2 | Time discretization | 78 |
| 2.7 | Two-phase flow simulation with interface capturing | 80 |
| 2.7.1 | Dam-break 2D | 80 |
| 2.7.2 | Rising bubble 2D | 83 |
| 2.7.3 | Rayleigh–Taylor instability 2D | 89 |
| 2.8 | Conclusion | 93 |
| | Bibliography | 93 |

Résumé en Français

Une fois l'interface capturée à l'aide de la méthode phase-field, le but est de déterminer son évolution dans le cadre d'un écoulement de deux fluides. Ceci permettra de connaître la dynamique du film de vapeur autour du solide et des bulles de vapeur créées par l'ébullition. Ce chapitre présente l'étude du couplage de la dynamique des fluides avec la méthode de capture d'interface phase-field. Dans la littérature, différents modèles proposant un tel couplage existent. Le présent chapitre s'inspire d'un de ces modèles et propose de considérer les équations d'Euler et les lois de mélange d'un système de deux fluides incompressibles et Newtonien à l'aide des solutions des équations de Cahn–Hilliard. Afin de prendre en compte les effets de capillarité présents lors de la trempe industrielle, l'étude fera appel à la théorie de Korteweg. Les forces visqueuses, les forces de pression, et la force de gravité sont également considérées pour établir un modèle couplé de capture d'interface et d'écoulement biphasique appelé : le modèle couplé de Cahn–Hilliard–Navier–Stokes incompressible.

De même qu'avec les seules équations de Cahn–Hilliard, une étude mathématique et numérique des équations couplées est nécessaire pour une meilleure compréhension de ce modèle. Pour initier cette étude, ce chapitre présente un rappel de quelques propriétés mathématiques de ces équations couplées ainsi que des éléments de preuves associées : l'estimation d'énergie et la dissipation de l'énergie totale du modèle continu.

Afin d'implémenter numériquement de ce modèle, une discrétisation spatiale et temporelle de ces équations est proposée. Puisqu'une méthode de résolution à pas fractionnaire sera ici adoptée, le modèle discret des équations de Cahn–Hilliard déterminé au chapitre précédent sera conservé. Il s'agira donc de discrétiser les équations de Navier–Stokes. La discrétisation spatiale est réalisée par la méthode des éléments finis \mathbb{P}_1 Lagrange et utilise la méthode de stabilisation VMS pour la résolution. Ce chapitre se conclut par une étape de validation dans laquelle est simulée une série de cas test d'écoulements biphasique avec capture d'interface sur maillage uniforme en 2D. Les résultats obtenus par la méthode phase-field sont comparés avec ceux de la méthode level-set issus de la littérature.

2.1 Introduction

In the previous chapter, an interface capturing method based on the Cahn–Hilliard equations has been introduced and studied, to develop a method to capture the time-space evolution of a diffuse interface separating two domains. The present chapter is dedicated to the multiphase framework. This means that domains separated by an interface correspond to different fluids. In this framework, the flow is governed by a dynamic that has to be determined. The goal of this chapter is to develop and study a model coupling the interface capturing method with the flow dynamics. Diffuse-interface models for single-component and binary fluids are discussed in [1] and under the well-known "model H" in [2]. In [3–5], authors study a diffuse interface model for the flow of two viscous incompressible Newtonian fluids of the same density in a bounded domain. Boyer & al. [6] describe some aspects of the diffuse interface modeling of incompressible flows, composed of three immiscible components, without phase change. In [7], Jamet made a study of the diffuse interface models in fluid mechanics.

The development of the coupled model will begin with a study dedicated to the balance equations induced by the Cahn–Hilliard model. Then, to have a model taking into account the capillary action, a section dedicated to the Korteweg theory of capillarity will be presented. The next section will allow determining the governing equations of the coupled model. Then a study of some mathematical properties of these equations is proposed. To have a numerical framework, a full space and time discretization of these equations will be established. Then some numerical properties of the discrete model will be presented. Finally, a series of numerical simulations will be performed to assess the discrete model.

2.2 Balance equations

One considers a two-phase flow of immiscible and incompressible fluids in a bounded connected domain $\Omega \subset \mathbb{R}^d$, where d is the spatial dimension. The phase function φ allows identifying the two Newtonian fluids and takes the value $+1$ in the first fluid, of density ϱ_1 and viscosity η_1 , and -1 in the second one, of density ϱ_2 and viscosity η_2 , with a thin, smooth transition region of width ε between the two fluids, as represented in Figure 2.1.

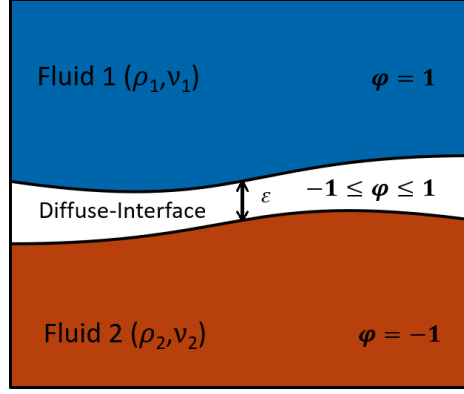


Figure 2.1: Two-fluid flow with the phase-field Cahn–Hilliard approach

By convention, the order parameter φ equals $+1$ in the heaviest phase, therefore one assumes that $\varrho_1 > \varrho_2$. From the order parameter φ , the global density and viscosity for the mixture are defined as follows:

$$\varrho(\varphi) = \frac{1 + \varphi}{2} \varrho_1 + \frac{1 - \varphi}{2} \varrho_2 \quad (2.1)$$

$$\eta(\varphi) = \frac{1 + \varphi}{2} \eta_1 + \frac{1 - \varphi}{2} \eta_2 \quad (2.2)$$

By using the relation (2.1), the continuity equation induced from the Cahn–Hilliard model is first looked for.

Proposition 2.2.1. *For φ solution of the Cahn–Hilliard equations (1.11)-(1.12) and a density defined as (2.1), the continuity equation is given by*

$$\partial_t (\varrho(\varphi)) + \nabla \cdot (\varrho(\varphi) \mathbf{u}) - \frac{\varrho_1 - \varrho_2}{2} \nabla \cdot (M(\varphi) \nabla \omega) = 0 \quad (2.3)$$

Proof. Let φ a solution of (1.11)-(1.12). From the relation (2.1),

$$\partial_t (\varrho(\varphi)) = \partial_t \left(\frac{\varrho_1 - \varrho_2}{2} \varphi + \frac{\varrho_1 + \varrho_2}{2} \right) = \frac{\varrho_1 - \varrho_2}{2} \partial_t (\varphi)$$

and

$$\begin{aligned} \nabla \cdot (\varrho(\varphi) \mathbf{u}) &= \nabla \cdot \left(\left(\frac{\varrho_1 - \varrho_2}{2} \varphi + \frac{\varrho_1 + \varrho_2}{2} \right) \mathbf{u} \right) \\ &= \frac{\varrho_1 - \varrho_2}{2} \nabla \cdot (\varphi \mathbf{u}) + \frac{\varrho_1 + \varrho_2}{2} \nabla \cdot \mathbf{u} \\ \nabla \cdot (\varrho(\varphi) \mathbf{u}) &= \frac{\varrho_1 - \varrho_2}{2} \nabla \cdot (\varphi \mathbf{u}) \text{ because of incompressibility } (\nabla \cdot \mathbf{u} = 0) \end{aligned}$$

By summing, it comes

$$\begin{aligned}
 \partial_t (\varrho(\varphi)) + \nabla \cdot (\varrho(\varphi) \mathbf{u}) &= \frac{\varrho_1 - \varrho_2}{2} \partial_t (\varphi) + \frac{\varrho_1 - \varrho_2}{2} \nabla \cdot (\varphi \mathbf{u}) \\
 &= \frac{\varrho_1 - \varrho_2}{2} (\partial_t (\varphi) + \nabla \cdot (\varphi \mathbf{u})) \\
 \partial_t (\varrho(\varphi)) + \nabla \cdot (\varrho(\varphi) \mathbf{u}) &= \frac{\varrho_1 - \varrho_2}{2} \nabla \cdot (M(\varphi) \nabla \omega) \text{ by Equation (1.11)}
 \end{aligned}$$

Therefore, the continuity equation is:

$$\partial_t (\varrho(\varphi)) + \nabla \cdot (\varrho(\varphi) \mathbf{u}) - \frac{\varrho_1 - \varrho_2}{2} \nabla \cdot (M(\varphi) \nabla \omega) = 0$$

□

The next step is to identify the temporal and convective term of the momentum equation coupling to the Cahn–Hilliard equation.

Proposition 2.2.2. *For φ solution of the Cahn–Hilliard equations (1.11)-(1.12) a density defined as (2.1), and an incompressible flow ($\nabla \cdot \mathbf{u} = 0$), the non-conservative form of the momentum equation is given by*

$$\begin{aligned}
 \partial_t (\varrho(\varphi) \mathbf{u}) + \nabla \cdot (\varrho(\varphi) \mathbf{u} \otimes \mathbf{u}) + \nabla \cdot (\mathbf{u} \otimes \mathbf{J}) &= \varrho(\varphi) \partial_t (\mathbf{u}) + (\varrho(\varphi) \mathbf{u} \cdot \nabla) \mathbf{u} \\
 &\quad + (\mathbf{J} \cdot \nabla) \mathbf{u}
 \end{aligned} \tag{2.4}$$

Proof. Let φ a solution of (1.11)-(1.12). From the relation (2.1),

$$\begin{aligned}
 \partial_t (\varrho(\varphi) \mathbf{u}) &= \partial_t (\varrho(\varphi)) \mathbf{u} + \varrho(\varphi) \partial_t (\mathbf{u}) \\
 &= \partial_t \left(\frac{\varrho_1 - \varrho_2}{2} \varphi + \frac{\varrho_1 + \varrho_2}{2} \right) \mathbf{u} + \varrho(\varphi) \partial_t (\mathbf{u}) \\
 \partial_t (\varrho(\varphi) \mathbf{u}) &= \frac{\varrho_1 - \varrho_2}{2} \partial_t (\varphi) \mathbf{u} + \varrho(\varphi) \partial_t (\mathbf{u})
 \end{aligned}$$

and

$$\begin{aligned}
 \nabla \cdot (\varrho(\varphi) \mathbf{u} \otimes \mathbf{u}) &= \nabla \cdot \left(\left(\frac{\varrho_1 - \varrho_2}{2} \varphi + \frac{\varrho_1 + \varrho_2}{2} \right) \mathbf{u} \otimes \mathbf{u} \right) \\
 &= \nabla \cdot \left(\left(\frac{\varrho_1 - \varrho_2}{2} \varphi \right) \mathbf{u} \otimes \mathbf{u} + \left(\frac{\varrho_1 + \varrho_2}{2} \right) \mathbf{u} \otimes \mathbf{u} \right) \\
 &= \frac{\varrho_1 - \varrho_2}{2} \nabla \cdot (\varphi \mathbf{u} \otimes \mathbf{u}) + \frac{\varrho_1 + \varrho_2}{2} \nabla \cdot (\mathbf{u} \otimes \mathbf{u}) \\
 &= \frac{\varrho_1 - \varrho_2}{2} (\nabla \cdot (\mathbf{u}) \varphi \mathbf{u} + (\mathbf{u} \cdot \nabla) (\varphi \mathbf{u}))
 \end{aligned}$$

$$\begin{aligned}
 & + \frac{\varrho_1 + \varrho_2}{2} \left(\underbrace{\nabla \cdot (\mathbf{u})}_{\mathbf{0}} \mathbf{u} + (\mathbf{u} \cdot \nabla) \mathbf{u} \right) \\
 \nabla \cdot (\varrho(\varphi) \mathbf{u} \otimes \mathbf{u}) & = \frac{\varrho_1 - \varrho_2}{2} (\nabla \cdot (\mathbf{u}) \varphi \mathbf{u} + (\mathbf{u} \cdot \nabla) \varphi \cdot \mathbf{u} + (\varphi \mathbf{u} \cdot \nabla) \mathbf{u}) \\
 & + \frac{\varrho_1 + \varrho_2}{2} (\mathbf{u} \cdot \nabla) \mathbf{u}
 \end{aligned}$$

Thus, by summing these terms, it comes

$$\begin{aligned}
 \partial_t (\varrho(\varphi) \mathbf{u}) + \nabla \cdot (\varrho(\varphi) \mathbf{u} \otimes \mathbf{u}) & = \frac{\varrho_1 - \varrho_2}{2} \partial_t (\varphi) \mathbf{u} + \varrho(\varphi) \partial_t (\mathbf{u}) \\
 & + \frac{\varrho_1 - \varrho_2}{2} (\nabla \cdot (\mathbf{u}) \varphi \mathbf{u} + (\mathbf{u} \cdot \nabla) \varphi \cdot \mathbf{u}) \\
 & + \frac{\varrho_1 - \varrho_2}{2} (\varphi \mathbf{u} \cdot \nabla) \mathbf{u} + \frac{\varrho_1 + \varrho_2}{2} (\mathbf{u} \cdot \nabla) \mathbf{u} \\
 & = \frac{\varrho_1 - \varrho_2}{2} (\partial_t (\varphi) + \nabla \cdot (\varphi \mathbf{u})) \mathbf{u} + \varrho(\varphi) \partial_t (\mathbf{u}) \\
 & + \frac{\varrho_1 - \varrho_2}{2} (\varphi \mathbf{u} \cdot \nabla) \mathbf{u} + \frac{\varrho_1 + \varrho_2}{2} (\mathbf{u} \cdot \nabla) \mathbf{u} \\
 & = \frac{\varrho_1 - \varrho_2}{2} (\partial_t (\varphi) + \nabla \cdot (\varphi \mathbf{u})) \mathbf{u} + \varrho(\varphi) \partial_t (\mathbf{u}) \\
 & + \left(\left(\frac{\varrho_1 - \varrho_2}{2} \varphi + \frac{\varrho_1 + \varrho_2}{2} \right) \mathbf{u} \cdot \nabla \right) \mathbf{u} \\
 & = \frac{\varrho_1 - \varrho_2}{2} \nabla \cdot (M(\varphi) \nabla \omega) \mathbf{u} + \varrho(\varphi) \partial_t (\mathbf{u}) \\
 & + (\varrho(\varphi) \mathbf{u} \cdot \nabla) \mathbf{u} \\
 & = \varrho(\varphi) \partial_t (\mathbf{u}) + (\varrho(\varphi) \mathbf{u} \cdot \nabla) \mathbf{u} \\
 & + \nabla \cdot \left(\underbrace{-\frac{\varrho_2 - \varrho_1}{2} M(\varphi) \nabla \omega}_{\mathbf{J}} \right) \mathbf{u} \\
 & = \varrho(\varphi) \partial_t (\mathbf{u}) + (\varrho(\varphi) \mathbf{u} \cdot \nabla) \mathbf{u} - (\nabla \cdot \mathbf{J}) \mathbf{u} \\
 \partial_t (\varrho(\varphi) \mathbf{u}) + \nabla \cdot (\varrho(\varphi) \mathbf{u} \otimes \mathbf{u}) & = \varrho(\varphi) \partial_t (\mathbf{u}) + (\varrho(\varphi) \mathbf{u} \cdot \nabla) \mathbf{u} + (\mathbf{J} \cdot \nabla) \mathbf{u} \\
 & - \nabla \cdot (\mathbf{u} \otimes \mathbf{J})
 \end{aligned}$$

Consequently, the non-conservative form of the momentum equation coupled to the Cahn–Hilliard equation is

$$\begin{aligned}
 \partial_t (\varrho(\varphi) \mathbf{u}) + \nabla \cdot (\varrho(\varphi) \mathbf{u} \otimes \mathbf{u}) + \nabla \cdot (\mathbf{u} \otimes \mathbf{J}) & = \varrho(\varphi) \partial_t (\mathbf{u}) + (\varrho(\varphi) \mathbf{u} \cdot \nabla) \mathbf{u} \\
 & + (\mathbf{J} \cdot \nabla) \mathbf{u}
 \end{aligned}$$

□

Non-conservative form of the momentum equation and continuity equation, induced by the Cahn–Hilliard model, have been determined in this section. It is the first step to obtaining the governing equations of an interface capturing based on the Cahn–Hilliard equations for multiphase flows. In fluid mechanics, the flow dynamics is given by the so-called Navier–Stokes equation. This equation corresponds to the non-conservative form of the momentum equation extended by modeled terms. To have a full coupled Cahn–Hilliard–Navier–Stokes model, the non-conservative form of the momentum equation (2.4) determined previously is used. In the following, the modeled terms considered in Navier–Stokes equations are those modeling the mass flux at the interface, the capillarity, the gravity, the pressure, and the viscous forces.

2.3 Korteweg's capillarity theory

Capillarity, or capillary action (Figure 2.2), is an inter-molecular phenomenon during which a liquid, like water, rises or falls in a narrow space such as a thin tube or the voids of a porous material against external forces, such that the gravity force.

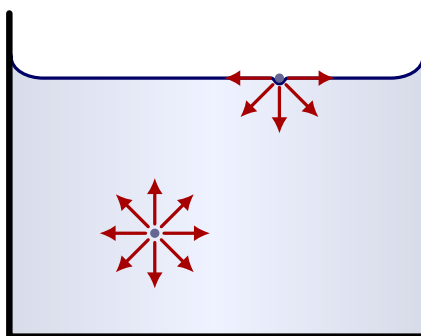


Figure 2.2: Capillary action

The use of capillary stress tensor to model the diffuse interface separating fluids and to model the forces associated has been developed in the literature. Anderson & al. [1] use these notions in a hydrodynamic description. The Van der Waals model of capillarity in the framework of liquid-vapor flows with phase change has been described in [7]. Antanovskii [8] derived a phase-field model of capillarity for non-isothermal, viscous, and quasi-compressible flow. Bresch & al. [9] proposed diffusive capillary models of Korteweg type to study their mathematical properties by assuming an isotherm flow.

Once Van der Waals [10] established a theory of the interface based on his thermodynamic model which allowed him to predict the thickness of the interface and to show that the interface thickness becomes infinite as the critical point is approached,

Korteweg [11] built on these theories. Specifically, he proposed a constitutive law for the capillary stress tensor based on the density and its spatial gradients. The capillarity stress tensor given by the Korteweg's capillarity theory

$$\mathbf{K} = \sigma \left(\left(\varrho(\varphi) \Delta \varrho(\varphi) + \frac{1}{2} |\nabla \varrho(\varphi)|^2 \right) \mathbf{I} - \nabla \varrho \otimes \nabla \varrho \right) \quad (2.5)$$

is called the Korteweg stress tensor. It implies a surface tension force in the tangential direction of the interface. Surface tension is an inter-molecular force involved in the capillary action. It refers to liquid molecules that are more closely bound together at the surface, making the top of the liquid more tight and dense than the rest of the liquid. Surface tension holds the liquid together at the top as it moves up during capillary action, holding the liquid molecules together like a drawstring.

The divergence of this tensor intervenes in the Navier–Stokes equation:

$$\begin{aligned} \nabla \cdot \mathbf{K} &= \nabla \cdot \left(\frac{\sigma}{2} (\Delta \varrho^2 - |\nabla \varrho|^2) \mathbf{I} - \sigma \nabla \varrho \otimes \nabla \varrho \right) \\ &= \nabla \cdot \left(\frac{\sigma}{2} (\Delta \varrho^2 - |\nabla \varrho|^2) \mathbf{I} \right) - \sigma \nabla \cdot (\nabla \varrho \otimes \nabla \varrho) \\ \nabla \cdot \mathbf{K} &= \nabla \left(\frac{\sigma}{2} (\Delta \varrho^2 - |\nabla \varrho|^2) \right) - \sigma \nabla \cdot (\nabla \varrho \otimes \nabla \varrho) \end{aligned}$$

Since $\nabla \varrho = \frac{\varrho_1 - \varrho_2}{2} \nabla \varphi$ by the relation (2.1),

$$\begin{aligned} \nabla \cdot (\nabla \varrho \otimes \nabla \varrho) &= \nabla \cdot \left(\frac{(\varrho_1 - \varrho_2)}{2} \nabla \varphi \otimes \frac{(\varrho_1 - \varrho_2)}{2} \nabla \varphi \right) \\ &= \nabla \cdot \left(\frac{(\varrho_1 - \varrho_2)^2}{4} \nabla \varphi \otimes \nabla \varphi \right) \\ &= \frac{(\varrho_1 - \varrho_2)^2}{4} \nabla \cdot (\nabla \varphi \otimes \nabla \varphi) + \underbrace{\nabla \varphi \otimes \nabla \varphi : \nabla \left(\frac{(\varrho_1 - \varrho_2)^2}{4} \right)}_0 \\ \nabla \cdot (\nabla \varrho \otimes \nabla \varrho) &= \frac{(\varrho_1 - \varrho_2)^2}{4} \nabla \cdot (\nabla \varphi \otimes \nabla \varphi) \end{aligned}$$

However, for (φ, ω) solutions of (1.11)-(1.12)

$$\begin{aligned} \nabla \cdot (\nabla \varphi \otimes \nabla \varphi) &= \Delta \varphi \nabla \varphi + \nabla \left(\frac{1}{2} |\nabla \varphi|^2 \right) \\ &= \left(\frac{\varepsilon^2}{\varepsilon^2} \Delta \varphi - \frac{1}{\varepsilon^2} f(\varphi) \right) \nabla \varphi + \nabla \left(\frac{1}{\varepsilon^2} F(\varphi) + \frac{1}{2} |\nabla \varphi|^2 \right) \end{aligned}$$

$$\begin{aligned}
 &= \frac{1}{\varepsilon^2} \underbrace{(\varepsilon^2 \Delta \varphi - f(\varphi))}_{-\omega} \nabla \varphi + \nabla \left(\frac{1}{\varepsilon^2} F(\varphi) + \frac{1}{2} |\nabla \varphi|^2 \right) \\
 \nabla \cdot (\nabla \varphi \otimes \nabla \varphi) &= -\frac{1}{\varepsilon^2} \omega \nabla \varphi + \nabla \left(F(\varphi) + \frac{1}{2} |\nabla \varphi|^2 \right)
 \end{aligned}$$

Consequently, the divergence of the capillarity stress tensor is given by:

$$\begin{aligned}
 \nabla \cdot \mathbf{K} &= \nabla \left(\frac{\sigma}{2} (\Delta \varrho(\varphi)^2 - |\nabla \varrho(\varphi)|^2) \right) \\
 &\quad - \sigma \frac{(\varrho_1 - \varrho_2)^2}{4} \left(\nabla \left(F(\varphi) + \frac{1}{2} |\nabla \varphi|^2 \right) - \frac{1}{\varepsilon^2} \omega \nabla \varphi \right)
 \end{aligned} \tag{2.6}$$

The Navier–Stokes equations coupled to the Cahn–Hilliard equations can now be determined.

2.4 The governing coupled equations

In Section 2.2, non-conservative form of the momentum equation has been determined with the help of the Cahn–Hilliard equations (1.11)–(1.12). These equations have also been used in Section 2.3 to have an expression of the capillary forces in function of the Cahn–Hilliard solutions. To have a full coupled Cahn–Hilliard–Navier–Stokes model for an incompressible two-fluid mixture of different densities with capillary forces involved, one models in addition the gravity forces with the help of a gravity vector \mathbf{g} and the pressure and viscous forces by the stress tensor for incompressible Newtonian fluids $\mathbf{S} = -P\mathbf{I} + 2\eta(\varphi)\mathbf{D}(\mathbf{u})$, where $\mathbf{D}(\mathbf{u}) = \frac{\nabla \mathbf{u} + \nabla \mathbf{u}^T}{2}$ is the strain tensor, P is the hydrodynamic pressure, and \mathbf{I} is the identity tensor. Consequently, the coupled equations in the domain Ω are given by:

$$\partial_t \varphi + \nabla \cdot (\varphi \mathbf{u}) - \nabla \cdot (M(\varphi) \nabla \omega) = 0, \tag{2.7}$$

$$\omega + \varepsilon^2 \Delta \varphi - f(\varphi) = 0, \tag{2.8}$$

$$\partial_t (\varrho(\varphi) \mathbf{u}) + \nabla \cdot (\varrho(\varphi) \mathbf{u} \otimes \mathbf{u}) + \nabla \cdot (\mathbf{u} \otimes \mathbf{J}) = \nabla \cdot (\mathbf{S} + \mathbf{K}) + \varrho(\varphi) \mathbf{g}, \tag{2.9}$$

$$\nabla \cdot \mathbf{u} = 0. \tag{2.10}$$

In Section 2.2, the relation (2.4) has been showed:

$$\begin{aligned}
 \partial_t (\varrho(\varphi) \mathbf{u}) + \nabla \cdot (\mathbf{u} \otimes \varrho(\varphi) \mathbf{u}) + \nabla \cdot (\mathbf{u} \otimes \mathbf{J}) &= \varrho(\varphi) \partial_t (\mathbf{u}) + (\varrho(\varphi) \mathbf{u} \cdot \nabla) \mathbf{u} \\
 &\quad + (\mathbf{J} \cdot \nabla) \mathbf{u}
 \end{aligned}$$

and in Section 2.3, the divergence of the capillary tensor (2.6) is given by:

$$\begin{aligned}
 \nabla \cdot \mathbf{K} &= \nabla \left(\frac{\sigma}{2} (\Delta \varrho(\varphi)^2 - |\nabla \varrho(\varphi)|^2) \right) \\
 &\quad - \sigma \frac{(\varrho_1 - \varrho_2)^2}{4} \left(\nabla \left(F(\varphi) + \frac{1}{2} |\nabla \varphi|^2 \right) - \frac{1}{\varepsilon^2} \omega \nabla \varphi \right)
 \end{aligned}$$

It does remain to deal with the divergence of the stress tensor \mathbf{S} :

$$\nabla \cdot \mathbf{S} = \nabla \cdot (-P\mathbf{I} + 2\eta(\varphi)\mathbf{D}(\mathbf{u})) = -\nabla P + \nabla \cdot (2\eta(\varphi)\mathbf{D}(\mathbf{u})) \quad (2.11)$$

which is summed with (2.6) to give:

$$\begin{aligned} \nabla \cdot (\mathbf{S} + \mathbf{K}) &= -\nabla P + \nabla \cdot (2\eta(\varphi)\mathbf{D}(\mathbf{u})) + \nabla \left(\frac{\sigma}{2} (\Delta \varrho^2 - |\nabla \varrho|^2) \right) \\ &\quad - \sigma \frac{(\varrho_1 - \varrho_2)^2}{4} \left(-\frac{1}{\varepsilon^2} \omega \nabla \varphi + \nabla \left(F(\varphi) + \frac{1}{2} |\nabla \varphi|^2 \right) \right) \\ \nabla \cdot (\mathbf{S} + \mathbf{K}) &= -\nabla p + \nabla \cdot (2\eta(\varphi)\mathbf{D}(\mathbf{u})) + \frac{\sigma}{\varepsilon^2} \omega \nabla \varphi \end{aligned}$$

where $p = P - \sigma \left(\frac{1}{2} (\Delta \varrho^2 - |\nabla \varrho|^2) + \frac{(\varrho_1 - \varrho_2)^2}{4} (F(\varphi) + \frac{1}{2} |\nabla \varphi|^2) \right)$ is the pressure.

Thus, the coupled Cahn–Hilliard–Navier–Stokes equations for non miscible and incompressible two-fluid flow in a domain the domain Ω are:

$$\partial_t \varphi + \nabla \cdot (\varphi \mathbf{u}) - \nabla \cdot (M(\varphi) \nabla \omega) = 0, \quad (2.12)$$

$$\omega + \varepsilon^2 \Delta \varphi - f(\varphi) = 0, \quad (2.13)$$

$$\begin{aligned} \varrho(\varphi) \partial_t (\mathbf{u}) + (\varrho(\varphi) \mathbf{u} \cdot \nabla) \mathbf{u} + (\mathbf{J} \cdot \nabla) \mathbf{u} \\ - \nabla \cdot (2\eta(\varphi)\mathbf{D}(\mathbf{u})) + \nabla p = \frac{\sigma}{\varepsilon^2} \omega \nabla \varphi + \varrho(\varphi) \mathbf{g}, \end{aligned} \quad (2.14)$$

$$\nabla \cdot \mathbf{u} = 0, \quad (2.15)$$

with the following initial and boundary conditions:

$$\mathbf{u}(\cdot, 0) = \mathbf{u}_0, \quad \varphi(\cdot, 0) = \varphi_0 \quad \text{in } \Omega, \quad (2.16)$$

$$\mathbf{u} \cdot \mathbf{n} = 0, \quad \frac{\partial \varphi}{\partial \mathbf{n}} = \frac{\partial \omega}{\partial \mathbf{n}} = 0 \quad \text{on } \partial \Omega \times (0, t_f], \quad t_f > 0. \quad (2.17)$$

One notes that the pressure p depends on the hydrodynamic pressure P , the order parameter φ , and the surface tension coefficient σ . The flow and the interface dynamics are governed by the Cahn–Hilliard–Navier–Stokes model which can also describe topological transitions like droplet coalescence.

2.5 Mathematical properties of the coupled equations

As in the previous chapter, the order parameter φ is assumed respecting the maximum principle in all the theoretical results introduced in the present chapter.

In this section, a theoretical study of the coupled model (2.12)-(2.15) established in the previous Section 2.4 will be done. Compared to the model (1.11)-(1.12)

introduced in Section 1.3, these equations describe the evolution in space and time of the macroscopic variables characterizing, on one hand, the mixture composition in the whole domain, by the variables φ and ω , and in another hand, the flow of the incompressible, diphasic, and non-homogeneous mixture, by the velocity field \mathbf{u} and the pressure p . As stated in Section 1.4 of the last chapter for the model (1.11)-(1.12), the mathematical study will rely on the existence and uniqueness results of the model (2.12)-(2.17). For the existence of weak solutions, a preliminary study to find the energy spaces for which these solutions belong is required. This study relies on the following energy estimate result:

Theorem 2.5.1. *If the solutions $(\varphi, \omega, \mathbf{u}, p)$ of (2.12)-(2.15) with a constant positive mobility ($M(\varphi) = M > 0$) the conditions (2.16)-(2.17) exist in the weak sense, then by denoting $\mathbf{H}^1(\Omega) := (H^1(\Omega))^d$*

$$\begin{aligned}\varphi &\in L^\infty([0, t_f]; H^1(\Omega)) \cap L^2([0, t_f]; H^2(\Omega)) \\ \omega &\in L^2([0, t_f]; H^1(\Omega)) \\ \mathbf{u} &\in \mathbf{L}^\infty([0, t_f]; \mathbf{L}^2(\Omega)) \cap \mathbf{L}^2([0, t_f]; \mathbf{H}^1(\Omega)) \\ p &\in L^2(\Omega)\end{aligned}$$

and the following energy estimate is obtained for a certain $c_1, c_2, c_3, c_4, c_5 > 0$:

$$\begin{aligned}&c_1 \|\mathbf{u}(t)\|_{L^2(\Omega)}^2 + c_2 \int_0^t \|\mathbf{D}(\mathbf{u}(s))\|_{L^2(\Omega)}^2 ds + c_3 \|\nabla \varphi(t)\|_{L^2(\Omega)}^2 \\ &+ c_4 \left\| \frac{\varphi^2(t) - 1}{2} \right\|_{L^2(\Omega)}^2 + c_5 \int_0^t \|\nabla \omega(s)\|_{L^2(\Omega)}^2 ds \\ &\leq c_1 \|\mathbf{u}_0\|_{L^2(\Omega)}^2 + c_3 \|\nabla \varphi_0\|_{L^2(\Omega)}^2 + c_4 \left\| \frac{\varphi_0^2 - 1}{2} \right\|_{L^2(\Omega)}^2\end{aligned}\tag{2.18}$$

Proof. For the proof, one can consider the gravitational field as a derivation of a gravitational potential: $\mathbf{g} = \nabla \mathcal{G}$ which can be included in the pressure gradient ∇p . Let $(\varphi, \omega, \mathbf{u}, p)$ weak solutions of (2.12)-(2.15) with the conditions (2.16)-(2.17). First, one multiplies Equation (2.12) by $\frac{\sigma}{\varepsilon^2} \omega$ and integrates it on Ω . Second, Equation (2.13) is multiplied by $-\frac{\sigma}{\varepsilon^2} \partial_t \varphi$ and integrated on Ω . Finally, Equation (2.14) is multiplied by \mathbf{u} and also integrated on Ω .

One recalls a useful identity which helps for the estimate energy:

Lemma 2.5.2. *For all vectors \mathbf{u}, \mathbf{v} and $\mathbf{w} \in \mathbb{R}^d$,*

$$\begin{aligned}(\mathbf{w} \cdot \nabla) \mathbf{u} \cdot \mathbf{v} &= \mathbf{v} \otimes \mathbf{w} : \nabla \mathbf{u} \\ &= \nabla \cdot (\mathbf{u} \cdot \mathbf{v} \otimes \mathbf{w}) - (\mathbf{w} \cdot \nabla) \mathbf{v} \cdot \mathbf{u} - \mathbf{u} \cdot \mathbf{v} \nabla \cdot \mathbf{w}\end{aligned}$$

By dealing with each term:

$$\begin{aligned}
 & \bullet \int_{\Omega} [\varrho(\varphi)\partial_t \mathbf{u} + (\varrho(\varphi)\mathbf{u} \cdot \nabla) \mathbf{u} + (\mathbf{J} \cdot \nabla)\mathbf{u}] \cdot \mathbf{u} \, d\mathbf{x} \\
 &= \int_{\Omega} \varrho(\varphi)\partial_t \left(\frac{1}{2}|\mathbf{u}|^2\right) \, d\mathbf{x} + \int_{\Omega} \frac{1}{2} [\nabla \cdot (\mathbf{u} \cdot \mathbf{u} \otimes \varrho(\varphi)\mathbf{u}) - |\mathbf{u}|^2 \nabla \cdot (\varrho(\varphi)\mathbf{u})] \, d\mathbf{x} \\
 &\quad + \int_{\Omega} \frac{1}{2} [\nabla \cdot (\mathbf{u} \cdot \mathbf{u} \otimes \mathbf{J}) - |\mathbf{u}|^2 \nabla \cdot \mathbf{J}] \, d\mathbf{x} \text{ by Lemma 2.5.2} \\
 &= \int_{\Omega} \left[\partial_t \left(\frac{\varrho(\varphi)}{2} |\mathbf{u}|^2 \right) - \frac{1}{2} |\mathbf{u}|^2 \partial_t (\varrho(\varphi)) \right] \, d\mathbf{x} + \int_{\Omega} \frac{1}{2} \nabla \cdot (\mathbf{u} \cdot \mathbf{u} \otimes \varrho(\varphi)\mathbf{u}) \, d\mathbf{x} \\
 &\quad - \int_{\Omega} |\mathbf{u}|^2 \nabla \cdot (\varrho(\varphi)\mathbf{u}) \, d\mathbf{x} + \int_{\Omega} \frac{1}{2} \nabla \cdot (\mathbf{u} \cdot \mathbf{u} \otimes \mathbf{J}) \, d\mathbf{x} - \int_{\Omega} |\mathbf{u}|^2 \nabla \cdot \mathbf{J} \, d\mathbf{x} \\
 &= \int_{\Omega} \partial_t \left(\frac{\varrho(\varphi)}{2} |\mathbf{u}|^2 \right) \, d\mathbf{x} + \int_{\Omega} \frac{1}{2} \nabla \cdot (\mathbf{u} \cdot \mathbf{u} \otimes \varrho(\varphi)\mathbf{u}) \, d\mathbf{x} + \int_{\Omega} \frac{1}{2} \nabla \cdot (\mathbf{u} \cdot \mathbf{u} \otimes \mathbf{J}) \, d\mathbf{x} \\
 &\quad - \int_{\Omega} \frac{1}{2} |\mathbf{u}|^2 \underbrace{[\partial_t (\varrho(\varphi)) + \nabla \cdot (\varrho(\varphi)\mathbf{u}) + \nabla \cdot \mathbf{J}]}_0 \, d\mathbf{x} \text{ (by equation (2.3))},
 \end{aligned}$$

However, $\int_{\Omega} \frac{1}{2} \nabla \cdot (\mathbf{u} \cdot \mathbf{u} \otimes \varrho(\varphi)\mathbf{u}) \, d\mathbf{x} = \int_{\Omega} \frac{1}{2} \nabla \cdot (\mathbf{u} \cdot \mathbf{u} \otimes \mathbf{J}) \, d\mathbf{x} = 0$
since $\mathbf{u} \cdot \mathbf{n} = 0$ on $\partial\Omega$ and by using the *divergence theorem*.

Therefore, it comes

$$\int_{\Omega} [\varrho(\varphi)\partial_t \mathbf{u} + (\varrho(\varphi)\mathbf{u} \cdot \nabla) \mathbf{u} + (\mathbf{J} \cdot \nabla)\mathbf{u}] \cdot \mathbf{u} \, d\mathbf{x} = \int_{\Omega} \partial_t \left(\frac{\varrho(\varphi)}{2} |\mathbf{u}|^2 \right) \, d\mathbf{x}.$$

- $\int_{\Omega} \nabla p \cdot \mathbf{u} \, d\mathbf{x} = \underbrace{\int_{\Omega} \nabla \cdot (p\mathbf{u}) \, d\mathbf{x}}_{\int_{\partial\Omega} p\mathbf{u} \cdot \mathbf{n} \, ds=0} - \underbrace{\int_{\Omega} p \nabla \cdot \mathbf{u} \, d\mathbf{x}}_0 = 0$ ($\mathbf{u} \cdot \mathbf{n} = 0$ on $\partial\Omega$ by (2.17)).
- $-\int_{\Omega} \nabla \cdot (2\eta(\varphi)\mathbf{D}(\mathbf{u})) \cdot \mathbf{u} \, d\mathbf{x}$
 $= -\int_{\Omega} \nabla \cdot (\mathbf{u} \cdot 2\eta(\varphi)\mathbf{D}(\mathbf{u})) \, d\mathbf{x} + \int_{\Omega} 2\eta(\varphi)|\mathbf{D}(\mathbf{u})|^2 \, d\mathbf{x} = \int_{\Omega} 2\eta(\varphi)|\mathbf{D}(\mathbf{u})|^2 \, d\mathbf{x}.$
 $\underbrace{\int_{\partial\Omega} \mathbf{u} \cdot 2\eta(\varphi)\mathbf{D}(\mathbf{u}) \cdot \mathbf{n} \, ds}_0 = 0$
- $\int_{\Omega} \frac{\sigma}{\varepsilon^2} \omega \nabla \varphi \cdot \mathbf{u} \, d\mathbf{x}.$
- $-\int_{\Omega} \frac{\sigma}{\varepsilon^2} \omega \partial_t \varphi \, d\mathbf{x}.$

- $-\int_{\Omega} \frac{\sigma}{\varepsilon^2} \varepsilon^2 \Delta \varphi \partial_t \varphi \, d\mathbf{x}$
 $= \int_{\Omega} \sigma \nabla(\partial_t \varphi) \cdot \nabla \varphi \, d\mathbf{x} - \underbrace{\int_{\partial\Omega} \sigma \partial_t \varphi \nabla \varphi \cdot \mathbf{n} \, ds}_{=0 \text{ because } \nabla \varphi \cdot \mathbf{n} = 0 \text{ on } \partial\Omega} = \int_{\Omega} \sigma \partial_t (\nabla \varphi) \cdot \nabla \varphi \, d\mathbf{x}.$
Therefore, $-\int_{\Omega} \frac{\sigma}{\varepsilon^2} \Delta \varphi \partial_t \varphi \, d\mathbf{x} = \int_{\Omega} \partial_t (\frac{\sigma}{2} |\nabla \varphi|^2) \, d\mathbf{x}.$
- $-\int_{\Omega} f(\varphi) \times (-\frac{\sigma}{\varepsilon^2} \partial_t \varphi) \, d\mathbf{x}$
 $= \int_{\Omega} \frac{\sigma}{\varepsilon^2} \partial_t \varphi f(\varphi) \, d\mathbf{x} = \int_{\Omega} \frac{\sigma}{\varepsilon^2} \partial_t (F(\varphi)) \, d\mathbf{x} = \partial_t \left(\int_{\Omega} \frac{\sigma}{\varepsilon^2} F(\varphi) \, d\mathbf{x} \right).$
- $\int_{\Omega} \frac{\sigma}{\varepsilon^2} \omega \partial_t \varphi \, d\mathbf{x}.$
- $\int_{\Omega} \frac{\sigma}{\varepsilon^2} \omega \mathbf{u} \cdot \nabla \varphi \, d\mathbf{x}.$
- $\int_{\Omega} \frac{\sigma}{\varepsilon^2} \omega \varphi \underbrace{\nabla \cdot \mathbf{u}}_0 \, d\mathbf{x} = 0.$
- $-\int_{\Omega} \nabla \cdot (M(\varphi) \nabla \omega) \frac{\sigma}{\varepsilon^2} \omega \, d\mathbf{x}$
 $= \int_{\Omega} \frac{\sigma}{\varepsilon^2} M(\varphi) |\nabla \omega|^2 \, d\mathbf{x} - \underbrace{\int_{\partial\Omega} \frac{\sigma}{\varepsilon^2} M(\varphi) \omega \nabla \omega \cdot \mathbf{n} \, ds}_{=0} \, d\mathbf{x} \quad (\nabla \omega \cdot \mathbf{n} = 0 \text{ on } \partial\Omega)$
Therefore, $-\int_{\Omega} \nabla \cdot (M(\varphi) \nabla \omega) \frac{\sigma}{\varepsilon^2} \omega \, d\mathbf{x} = \int_{\Omega} \frac{\sigma}{\varepsilon^2} M(\varphi) |\nabla \omega|^2 \, d\mathbf{x}.$

By summing all these terms, it comes

$$\begin{aligned}
& \partial_t \left(\int_{\Omega} \frac{\rho(\varphi)}{2} |\mathbf{u}|^2 \, d\mathbf{x} \right) + \int_{\Omega} 2\eta(\varphi) |\mathbf{D}(\mathbf{u})|^2 \, d\mathbf{x} - \int_{\Omega} \frac{\sigma}{\varepsilon^2} \omega \partial_t \varphi \, d\mathbf{x} \\
& + \partial_t \left(\int_{\Omega} \frac{\sigma}{2} |\nabla \varphi|^2 \, d\mathbf{x} \right) + \partial_t \left(\int_{\Omega} \frac{\sigma}{\varepsilon^2} F(\varphi) \, d\mathbf{x} \right) + \int_{\Omega} \frac{\sigma}{\varepsilon^2} \omega \partial_t \varphi \, d\mathbf{x} \\
& + \int_{\Omega} \frac{\sigma}{\varepsilon^2} \omega \mathbf{u} \cdot \nabla \varphi \, d\mathbf{x} + \int_{\Omega} \frac{\sigma}{\varepsilon^2} M(\varphi) |\nabla \omega|^2 \, d\mathbf{x} \\
& = \int_{\Omega} \frac{\sigma}{\varepsilon^2} \omega \mathbf{u} \cdot \nabla \varphi \, d\mathbf{x}
\end{aligned}$$

which means,

$$\begin{aligned} & \partial_t \left(\int_{\Omega} \frac{\varrho(\varphi)}{2} |\mathbf{u}|^2 \, d\mathbf{x} \right) + \int_{\Omega} 2\eta(\varphi) |\mathbf{D}(\mathbf{u})|^2 \, d\mathbf{x} + \partial_t \left(\int_{\Omega} \frac{\sigma}{2} |\nabla \varphi|^2 \, d\mathbf{x} \right) \\ & + \partial_t \left(\int_{\Omega} \frac{\sigma}{\varepsilon^2} F(\varphi) \, d\mathbf{x} \right) + \int_{\Omega} \frac{\sigma}{\varepsilon^2} M(\varphi) |\nabla \omega|^2 \, d\mathbf{x} = 0 \end{aligned} \quad (2.19)$$

Because the density $\varrho(\varphi)$ and the viscosity $\eta(\varphi)$ are bounded for any φ , there exists $\varrho_{min} > 0$ and $\eta_{min} > 0$ such that

$$\varrho_{min} \leq \varrho(\varphi), \quad \forall \varphi$$

and

$$\eta_{min} \leq \eta(\varphi), \quad \forall \varphi$$

Because $F(\varphi) = \left(\frac{\varphi^2 - 1}{2} \right)^2$ and by assuming the mobility is constant positive: $M(\varphi) = M > 0$, it comes

$$\begin{aligned} & \frac{\varrho_{min}}{2} \partial_t \left(\|\mathbf{u}\|_{L^2(\Omega)}^2 \right) + 2\eta_{min} \|\mathbf{D}(\mathbf{u})\|_{L^2(\Omega)}^2 + \frac{\sigma}{2} \partial_t \left(\|\nabla \varphi\|_{L^2(\Omega)}^2 \right) \\ & + \frac{\sigma}{\varepsilon^2} \partial_t \left(\left\| \frac{\varphi^2 - 1}{2} \right\|_{L^2(\Omega)}^2 \right) + M \frac{\sigma}{\varepsilon^2} \|\nabla \omega\|_{L^2(\Omega)}^2 \leq 0 \end{aligned}$$

By integrating with respect to the time t ,

$$\begin{aligned} & \frac{\varrho_{min}}{2} \|\mathbf{u}(t)\|_{L^2(\Omega)}^2 - \frac{\varrho_{min}}{2} \|\mathbf{u}_0\|_{L^2(\Omega)}^2 + 2\eta_{min} \int_0^t \|\mathbf{D}(\mathbf{u}(s))\|_{L^2(\Omega)}^2 \, ds \\ & + \frac{\sigma}{2} \|\nabla \varphi(t)\|_{L^2(\Omega)}^2 - \frac{\sigma}{2} \|\nabla \varphi_0\|_{L^2(\Omega)}^2 + \frac{\sigma}{\varepsilon^2} \left\| \frac{\varphi^2(t) - 1}{2} \right\|_{L^2(\Omega)}^2 - \frac{\sigma}{\varepsilon^2} \left\| \frac{\varphi_0^2 - 1}{2} \right\|_{L^2(\Omega)}^2 \\ & + M \frac{\sigma}{\varepsilon^2} \int_0^t \|\nabla \omega(s)\|_{L^2(\Omega)}^2 \, ds \leq 0 \end{aligned}$$

Finally, the following energy estimate is obtained:

$$\begin{aligned} & \frac{\varrho_{min}}{2} \|\mathbf{u}(t)\|_{L^2(\Omega)}^2 + 2\eta_{min} \int_0^t \|\mathbf{D}(\mathbf{u}(s))\|_{L^2(\Omega)}^2 \, ds + \frac{\sigma}{2} \|\nabla \varphi(t)\|_{L^2(\Omega)}^2 \\ & + \frac{\sigma}{\varepsilon^2} \left\| \frac{\varphi^2(t) - 1}{2} \right\|_{L^2(\Omega)}^2 + M \frac{\sigma}{\varepsilon^2} \int_0^t \|\nabla \omega(s)\|_{L^2(\Omega)}^2 \, ds \\ & \leq \frac{\varrho_{min}}{2} \|\mathbf{u}_0\|_{L^2(\Omega)}^2 + \frac{\sigma}{2} \|\nabla \varphi_0\|_{L^2(\Omega)}^2 + \frac{\sigma}{\varepsilon^2} \left\| \frac{\varphi_0^2 - 1}{2} \right\|_{L^2(\Omega)}^2 \end{aligned} \quad (2.20)$$

This energy estimate gives a control of the solutions by the initial data. From this estimate, one deduces that

$$\begin{aligned}\varphi &\in L^\infty([0, t_f]; H^1(\Omega)) \cap L^2([0, t_f]; H^2(\Omega)) \\ \omega &\in L^2([0, t_f]; H^1(\Omega)) \\ \mathbf{u} &\in \mathbf{L}^\infty([0, t_f]; \mathbf{L}^2(\Omega)) \cap \mathbf{L}^2([0, t_f]; \mathbf{H}^1(\Omega)) \\ p &\in L^2(\Omega)\end{aligned}$$

□

From the proof and the energy equation (2.19), the property of decay of energy is directly deduced:

$$\frac{dE_{tot}}{dt} = - \int_{\Omega} 2\eta(\varphi)|\mathbf{D}(\mathbf{u})|^2 d\mathbf{x} - \int_{\Omega} \frac{\sigma}{\varepsilon^2} M(\varphi)|\nabla\omega|^2 d\mathbf{x} \leq 0, \quad (2.21)$$

where the total energy is

$$E_{tot}(\mathbf{u}, \varphi, t) = \int_{\Omega} \frac{\varrho(\varphi)}{2} \|\mathbf{u}\|^2 d\mathbf{x} + \int_{\Omega} \frac{\sigma}{2} \|\nabla\varphi\|^2 d\mathbf{x} + \int_{\Omega} \frac{\sigma}{\varepsilon^2} F(\varphi) d\mathbf{x}. \quad (2.22)$$

In the literature, authors studied the existence and uniqueness properties of the coupled and incompressible Cahn–Hilliard–Navier–Stokes equations. In [5], Abels showed the existence of global weak solutions for any dimension d , their regularity and uniqueness for $d = 2$ and the asymptotic behavior as $t \rightarrow \infty$ of the Cahn–Hilliard–Navier–Stokes model for two-phase flows of viscous, incompressible fluids with matched densities. He also showed in [12] the existence of weak solutions for this model with general densities. Then, Abels & al. [13, 14], extended the proof in the case of degenerate mobility. The existence of a global-in-time weak solutions of a model similar to (2.12)-(2.17) has been established in [15]. In [16], Boyer obtained global existence results of weak solutions of the model with matched densities, even with degenerate mobility, for any dimension d and an existence and uniqueness result of strong solutions, global for $d = 2$ and local for $d = 3$. However, the global existence of strong solutions for the model with general densities with $d = 3$ remains an open question, which is already the case for the incompressible Navier–Stokes equations.

The mathematical aspects of the Cahn–Hilliard equations (2.12)-(2.13) viewed in the end of Section 1.4 remain available in the current study. In the following, the numerical implementation of the coupled system will be established, so which requires a discretization of this system.

2.6 Space and time discretization

In this section, a numerical resolution of the coupled system (2.12)-(2.15) by a fractional step approach is proposed. This means the Cahn–Hilliard mixed formulation is first solved and at each time step n , the solutions φ^n and ω^n are used to solve then \mathbf{u}^n and p^n from the incompressible Navier–Stokes equations. To solve the Cahn–Hilliard equations, the system (2.12)-(2.13) is discretized as explained in 1.5. Once the Cahn–Hilliard matrix system (1.31) is solved, the incompressible Navier–Stokes equations (2.14)-(2.15) are then solved. These equations allow modeling physical phenomena like weather, ocean current, turbulent flow, hemodynamics, multiphase flow, etc.

2.6.1 Finite element discretization

Like the Cahn–Hilliard equations in 1.5.1, the space discretization of the incompressible Navier–Stokes equations (2.14)-(2.15) is based on the \mathbb{P}_1 finite element method. This starts by establishing the weak formulation of the equations (2.14)-(2.15). In order to find a variational formulation of the Navier–Stokes equations, consider the following infinite-dimensional spaces:

$$\mathcal{V}_{div} = \{\mathbf{u} \in \mathbf{H}^1(\Omega) \text{ such that } (\nabla \cdot \mathbf{u}, v) = 0 \ \forall v \in L^2(\Omega)\}, \quad (2.23)$$

$$\mathcal{V}_0 = \{\mathbf{u} \in \mathcal{V}_{div} \text{ such that } \mathbf{u} = 0 \text{ on } \partial\Omega\} \quad (2.24)$$

$$\mathcal{Q} = L^2(\Omega). \quad (2.25)$$

Let $\mathbf{V}_{div} = \mathcal{V}_{div} \times \mathcal{Q}$ and $\mathbf{V}_0 = \mathcal{V}_0 \times \mathcal{Q}$. The weak formulation of (2.14)-(2.15) is reads: given \mathbf{u}_0 , for $t_f > 0$, find

$$(\mathbf{u}, p) \in \mathbf{V}_{div}$$

such that for all $(\mathbf{v}, q) \in \mathbf{V}_0$

$$\begin{aligned} & (\varrho(\varphi)\partial_t \mathbf{u}, \mathbf{v}) + (((\varrho(\varphi)\mathbf{u} + \mathbf{J}) \cdot \nabla) \mathbf{u}, \mathbf{v}) \\ & + (2\eta(\varphi)\mathbf{D}(\mathbf{u}) : \mathbf{D}(\mathbf{v})) + (\nabla p, \mathbf{v}) = \left(\frac{\sigma}{\varepsilon^2}\omega \nabla \varphi, \mathbf{v}\right) + (\varrho(\varphi)\mathbf{g}, \mathbf{v}), \end{aligned} \quad (2.26)$$

$$(\nabla \cdot \mathbf{u}, q) = 0, \quad (2.27)$$

$$\mathbf{u}(\cdot, 0) = \mathbf{u}_0 \in \mathcal{V}_0, \quad (2.28)$$

The standard Galerkin formulations are not robust to simulate convection-dominated flow because it suffers from spurious oscillations that pollute the solution. Stabilized methods are getting increasing attention in computational fluid dynamics because they are designed to solve these drawbacks typical of the standard Galerkin method. The Variational Multiscale method (VMS) is a technique used for deriving

models and numerical methods for multiscale phenomena [17]. The VMS framework has been widely used to design stabilized finite element methods in which stability of the standard Galerkin method is not ensured both in terms of singular perturbation and of compatibility conditions with the finite element spaces [18]. The VMS [19] is a technique used to get mathematical models and numerical methods which are able to catch multiscale phenomena. This method is usually adopted for problems with huge scale ranges, which are separated into a number of scale groups [20]. The VMS deals with mixed variational formulations for solving the Navier–Stokes equations. The main idea of the method is to decompose the unknown into two components, coarse and fine, corresponding to the fine and large scales of resolution. The fine scale solution is determined analytically eliminating it from the problem of the coarse scale equation.

In order to discretize in space the Navier–Stokes equations, consider the function space of finite element:

$$\mathcal{X}_h = \{u_h \in \mathcal{C}^0(\bar{\Omega}) \text{ such that } u_{h|K} \in \mathbb{P}_1, K \in \mathcal{T}_h\}, \quad (2.29)$$

of piecewise Lagrangian Polynomials of degree 1 over the domain Ω triangulated with a mesh \mathcal{T}_h made of elements of diameters h_K , $K \in \mathcal{T}_h$. Let introduce a multiscale direct-sum decomposition of the space \mathcal{V} which represents either \mathcal{V}_{div} and \mathcal{V}_0 [21]:

$$\mathcal{V} = \mathcal{V}_h \oplus \mathcal{V}'$$

being

$$\mathcal{V}_h = \mathcal{V}_{div,h} := \mathcal{V}_{div,h} \times \mathcal{Q} \text{ or } \mathcal{V}_h = \mathcal{V}_{0,h} := \mathcal{V}_{0,h} \times \mathcal{Q}$$

the finite dimensional function space associated to the coarse scale, and

$$\mathcal{V}' = \mathcal{V}'_{div} := \mathcal{V}'_{div} \times \mathcal{Q} \text{ or } \mathcal{V}' = \mathcal{V}'_0 := \mathcal{V}'_0 \times \mathcal{Q}$$

the infinite-dimensional fine scale function space, with

$$\begin{aligned} \mathcal{V}_{div,h} &= \mathcal{V}_{div} \cap \mathcal{X}_h \\ \mathcal{V}_{0,h} &= \mathcal{V}_0 \cap \mathcal{X}_h \end{aligned}$$

and

$$\mathcal{Q}_h = \mathcal{Q} \cap \mathcal{X}_h$$

Thus, (2.26)-(2.28) can be written under the following \mathbb{P}_1 finite element formulation by the Galerkin approximation : given \mathbf{u}_0 , for $t_f > 0$, find

$$\mathbf{u} = \mathbf{u}_h + \mathbf{u}' \in \mathcal{V}_{div,h} \oplus \mathcal{V}'_{div}$$

and

$$p = p_h + p' \in \mathcal{Q}_h \oplus \mathcal{Q}'$$

such that for all $\mathbf{v} = \mathbf{v}_h + \mathbf{v}' \in \mathcal{V}_{0,h} \oplus \mathcal{V}'_0$ and all $q = q_h + q' \in \mathcal{Q}_h \oplus \mathcal{Q}'$

$$\begin{aligned} & (\varrho \partial_t(\mathbf{u}_h + \mathbf{u}'), \mathbf{v}_h + \mathbf{v}') \\ & + ((\varrho(\mathbf{u}_h + \mathbf{u}') + \mathbf{J}) \cdot \nabla(\mathbf{u}_h + \mathbf{u}'), \mathbf{v}_h + \mathbf{v}') \\ & + (2\eta(\varphi)\mathbf{D}(\mathbf{u}_h + \mathbf{u}') : \mathbf{D}(\mathbf{v}_h + \mathbf{v}')) \\ & + (\nabla(p_h + p'), \mathbf{v}_h + \mathbf{v}') = \left(\frac{\sigma}{\varepsilon^2} \omega \nabla \varphi, \mathbf{v}_h + \mathbf{v}' \right) \end{aligned} \quad (2.30)$$

$$\begin{aligned} & + (\varrho \mathbf{g}, \mathbf{v}_h + \mathbf{v}'), \\ & (\nabla \cdot (\mathbf{u}_h + \mathbf{u}'), q_h + q') = 0, \end{aligned} \quad (2.31)$$

$$\mathbf{u}(\cdot, 0) = \mathbf{u}_0 \in \mathcal{V}_{h,0} \oplus \mathcal{V}'_0, \quad (2.32)$$

which can be rewritten as follows: given \mathbf{u}_0 , for $t_f > 0$ find

$$\mathbf{u}_h + \mathbf{u}' \in \mathcal{V}_{div,h} \oplus \mathcal{V}'_{div}$$

and

$$p_h + p' \in \mathcal{Q}_h \oplus \mathcal{Q}'$$

such that the coarse scale formulation of (2.30)-(2.32) is given by: for all $(\mathbf{v}_h, q_h) \in \mathcal{V}_{0,h}$,

$$\begin{aligned} & (\varrho \partial_t(\mathbf{u}_h + \mathbf{u}'), \mathbf{v}_h) \\ & + ((\varrho(\mathbf{u}_h + \mathbf{u}') + \mathbf{J}) \cdot \nabla(\mathbf{u}_h + \mathbf{u}'), \mathbf{v}_h) \\ & + (2\eta(\varphi)\mathbf{D}(\mathbf{u}_h + \mathbf{u}') : \mathbf{D}(\mathbf{v}_h)) + (\nabla(p_h + p'), \mathbf{v}_h) = \left(\frac{\sigma}{\varepsilon^2} \omega \nabla \varphi, \mathbf{v}_h \right) \end{aligned} \quad (2.33)$$

$$+ (\varrho \mathbf{g}, \mathbf{v}_h),$$

$$(\nabla \cdot (\mathbf{u}_h + \mathbf{u}'), q_h) = 0, \quad (2.34)$$

$$\mathbf{u}_h(t=0) = \mathbf{u}_{h,0} \in \mathcal{V}_{h,0}, \quad (2.35)$$

and the fine scale formulation is given by: for all $(\mathbf{v}', q') \in \mathcal{V}'_0$

$$\begin{aligned} & (\varrho \partial_t(\mathbf{u}_h + \mathbf{u}'), \mathbf{v}') \\ & + ((\varrho(\mathbf{u}_h + \mathbf{u}') + \mathbf{J}) \cdot \nabla(\mathbf{u}_h + \mathbf{u}'), \mathbf{v}') \\ & + (2\eta(\varphi)\mathbf{D}(\mathbf{u}_h + \mathbf{u}') : \mathbf{D}(\mathbf{v}')) \\ & + (\nabla(p_h + p'), \mathbf{v}') = \left(\frac{\sigma}{\varepsilon^2} \omega \nabla \varphi, \mathbf{v}' \right) \end{aligned} \quad (2.36)$$

$$\begin{aligned} & + (\varrho \mathbf{g}, \mathbf{v}'), \\ & (\nabla \cdot (\mathbf{u}_h + \mathbf{u}'), q') = 0, \end{aligned} \quad (2.37)$$

$$\mathbf{u}'(t=0) = \mathbf{u}'_0 \in \mathcal{V}'_0, \quad (2.38)$$

As in [22], one assumes that the convective velocity of the non-linear term may be approximated using only the large scale component $(\mathbf{u}_h + \mathbf{u}') \cdot \nabla(\mathbf{u}_h + \mathbf{u}') \approx \mathbf{u}_h \cdot \nabla(\mathbf{u}_h + \mathbf{u}')$ and the sub-scales are considered quasi-static, and not tracked in time.

By expressing \mathbf{u}' and p' as in [23], substituting them into the coarse scale formulation, and integrating by parts, the system (2.33)-(2.35) becomes: given \mathbf{u}_0 , for $t_f > 0$ find $(\mathbf{u}_h, p_h) \in \mathcal{V}_{div,h}$ such that for all for all $(\mathbf{v}_h, q_h) \in \mathcal{V}_{0,h}$

$$\begin{aligned} & (\varrho \partial_t \mathbf{u}_h, \mathbf{v}_h) + ((\varrho \mathbf{u}_h + \mathbf{J}) \cdot \nabla \mathbf{u}_h, \mathbf{v}_h) \\ & - \sum_K (\tau_u \mathcal{R}_u, \varrho \mathbf{u}_h \nabla \mathbf{v}_h)_K + (2\eta(\varphi)\mathbf{D}(\mathbf{u}_h) : \mathbf{D}(\mathbf{v}_h)) \\ & - (p_h, \nabla \cdot \mathbf{v}_h) - \sum_K (\tau_p \mathcal{R}_p, \nabla \cdot \mathbf{v}_h)_K = \left(\frac{\sigma}{\varepsilon^2} \omega \nabla \varphi, \mathbf{v}_h \right) \end{aligned} \quad (2.39)$$

$$+ (\varrho \mathbf{g}, \mathbf{v}_h),$$

$$(\nabla \cdot \mathbf{u}_h, q_h) - \sum_K (\tau_u \mathcal{R}_u, \nabla q_h)_K = 0, \quad (2.40)$$

$$\mathbf{u}_h(t=0) = \mathbf{u}_{h,0} \in \mathcal{U}_{h,0}, \quad (2.41)$$

where \sum_K stands for the summation over all the elements K of the partition \mathcal{T}_h , $(\cdot, \cdot)_K$ denotes the L^2 inner product in each element K , τ_u and τ_p are stabilization parameters given by [24], and \mathcal{R}_u and \mathcal{R}_p are residuals defined as follows:

$$\begin{aligned} \mathcal{R}_u &= \varrho(\varphi)\mathbf{g} + \frac{\sigma}{\varepsilon^2} \omega \nabla \varphi - \varrho(\varphi) \partial_t \mathbf{u}_h - \varrho(\varphi) \mathbf{u}_h \cdot \nabla \mathbf{u}_h \\ & - p_h - \nabla \cdot (2\eta(\varphi)\mathbf{D}(\mathbf{u}_h)), \end{aligned} \quad (2.42)$$

$$\mathcal{R}_p = -\nabla \cdot \mathbf{u}_h. \quad (2.43)$$

The terms $\sum_K (\tau_u \mathcal{R}_u, \varrho \mathbf{u}_h \nabla \mathbf{v}_h)_K$, $\sum_K (\tau_p \mathcal{R}_p, \nabla \cdot \mathbf{v}_h)_K$, and $\sum_K (\tau_u \mathcal{R}_u, \nabla q_h)_K$ represent the effects of the sub-grid scales and deal with the instability in convection

dominated regime. The VMS method allows getting P1/P1 solutions for the velocity and the pressure.

2.6.2 Time discretization

For the time discretization, semi-implicit BDF-schemes based on Newton–Gregory backward polynomials are used to extrapolate the nonlinear terms. By considering BDF- σ the time derivative is approximated as follows

$$\partial_t \mathbf{u}_h \approx \frac{\alpha_\sigma \mathbf{u}_h^{n+1} - \mathbf{u}_h^{n,\sigma}}{\Delta t}, \quad (2.44)$$

with

$$\alpha_\sigma = \begin{cases} 1 & \text{for } \sigma = 1, \\ \frac{3}{2} & \text{for } \sigma = 2, \\ \frac{11}{6} & \text{for } \sigma = 3. \end{cases} \quad (2.45)$$

and

$$\mathbf{u}_h^{n+1,\sigma} = \begin{cases} \mathbf{u}_h^n & \text{for } n \geq 0 \text{ and } \sigma = 1, \\ 2\mathbf{u}_h^n - \mathbf{u}_h^{n-1} & \text{for } n \geq 1 \text{ and } \sigma = 2, \\ 3\mathbf{u}_h^n - 3\mathbf{u}_h^{n-1} + \mathbf{u}_h^{n-2} & \text{for } n \geq 2 \text{ and } \sigma = 3. \end{cases} \quad (2.46)$$

Thus, the linearized semi-implicit formulation of the Navier–Stokes equations is:

$$\begin{aligned} & \left(\varrho^n \frac{\alpha_\sigma \mathbf{u}_h^{n+1} - \mathbf{u}_h^{n,\sigma}}{\Delta t}, \mathbf{v}_h \right) + \left((\varrho^{n+1} \mathbf{u}_h^{n+1,\sigma} + \mathbf{J}^{n+1}) \cdot \nabla \mathbf{u}_h^{n+1}, \mathbf{v}_h \right) \\ & - \sum_K (\tau_u^{n+1,\sigma} \mathcal{R}_u^{n+1,\sigma}, \varrho^{n+1} \mathbf{u}_h^{n+1,\sigma} \nabla \mathbf{v}_h)_K + (2\eta^{n+1} \mathbf{D}(\mathbf{u}_h^{n+1,\sigma}) : \mathbf{D}(\mathbf{v}_h)) \\ & - (p_h^{n+1}, \nabla \cdot \mathbf{v}_h) - \sum_K (\tau_p^{n+1,\sigma} \mathcal{R}_p^{n+1}, \nabla \cdot \mathbf{v}_h)_K \end{aligned} \quad (2.47)$$

$$\begin{aligned} & = \left(\frac{\sigma}{\varepsilon^2} \omega^{n+1} \nabla \varphi^{n+1}, \mathbf{v}_h \right) + (\varrho^{n+1} \mathbf{g}, \mathbf{v}_h), \\ & \quad (\nabla \cdot \mathbf{u}_h^{n+1}, q_h) - \sum_K (\tau_u^{n+1,\sigma} \mathcal{R}_u^{n+1,\sigma}, \nabla q_h)_K = 0, \end{aligned} \quad (2.48)$$

with the following discretized residuals:

$$\begin{aligned} \mathcal{R}_u^{n+1,\sigma} &= \varrho^n \frac{\alpha_\sigma \mathbf{u}_h^{n+1} - \mathbf{u}_h^{n,\sigma}}{\Delta t} + \varrho^{n+1} \mathbf{u}_h^{n+1,\sigma} \cdot \nabla \mathbf{u}_h^{n+1} + \nabla p_h^{n+1} \\ & \quad - 2\eta^{n+1} \mathbf{D}(\mathbf{u}_h^{n+1}) - \frac{\sigma}{\varepsilon^2} \omega^{n+1} \nabla \varphi^{n+1} - \varrho^{n+1} \mathbf{g}, \end{aligned} \quad (2.49)$$

$$\mathcal{R}_p^{n+1} = \nabla \cdot \mathbf{u}_h^{n+1} \quad (2.50)$$

and the following discretized stabilization parameters:

$$\tau_{\mathbf{u}}^{n+1,\sigma} = \left(\left(\frac{c_1 \eta^{n+1}}{\varrho^{n+1} h^2} \right)^2 + \left(\frac{c_2 \|\mathbf{u}_h^{n+1,\sigma}\|_K}{h} \right)^2 \right)^{-\frac{1}{2}}, \quad (2.51)$$

$$\tau_p^{n+1,\sigma} = \left(\left(\frac{\eta^{n+1}}{\varrho^{n+1}} \right)^2 + \left(\frac{c_2 \|\mathbf{u}_h^{n+1,\sigma}\|_K h}{c_1} \right)^2 \right)^{-\frac{1}{2}} \quad (2.52)$$

Thus, by denoting y , y^* and y' the discrete solutions y^{n+1} , y^n and y^{n-1} to simplify, the discretized coupled Cahn–Hilliard–Navier–Stokes equations are solved by a fractional step resolution as follows:

1. Solving the Cahn–Hilliard equations, for example with the classical scheme (1.31):

$$\left(\frac{\varphi_h - \varphi_h^*}{\Delta t}, \psi_h \right) + (\mathbf{u}^* \cdot \nabla \varphi_h, \psi_h) + M(\nabla \omega_h, \nabla \psi_h) = 0, \quad (2.53)$$

$$(\omega_h, \chi_h) - \varepsilon^2 (\nabla \varphi_h, \nabla \chi_h) - (\varphi_h ((\varphi_h^*)^2 - 1), \chi_h) = 0, \quad (2.54)$$

2. Then, the incompressible Navier–Stokes equations are solved with the VMS method:

$$\begin{aligned} & \left(\varrho^* \frac{\alpha_\sigma \mathbf{u}_h - \mathbf{u}_h^{*,\sigma}}{\Delta t}, \mathbf{v}_h \right) + ((\varrho \mathbf{u}_h^\sigma + \mathbf{J}) \cdot \nabla \mathbf{u}_h, \mathbf{w}_h) \\ & - \sum_K (\tau_{\mathbf{u}}^\sigma \mathcal{R}_{\mathbf{u}}^\sigma, \varrho \mathbf{u}_h^\sigma \nabla \mathbf{v}_h)_K + (2\eta \mathbf{D}(\mathbf{u}_h^\sigma) : \mathbf{D}(\mathbf{v}_h)) \\ & - (p_h, \nabla \cdot \mathbf{v}_h) - \sum_K (\tau_p^\sigma \mathcal{R}_p, \nabla \cdot \mathbf{v}_h)_K \end{aligned} \quad (2.55)$$

$$\begin{aligned} & = \left(\frac{\sigma}{\varepsilon^2} \omega \nabla \varphi, \mathbf{v}_h \right) + (\varrho \mathbf{g}, \mathbf{v}_h), \\ & (\nabla \cdot \mathbf{u}_h, q_h) - \sum_K (\tau_{\mathbf{u}}^\sigma \mathcal{R}_{\mathbf{u}}^\sigma, \nabla q_h)_K = 0, \end{aligned} \quad (2.56)$$

2.7 Two-phase flow simulation with interface capturing

To validate the implemented methods of the present Cahn–Hilliard–Navier–Stokes model, two-dimensional time-dependent numerical test cases are presented in this section: a dam-break test according to the benchmark defined in [25] and a rising bubble test case presented in [26, 27]. In the next simulations, the meshes are considered uniform, and the effects of flux mass are neglected: $\mathbf{J}=\mathbf{0}$. The results obtained with the proposed approach are compared with those obtained by other approaches that can be found in the literature.

2.7.1 Dam-break 2D

One considers a fluid column (water) inside a fluid domain (air) $\Omega = [0; L_x] \times [0; L_y]$ as presented in Figure 2.3.

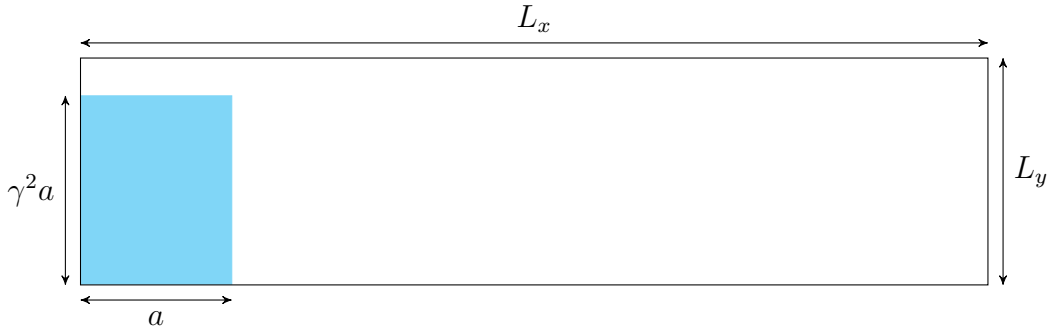


Figure 2.3: Dam-break benchmark

In this test case, the water column will collapse under the only gravity effect $g=9.81$. Surface tension is assumed neglected: $\sigma=0$. All the parameters related to the test case are depicted in Table 2.1:

| | | | |
|----------------|---------------------|-----------------|-------------------|
| ρ_{water} | 1000 | Δt | $4 \cdot 10^{-4}$ |
| η_{water} | 10^{-2} | L_x | 0.5 |
| ρ_{air} | 1 | L_y | 0.15 |
| η_{air} | 10^{-3} | a | 0.06 |
| M | 10^{-6} | γ^2 | 2 |
| ε | $3.2 \cdot 10^{-3}$ | $Nb_{elements}$ | 300,000 |
| t_f | 10 | h | $8 \cdot 10^{-4}$ |

Table 2.1: Parameters of the dam-break test case

Figure 2.4 presents the evolution of the phase-field solution for the 2D dam-break at different time with a uniform mesh composed of 300,000 elements of mesh size h , after performing the simulation in parallel with 4 cores.

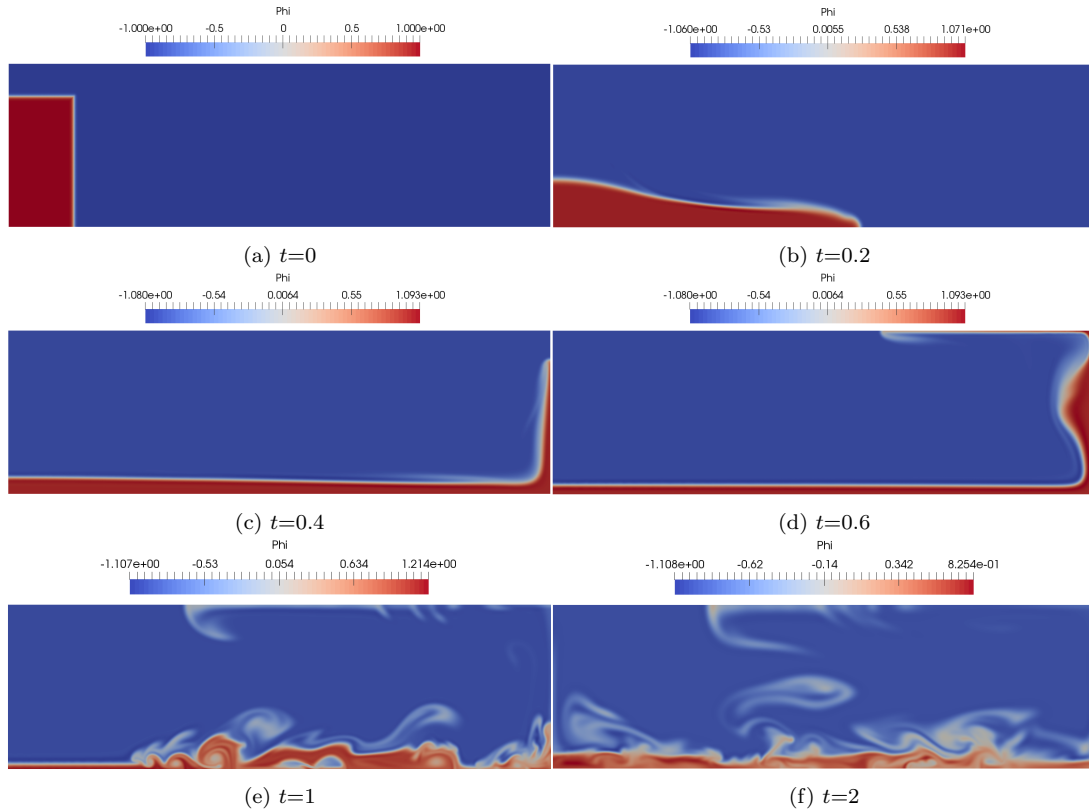


Figure 2.4: Phase-field solution at $t=0, 0.2, 0.4, 0.6, 1,$ and 2 of the dam-break evolution

Experimental results are available from [28] and make this benchmark suitable for validation. Numerical results by the level-set method have been done as studied in [29]. In Figure 2.5a, the non-dimensional evolution of the front position is compared for the different methods as well as the non-dimensional evolution of the column height in Figure 2.5b.

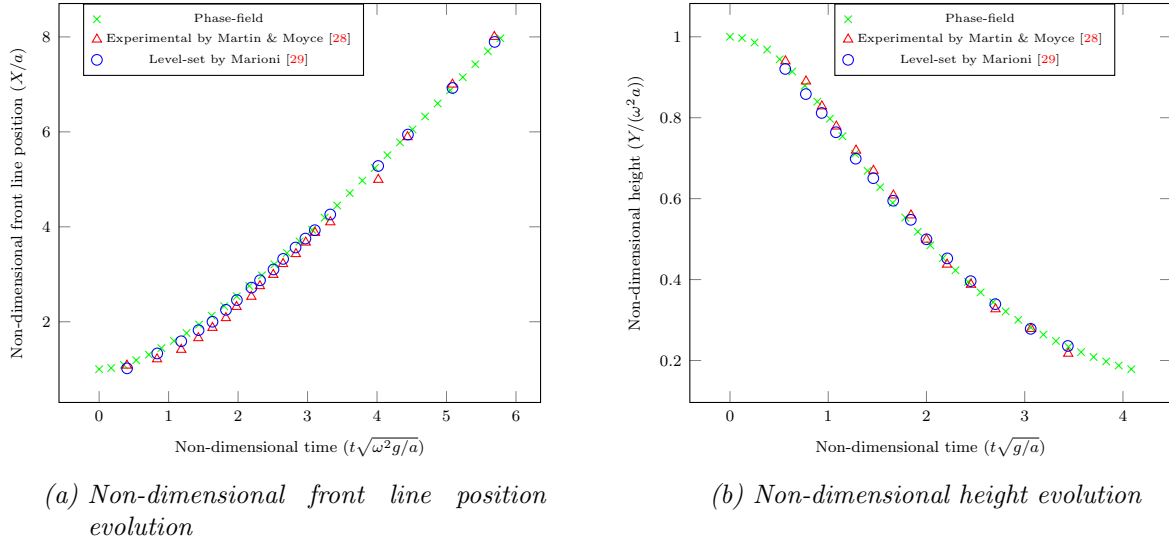


Figure 2.5: Non-dimensional evolution of the front position and the height column

The results are in agreement in the two cases for the different methods. The simulation until the final time t_f has been performed in 71h 10min.

2.7.2 Rising bubble 2D

One considers a bubble of light fluid Ω_{LF} surrounded by a heavier fluid Ω_{HF} as presented in Figure 2.6. This bubble rises due to gravitational force. The motion

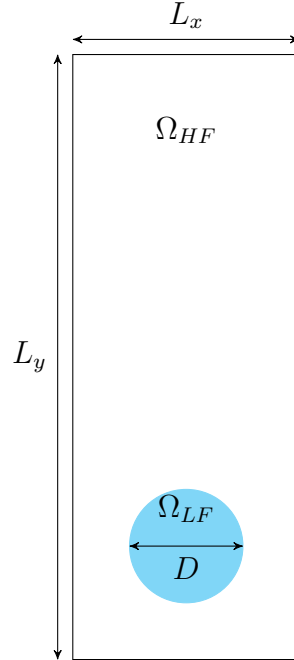


Figure 2.6: Rising bubble benchmark

gives rise to a deformation of the bubble shape which depends also on the value of the tension surface coefficient σ . The parameters for the benchmark test are summarized in Table 2.2.

| | | | |
|---------------|-------------------|----------------|-----------|
| ρ_{HF} | 1000 | Δt | 10^{-3} |
| η_{HF} | 10 | L_x | 1 |
| ρ_{LF} | 1 | L_y | 2 |
| η_{LF} | 0.1 | D | 0.5 |
| M | 10^{-6} | g | 0.98 |
| ε | $2 \cdot 10^{-2}$ | σ | 1.96 |
| t_f | 5 | $N_{elements}$ | 200,000 |

Table 2.2: Parameters of the rising bubble test case

Figure 2.7 presents the configuration for the bubble at $t=0$, $t=1$, $t=2$, $t=3$, $t=4$, $t=5$ with a uniform mesh composed of 200,000 elements of mesh size $h=0.005$ after performing the simulation in parallel with 4 cores.

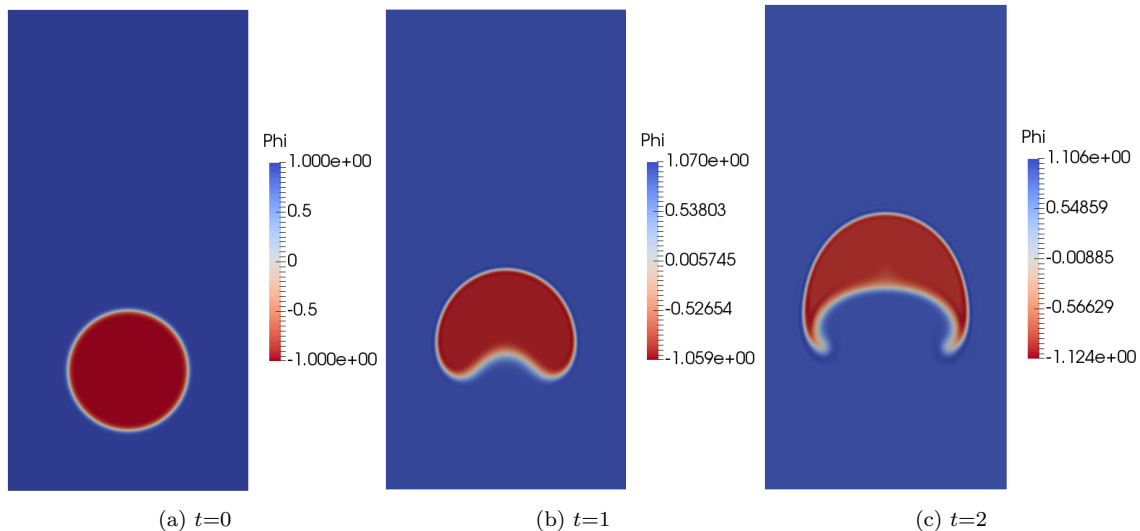


Figure 2.7: Phase-field solution of the bubble evolution at $t=0$, 1, and 2 with $\sigma=1.96$

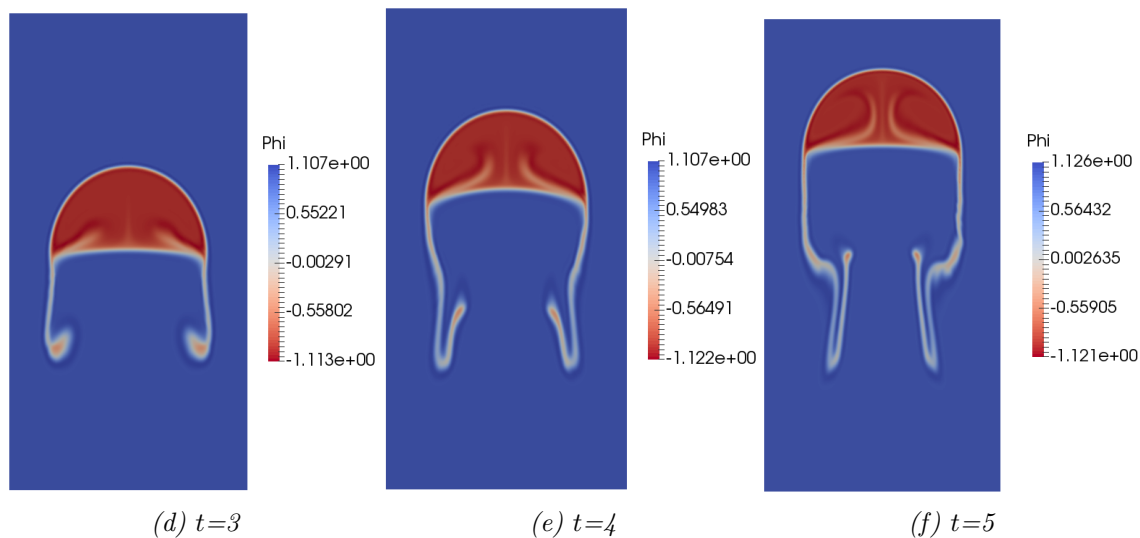
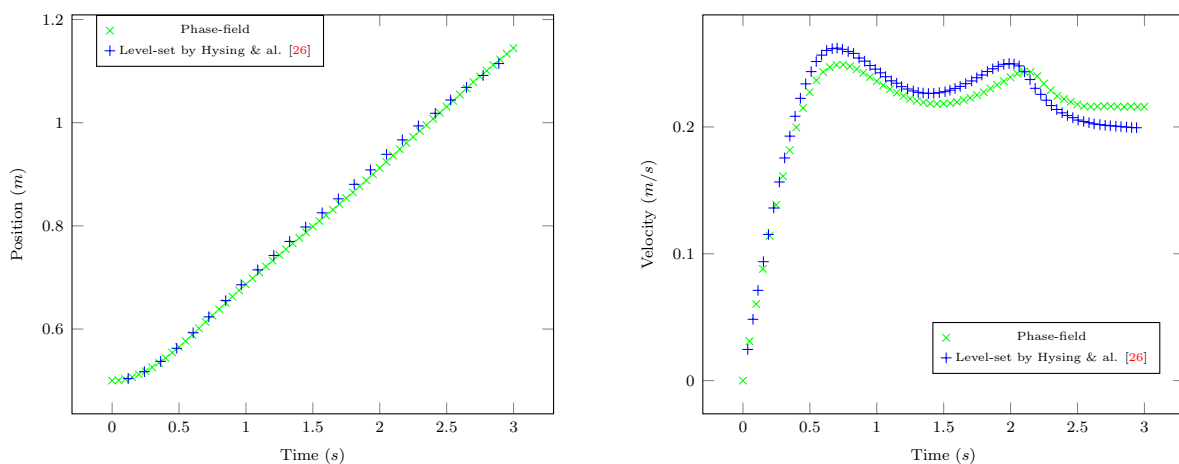


Figure 2.7: Phase-field solution of the bubble evolution at $t=3$, 4, and 5 with $\sigma=1.96$

As for the dam-break benchmark, the velocity is unknown and the Navier–Stokes equations admits the gravity as a source term. Numerical results by the level-set method have been done as studied in [26] and benchmark quantities as the position of the bubble mass center and the rise velocity of the bubble mass center have been measured. The position of the bubble mass center is defined by $\mathbf{x}_C = \frac{1}{|\Omega_{air}|} \int_{\Omega_{air}} \mathbf{x} \, d\mathbf{x}$ and the rise velocity of the bubble mass center is defined by $\mathbf{u}_C = \frac{1}{|\Omega_{air}|} \int_{\Omega_{air}} \mathbf{u} \, d\mathbf{x}$. In Figure 2.8a, the position evolution of the bubble mass center is presented for both level-set and phase-field methods and the velocity component evolution of the bubble mass center in the direction opposite to the gravitational vector are shown in Figure 2.8b. The results are in agreement in the two cases for the both methods.



(a) Position evolution of the bubble mass center

(b) Velocity evolution of the bubble mass center

Figure 2.8: Position and velocity evolution of the bubble mass center for $\sigma=1.96$

By changing the physical properties of the bubble and the tension surface coefficient and setting them as in [26]: $\rho_{LF}=100$, $\eta_{LF}=1$, and $\sigma=24.5$, a new simulation is performed with the same previous values for the other parameters. Figure 2.9 presents the configuration of the rising bubble 2D case with a uniform mesh composed of 200,000 elements at $t=0$, $t=1$, $t=2$, $t=3$, $t=4$, and $t=5$.

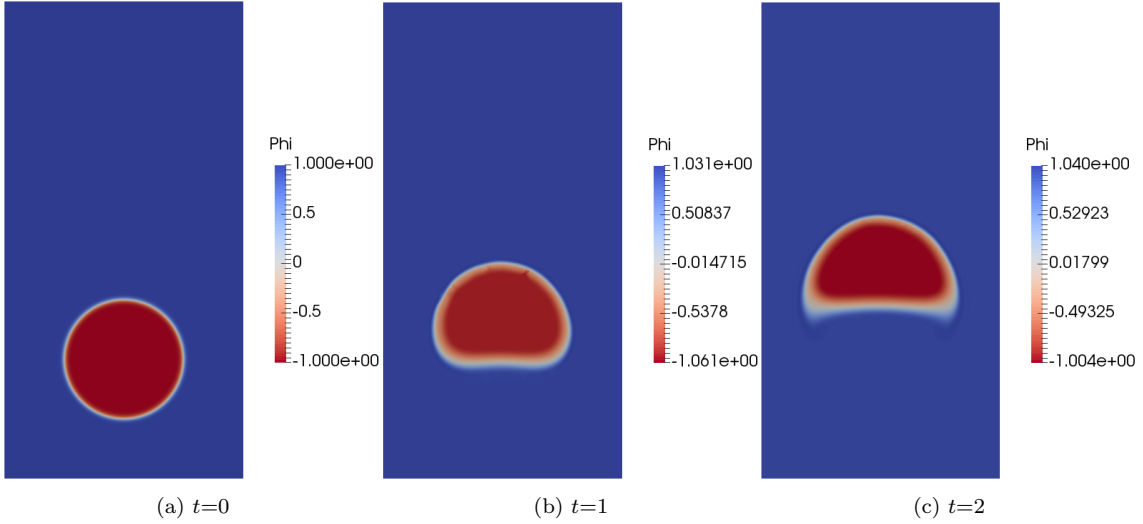


Figure 2.9: Phase-field solution of the bubble evolution at $t=0$, 1, and 2 with $\sigma=24.5$

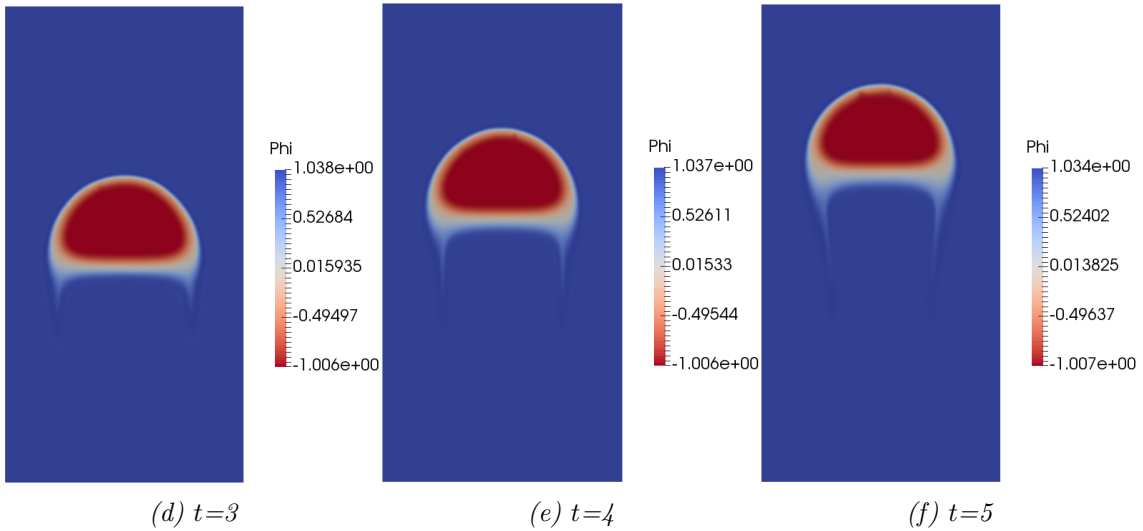
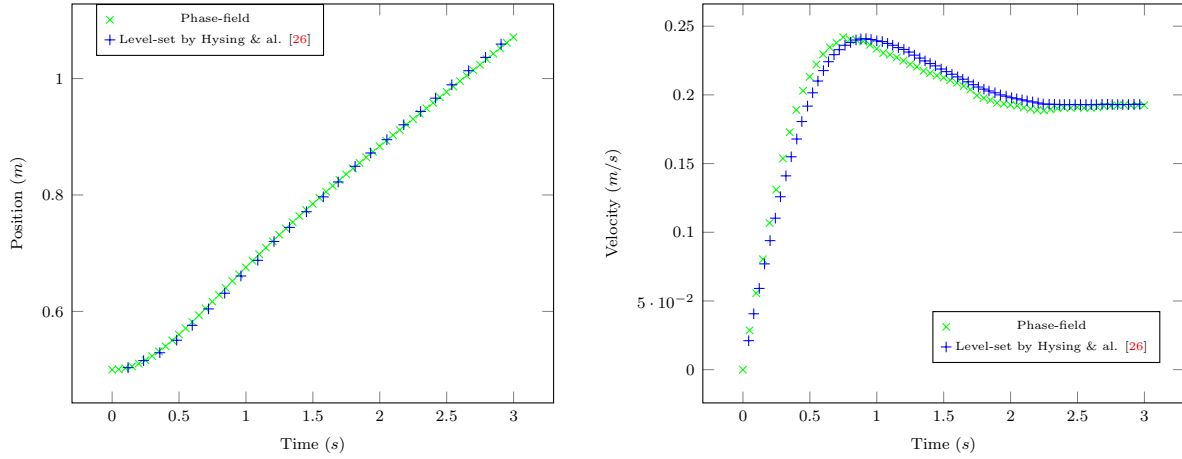


Figure 2.9: Phase-field solution of the bubble evolution at $t=3$, 4, and 5 with $\sigma=24.5$

In Figure 2.10a, the position evolution of the bubble mass center is presented for both level-set and phase-field methods and the velocity component evolution of the bubble mass center in the direction opposite to the gravitational vector are shown in Figure 2.10b.



(a) Position evolution of the bubble mass center

(b) Velocity evolution of the bubble mass center

Figure 2.10: Position and velocity evolution of the bubble mass center for $\sigma=24.5$

The results are similar in the two cases for the both methods. The simulation took 22h 27min to perform the rising bubble until the final time $t_f=5s$ in both case for $\sigma=1.96$ and $\sigma=24.5$.

In this test case, because of the values chosen for the parameters, the convection is weaker than the case with $\sigma=1.96$. Indeed, as expected, by comparing the velocity magnitude of these both cases at the final time $t_f=5$ s, the velocity is weaker in the case with a surface tension coefficient $\sigma=24.5$ ($\|\mathbf{u}_h(\cdot, t = 5)\|_{\ell^2} = 0.23759$) than the case with $\sigma=1.96$ ($\|\mathbf{u}_h(\cdot, t = 5)\|_{\ell^2} = 0.31784$). As a consequence, the overshoots/undershoots, existing because of the convection numerical scheme, are less amplified with $\sigma=24.5$ than $\sigma=1.96$. However, numerical diffusion persists and accumulates, in one hand because of the convection scheme in \mathbb{P}_1 and in other hand because of the diffusion operator $\Delta\omega$ of order 4 on φ , with a mobility M considered as positive and constant which plays therefore a role of diffusion coefficient. An approximate view of the numerical diffusion for values of the order parameter φ between -1 and 1 at the final time $t_f=5$ s is represented in Figure 2.11 (Figure 2.11b is the same as Figure 2.9f).

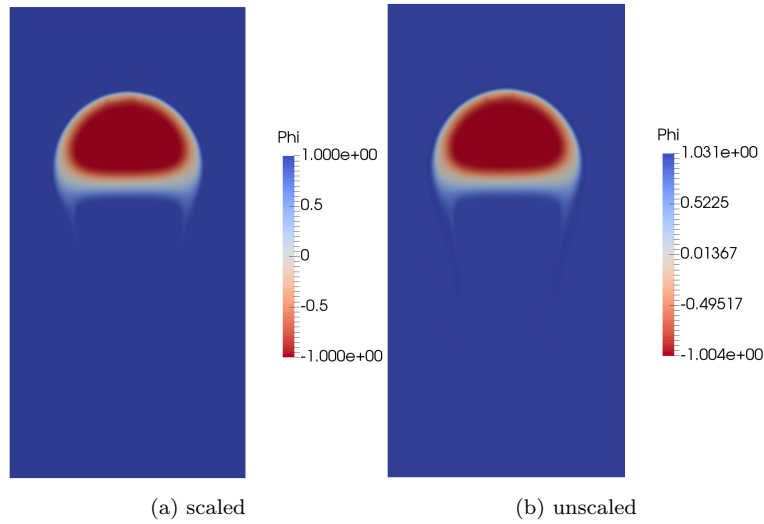


Figure 2.11: Phase field solution of the rising bubble evolution at $t_f=5$ with scaled (left) and unscaled (right) values of varphi

2.7.3 Rayleigh–Taylor instability 2D

In this test case, the Rayleigh–Taylor instability, where a heavy fluid Ω_{HF} falls into a lighter and underlying fluid Ω_{LF} , is simulated. This two layers of fluid, as represented in Figure 2.12, are initially at rest in the rectangular domain $\Omega = [0, L_x] \times [0, L_y]$. It is the problem for fluid mixing induced by unstable stratification as documented in [30].

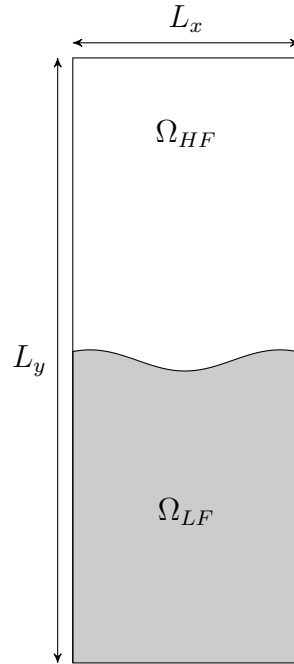


Figure 2.12: Rayleigh–Taylor instability

The transition between the two fluids is regularized and initialized as the following phase-field function:

$$\varphi_0(x) = 0.05 \cos(2\pi(x - 0.5)) + 2 \quad (2.57)$$

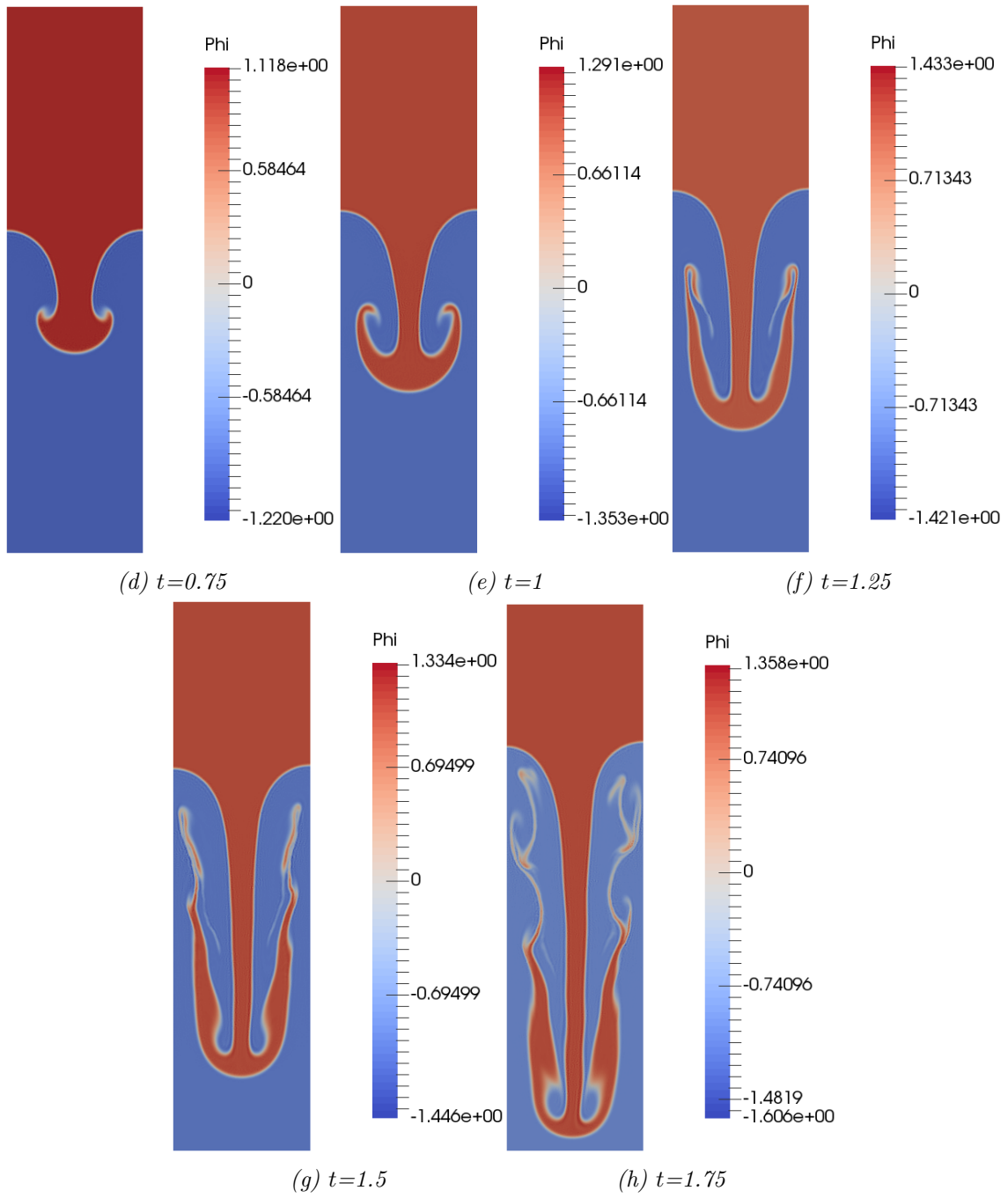


Figure 2.13: Phase-field solution of the Rayleigh–Taylor instability at $t=0.75$, 1 , 1.25 , 1.5 , and 1.75

The above results are in good agreement with those from [30]. Compared to the rising bubble case in Subsection 2.7.2, the filaments of the heavy fluid are more chaotic and unstable. This is essentially due to a dominated convection (at $t=1.75$, $\|\mathbf{u}_h(\cdot, t = 1.75)\|_{\ell^2} = 4.0174$) despite the presence of the numerical diffusion. This can be seen so with an approximate visualization of the numerical diffusion for values of the order parameter φ between -1 and 1 at the final time $t_f=5s$ is represented in Figure 2.14 (Figure 2.14b is the same as Figure 2.13h).

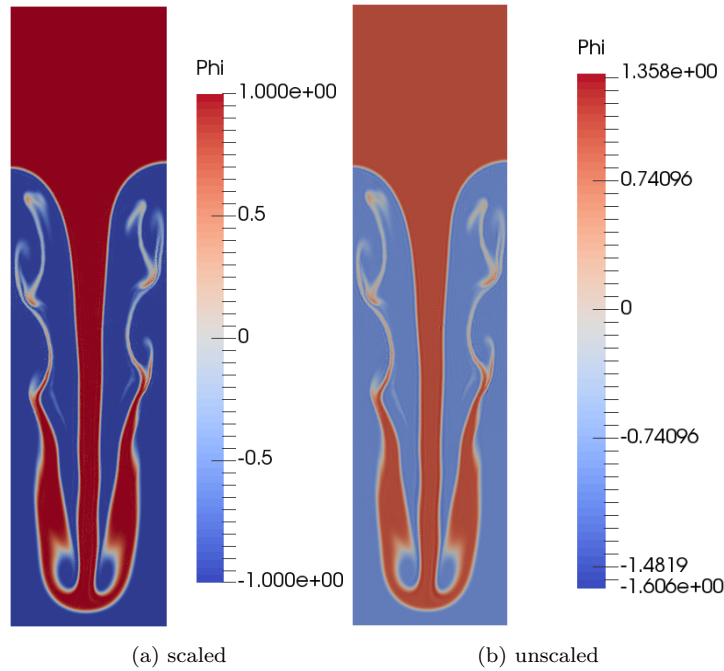


Figure 2.14: Phase field solution of the Rayleigh–Taylor instability evolution at $t=1.75$ with scaled (left) and unscaled (right) values of φ

As a consequence of the present dominated convection, extremal values of φ are bigger than the rising bubble case. In the present case, it took 54min to obtain $t=1.75s$ and 37h 40min to simulate $t_f=115s$.

2.8 Conclusion

In this chapter, the phase-field method to capture an interface has been coupled to the multiphase flow framework. As a consequence, the coupled Cahn–Hilliard–Navier–Stokes equations have been established to model this kind of problem. Capillary action has been taken into account in the model to introduce the wetting effect. Some properties of these coupled equations have been presented and proved. A series of numerical test cases have been simulated by solving the discrete model with a fractional step way. Comparisons with the results of the literature have been done as a validation step. Initially observed in the previous chapter, numerical diffusion, and overshoots/undershoots on the order parameter φ are still observed in these simulations, because of the convection numerical scheme and fourth-order diffusion in a finite element \mathbb{P}_1 framework. Despite these numerical aspects, the validation criteria of the different test cases give results in agreement with other numerical and experimental results. This means that these validation criteria are not so sensitive to the observed numerical drawbacks. In the next chapter, a numerical improvement will be approached to achieve more realistic cases.

Bibliography

- [1] D. M. Anderson, G. B. McFadden, and A. A. Wheeler. Diffuse-interface in fluid mechanics. *Annual Review of Fluid Mechanics*, 30(1):139–165, 1998. [61](#), [65](#)
- [2] P. C. Hohenberg and B. I. Halperin. Theory of dynamic critical phenomena. *Reviews of Modern Physics*, 49(3):435–479, 1977. Publisher: American Physical Society. [61](#)
- [3] D. Jacqmin. Calculation of Two-Phase Navier–Stokes Flows Using Phase-Field Modeling. *Journal of Computational Physics*, 155(1):96–127, 1999. [61](#)
- [4] F. Yue, C. Feng, S. Liu, and B. Shen. A diffuse-interface method for simulating two-phase flows of complex fluids. *Journal of Fluid Mechanics*, 515(1):293–317, 2004.
- [5] H. Abels. On a diffuse interface model for two-phase flows of viscous, incompressible fluids with matched densities. 194(2):463–506, 2009. [61](#), [73](#)
- [6] F. Boyer, C. Lapuerta, S. Minjeaud, and B. Piar. Cahn–Hilliard/Navier–Stokes model for the simulation of three-phase flows. *Transport in Porous Media*, 82(3):463–483, 2010. [61](#)
- [7] D. Jamet. Diffuse interface models in fluid mechanics. Technical report, CEA Grenoble, 2014. [61](#), [65](#)

- [8] L.K. Antanovskii. A phase field model of capillarity. *Physics of Fluids*, 7(4):747–753, Apr 1995. [65](#)
- [9] D. Bresch and B. Desjardins. Quelques modèles diffusifs capillaires de type Korteweg. *Comptes Rendus Mécanique*, 332(11):881–886, 2004. [65](#)
- [10] J. D. Van Der Waals. The thermodynamic theory of capillarity under the hypothesis of a continuous variation of density. *Journal of Statistical Physics*, 20(2):200–244, 1894. [65](#)
- [11] G. H. Korteweg. Sur la forme que prennent les équations du mouvement des fluides si l'on tient compte des forces capillaires causées par des variations de densité considérables mais continues et sur la théorie de la capillarité dans l'hypothèse d'une variation continue de la densité. *Archive Néerlandaises sci exactes et nat*, 6(2):1–27, 1901. [66](#)
- [12] H. Abels. Existence of Weak Solutions for a Diffuse Interface Model for Viscous, Incompressible Fluids with General Densities. *Communications in Mathematical Physics*, 289(1):45–73, 2009. [73](#)
- [13] H. Abels, H. Garcke, and G. Grun. Thermodynamically consistent, frame indifferent diffuse interface models for incompressible two-phase flows with different densities. *Mathematical Models and Methods in Applied Sciences*, 22(03), 2012. [73](#)
- [14] H. Abels, D. Depner, and H. Garcke. On an incompressible Navier–Stokes/Cahn–Hilliard system with degenerate mobility. *Annales de l'I.H.P. Analyse non linéaire*, 30(6):1175–1190, 2013. [73](#)
- [15] C. Liu and J. Shen. A phase field model for the mixture of two incompressible fluids and its approximation by a Fourier-spectral method. *Physica D: Nonlinear Phenomena*, 179(3):211–228, 2003. [73](#)
- [16] F. Boyer. A theoretical and numerical model for the study of incompressible mixture flows. *Computers and Fluids*, 31(1):41–68, 2002. [73](#)
- [17] T.J.R. Hughes, G. Scovazzi, and L.P. Franca. *Multiscale and Stabilized Methods*. Encyclopedia of Computational Mechanics. John Wiley & Sons, Ltd, 2004. [75](#)
- [18] R. Codina, S. Badia, J. Baiges, and J. Principe. *Variational Multiscale Methods in Computational Fluid Dynamics*. John Wiley & Sons, Ltd, 2017. [75](#)

-
- [19] Thomas J. R. Hughes. Multiscale phenomena: Green’s functions, the Dirichlet-to-Neumann formulation, subgrid scale models, bubbles and the origins of stabilized methods. *Computer Methods in Applied Mechanics and Engineering*, 127(1):387–401, 1995. [75](#)
- [20] U. Rasthofer and V. Gravemeier. Recent Developments in Variational Multiscale Methods for Large-Eddy Simulation of Turbulent Flow. *Archives of Computational Methods in Engineering*, 25(3):647–690, 2018. [75](#)
- [21] D. Forti and L. Dedè. Semi-implicit BDF time discretization of the Navier–Stokes equations with VMS-LES modeling in a High Performance Computing framework. *Computers & Fluids*, 117:168–182, 2015.
- [22] R Codina. Stabilized finite element approximation of transient incompressible flows using orthogonal subscales. *Computer Methods in Applied Mechanics and Engineering*, 191(39–40):4295–4321, 2002. [77](#)
- [23] T. Coupez and E. Hachem. Solution of high-Reynolds incompressible flow with stabilized finite element and adaptive anisotropic meshing. *Computer Methods in Applied Mechanics and Engineering*, 267:65–85, 2013. [77](#)
- [24] R Codina. On stabilized finite element methods for linear systems of convection–diffusion–reaction equations. *Computer Methods in Applied Mechanics and Engineering*, 188(1–3):61–82, 2000. [77](#)
- [25] P. H. Chiu and Y. T. Lin. A conservative phase field method for solving incompressible two-phase flows. *Journal of Computational Physics*, 230(1):185–204, 2011. [80](#)
- [26] S. Hysing, S. Turek, D. Kuzmin, N. Parolini, E. Burman, S. Ganesan, and L. Tobiska. Quantitative benchmark computations of two-dimensional bubble dynamics. *International Journal for Numerical Methods in Fluids*, 60(11):1259–1288, 2009. [80](#), [85](#), [86](#), [87](#)
- [27] S. Aland and A. Voigt. Benchmark computations of diffuse interface models for two-dimensional bubble dynamics. *International Journal for Numerical Methods in Fluids*, 69(3):747–761, 2012. [80](#)
- [28] J. C. Martin, W. J. Moyce, W. G. Penney, A. T. Price, and C. Thornhill. An experimental study of the collapse of liquid columns on a rigid horizontal plane. *Philosophical Transactions of the Royal Society of London. Series A, Mathematical and Physical Sciences*, 244:312 – 324, 1952. [82](#)

BIBLIOGRAPHY

- [29] L. Marioni, M. Khalloufi, F. Bay, and E. Hachem. Two-fluid flow under the constraint of external magnetic field: Revisiting the dam-break benchmark. *International Journal of Numerical Methods for Heat & Fluid Flow*, 27(11):2565–2581, 2017. [82](#)
- [30] G. Tryggvason. Numerical simulation of Rayleigh—Taylor instability. *J. Comput. Phys.*, 75(2):253–282, 1988. [89](#), [92](#)

Chapter 3

Anisotropic mesh adaptation for phase-field methods

Contents

| | | |
|------------|--------------------------------|------------|
| 3.1 | Introduction | 99 |
| 3.2 | Edge-based metric | 100 |
| 3.2.1 | Length distribution tensor | 100 |
| 3.2.2 | Edge based error estimation | 101 |
| 3.2.3 | Gradient recovery procedure | 101 |
| 3.2.4 | Metric construction | 102 |
| 3.2.5 | Mesh adaptation criteria | 103 |
| 3.3 | Numerical experiments | 104 |
| 3.3.1 | Dam-break 2D | 104 |
| 3.3.2 | Rising bubble 2D | 107 |
| 3.3.3 | Rayleigh–Taylor instability 2D | 112 |
| 3.3.4 | Dam-break 3D | 117 |
| 3.3.5 | Rising bubble 3D benchmark | 120 |
| 3.3.6 | Rayleigh–Taylor instability 3D | 122 |
| 3.4 | Conclusion | 124 |
| | Bibliography | 125 |

Résumé en Français

Dans les chapitres précédents, une méthodologie permettant de numériquement capturer l'interface séparant deux fluides et suivre son évolution ainsi que celle de la dynamique de ces deux fluides a été présentée. Des cas test appliquant cette méthodologie ont été numériquement simulés en 2D sur maillage uniforme. Dans l'optique de simuler des cas industriels en ayant une capture précise de l'interface, la simulation numérique sur maillage uniforme devient rapidement très coûteuse en temps de calcul. Se pose donc la question de la réduction du temps de calcul sans perte de la précision.

Ce chapitre présente la méthode d'adaptation de maillage anisotrope consistant à raffiner le maillage dans les zones d'intérêts et grossir le maillage ailleurs. Les zones d'intérêts sont les zones à fort gradient d'un ou plusieurs champs donnés. Le procédé d'adaptation de maillage anisotrope permet de construire une nouvelle métrique basée sur le gradient de ce(s) champ(s) à travers un algorithme automatisé. Ces champs sont appelés critères d'adaptation. Il peut s'agir par exemple du champ de vitesse, pour raffiner le maillage dans les endroits à fort gradient de vitesse c'est-à-dire où a lieu la dynamique, du champ de température, pour un maillage plus fin là où ont lieu les plus forts échanges thermiques, et/ou d'autres champs.

Dans les travaux présentés ici, la zone d'intérêt concerne uniquement l'interface séparant les deux fluides. De ce fait, il est pertinent de choisir un champ décrivant l'interface comme critère d'adaptation. À partir du présent chapitre, le critère d'adaptation sélectionné est l'énergie libre. En effet, de par son fort gradient dans la zone de transition séparant les deux fluides, c'est-à-dire à l'interface, ce champ permet d'obtenir une interface précisément décrite et un maillage bien raffiné en son voisinage.

Ce chapitre présente ensuite une application de la méthode d'adaptation de maillage anisotrope avec ce choix de critère d'adaptation à travers une série d'expériences numériques. Les expériences numériques du chapitre précédent ont toutes été reprises et simulées à nouveau. Il a notamment été observé une diminution de la diffusion numérique avec le maillage anisotrope comparé au maillage uniforme, ainsi qu'une meilleure conservation du volume de chacune des deux phases subissant l'écoulement.

L'adaptation de maillage anisotrope a aussi permis de réaliser ces expériences numériques en 3D, ce qui était sans espoir avec le maillage uniforme du fait du fort coût de calcul requis. Cette réussite permet donc d'espérer une simulation numérique plus réaliste d'un refroidissement d'une pièce industrielle lors de la trempe.

3.1 Introduction

To improve the efficiency of finite element methods and to provide an accurate computation of small scale feature the interface evolution, a numerical technique consists of local mesh refinement. Anisotropic mesh adaptation plays a key role in simulation problems for which interfaces are involved. This method can capture the interfaces with good accuracy at a low number of elements in the mesh. The purpose is to combine the phase-field approach with local mesh refinement around the zero isovalue of the order parameter φ , which corresponds to the interface region. The key to the anisotropic mesh adaptation is to generate highly stretched and well-oriented elements to have a good capture of the sharp gradients. Elements can then be stretched in particular directions according to the solution features. In the literature, several approaches to anisotropic mesh adaptation exist. In [1–3], the approaches rely on local modifications of an existing mesh. Specifically, they use a metric field to redefine the geometric distances allowing to adapt the mesh size according to mesh directions. In [4], authors have developed a mesh adaptation method based on *a posteriori* error estimation. This method produces metrics from the error analysis of the discretization error which steers the remeshing. In the following, the anisotropic mesh adaptation technique adopted is extracted from [5–7]. The method is driven by directional error estimators. The mesh is dynamically adapted to the adaptation criterion. The purpose is to refine the interface region. The refinement will then affect both the density of elements and their shapes around the interface. Therefore, the mesh will be anisotropically adapted and stretched along the direction of the considered criterion. Compared to an isotropic refinement, a large number of elements is saved. The adopted technique needs first a metric map prescribing a mesh size according to the principal directions in the domain, which are given by the eigenvectors of the metric while the mesh size h is given by the eigenvalues. The metric \mathbf{M} is a positive definite symmetric tensor [8–10], representing a local base modifying the distance computation from the Euclidean space to the metric space, such that:

$$\|\mathbf{x}\|_{\mathbf{M}} = \sqrt{\mathbf{x}^T \cdot \mathbf{M} \cdot \mathbf{x}} \quad (3.1)$$

for a vector \mathbf{x} of the Euclidean space. The scalar product associated to the metric space is given by

$$\langle \mathbf{x}, \mathbf{y} \rangle_{\mathbf{M}} := \mathbf{x}^T \cdot \mathbf{M} \cdot \mathbf{y} \quad (3.2)$$

An accurate description of the interface is obtained by using the normal direction as the principal direction of mesh refinement. It comes that a mesh size can be prescribed around the interface while a larger mesh size is considered far from the interface. A new metric can be then defined from the principal direction and the

non-uniform mesh size of the domain. This metric corresponds to an isotropic metric far from the interface and to an anisotropic metric near the interface.

3.2 Edge-based metric

The process of anisotropic mesh adaptation described previously is automated. It relies on the *a posteriori* definition of a metric field driving the remeshing procedure so that the interpolation error is minimized. This strategy is based on a statistical representation of the distribution of edges sharing a vertex, called *length distribution tensor*. The definition of an edge-based error estimator with a gradient recovery method, as proposed in [6], allows linking the length distribution tensor to the interpolation error. Once the optimal metric has been obtained, the mesh generation and adaptation method, based on a topological representation, is applied to obtain the new mesh. This metric construction is commonly used for dynamic mesh adaptation based on the variation of several fields.

3.2.1 Length distribution tensor

Let \mathbf{x}^i and \mathbf{x}^j two vertices of the edge \mathbf{x}^{ij} . Let $\Gamma(i)$ the set of nodes \mathbf{x}^j sharing an edge with \mathbf{x}^i . As stated by [6], The problem of finding a unitary metric \mathbf{M}^i associated to the *i*-th node can be formulated as the following least square problem:

$$\mathbf{M}^i = \operatorname{argmin}_{\mathbf{M} \in \mathbb{R}_{sym}^{d \times d}} \left(\sum_{j \in \Gamma(i)} \mathbf{M} \mathbf{x}^{ij} \cdot \mathbf{x}^{ij} - |\Gamma(i)| \right)^2 \quad (3.3)$$

For a finite element admissible mesh, vertices of $\Gamma(i)$ has to form at least d non co-linear edges with vertex \mathbf{x}^i .

Definition 3.2.1. The *length distribution tensor* denoted by \mathbf{X}^i is defined as follows:

$$\mathbf{X}^i := \frac{1}{|\Gamma(i)|} \left(\sum_{j \in \Gamma(i)} \mathbf{x}^{ij} \otimes \mathbf{x}^{ij} \right) \quad (3.4)$$

The length distribution tensor gives an average representation of the distribution of edges in $\Gamma(i)$

Proposition 3.2.2. An approximated solution of the problem (3.3) is given by:

$$\mathbf{M}^i = \frac{1}{d} (\mathbf{X}^i)^{-1} \quad (3.5)$$

3.2.2 Edge based error estimation

Let \mathcal{V}_h the finite element space defined in (1.21):

$$\mathcal{V}_h = \{v_h \in \mathcal{C}^0(\bar{\Omega}) \text{ such that } v_h|_K \in \mathbb{P}_1, K \in \mathcal{T}_h\}$$

where the triangulation \mathcal{T}_h of Ω is a family of disjoint elements K such that

$$\Omega = \bigsqcup_{K \in \mathcal{T}_h} K.$$

Let $u \in \mathcal{C}^2(\Omega)$ a regular function. Let $\Pi_h : \mathcal{C}^2(\Omega) \rightarrow \mathcal{V}_h$ a Lagrange interpolation operator such that, by denoting u^i the node value of $\Pi_h u$ at \mathbf{x}^i , for all $i \in \{1, \dots, N\}$ where N is the number of nodes:

$$u^i := \Pi_h u(\mathbf{x}^i) \quad (3.6)$$

In the case of continuous element \mathbb{P}_1 , the gradient of $\Pi_h u$ is a piecewise constant field but it is continuous along the edges in the direction of the edges, therefore

$$u^j = u^i + \nabla \Pi_h u \cdot \mathbf{x}^{ij} \quad (3.7)$$

By denoting $u^{ij} := u^j - u^i$, as established in [6], the following result is obtained:

Proposition 3.2.3. *The inequality of the interpolation error gradient projected along an edge \mathbf{x}^{ij} is given by:*

$$|(\nabla \Pi_h u - \nabla u) \cdot \mathbf{x}^{ij}| \leq \max_{\mathbf{y} \in [\mathbf{x}^i, \mathbf{x}^j]} |\mathbf{H}_u(\mathbf{y}) \mathbf{x}^{ij} \cdot \mathbf{x}^{ij}| \quad (3.8)$$

where $\mathbf{H}_u := \left[\frac{\partial^2 u}{\partial x_i \partial x_j} \right]_{1 \leq i, j \leq N}$ is the associated Hessian.

3.2.3 Gradient recovery procedure

An interpolation operator enabling the building of a continuous gradient can be defined directly at the node of the mesh and depending only on the given interpolation values. This interpolation operator is based on the length distribution tensor and the projection of the gradient along the edges. By denoting $\mathbf{g}^i := \nabla u(\mathbf{x}^i)$ the exact value of ∇u at node i and considering its Lagrange interpolate $\mathbf{g}_h^i := \Pi_h \nabla u(\mathbf{x}^i)$, it comes:

$$\mathbf{g}^j = \mathbf{g}^i + \nabla \mathbf{g}_h \cdot \mathbf{x}^{ij} \quad (3.9)$$

where $\mathbf{g}_h := \Pi_h \nabla u$.

And the projection of the gradient along the edges \mathbf{x}^{ij} is given by

$$(\nabla \mathbf{g}_h \cdot \mathbf{x}^{ij}) \cdot \mathbf{x}^{ij} = (\mathbf{g}^j - \mathbf{g}^i) \cdot \mathbf{x}^{ij} \quad (3.10)$$

Definition 3.2.4. By denoting $\mathbf{g}^{ij} := \mathbf{g}^j - \mathbf{g}^i$, the error along the edges \mathbf{x}^{ij} is defined by:

$$e^{ij} := |\mathbf{g}^{ij} \cdot \mathbf{x}^{ij}| \quad (3.11)$$

This error sampling is the exact interpolation error along the edge and enables the evaluation of the global L^2 error. The error (3.11) can be evaluated only if the gradient of u is known and continuous at the nodes of the mesh. This means that the solution must be at least in $\mathcal{C}^2(\Omega)$.

To overcome this constraint, a recovery procedure can be considered as proposed in [6] by defining the following local optimization problem:

$$\mathbf{g}^i = \underset{\mathbf{g}}{\operatorname{argmin}} \left(\sum_{j \in \Gamma(i)} |(\mathbf{g} - \nabla u_h) \cdot \mathbf{x}^{ij}|^2 \right) = \underset{\mathbf{g}}{\operatorname{argmin}} \left(\sum_{j \in \Gamma(i)} |\mathbf{g}\mathbf{x}^{ij} - u^{ij}|^2 \right) \quad (3.12)$$

by using (3.7), where u_h is the approximated solution. Solving

$$0 = \sum_{j \in \Gamma(i)} ((\mathbf{g}^i \mathbf{x}^{ij}) \cdot \mathbf{x}^{ij} - u^{ij} \cdot \mathbf{x}^{ij}) = \sum_{j \in \Gamma(i)} (\mathbf{g}^i (\mathbf{x}^{ij} \otimes \mathbf{x}^{ij}) - u^{ij} \cdot \mathbf{x}^{ij}) \quad (3.13)$$

and taking

$$\mathbf{u}^i := \sum_{j \in \Gamma(i)} u^{ij} \cdot \mathbf{x}^{ij} \quad (3.14)$$

allows to obtain the following solution of (3.12):

$$\mathbf{g}^i = (\mathbf{X}^i)^{-1} \mathbf{u}^i \quad (3.15)$$

3.2.4 Metric construction

Once the gradient recovery procedure is performed, the next step is to relate the error indicator e^{ij} defined in (3.11) to an adequate metric for the anisotropic mesh adaptation. Indeed, during the mesh adaptation procedure, the length of an edge is changed in the edge direction of a stretching factor. According to [6], this stretching factor, denoted by $s \in \mathbb{R}^+$, considers the edge transformation in its own direction and verifies:

$$\begin{aligned} \mathbf{x}^{ij} &\mapsto s\mathbf{x}^{ij} \\ \bar{e}^{ij} &:= |\mathbf{g}^{ij} \cdot s\mathbf{x}^{ij}| = s^2 e^{ij} \end{aligned} \quad (3.16)$$

with e^{ij} defined in (3.11). To obtain a new metric depending on the error \bar{e}^{ij} defined in (3.16) and taking into account the edge stretching, it is necessary to calculate a new length for each edge and to use it for rebuilding the length distribution tensor introduced in (3.4).

Definition 3.2.5. One defines s^{ij} , $i, j \in \mathcal{N}$ be the set of edges stretching factors by:

$$\tilde{e}^{ij} := (s^{ij})^2 e^{ij} |\tilde{\mathbf{x}}^{ij}| := s^{ij} |\mathbf{x}^{ij}| \quad (3.17)$$

where \tilde{e}^{ij} and $|\tilde{\mathbf{x}}^{ij}|$ denote respectively the target error and associated edge length.

The new metric is obtained from the following result [6]:

Theorem 3.2.6. *Let E the set of edges of a mesh and $p \in [1, d]$ be an exponent to be defined. Then, the continuous metric field defined at the mesh nodes is:*

$$\mathbf{M}^i := \left(\frac{1}{d} \sum_{j \in \Gamma(i)} (s^{ij})^2 \mathbf{x}^{ij} \otimes \mathbf{x}^{ij} \right)^{-1} \quad (3.18)$$

where

$$s^{ij} = \left(\frac{\lambda}{e^{ij}} \right)^{1/p} \quad (3.19)$$

and

$$\lambda = \left(\frac{\sum_i \sum_{j \in \Gamma(i)} (e^{ij})^{\frac{p}{p+2}}}{\text{card}(E)} \right)^{1/p} \quad (3.20)$$

minimizes the error for a fixed number of edges $\text{card}(E)$. Moreover, if $s^{ij} = 1$ for all $i \in \mathcal{N}$ and all $j \in \Gamma(i)$, then the mesh is optimal.

It is important to note that, in the mesh adaptation method of the present work, the stretching factor s^{ij} is computed so that the number of edges is fixed.

3.2.5 Mesh adaptation criteria

The aim is to apply the anisotropic mesh adaptation so that the interface is better captured. Different fields can be used as a criterion for mesh adaptation in function of the fields of interest. To well capture the interface, a criterion based on the order parameter φ , which describes the interface, seems to be obvious. Therefore, the phase-field solution φ can be chosen as a criterion for mesh adaptation. In the present work, the free energy $F(\varphi) = \frac{(\varphi^2 - 1)^2}{4}$ from (1.2), directly related to φ , is the field that will be chosen for its usefulness in mesh adaptation. Thanks to its property for which this free energy is non-null in the interface region and vanishes away from the interface at any time, it is a good criterion that represents accurately

the interface area. To have a field that doesn't dominate the error estimator e^{ij} and to take into account the variations of this variable, the considered field is normalized. In the case of the free energy $F(\varphi)$, it is normalized by its maximum.

In practice, the mesh adaptation method considered here can increase the computation cost of a simulation. In this case, it could be judicious to have an adaptation frequency that avoids the adaptation at each time step. The purpose is to determine the optimal frequency to reduce computation costs. The optimal frequency is difficult to determine. However, it can be approached with the help of information, like the initial number of elements in the domain or even near to the interface, the considered time step, and the velocity magnitude in the areas of interest,... The anisotropic mesh adaptation enables to performance of simulations quicker while reducing computation costs and obtaining a more accurate solution. In this case, simulations of 3D cases are more feasible than with a uniform mesh.

3.3 Numerical experiments

Now the anisotropic adaptation mesh method is explained, the following is dedicated to numerical simulation of test cases. The method will be applied to the test cases previously introduced and compared with the previous outcomes. The test cases considered are those of the multiphase flow framework studied in Section 2.7 of the last chapter.

3.3.1 Dam-break 2D

The present test case is dedicated to the dam-break 2D simulation, as introduced in 2.7.1, within the framework of anisotropic mesh adaptation explained previously. The water column, as represented in 2.3 collapses again in the air domain because the gravity force $\mathbf{g} = (0, -g)$, where $g = 9.81$. With mesh adaptation, one can reduce the number of elements while reducing the mesh size locally, in the neighborhood of the interface. This involves that the interface thickness can also be decreased. Compared to the previous chapter, some parameters have been modified. The parameters related to this test case with mesh adaptation are summarized in Table 3.1.

| | | | |
|----------------|-----------|-----------------|--------|
| ρ_{water} | 1000 | Δt | 0.0004 |
| η_{water} | 0.01 | L_x | 0.5 |
| ρ_{air} | 1 | L_y | 0.15 |
| η_{air} | 0.001 | a | 0.06 |
| M | 10^{-6} | γ^2 | 2 |
| g | 9.81 | σ | 0 |
| ε | 0.001 | $Nb_{elements}$ | 20,000 |
| t_f | 10 | h_{min} | 0.0001 |

Table 3.1: Parameters of the 2D dam-break test case with mesh adaptation

The simulation has been performed on 4 cores, with a visualization file created every 25-time step. In this simulation, the remeshing is performed every 3-time step. Figure 3.1 represents the evolution of the phase-field solution and the adapted mesh at different time.

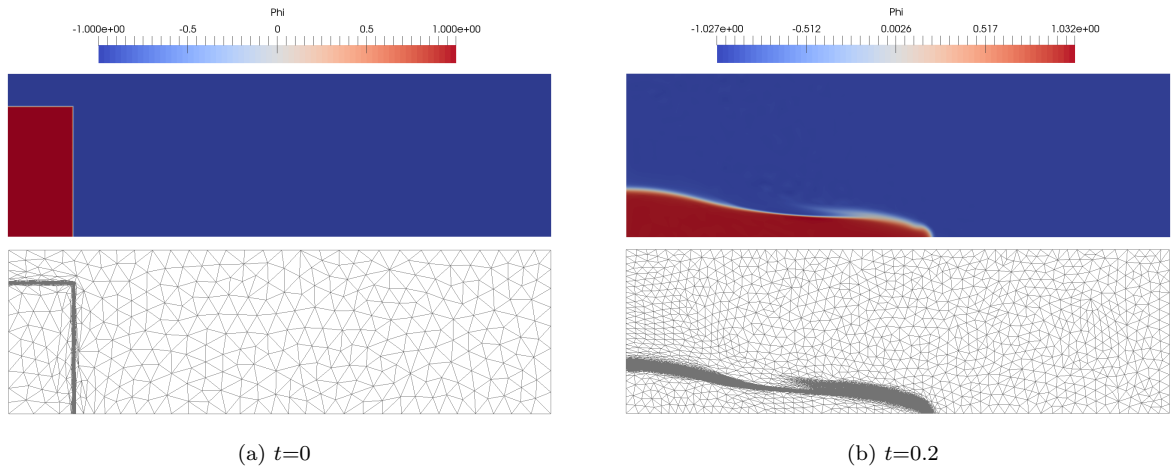


Figure 3.1: Phase-field solution at $t=0$ and 0.2 of the dam-break evolution with mesh adaptation

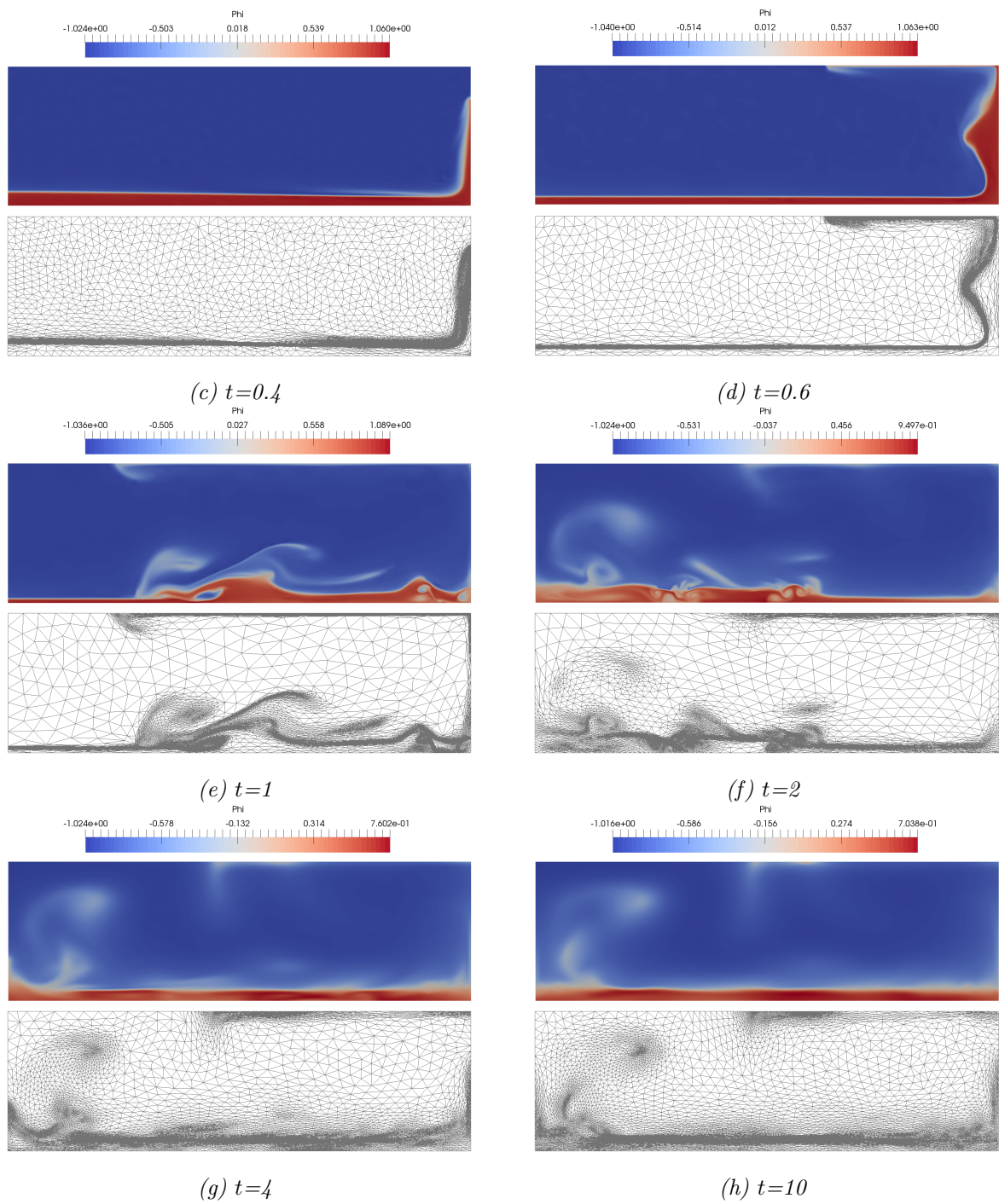


Figure 3.1: Phase-field solution at $t=0.4, 0.6, 1, 2, 4,$ and 10 of the dam-break evolution with mesh adaptation

In Figure 3.1, the effect of the mesh adaptation are clearly remarkable. The mesh is well refined in the interface area while it is coarsed far from the interface. As a consequence, the interface is at least as well as captured with only 20,000 elements than the 300,000 elements of the uniform mesh case.

As done in the previous chapter with the uniform mesh, a comparison with experimental results [11] and numerical results by the level-set method [12] is established. Specifically, the non-dimensional evolution of the front position is compared in Figure 3.2a as well as the non-dimensional evolution of the height in Figure 3.2b.

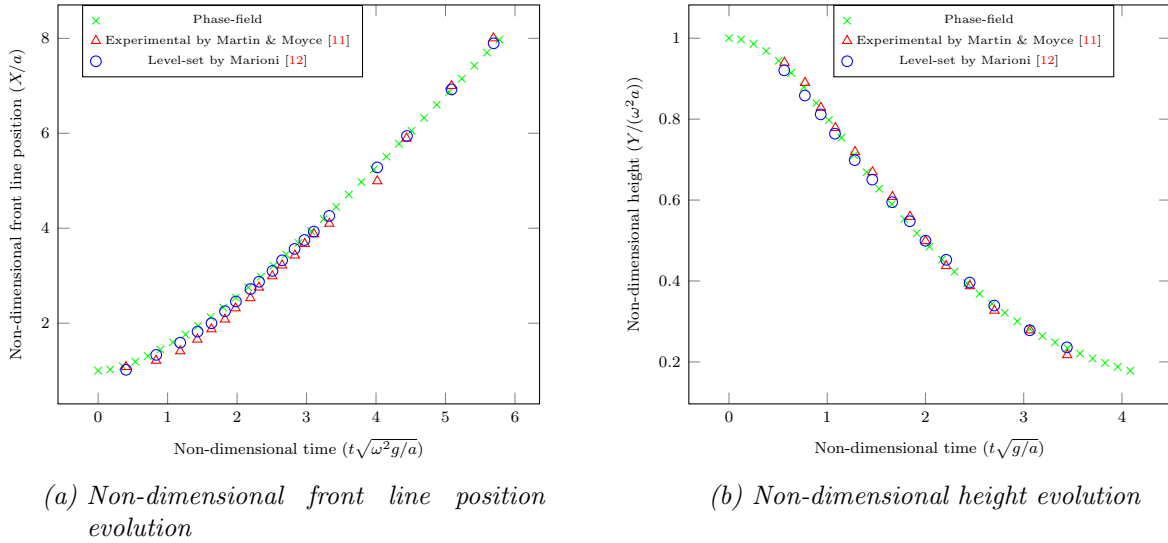


Figure 3.2: Non-dimensional evolution of the front position and the height column within the mesh adaptation framework

The results are the same as those observed in the previous chapter: they agree with the other methods. The simulation until the final time t_f has been performed in 9h 45min, compared to 71h 10min with the uniform mesh.

3.3.2 Rising bubble 2D

The present test case is the same one introduced in 2.7.2. A bubble of light fluid is surrounded by a heavier fluid and rises under the gravity effect and surface tension forces. The considered parameters summarized in Table 3.2.

| | | | |
|----------------|-----------|-----------------|--------|
| ϱ_{HF} | 1000 | Δt | 0.001 |
| η_{HF} | 10 | L_x | 1 |
| ϱ_{LF} | 1 | L_y | 2 |
| η_{LF} | 0.1 | D | 0.5 |
| M | 10^{-6} | g | 0.98 |
| ε | 0.008 | σ | 1.96 |
| t_f | 5 | $Nb_{elements}$ | 10,000 |

Table 3.2: Parameters of the rising bubble test case with anisotropic mesh adaptation

The minimum mesh size is fixed at $h_{min}=10^{-4}$ so that the interface region is well refined because of the anisotropic mesh adaptation. The adaptation step happens every 5 increments of time. The simulation has been performed in parallel on 4 cores, with a visualization file created every 50-time step. Figure 3.3 shows the evolution of the parameter order φ and the adapted mesh at time $t=0, 1, 2, 3, 4,$ and 5.

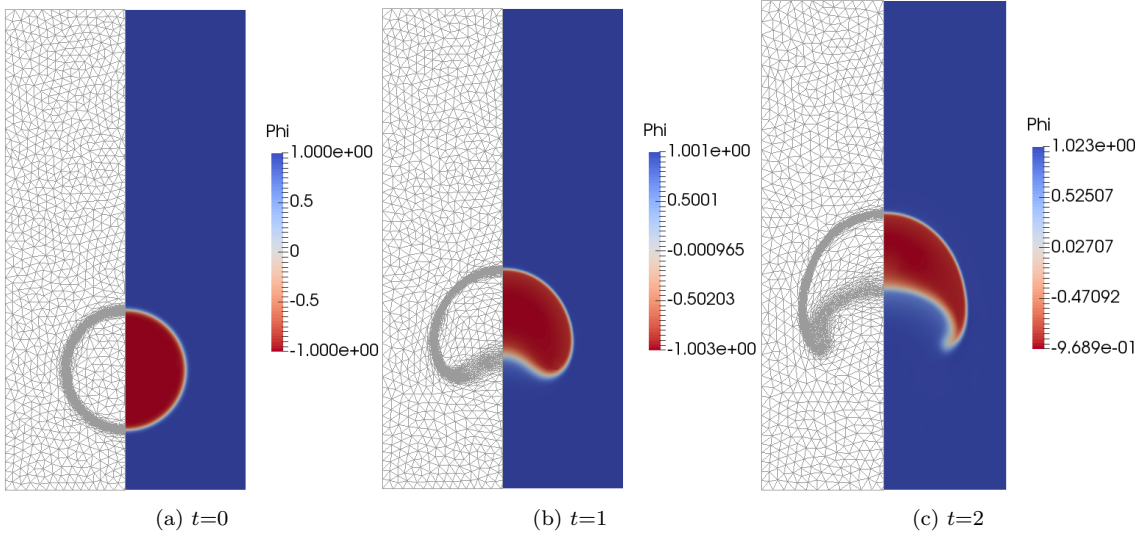


Figure 3.3: Phase-field solution and adapted mesh of the bubble evolution at $t=0, 1,$ and 2 with $\sigma=1.96$

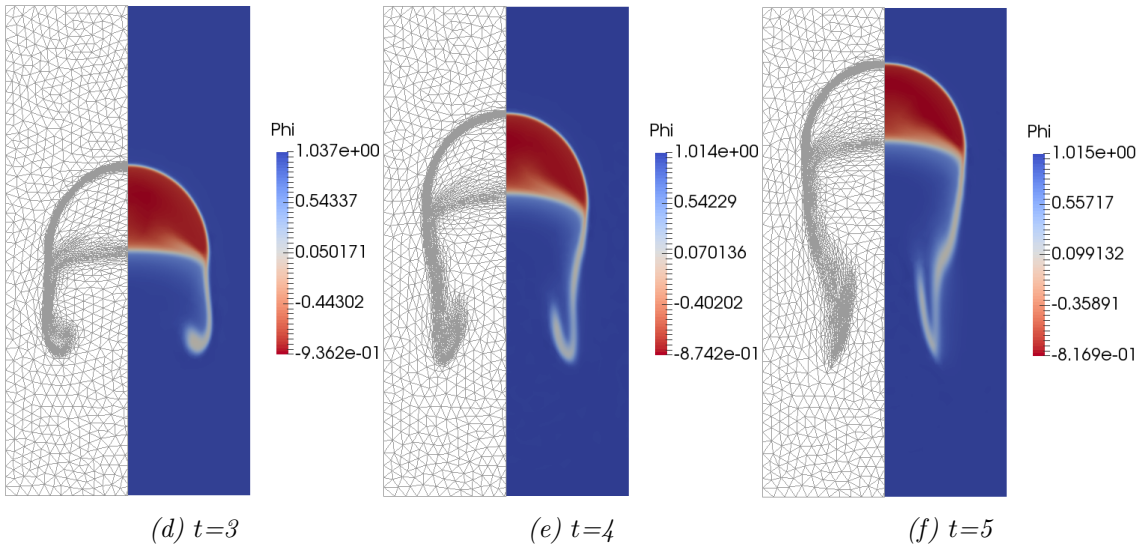


Figure 3.3: Phase-field solution and adapted mesh of the bubble evolution at $t=3$, 4, and 5 with $\sigma=1.96$

By representing the position and velocity evolution of the bubble mass center over time respectively in Figure 3.4a and 3.4b, the comparison with the level-set method [13] gives the same results as the previous chapter with a uniform mesh.

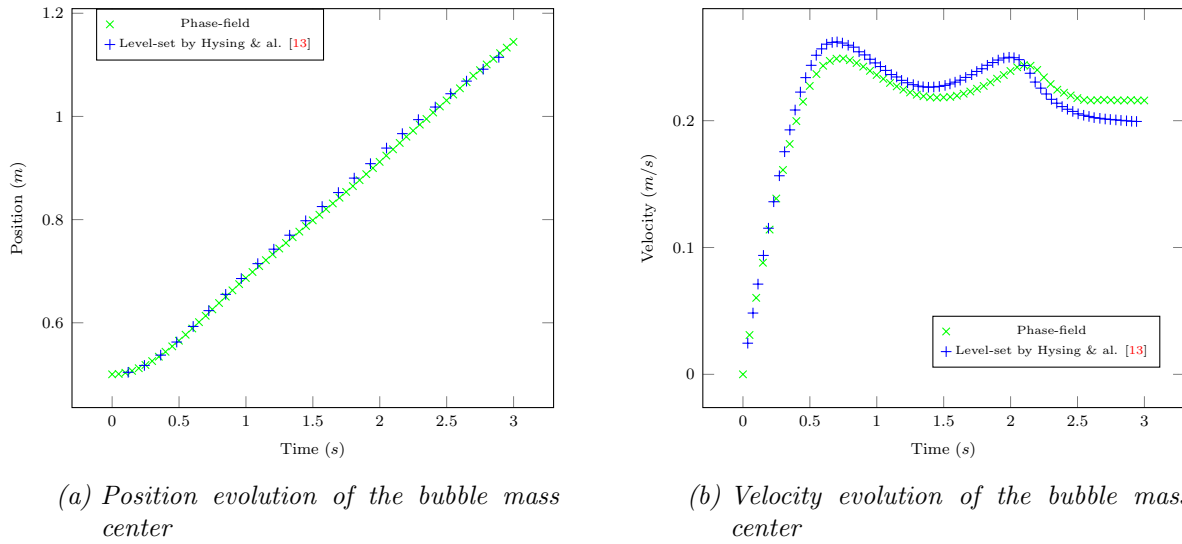


Figure 3.4: Position and velocity evolution of the bubble mass center for $\sigma=1.96$ with mesh adaptation

As in the previous chapter, a simulation of the rising bubble with another value

of the surface tension coefficient $\sigma=24.5$ has been performed. Compared to the previous case, only the surface tension coefficient and the physical properties of the bubble have been changed as defined in [13] with a light fluid density $\rho_{LF}=100$ and a light fluid viscosity $\eta_{LF}=1$. The simulation has also been performed on 4 cores. The adapted mesh and the phase-field solution of the rising bubble are presented in Figure 3.5 at time $t=0, 1, 2, 3, 4,$ and 5 .

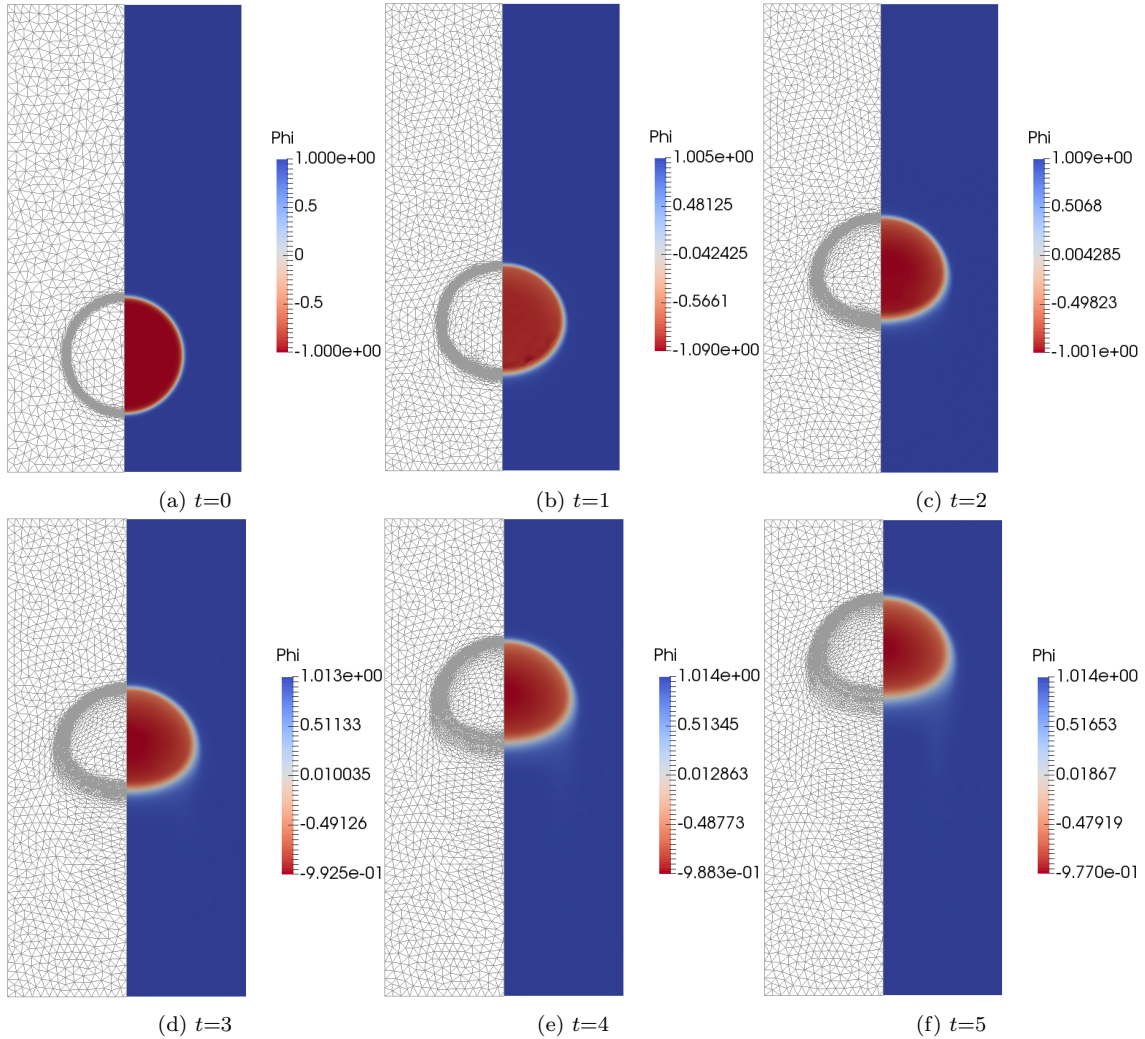
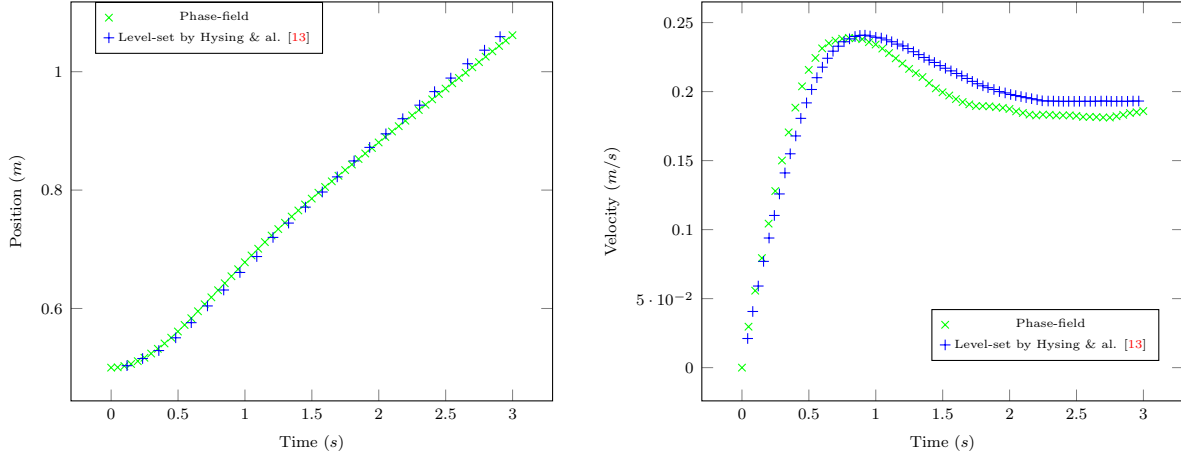


Figure 3.5: Phase-field solution and adapted mesh of the bubble evolution at $t=0, 1, 2, 3, 4,$ and 5 with $\sigma=24.5$

Position and velocity evolution of the bubble mass center over time are represented again, respectively in Figure 3.6a and 3.6b. The results are the same as those obtained in the uniform mesh case.



(a) Position evolution of the bubble mass center

(b) Velocity evolution of the bubble mass center

Figure 3.6: Position and velocity evolution of the bubble mass center for $\sigma=24.5$ with mesh adaptation

In Figure 3.3 and 3.5, the numerical diffusion is less present than the uniform mesh case in Figure 2.7 and 2.9. Unlike the uniform mesh case, there are no undershoots at some instants like $t=3$, $t=4$ and $t=5$ with mesh adaptation when $\sigma=1.96$ neither when $\sigma=24.5$, which means $\varphi \geq -1$. However, there are still overshoots for each time t presented in Figure 3.3 and 3.5 but they are less marked than in Figure 2.7 and 2.9. In the case of a surface tension coefficient $\sigma=1.96$, the maximum value of the parameter order noted in Figure 3.3 is reached for $|\varphi|_{max}=1.023$ with mesh adaptation compared to $|\varphi|_{max}=1.126$ noted in Figure 2.7 with the uniform mesh. The same observation is done for a surface tension coefficient $\sigma=24.5$ but with other values of $|\varphi|_{max}$.

The simulation took 24min to perform the rising bubble until the final time $t_f=5s$ in both cases for $\sigma=1.96$ and $\sigma=24.5$ with mesh adaptation compared to 22h 27min with a uniform mesh as stated in Chapter 2. With the uniform mesh, there were 200,000 elements while with the adapted mesh, it has been reduced to 10,000 elements.

3.3.3 Rayleigh–Taylor instability 2D

The test case of the Rayleigh–Taylor instability has been introduced in the previous chapter. It consists of the falling of a heavy fluid into a lighter and underlying fluid. The framework is the same as described in 2.7.3 with a set of parameters summarized in the following Table 3.3:

| | | | |
|----------------|-----------|-----------------|-------|
| ϱ_{HF} | 3 | Δt | 0.001 |
| η_{HF} | 0.0135 | L_x | 1 |
| ϱ_{LF} | 1 | L_y | 4 |
| η_{LF} | 0.0045 | σ | 0.03 |
| M | 10^{-6} | g | 9.8 |
| ε | 0.01 | h_{min} | 0.001 |
| t_f | 115 | $Nb_{elements}$ | 5,000 |

Table 3.3: Parameters of the Rayleigh–Taylor instability test case with anisotropic mesh adaptation

The adaptation step happens every 3 increments of time. The simulation has been performed on one core, with a visualization file created every 50-time step. The evolution of the instability and the adapted mesh at different time t are shown in Figure 3.7.

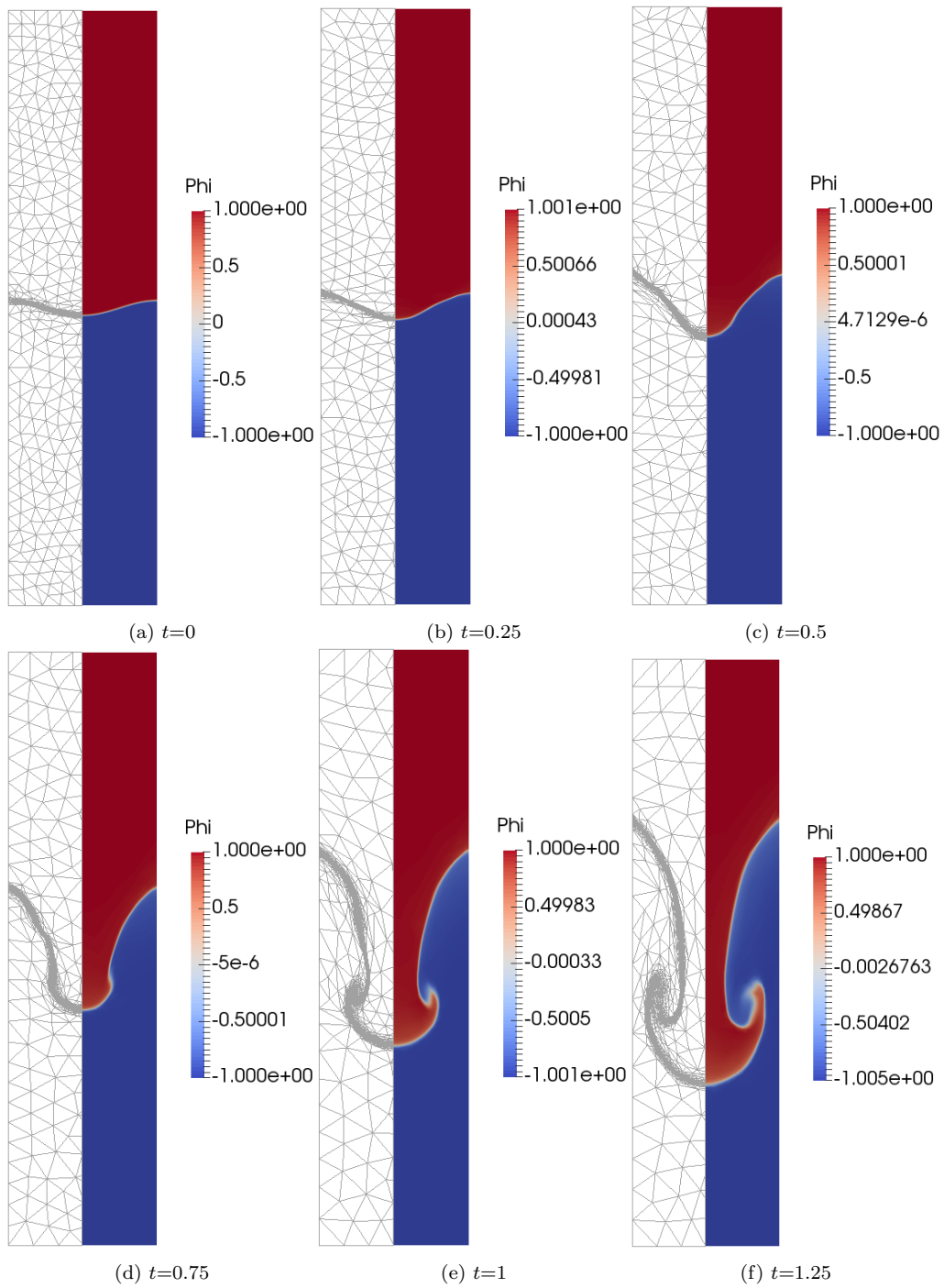


Figure 3.7: Phase-field and adapted mesh solution of the Rayleigh–Taylor instability at $t=0, 0.25, 0.5, 0.75, 1,$ and 1.25

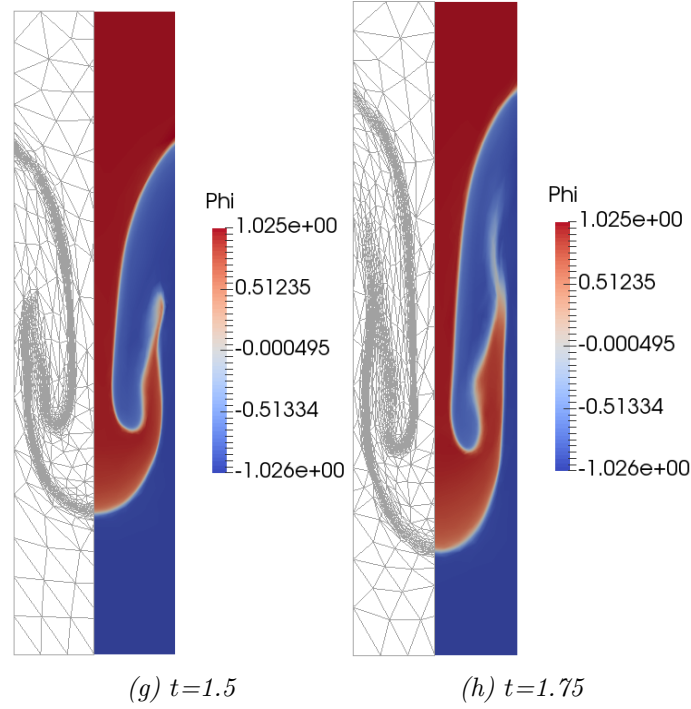


Figure 3.7: Phase-field solution and adapted mesh of the Rayleigh–Taylor instability at $t=1.5$ and 1.75

It appears a clear representation of the interface with a well refined mesh in the interface region. Compared to Figure 2.13 presenting the evolution of the instability with a uniform mesh, several observations can be done. First, the numerical diffusion has much more decreased and the phases are much less mixed. Second, the overshoots and undershoots are really less marked. By analyzing the value range of the parameter order φ in Figure 3.7, it rarely exceeds the initial and desired value range of φ , which means $[-1,1]$. Values of φ are really out of this range in Figure 3.7g and 3.7h with an absolute extreme value of $|\varphi|_{max}=1.026$. It is smaller than what observed in Figure 2.13 with a uniform mesh for which this value has already been reached after only $t=0.25$ and $|\varphi|_{max}=1.606$ as noted in Figure 2.13h at $t=1.75$. Third, by comparing the phase-field solution of the lighter fluid at the final time $t_f=115s$ for the uniform mesh (Figure 3.8a) and the adapted mesh (Figure 3.8b), a remarkable difference is visible.

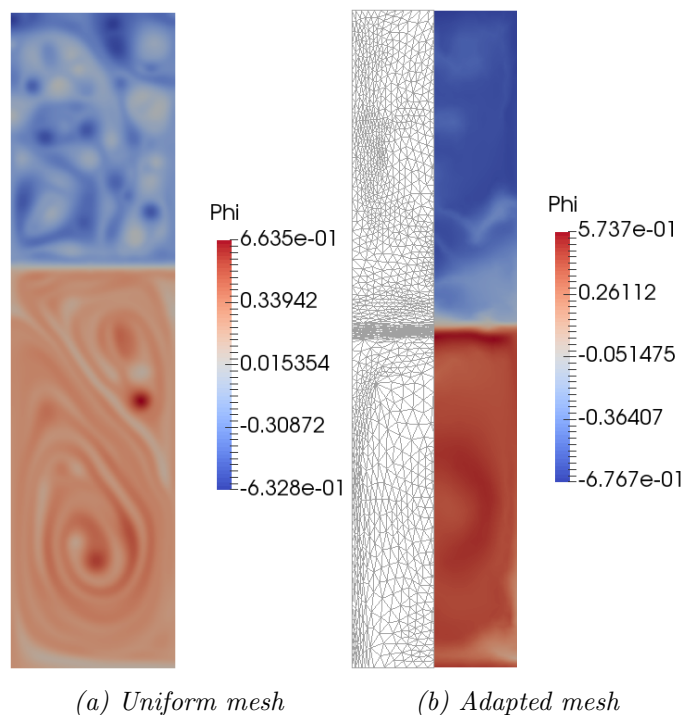


Figure 3.8: Phase-field solution of the Rayleigh–Taylor instability at $t=115$ for the uniform mesh and the adapted mesh

Indeed, despite the numerical diffusion, it seems that the volume of the lighter volume has more decreased in the case of the uniform mesh than the case of the adapted mesh. It is clearly indicated by the level of the interface separating the both phases. By measuring the relative volume loss of the lighter fluid over all the simulation for the cases of uniform and adapted mesh, this observation is quantitatively validated in Figure 3.9.

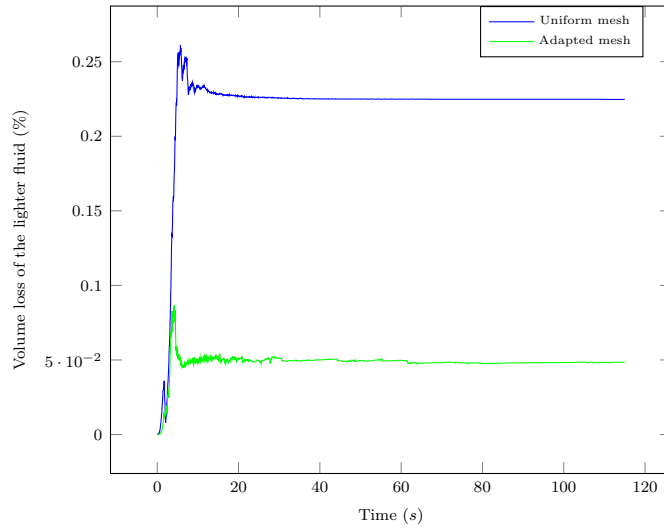


Figure 3.9: Volume loss evolution over time of the lighter fluid for the uniform and adapted mesh

From the graphs, it is obvious to note that the volume loss of the lighter fluid in the uniform mesh case is 25% while in the adapted mesh, it is only 5%. As remarked previously, the mesh adaptation helps to reduce numerical diffusion. This means the mobility of the species is closer to the fixed value of M and less amplified by numerical diffusion, so that the volume loss is better controlled.

The simulation has been performed on one core and took 12min to obtain $t=1.75s$ compared to 54min with the uniform mesh on 4 cores. To simulate $t_f=115s$, it took 8h 35min while the simulation with the uniform mesh took 37h 40min on 4 cores.

3.3.4 Dam-break 3D

In this test case, the dam-break is simulated in 3 dimensions of space. As in the 2D case, this test case considers a water column that collapses under the only gravity effect as represented in Figure 3.10.

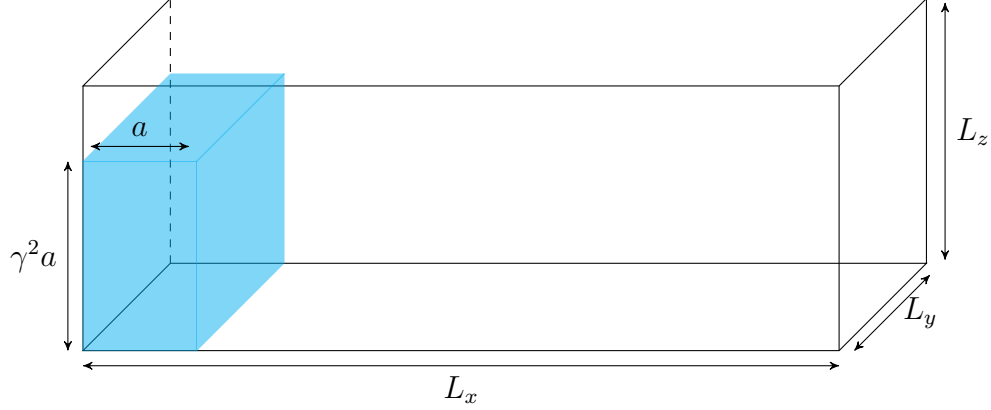


Figure 3.10: Dam-break benchmark 3D

To perform this simulation, an anisotropic mesh adaptation method has been considered. As established previously, the surface tension effect is neglected. The parameters of this test case are set as depicted in Table 3.4:

| | | | |
|----------------|-----------|-----------------|---------|
| ρ_{water} | 1000 | Δt | 0.0001 |
| η_{water} | 0.01 | L_x | 0.5 |
| ρ_{air} | 1 | L_y | 0.15 |
| η_{air} | 0.001 | L_z | 0.15 |
| M | 10^{-6} | a | 0.06 |
| g | 9.81 | γ^2 | 2 |
| ε | 0.004 | $Nb_{elements}$ | 500,000 |
| t_f | 3 | h_{min} | 0.0004 |

Table 3.4: Parameters for the simulation of the dam-break test case in 3D

The simulation has been performed on 20 cores, with a visualization file created every 100-time step. In this simulation, the remeshing is performed every 10-time step. The evolution of the phase-field solution and the adapted mesh in 3D at different time is represented in Figure 3.11.

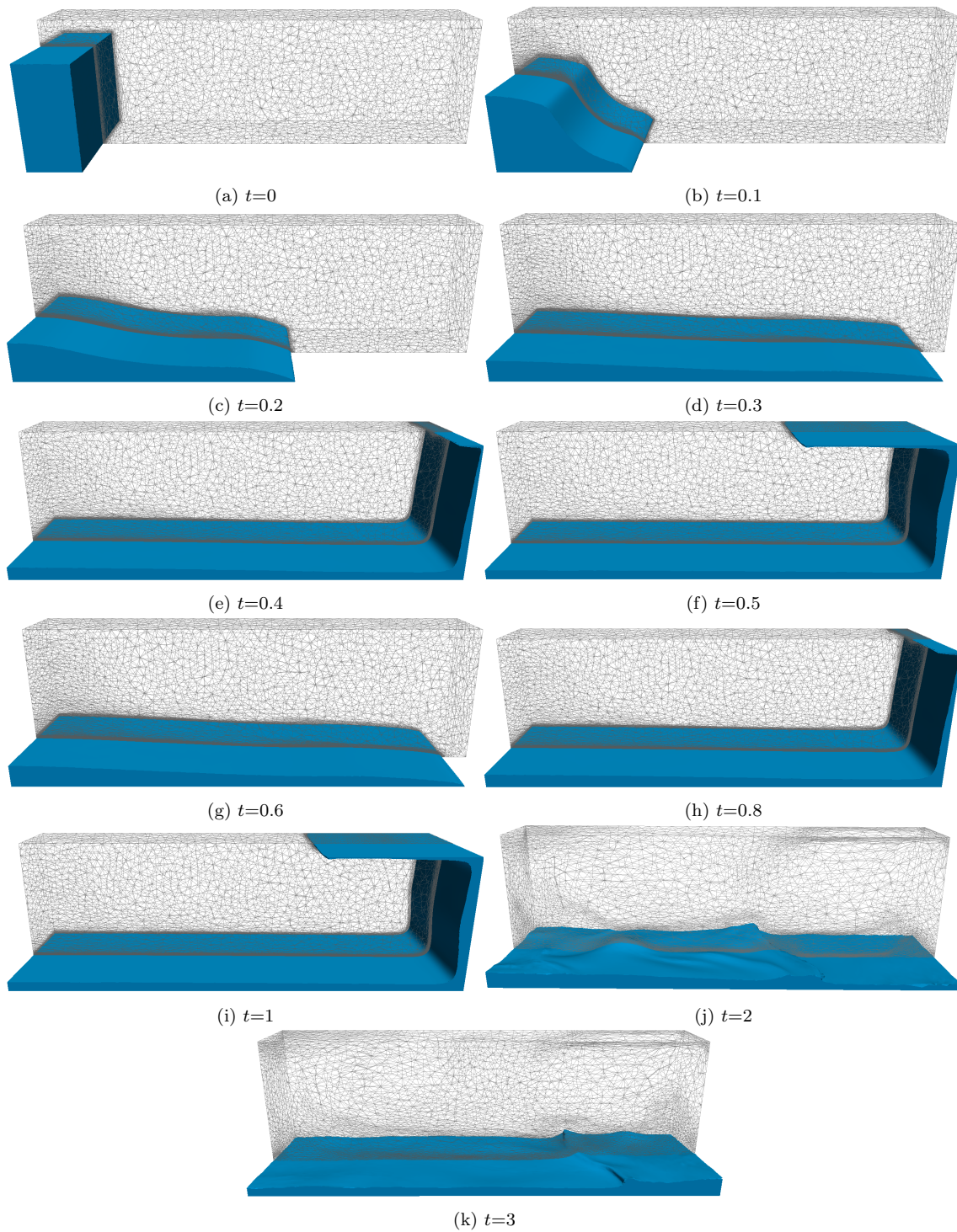


Figure 3.11: Dam-break evolution from time $t=0$ to $t=3$

As established in the 2D case, the numerical simulation, which is more realistic in 3D, has been compared to the experimental benchmark [11]. Figure 3.12 compares the evolution of the non-dimensional front line position and height over the non-dimensional time for the experimental method and two numerical methods, the level-set approach of [12] and the phase-field approach described in the present work.

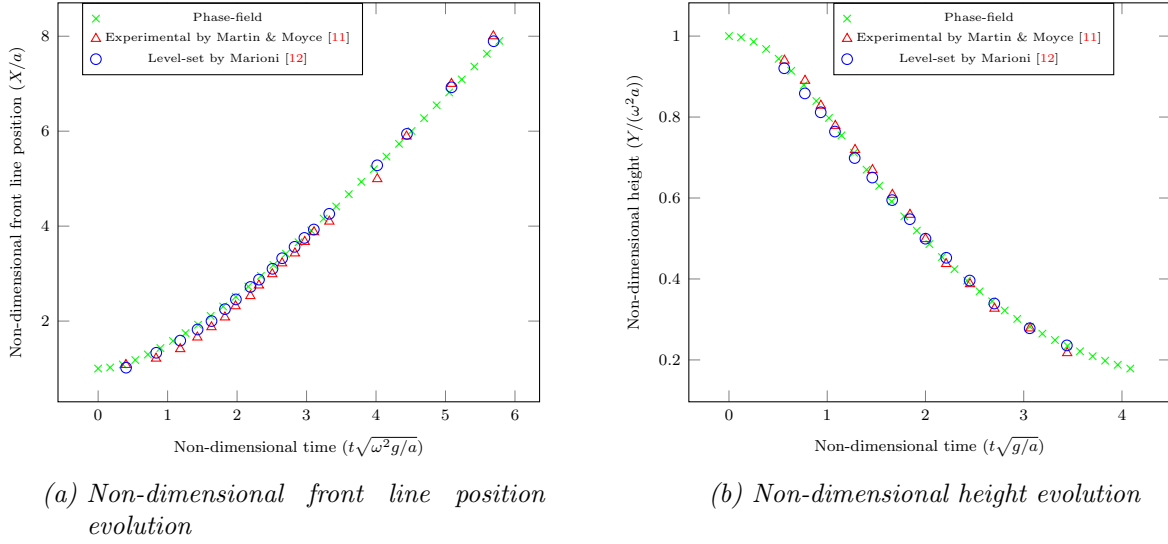


Figure 3.12: Non-dimensional evolution of the front position and the height of the dam-break in 3D

The numerical and experimental results present good similarities. To be more precise, by computing the relative ℓ^2 -error between the numerical results obtained with the phase-field method and the experimental results [11], the error is 4.91% on the non-dimensional front line position and 1.97% on the non-dimensional height. The simulation on 20 cores has been performed in 209h 24min to reach $t_f=3s$.

3.3.5 Rising bubble 3D benchmark

This part is still about 3D test cases. The purpose is to simulate the rising bubble case initially introduced previously in 2D. In this test case, a spherical bubble of a light fluid is rising within a column of a heavier fluid as represented in Figure 3.13.

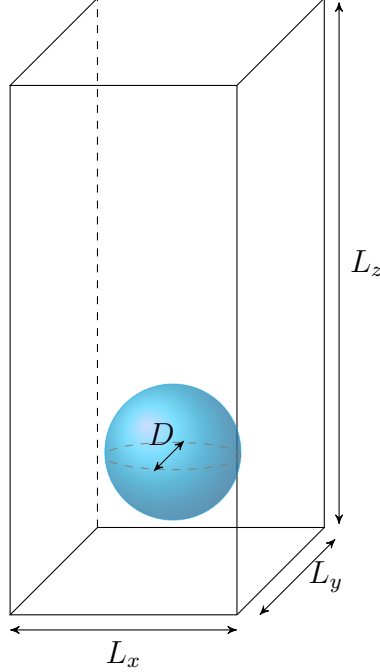


Figure 3.13: Rising bubble benchmark 3D

The parameters of the test case are summarized in Table 3.5.

| | | | |
|---------------|-----------|----------------|---------|
| ρ_{HF} | 1000 | Δt | 0.001 |
| η_{HF} | 10 | L_x | 1 |
| ρ_{LF} | 1 | L_y | 1 |
| η_{LF} | 0.1 | L_z | 2 |
| M | 10^{-6} | D | 0.5 |
| g | 0.98 | σ | 1.96 |
| ε | 0.004 | $N_{elements}$ | 500,000 |
| t_f | 3 | h_{min} | 0.0001 |

Table 3.5: Parameters for the simulation of the dam-break test case in 3D

The simulation has been performed on 32 cores, with a visualization file created every 50-time step. In this simulation, the remeshing is performed every 5-time step.

The evolution of the phase-field solution and the adapted mesh in 3D at different time is represented in Figure 3.14.

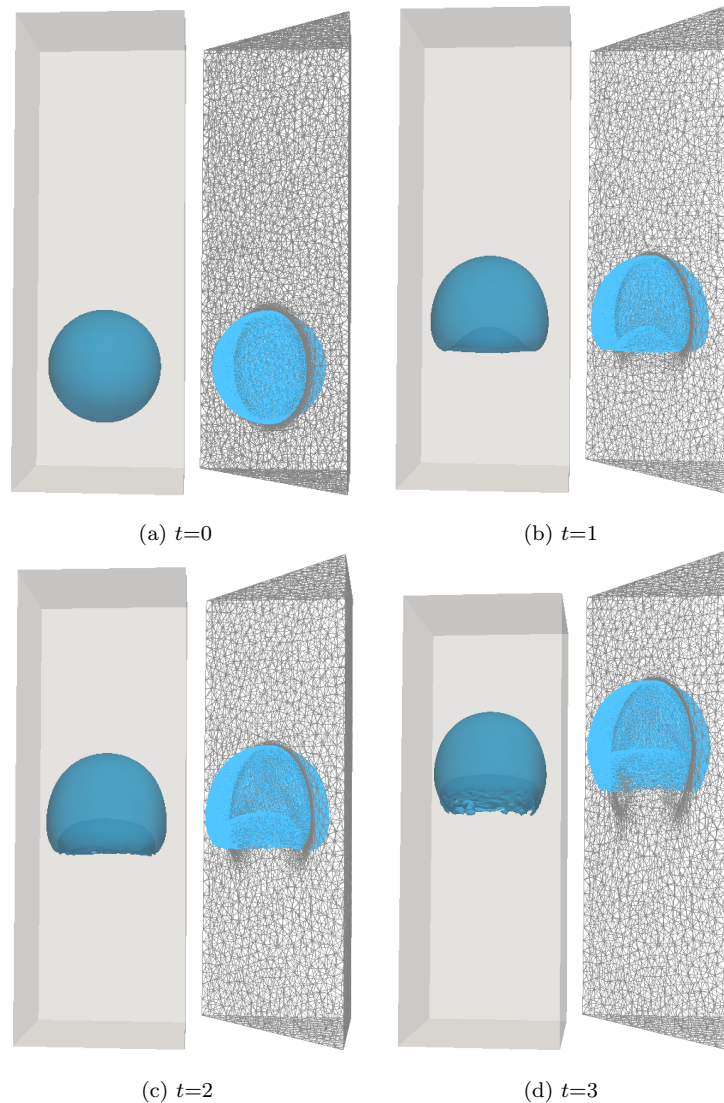


Figure 3.14: Interface evolution at $t=0$, 1 , 2 , and 3 of the rising bubble in 3D

The interface separating the bubble from the rest of the domain is well refined over all the rising. The dynamics are similar to what has been observed in the 2D case. The simulation of the 3D test case of the rising bubble took 67h 11min.

3.3.6 Rayleigh–Taylor instability 3D

The last test case of this chapter is about the Rayleigh–Taylor instability in 3D. Two layers of fluid, as represented in Figure 3.15, are initially at rest in the rectangular paver $\Omega = [0, L_x] \times [0, L_y] \times [0, L_z]$.

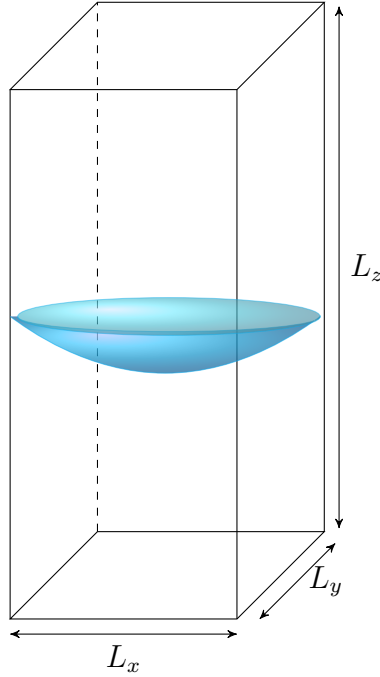


Figure 3.15: Rayleigh–Taylor instability 3D

The transition between the two fluids is regularized and initialized as the following phase-field function:

$$\varphi_0(x, y) = 0.05 \cos(2\pi(x - 0.5)) + 0.05 \cos(2\pi(y - 0.5)) + 2 \quad (3.21)$$

The movement gives a deformation of the shape of the fluid. The parameters for the test case are summarized in Table 2.3.

| | | | |
|-------------|-----------|-----------------|---------|
| ρ_{HF} | 3 | Δt | 0.001 |
| η_{HF} | 0.135 | L_x | 1 |
| ρ_{LF} | 1 | L_y | 1 |
| η_{LF} | 0.1 | L_z | 4 |
| M | 10^{-6} | ε | 0.02 |
| g | 9.81 | σ | 0.03 |
| t_f | 1.4 | $Nb_{elements}$ | 750,000 |

Table 3.6: Parameters for the simulation of the 3D test case of Rayleigh–Taylor instability

The test case of Rayleigh–Taylor instability simulation has been simulated on 32 cores, with a visualization file created every 50-time step. In this simulation, the remeshing is performed every 5-time step. The evolution of the interface and the adapted mesh in 3D at different time is represented in Figure 3.16.

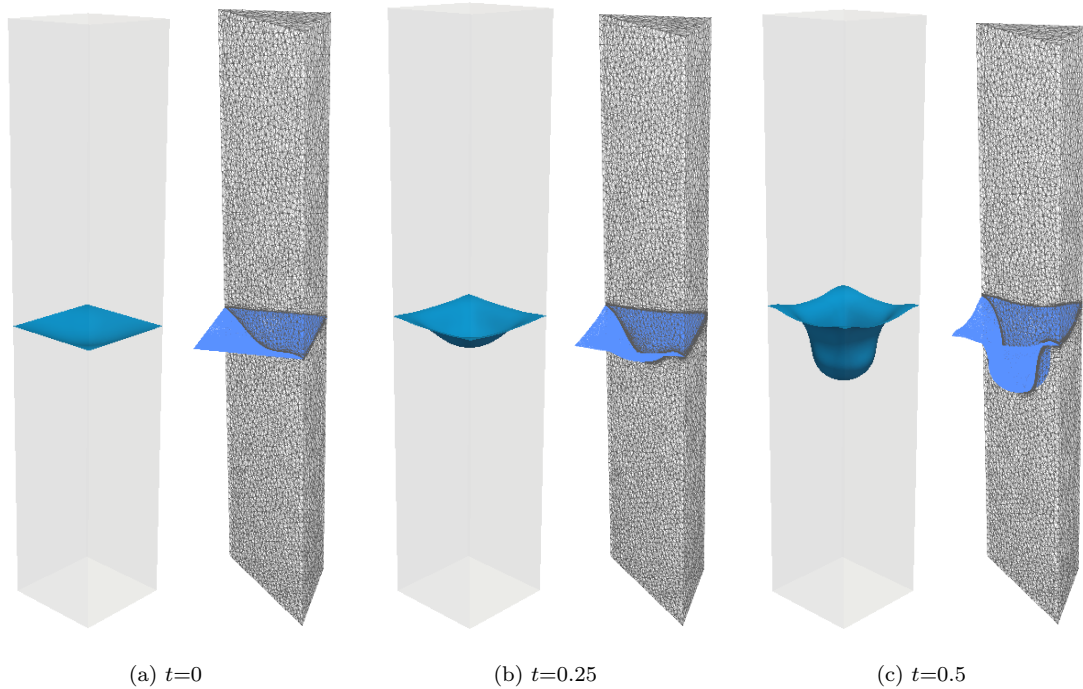


Figure 3.16: Interface evolution at $t=0$, 0.25 , and 0.5 of the Rayleigh–Taylor instability in 3D

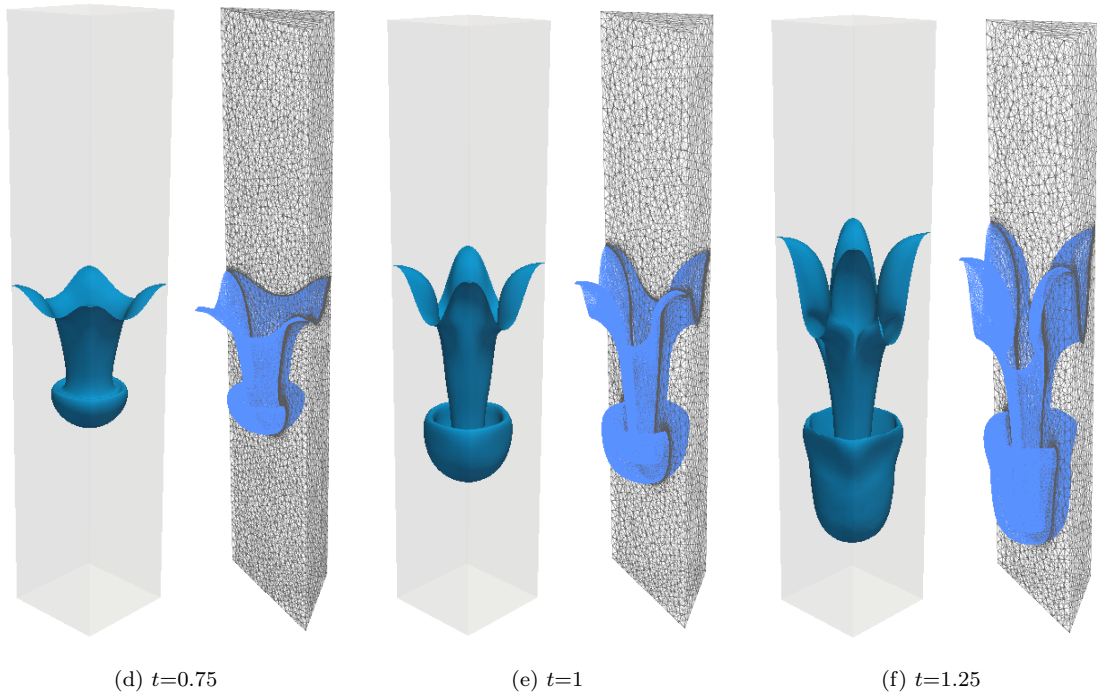


Figure 3.16: Interface evolution at $t=0.75$, 1 , and 1.25 of the Rayleigh–Taylor instability in 3D

Similar dynamics to the 2D case are observed in the 3D case. The interface is well-captured over the transport duration with a fine mesh in its region. The simulation of the 3D test case of the Rayleigh–Taylor instability took 33h 46min.

3.4 Conclusion

With the anisotropic mesh adaptation method applied in the presented simulations, the diffusion effect is less marked than with the uniform mesh. The undershoots and overshoots are also less amplified in the adapted mesh case than in the uniform mesh. This is explained by a large number of refined elements around the interface with a small mesh size. The validation results are the same as those obtained in the previous chapter and have not been impacted by mesh adaptation. Moreover, better conservation of the volume of the different phases is relevantly observed with mesh adaptation compared to the uniform mesh. This is due to a weaker diffusion because of the large number of refined elements around the interface. As remarked in the different test cases, simulations are highly quicker with mesh adaptation than without. Simulations in 3D are now feasible with mesh adaptation.

Bibliography

- [1] T. Coupez. A mesh improvement method for 3d automatic remeshing. *Numerical Grid Generation in Computational Fluid Dynamics and Related Fields*, Pineridge Press, pages 615–626, 1994. [99](#)
- [2] X. Li, M. S. Shephard, and M. W. Beall. 3d anisotropic mesh adaptation by mesh modification. *Comput. Methods Appl. Mech. Engrg.*, 194:4915—4950, 2005.
- [3] M. S. Shephard, J. E. Flaherty, K. E. Jansen, X. Li, X. Luo, N. Chevaugnon, M. W. Remacle, J. F. Beall, and R. M. Obara. Adaptive mesh generation for curved domains. *Appl. Numer. Math.*, 52:251—271, 2005. [99](#)
- [4] L. Formaggia and S. Perotto. New anisotropic a priori error estimate. *Numer. Math.*, 89:641—667, 2001. [99](#)
- [5] T. Coupez. Génération de maillage et adaptation de maillage par optimisation locale. *Revue européenne des éléments finis*, 9(4):403–423, 2000. [99](#)
- [6] T. Coupez. Metric construction by length distribution tensor and edge based error for anisotropic adaptive meshing. *Journal of Computational Physics*, 230(7):2391—2405, 2011. [100](#), [101](#), [102](#), [103](#)
- [7] T. Coupez and E. Hachem. Solution of high-Reynolds incompressible flow with stabilized finite element and adaptive anisotropic meshing. *Computer Methods in Applied Mechanics and Engineering*, 267:65–85, 2013. [99](#)
- [8] P. J. Frey and F. Alauzet. Anisotropic mesh adaptation for cfd computations. *Computer Methods in Applied Mechanics and Engineering*, 194(48–49):5068—5082, 2005. [99](#)
- [9] J.-F. Remacle, X. Li, M. S. Shephard, and J. E. Flaherty. Anisotropic adaptive simulation of transient flows. *International Journal for Numerical Methods in Engineering*, 62:899—923, 2005.
- [10] C. Gruau and T. Coupez. 3d tetrahedral, unstructured and anisotropic mesh generation with adaptation to natural and multidomain metric. *Computer Methods in Applied Mechanics and Engineering*, 194:4951—4976, 2005. [99](#)
- [11] J. C. Martin, W. J. Moyce, W. G. Penney, A. T. Price, and C. Thornhill. An experimental study of the collapse of liquid columns on a rigid horizontal plane. *Philosophical Transactions of the Royal Society of London. Series A, Mathematical and Physical Sciences*, 244:312 – 324, 1952. [107](#), [119](#)

- [12] L. Marioni, M. Khalloufi, F. Bay, and E. Hachem. Two-fluid flow under the constraint of external magnetic field: Revisiting the dam-break benchmark. *International Journal of Numerical Methods for Heat & Fluid Flow*, 27(11):2565–2581, 2017. [107](#), [119](#)

- [13] S. Hysing, S. Turek, D. Kuzmin, N. Parolini, E. Burman, S. Ganesan, and L. Tobiska. Quantitative benchmark computations of two-dimensional bubble dynamics. *International Journal for Numerical Methods in Fluids*, 60(11):1259–1288, 2009. [109](#), [110](#), [111](#)

Chapter 4

Applications to boiling

Contents

| | | |
|------------|---|------------|
| 4.1 | Introduction | 130 |
| 4.2 | Liquid-to-vapor phase change and heat transfer | 130 |
| 4.3 | Convection-diffusion-reaction for cooling | 140 |
| 4.4 | Numerical simulation | 142 |
| 4.4.1 | Stefan problem | 142 |
| 4.4.2 | Boiling case | 143 |
| 4.5 | Industrial applications | 148 |
| 4.5.1 | 3D quenching of a solid | 149 |
| 4.5.2 | 3D quenching of two identical solids | 154 |
| 4.5.3 | 3D queching of a large solid with a complex geometry | 159 |
| 4.6 | Conclusion | 163 |
| | Bibliography | 163 |

Résumé en Français

Avec les chapitres précédents, il est désormais possible de numériquement simuler un écoulement à deux phases séparées par une interface capturée par la méthode phase-field. Afin de réaliser une simulation numérique d'une trempe industrielle refroidissant une pièce, il est nécessaire de prendre en compte un solide, des échanges thermiques entre les phases, et un changement de phase eau/vapeur. Ceci a déjà été traité avec un cadre level-set pour la modélisation des interfaces eau/vapeur et vapeur/solide dans des travaux précédents.

Dans le présent chapitre, le cadre level-set est repris à la seule différence que l'interface séparant les deux fluides eau/vapeur est modélisée à l'aide de la méthode phase-field. Un écoulement multiphasique (solide-eau-vapeur) où chaque phase est munie de propriétés thermo-physiques. Ces propriétés, en plus de la fonction level-set et du paramètre d'ordre, permettent de déterminer les lois de mélange du système eau/vapeur/solide intervenant dans les équations décrivant le mouvement du mélange eau-vapeur avec changement de phase et échange thermique.

Pour modéliser le changement de phase ayant lieu durant la vaporisation de l'eau, les équations de Cahn–Hilliard sont réécrites à l'aide d'un bilan de masse dans chacune des phases eau et vapeur en faisant intervenir le taux de transfert de masse de l'eau vers la vapeur. Ce taux de transfert de masse est calculé par la condition de Stefan à l'aide du champ de température qui doit ainsi être résolu. La résolution de champ permet ainsi de connaître les échanges thermiques ayant lieu dans l'ensemble du système à chaque instant. Pour résoudre ce modèle thermique correspondant à une équation de type convection-réaction-diffusion, une méthode de stabilisation élément fini est utilisée. Tout comme avec le modèle de Cahn–Hilliard–Navier–Stokes du chapitre précédent, une résolution à pas fractionnaire est utilisée pour le modèle couplé incluant la thermique.

Cette résolution est appliquée sur une série d'expériences numériques présentées dans ce chapitre. Il s'agira en premier lieu d'évaluer la précision du modèle de changement de phase en comparant la solution numérique obtenue et la solution analytique du cas de Stefan 2D. Vient ensuite une première simulation numérique de la trempe industrielle en 2D par le modèle de Cahn–Hilliard–Navier–Stokes avec la thermique. Enfin, ce chapitre se conclut par des exemples d'applications industrielles sur des pièces de différentes géométries afin de réaliser une simulation numérique 3D de leur trempe comme preuve de concept.

4.1 Introduction

Multiphase flow and heat transfer are widely considered for the optimization of many engineering systems, such as nuclear safety [1] or quenching process [2]. This kind of process presents an interaction between three phases: an immersed solid, surrounded by a thin vapor film, within a liquid domain for cooling the hot solid. In the following, the liquid is assumed vaporizing. The existing vapor film is due to the high thermal gradient at the interface of the solid. This film of vapor acts as a thermal mantle which decreases the cooling rate of the material. The system is mainly driven by the vaporization phenomenon. To better understand the quenching process and the happening cooling, a study involving multiphase flow, phase, change, heat transfer, and fluid-solid interaction is required. The classical well-known methods to simply and quickly deduce the cooling of a solid, without any knowledge of the fluid behavior, rely on the use of empirical heat transfer coefficients. However, these are limited to particular scenarios and for a specific geometrical evolution of the flow.

The quenching process modeling introduces several challenges that have to be overcome to get a good model of the process. One of them is about the liquid-to-vapor phase change. In this chapter, the interface capturing with multiphase flow combined with the framework of boiling will be presented to enable the simulation of liquid/vapor interaction within the quenching process. The current existing framework to capture the liquid/vapor interface is based on the level-set method [3]. In the following, a proof of concept of the Cahn–Hilliard model replacing the level-set method for the liquid/vapor interface will be done. The first section is dedicated to the setup of an approach of a model combining the phase-field and multiphase flow model presented in the previous chapters with a liquid-to-vapor phase change and heat transfer. The obtained governing equations will then be established. A series of numerical simulations have been performed to have a first glimpse of the unified solver’s abilities. In the last section, examples of industrial cases simulation of quenching will be presented.

4.2 Liquid-to-vapor phase change and heat transfer

Until now, all the multiphase flow study has been done in the isothermal and incompressible framework. To consider a phase change in the model, the incompressible approach should be modified and the velocity field is not solenoidal anymore.

Proposition 4.2.1. *When the incompressible flow assumption is not enforced, it*

comes that the divergence of velocity field is obtained as follow:

$$\nabla \cdot \mathbf{u} = \frac{\varrho_2 - \varrho_1}{\varrho_1 + \varrho_2} \nabla \cdot (M(\varphi) \nabla \omega) \quad (4.1)$$

Proof. By considering the mass conservation law,

$$\partial_t (\varrho(\varphi)) + \nabla \cdot (\varrho(\varphi) \mathbf{u}) = 0.$$

However, by replacing the density $\varrho(\varphi)$ by (2.1), it comes

$$\begin{aligned} \partial_t (\varrho(\varphi)) + \nabla \cdot (\varrho(\varphi) \mathbf{u}) &= \frac{\varrho_1 - \varrho_2}{2} (\partial_t (\varphi) + \nabla \cdot (\varphi \mathbf{u})) + \frac{\varrho_1 + \varrho_2}{2} \nabla \cdot \mathbf{u} \\ &= \frac{\varrho_1 - \varrho_2}{2} \nabla \cdot (M(\varphi) \nabla \omega) + \frac{\varrho_1 + \varrho_2}{2} \nabla \cdot \mathbf{u} \end{aligned}$$

by using Equation (1.11). Therefore, the mass conservation law is respected if and only if

$$\frac{\varrho_1 - \varrho_2}{2} \nabla \cdot (M(\varphi) \nabla \omega) + \frac{\varrho_1 + \varrho_2}{2} \nabla \cdot \mathbf{u} = 0$$

which means

$$\nabla \cdot \mathbf{u} = \frac{\varrho_2 - \varrho_1}{\varrho_1 + \varrho_2} \nabla \cdot (M(\varphi) \nabla \omega)$$

□

The relation (4.1) corresponds to the phase movement at the diffuse interface due to the species mobility. To take into account the phase change due to the temperature field influence, like in the vaporization case, this field should intervene in the model. The Cahn–Hilliard model should then be extended by accounting for the dynamics of energy transfer [4]. In Chapter 1, a free energy has been introduced by the relation (1.2). This free energy is only related to the parameter order φ . However, the logarithmic form of the energy is dependent of the temperature [5–7]:

$$F(\varphi, T) = -\frac{T_c}{2} \varphi^2 + \frac{T}{2} ((1 + \varphi) \ln(1 + \varphi) + (1 - \varphi) \ln(1 - \varphi)) \quad (4.2)$$

where T_c is the critical temperature. This form is ideal to allow the respect of maximum principle on φ which can then belong to the interval $[-1, 1]$ of the admissible physically values [8]. However, to develop a finite element scheme of the Cahn–Hilliard equations, it could be difficult to have a discretized form of these equations with this logarithmic free energy. Then, as adopted in Chapter 1, it is easier to deal with a polynomial form, which has similar properties to the logarithmic form (*cf.* Chap 1). In the phase change case, it is desirable to have free energy dependent on the temperature field. It is possible to obtain a polynomial form of the free energy dependent on the temperature field, as suggested by the following result:

Proposition 4.2.2. *The quartic form of the free energy (4.2) is given by*

$$F(\varphi, T) = \frac{T}{2} \cdot \frac{\varphi^4}{6} + (T - T_c) \frac{\varphi^2}{2} \quad (4.3)$$

Proof. By a Taylor development of (4.2) on φ in the neighborhood of 0:

$$F(\varphi) \underset{\varphi \rightarrow 0}{=} -\frac{T_c}{2} \varphi^2 + \frac{T}{2} F(0) + \sum_{k=1}^n F^{(k)}(0) \frac{\varphi^k}{k!} + \mathcal{O}(\varphi^{n+1})$$

where

$$\begin{aligned} F^{(k)}(\varphi) &= \frac{d^k}{d\varphi^k} ((1 + \varphi) \ln(1 + \varphi) + (1 - \varphi) \ln(1 - \varphi)) \\ &= \frac{d^k}{d\varphi^k} ((1 + \varphi) \ln(1 + \varphi) - (1 + \varphi) + (1 - \varphi) \ln(1 - \varphi) - (1 - \varphi)) \\ &\quad + \underbrace{\frac{d^k}{d\varphi^k} ((1 + \varphi) + (1 - \varphi))}_0 \end{aligned}$$

However, by noting $x = 1 + \varphi$

$$\frac{d}{dx} (x \ln(x) - x) = \ln(x)$$

therefore,

$$x \ln(x) - x = \int \ln(x) dx.$$

Since

$$\begin{aligned} \frac{d}{d\varphi} ((1 + \varphi) \ln(1 + \varphi) - (1 + \varphi)) &= \ln(1 + \varphi) \\ \frac{d}{d\varphi} ((1 - \varphi) \ln(1 - \varphi) - (1 - \varphi)) &= -\ln(1 - \varphi), \end{aligned}$$

it comes

$$F^{(k)}(\varphi) = \frac{d^{k-1}}{d\varphi^{k-1}} (\ln(1 + \varphi) - \ln(1 - \varphi))$$

Therefore

$$\begin{aligned} \sum_{k=1}^n F^{(k)}(\varphi) \frac{\varphi^k}{k!} &= \sum_{k=1}^n \frac{d^{k-1}}{d\varphi^{k-1}} (\ln(1 + \varphi) - \ln(1 - \varphi)) \frac{\varphi^k}{k!} \\ &= (\ln(1 + \varphi) - \ln(1 - \varphi)) \varphi \end{aligned}$$

$$+ \sum_{k=1}^{n-1} \frac{d^k}{d\varphi^k} (\ln(1 + \varphi) - \ln(1 - \varphi)) \frac{\varphi^{k+1}}{(k+1)!}$$

However,

$$\begin{aligned} \frac{d^k}{d\varphi^k} \ln(1 + \varphi) &= \frac{(-1)^{k-1}(k-1)!}{(1+\varphi)^k} \\ \frac{d^k}{d\varphi^k} \ln(1 - \varphi) &= \frac{(-1)(k-1)!}{(1-\varphi)^k} \end{aligned}$$

therefore,

$$\begin{aligned} \sum_{k=1}^n F^{(k)}(\varphi) \frac{\varphi^k}{k!} &= (\ln(1 + \varphi) - \ln(1 - \varphi)) \varphi \\ &+ \sum_{k=1}^{n-1} \left(\frac{(-1)^{k-1}(k-1)!}{(1+\varphi)^k} + \frac{(k-1)!}{(1-\varphi)^k} \right) \frac{\varphi^{k+1}}{(k+1)!} \end{aligned}$$

Thus,

$$\begin{aligned} \sum_{k=1}^n F^{(k)}(0) \frac{\varphi^k}{k!} &= \sum_{k=1}^{n-1} ((-1)^{k-1}(k-1)! + (k-1)!) \frac{\varphi^{k+1}}{(k+1)!} \\ &= \sum_{k=1}^{n-1} ((-1)^{k-1} + 1) \frac{\varphi^{k+1}(k-1)!}{(k+1)!}. \end{aligned}$$

Hence,

$$F(\varphi) \underset{\varphi \rightarrow 0}{=} -\frac{T_c}{2} \varphi^2 + 0 + \frac{T}{2} \sum_{k=1}^{n-1} ((-1)^{k-1} + 1) \frac{\varphi^{k+1}}{k(k+1)}.$$

However,

$$(-1)^{k-1} + 1 = \begin{cases} 0 & \text{if } k \text{ is even} \\ 2 & \text{if } k \text{ is odd} \end{cases}$$

and

$$\sum_{k=1}^{n-1} ((-1)^{k-1} + 1) \frac{\varphi^{k+1}}{k(k+1)} = \sum_{k=0}^{n-2} ((-1)^k + 1) \frac{\varphi^{k+2}}{(k+1)(k+2)},$$

therefore, by changing the index $k \rightarrow k+1$,

$$\sum_{k=0}^{n-2} ((-1)^k + 1) \frac{\varphi^{k+2}}{(k+1)(k+2)} = \sum_{k=0}^{\frac{n-2}{2}} 2 \cdot \frac{\varphi^{2k+2}}{(2k+1)(2k+2)},$$

whence

$$F(\varphi) \underset{\varphi \rightarrow 0}{=} -\frac{T_c}{2}\varphi^2 + \frac{T}{2} \sum_{k=0}^{\frac{n-2}{2}} 2 \cdot \frac{\varphi^{2k+2}}{(2k+1)(2k+2)} + \mathcal{O}(\varphi^{n+1}).$$

Thus,

$$F(\varphi) \underset{\varphi \rightarrow 0}{=} -\frac{T_c}{2}\varphi^2 + T \sum_{k=0}^{\frac{n-2}{2}} \frac{\varphi^{2k+2}}{(2k+1)(2k+2)} + \mathcal{O}(\varphi^{n+1})$$

is the polynomial form of the free energy (4.2). By taking $n=4$, the quartic form is obtained. \square

This new form of F is the one involved in the free energy functional:

$$\mathcal{E}(\varphi, T) := \int_{\Omega} F(\varphi, T) + \frac{\varepsilon^2}{2} |\nabla \varphi|^2 \, d\mathbf{x} \quad (4.4)$$

which allows to obtain a new expression of the chemical potential ω .

Proposition 4.2.3. *The chemical potential associated to the free energy (4.4) is given by*

$$\omega(\varphi, T) = \frac{T}{2} \cdot \frac{\varphi^3}{3} + (T - T_c)\varphi - \varepsilon^2 \Delta \varphi \quad (4.5)$$

Proof. By using **Definition 1.3.1** of the chemical potential, one follows the same reasoning of the proof of **Proposition 1.3.3**. \square

Definition 4.2.4. One defines the *entropy* s , in the thermodynamic sens, as the first derivative of the free energy functional \mathcal{E} with respect to the temperature T :

$$s := \frac{\delta \mathcal{E}}{\delta T}$$

Proposition 4.2.5. *The entropy s is related to the order parameter φ by the following relation:*

$$s(\varphi) = \frac{\varphi^4}{12} + \frac{\varphi}{2} \quad (4.6)$$

Proof. By noting,

$$\mathcal{E}[\varphi, T] = \mathcal{F}[\varphi, T] + \mathcal{G}[\varphi, T]$$

where,

$$\mathcal{F}[\varphi, T] = \int_{\Omega} F(\varphi, T) \, d\mathbf{x} \quad \text{and} \quad \mathcal{G}[\varphi, T] = \int_{\Omega} \frac{\varepsilon^2}{2} |\nabla \varphi|^2 \, d\mathbf{x},$$

it comes by applying **Lemma 1.3.4** with the variable T ,

$$\frac{\delta \mathcal{F}[\varphi, T]}{\delta T} = \frac{\partial}{\partial T} F(\varphi, T) = \frac{\varphi^4}{12} + \frac{\varphi}{2}$$

Let $\lambda \in \mathbb{R}$ and $\psi \in H^1(\Omega)$, then

$$\mathcal{G}[\varphi, T + \lambda\psi] = \int_{\Omega} \frac{\varepsilon^2}{2} |\nabla \varphi|^2 \, d\mathbf{x} + \int_{\Omega} \psi \cdot 0 \, d\mathbf{x}$$

which means that,

$$\frac{\delta \mathcal{G}[\varphi]}{\delta \varphi} = 0$$

Thus,

$$s := \frac{\delta \mathcal{E}[\varphi, T]}{\delta T} = \frac{\delta \mathcal{F}[\varphi, T]}{\delta T} + \frac{\delta \mathcal{G}[\varphi, T]}{\delta T} = \frac{\varphi^4}{12} + \frac{\varphi}{2}$$

□

With these new contributions, the Cahn–Hilliard equations need to be rewritten to take them into account. A new equation on the entropy s should be considered [9] so that the Cahn–Hilliard model is extended. Ideally, the non-isothermal Cahn–Hilliard model should be derived from the fundamental laws of thermodynamics. Gurtin [10] considered an approach based on a balance law for micro-forces, which extends the models derived by Alt & al. [4] based on an entropy principle to non-isotropic materials and to systems that are far from equilibrium. Miranville & al. [11] extended this approach to the Ginzburg–Landau equation.

After obtaining the non-isothermal Cahn–Hilliard model, considering the balance equations as done in Section 2.2 is the next step. The mass balance needs to be determined to respect the conservation laws. Then, by following the approach of Chapter 2, a temperature-dependent and coupled Cahn–Hilliard–Navier–Stokes with phase change. It rests to determine the evolution equation on the temperature T . This equation should derive from the energy conservation law. Thus, a full coupled Cahn–Hilliard–Navier–Stokes model with heat transfer and phase change is obtained. As explained in Section 1.4, a such model needs to be studied physically, mathematically, and numerically. This is out of the scope of the present work and is not treated. In the following, an approximate and simpler approach will be adopted to solve numerically the models of the involved phenomena.

In multiphase flows, the concern is to be able to accurately compute the velocity and temperature fields in the whole domain, capture interfaces moving at high velocity, and quantify mass transfer rate in a thickness around the interface to model the phase change. To establish a first version of unified solvers allowing the simulation of multiphase flows with heat transfer and phase change due to vaporization, a study on the mass balance shall be done. This study begins with the mass conservation of the phase (liquid l or vapor v) in an arbitrary volume element fixed in space. One reminds the mixing law for the density established in Section 2.2 and applied to a liquid/vapor system of densities $\varrho_l > \varrho_v$:

$$\varrho(\varphi) = \varrho_l \frac{1 + \varphi}{2} + \varrho_v \frac{1 - \varphi}{2} \quad (4.7)$$

The local densities of the liquid l and the vapor v in a volume element are defined by:

$$\bar{\varrho}_l = \varrho_l \frac{1 + \varphi}{2}, \quad (4.8)$$

$$\bar{\varrho}_v = \varrho_v \frac{1 - \varphi}{2} \quad (4.9)$$

If a liquid-to-vapor phase change is considered, then by denoting \dot{m} [$\text{kg}\cdot\text{m}^{-2}\cdot\text{s}^{-1}$] the mass transfer rate leaving the liquid to the vapor and $\delta(\varphi, \omega)$ [m^{-1}] a smoothed representation of the interface between the two phases, the continuity equation within the liquid phase is

$$\partial_t \bar{\varrho}_l + \nabla \cdot (\bar{\varrho}_l \mathbf{u}) = -\dot{m} \delta(\varphi, \omega) \quad (4.10)$$

because a liquid has left, and within the vapor phase

$$\partial_t \bar{\varrho}_v + \nabla \cdot (\bar{\varrho}_v \mathbf{u}) = \dot{m} \delta(\varphi, \omega) \quad (4.11)$$

because a vapor has been created. By using the expressions (4.8) and (4.9) of the local densities, it comes

$$\frac{\varrho_l}{2} \partial_t \varphi + \frac{\varrho_l}{2} \nabla \cdot (\varphi \mathbf{u}) = -\dot{m} \delta(\varphi, \omega), \quad (4.12)$$

$$-\frac{\varrho_v}{2} \partial_t \varphi - \frac{\varrho_v}{2} \nabla \cdot (\varphi \mathbf{u}) = \dot{m} \delta(\varphi, \omega) \quad (4.13)$$

therefore,

$$\partial_t \varphi + \nabla \cdot (\varphi \mathbf{u}) = -\frac{2}{\varrho_l} \dot{m} \delta(\varphi, \omega), \quad (4.14)$$

$$\partial_t \varphi + \nabla \cdot (\varphi \mathbf{u}) = -\frac{2}{\varrho_l} \dot{m} \delta(\varphi, \omega). \quad (4.15)$$

By summing the relations (4.15) and (4.17), it comes

$$\partial_t \varphi + \nabla \cdot (\varphi \mathbf{u}) = -\dot{m} \delta(\varphi, \omega) \cdot \left(\frac{1}{\varrho_l} + \frac{1}{\varrho_v} \right) \quad (4.16)$$

One reminds the Cahn–Hilliard equations:

$$\partial_t \varphi + \nabla \cdot (\varphi \mathbf{u}) - \nabla \cdot (M(\varphi) \nabla \omega) = 0 \quad (4.17)$$

$$\omega + \varepsilon^2 \Delta \varphi - \varphi(\varphi^2 - 1) = 0 \quad (4.18)$$

By using Equation (4.17) within Equation (4.16), it comes

$$\nabla \cdot (M(\varphi) \nabla \omega) = -\dot{m} \delta(\varphi, \omega) \cdot \left(\frac{1}{\varrho_l} + \frac{1}{\varrho_v} \right) \quad (4.19)$$

With Proposition 4.2.1, the divergence of velocity field becomes

$$\nabla \cdot \mathbf{u} = -\dot{m} \delta(\varphi, \omega) \frac{\varrho_v - \varrho_l}{\varrho_l + \varrho_v} \cdot \left(\frac{1}{\varrho_l} + \frac{1}{\varrho_v} \right) \quad (4.20)$$

which gives

$$\nabla \cdot \mathbf{u} = \frac{\dot{m} \delta(\varphi, \omega)}{\varrho_l + \varrho_v} \cdot \left(\frac{\varrho_l}{\varrho_v} - \frac{\varrho_v}{\varrho_l} \right) \quad (4.21)$$

The relation (4.21) corresponds to the mass transfer occurring at the interface between the vapor and the liquid because of the phase change during vaporization. By using the relations (4.19) and (4.21), the Cahn–Hilliard equations (4.17)–(4.18) with liquid-to-vapor phase change become

$$\partial_t \varphi + (\mathbf{u} \cdot \nabla) \varphi + \frac{\dot{m} \delta(\varphi, \omega)}{\varrho_l + \varrho_v} \cdot \left(\frac{\varrho_l}{\varrho_v} - \frac{\varrho_v}{\varrho_l} \right) \varphi - \dot{m} \delta(\varphi, \omega) \cdot \left(\frac{1}{\varrho_l} + \frac{1}{\varrho_v} \right) = 0, \quad (4.22)$$

$$\omega + \varepsilon^2 \Delta \varphi - \varphi(\varphi^2 - 1) = 0 \quad (4.23)$$

As done in Section 2.2, the next step is to identify the temporal and convective term of the momentum equation coupling to the Cahn–Hilliard equation.

Proposition 4.2.6. *For φ solution of the Cahn–Hilliard equations (4.22) – (4.23) and a density defined as (4.7), the temporal and convective term of the momentum equation is given by*

$$\begin{aligned} \partial_t (\varrho(\varphi) \mathbf{u}) + \nabla \cdot (\mathbf{u} \otimes (\varrho(\varphi) \mathbf{u} + \mathbf{J})) &= \varrho(\varphi) \partial_t (\mathbf{u}) + ((\varrho(\varphi) \mathbf{u} + \mathbf{J}) \cdot \nabla) \mathbf{u} \\ &+ \frac{\dot{m} \delta(\varphi, \omega)}{2} \left(\frac{\varrho_l}{\varrho_v} - \frac{\varrho_v}{\varrho_l} \right) \mathbf{u} \end{aligned} \quad (4.24)$$

where \mathbf{J} is the mass flux at the interface defined by:

$$\mathbf{J} = \frac{\varrho_v - \varrho_l}{2} M(\varphi) \nabla \omega \quad (4.25)$$

Proof. It is the same proof as that of Proposition 2.2.2 by considering the non-zero divergence of the field (4.21). \square

By following the steps of Section 2.4, it comes to a new coupled Cahn–Hilliard–Navier–Stokes equations with a liquid-to-vapor phase change:

$$\partial_t \varphi + (\mathbf{u} \cdot \nabla) \varphi + \frac{\dot{m} \delta(\varphi, \omega)}{\varrho_l + \varrho_v} \cdot \left(\frac{\varrho_l}{\varrho_v} - \frac{\varrho_v}{\varrho_l} \right) \varphi - \dot{m} \delta(\varphi, \omega) \cdot \left(\frac{1}{\varrho_l} + \frac{1}{\varrho_v} \right) = 0, \quad (4.26)$$

$$\omega + \varepsilon^2 \Delta \varphi - \varphi(\varphi^2 - 1) = 0, \quad (4.27)$$

$$\begin{aligned} & \varrho(\varphi) \partial_t (\mathbf{u}) + (\varrho(\varphi) \mathbf{u} \cdot \nabla) \mathbf{u} + (\mathbf{J} \cdot \nabla) \mathbf{u} \\ & + \frac{\dot{m} \delta(\varphi, \omega)}{2} \left(\frac{\varrho_l}{\varrho_v} - \frac{\varrho_v}{\varrho_l} \right) \mathbf{u} - \nabla \cdot (2\eta(\varphi) \mathbf{D}(\mathbf{u})) + \nabla p = \frac{\sigma}{\varepsilon^2} \omega \nabla \varphi + \varrho(\varphi) \mathbf{g}, \end{aligned} \quad (4.28)$$

$$\nabla \cdot \mathbf{u} = \frac{\dot{m} \delta(\varphi, \omega)}{\varrho_l + \varrho_v} \cdot \left(\frac{\varrho_l}{\varrho_v} - \frac{\varrho_v}{\varrho_l} \right), \quad (4.29)$$

One considers a three-phase flow composed of a solid immersed inside two immiscible fluids (water and vapor, for example) in a bounded connected domain $\Omega \subset \mathbb{R}^d$, where d is the spatial dimension. A level-set function α defines the solid/vapor interface. An order parameter φ identifies the two Newtonian fluids and takes the value -1 in the vapor and $+1$ in the water with a thin, smooth transition region of width ε between the two fluids. Consequently the water/vapor interface is described by the zero isocontour of the phase indicator $\varphi : \Gamma_t := \{\mathbf{x} \in \Omega \text{ such that } \varphi(\mathbf{x}, t) = 0\}, \forall t \in \mathbb{R}_+$. In the monolithic approach, all the different phases considered (solid, liquid, gas) are immersed in a single domain. To avoid a discontinuity at the solid/vapor interface, a smooth Heaviside function is computed to distribute in space the corresponding physical properties. This Heaviside function is given by:

$$H_\varepsilon(\alpha) = \begin{cases} 1 & \text{if } \alpha > \varepsilon \\ \frac{1}{2} \left(1 + \frac{\alpha}{\varepsilon} + \frac{1}{\pi} \sin \left(\frac{\pi \alpha}{\varepsilon} \right) \right) & \text{if } |\alpha| \leq \varepsilon \\ 0 & \text{if } \alpha < -\varepsilon \end{cases} \quad (4.30)$$

The material properties such as density ρ , dynamic viscosity η and the heat capacity c_p are therefore computed, for the solid/vapor mixing law, as follows:

$$\rho_{vs}(\alpha) = \rho_s H_\varepsilon(\alpha) + \rho_v (1 - H_\varepsilon(\alpha)), \quad (4.31)$$

$$\eta_{vs}(\alpha) = \eta_s H_\varepsilon(\alpha) + \eta_v (1 - H_\varepsilon(\alpha)), \quad (4.32)$$

$$\rho_{vs} c_p^{vs}(\alpha) = \rho_s c_p^s H_\varepsilon(\alpha) + \rho_v c_p^v (1 - H_\varepsilon(\alpha)). \quad (4.33)$$

However, using a linear mixing law for the thermal conductivity would lead to inaccurate results. According to [12], a harmonic mixing laws is recommended to

ensure the conservation of the heat flux:

$$k_{vs} = \left(\frac{H_\varepsilon(\alpha)}{k_s} + \frac{1-H_\varepsilon(\alpha)}{k_v} \right)^{-1} \quad (4.34)$$

This method only requires knowledge of the material properties and deals naturally with conjugate heat transfer.

To determine the material properties for the water/vapor mixing law, the phase-field φ and the solid/vapor mixing law are used as follows:

$$\rho(\varphi) = \rho_w \frac{1+\varphi}{2} + \rho_{vs} \frac{1-\varphi}{2}, \quad (4.35)$$

$$\eta(\varphi) = \eta_w \frac{1+\varphi}{2} + \eta_{vs} \frac{1-\varphi}{2}, \quad (4.36)$$

$$\rho c_p(\varphi) = \rho_w c_p^w \frac{1+\varphi}{2} + \rho_{vs} c_p^{vs} \frac{1-\varphi}{2}, \quad (4.37)$$

$$k = \left(\frac{1}{k_w} \frac{1+\varphi}{2} + \frac{1}{k_{vs}} \frac{1-\varphi}{2} \right)^{-1} \quad (4.38)$$

Then, a hybrid definition of both interfaces by the level-set method for the solid/vapor interface and the phase-field method for the vapor/water interface is obtained as shown in Figure 4.1.

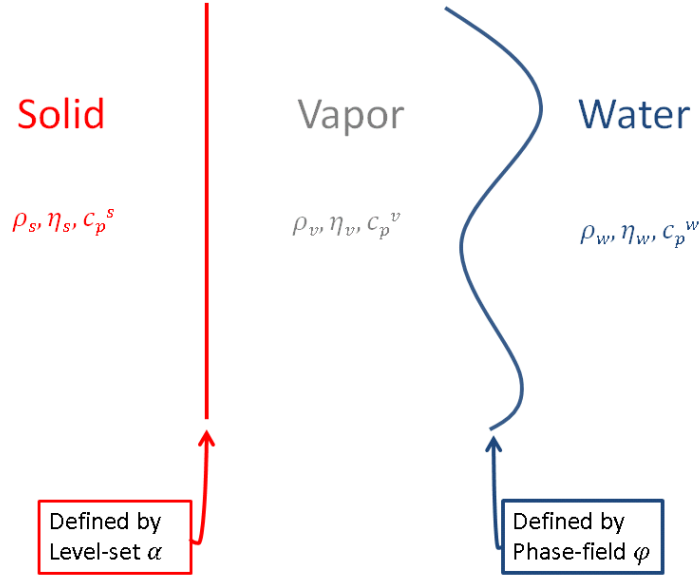


Figure 4.1: Level-set and phase-field hybrid interfaces

The mass transfer rate is defined using the heat released by a volume V of liquid that has vaporized between the time t and $t + \Delta t$. Considering a domain composed

of water and vapor (see Figure 4.2), the position of the interface at the time t is given by $x(t)$. The heat released Q by a volume V of liquid that has vaporized



Figure 4.2: Volume that has vaporized between t and $t + \Delta t$

during the elapsed time between t and $t + \Delta t$ is:

$$Q = \rho V \mathcal{L} \quad (4.39)$$

where \mathcal{L} is the latent heat. The heat fluxes are defined on a surface of area A , respectively in the vapor and the water by $-k_v \nabla T_v$ and $-k_w \nabla T_w$:

$$Q = \int_t^{t+\Delta t} \int_A [-k_v \nabla T_v \cdot \mathbf{e}_x + k_w \nabla T_w \cdot \mathbf{e}_x] da dr \quad (4.40)$$

where $\mathbf{e}_x = (1, 0)$. Dividing by Δt and passing to the limit:

$$\lim_{\Delta t \rightarrow 0} \rho \mathcal{L} \frac{x(t + \Delta t) - x(t)}{\Delta t} = \lim_{\Delta t \rightarrow 0} \frac{1}{\Delta t} \int_t^{t+\Delta t} [-k_v \nabla T_v \cdot \mathbf{e}_x + k_w \nabla T_w \cdot \mathbf{e}_x] dr \quad (4.41)$$

The velocity of the interface, the so-called Stefan condition, is then obtained:

$$\rho \mathcal{L} \frac{dx}{dt} = (-k_v \nabla T_v + k_w \nabla T_w) \cdot \mathbf{e}_x \quad (4.42)$$

The mass flux leaving the interface can then be evaluated from the conductive heat flux as

$$\dot{m} = \frac{-k \nabla T}{\mathcal{L}} \quad (4.43)$$

4.3 Convection-diffusion-reaction for cooling

The classical convection-diffusion-reaction equation involving the energy absorbed by vaporization is given by:

$$\rho c_p (\partial_t T + (\mathbf{u} \cdot \nabla) T) = \nabla \cdot (k \nabla T) - \rho_v [\mathcal{L} + (c_p^v - c_p^w)(T - T_{sat})] \frac{\varphi^- - \varphi^{--}}{\Delta t} \quad (4.44)$$

where φ^- and φ^{--} denote the phase-field solution respectively at the last and second to last time step.

By combining (4.41) with the system (4.26)-(4.29), multiphase flow and interface capturing with phase change and heat transfer is governed by the following system of equations:

$$\partial_t \varphi + (\mathbf{u} \cdot \nabla) \varphi + \frac{\dot{m} \delta(\varphi, \omega)}{\varrho_l + \varrho_v} \cdot \left(\frac{\varrho_l}{\varrho_v} - \frac{\varrho_v}{\varrho_l} \right) \varphi - \dot{m} \delta(\varphi, \omega) \cdot \left(\frac{1}{\varrho_l} + \frac{1}{\varrho_v} \right) = 0, \quad (4.45)$$

$$\omega + \varepsilon^2 \Delta \varphi - \varphi(\varphi^2 - 1) = 0, \quad (4.46)$$

$$\begin{aligned} & \varrho(\varphi) \partial_t (\mathbf{u}) + (\varrho(\varphi) \mathbf{u} \cdot \nabla) \mathbf{u} + (\mathbf{J} \cdot \nabla) \mathbf{u} \\ & + \frac{\dot{m} \delta(\varphi, \omega)}{2} \left(\frac{\varrho_l}{\varrho_v} - \frac{\varrho_v}{\varrho_l} \right) \mathbf{u} - \nabla \cdot (2\eta(\varphi) \mathbf{D}(\mathbf{u})) + \nabla p = \frac{\sigma}{\varepsilon^2} \omega \nabla \varphi + \varrho(\varphi) \mathbf{g}, \end{aligned} \quad (4.47)$$

$$\nabla \cdot \mathbf{u} = \frac{\dot{m} \delta(\varphi, \omega)}{\varrho_l + \varrho_v} \cdot \left(\frac{\varrho_l}{\varrho_v} - \frac{\varrho_v}{\varrho_l} \right), \quad (4.48)$$

$$\begin{aligned} & \rho c_p(\varphi) (\partial_t T + (\mathbf{u} \cdot \nabla) T) = \nabla \cdot (k \nabla T) \\ & - \rho_v [\mathcal{L} + (c_p^v - c_p^w)(T - T_{sat})] \frac{\varphi^- - \varphi^{--}}{\Delta t}. \end{aligned} \quad (4.49)$$

with the following initial and boundary conditions:

$$\varphi(\cdot, 0) = \varphi_0, \quad \mathbf{u}(\cdot, 0) = \mathbf{u}_0, \quad T(\cdot, 0) = T_0 \quad \text{in } \Omega, \quad (4.50)$$

$$\frac{\partial \varphi}{\partial \mathbf{n}} = \frac{\partial \omega}{\partial \mathbf{n}} = 0, \quad \mathbf{u} \cdot \mathbf{n} = 0, \quad T = T_w \quad \text{on } \partial \Omega \times (0, t_f], \quad t_f > 0. \quad (4.51)$$

Equations (4.45)-(4.48) are numerically solved by the numerical approach described in Chapters 1 and 2. The convection-diffusion-reaction equation (4.49) solves the temperature T by a stabilized finite element approach similar to that introduced in Chapter 2. A fractional step approach is proposed to solve the system (4.45)-(4.51)

4.4 Numerical simulation

In this section, the abilities of the present Navier–Stokes–Cahn–Hilliard model extended by the phase change model and heat transfer are tested.

4.4.1 Stefan problem

One considers, first, the one-dimensional Stefan benchmark. It is a well-known problem and serves as a benchmark to assess the accuracy of phase change models [13–15]. Figure 4.3 defines schematically the classical Stefan problem.

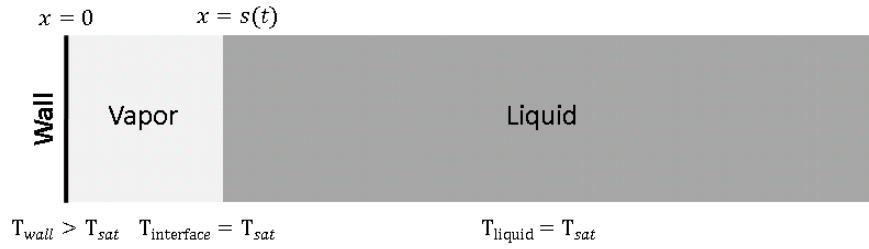


Figure 4.3: Initial setup of the Stefan problem

The domain is initially filled with water. The temperature at the wall is set constant and higher than the saturation temperature. The water is at saturation temperature. The position of the interface is given by

$$s(t) = 2\chi\sqrt{\alpha_v t} \quad (4.52)$$

where α_v is the thermal diffusivity defined by $\alpha_v = k_v/(\rho_v c_p^v)$ and χ is solution of the transcendental equation:

$$\frac{T_{sat} - T_{wall}}{\sqrt{\pi}L} c_p^v = \chi \operatorname{erf}(\chi) \exp(\chi^2) \quad (4.53)$$

derived in the case of a constant temperature in the liquid. The temperature in the vapor at a given time t is given by

$$T(x, t) = T_{wall} + \frac{T_{sat} - T_{wall}}{\operatorname{erf}(\chi)} \operatorname{erf}\left(\frac{x}{2\sqrt{\alpha_v t}}\right) \quad (4.54)$$

One considers the physical properties for the water and the vapor given in Table 4.1 and we consider $T_{wall} - T_{water} = 10^\circ C$.

| | $\rho [kg \cdot m^{-3}]$ | $\eta [Pa \cdot s]$ | $c_p [J \cdot kg^{-1} \cdot K^{-1}]$ | $k [W \cdot m^{-1} \cdot K^{-1}]$ | $L_{sat} [J \cdot kg^{-1}]$ |
|-------|--------------------------|----------------------|--------------------------------------|-----------------------------------|-----------------------------|
| Vapor | $5.97 \cdot 10^{-1}$ | $1.26 \cdot 10^{-5}$ | 2030 | $2.5 \cdot 10^{-2}$ | |
| Water | 958.4 | $2.8 \cdot 10^{-4}$ | 4216 | $6.79 \cdot 10^{-1}$ | $2.26 \cdot 10^6$ |

Table 4.1: Physical properties for the vapor and the water

At $t > 0$, a phase change occurs and induces a motion of the interface between the vapor and the water. The convective term in the energy conservation equation is neglected in both phases. Figure 4.4 shows the evolution of the interface for both the analytical and the numerical solution according having good agreement.

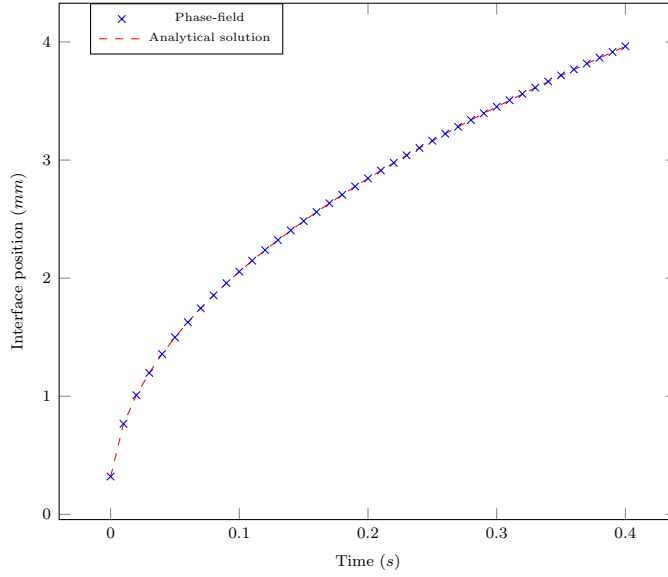


Figure 4.4: Evolution of the interface position for the Stefan problem

4.4.2 Boiling case

One considers an immersed solid inside a water/vapor environment as presented in Figure 4.5. A vapor film is assumed to exist and surround the solid at the initialization. The thickness of this vapor film from the solid surface is initially fixed at ε_{vap} . The solid, vapor and water temperatures are respectively supposed initialized at $T_s = 985^\circ C$, $T_v = 100^\circ C$ and $T_w = 20^\circ C$. There is a slip condition at the domain boundary : $\mathbf{u} \cdot \mathbf{n} = 0$, where \mathbf{n} is the normal to the boundary.

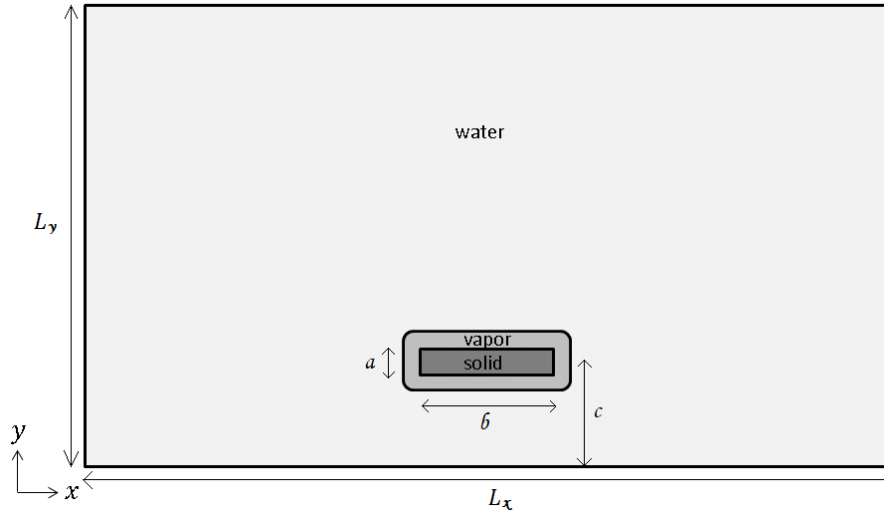


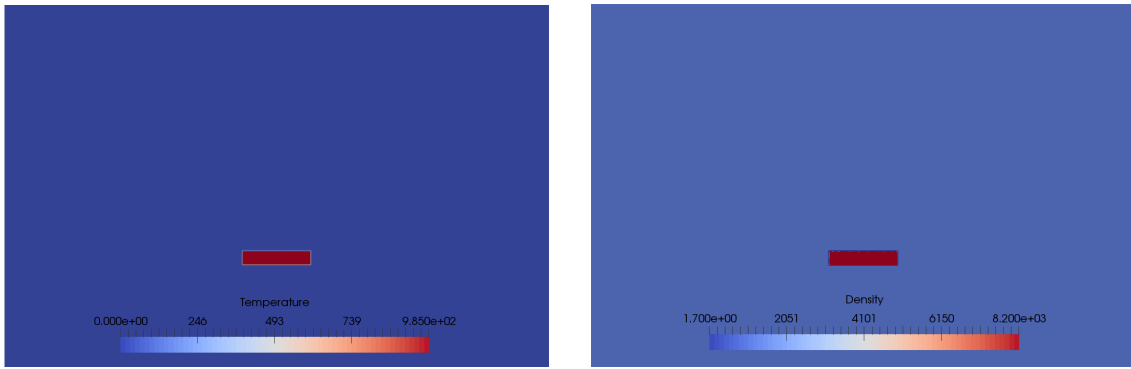
Figure 4.5: Solid immersed in a water/vapor environment

In this study case, the solid heat will cause boiling and then create vapor bubbles from the phase change of the water near the solid. These bubbles, for which the density is less than that of water, will go back up to the surface. The solid is cooling over time because of the lower temperature of the environment where it is immersed. The surface tension forces are taken into account at the water/vapor interface: the surface tension coefficient is set at $\sigma = 6 \cdot 10^{-2}$. All the parameters related to the study case are depicted in the following Table 4.2:

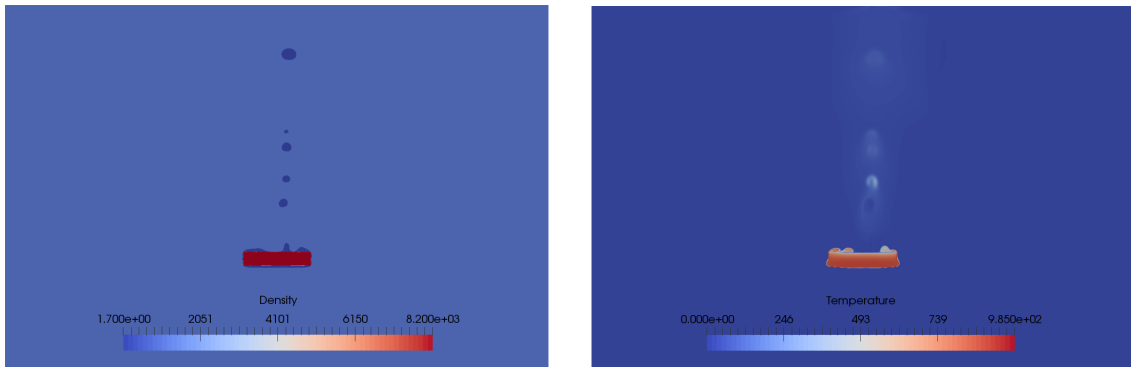
| | | | |
|----------|----------------------|---------------------|----------------------|
| ρ_w | 1000 | Δt | 10^{-3} |
| η_w | $5 \cdot 10^{-3}$ | M | 10^{-6} |
| ρ_v | 1.7 | ε | $2 \cdot 10^{-3}$ |
| η_v | $9.99 \cdot 10^{-4}$ | \mathcal{L} | $2.26 \cdot 10^6$ |
| ρ_s | 8200 | T_{sat} | 100 |
| η_s | 10^{-3} | $Nb_{elements}$ | 20,000 |
| t_f | 23 | h_{min} | $2.5 \cdot 10^{-4}$ |
| L_x | $6 \cdot 10^{-1}$ | L_y | $4 \cdot 10^{-1}$ |
| a | $1.5 \cdot 10^{-2}$ | b | $7.5 \cdot 10^{-2}$ |
| c | $1.2 \cdot 10^{-1}$ | ε_{vap} | $1.25 \cdot 10^{-3}$ |

Table 4.2: Parameters of the boiling case

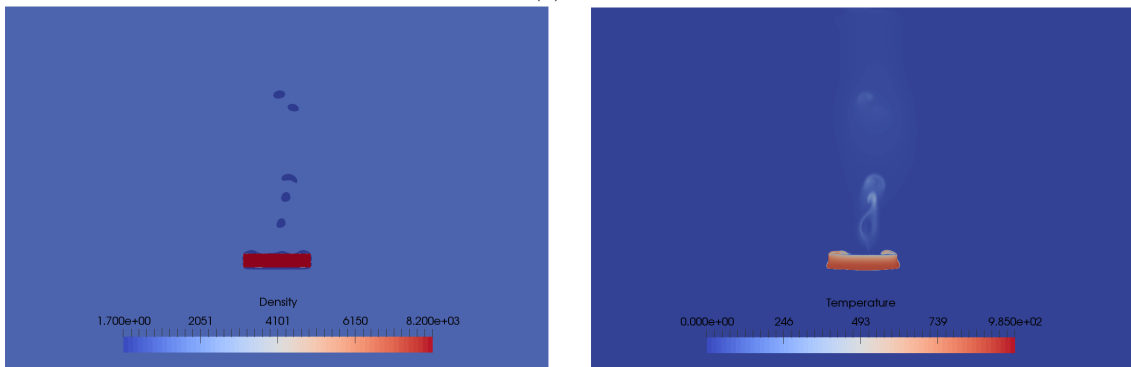
Figure 4.6 shows the dynamics (left) and temperature (right) evolution of the multiphase flow during the quenching simulation time.



(a) $t=0$



(b) $t=5$



(c) $t=10$

Figure 4.6: Dynamics (left) and temperature (right) evolution during the quenching duration

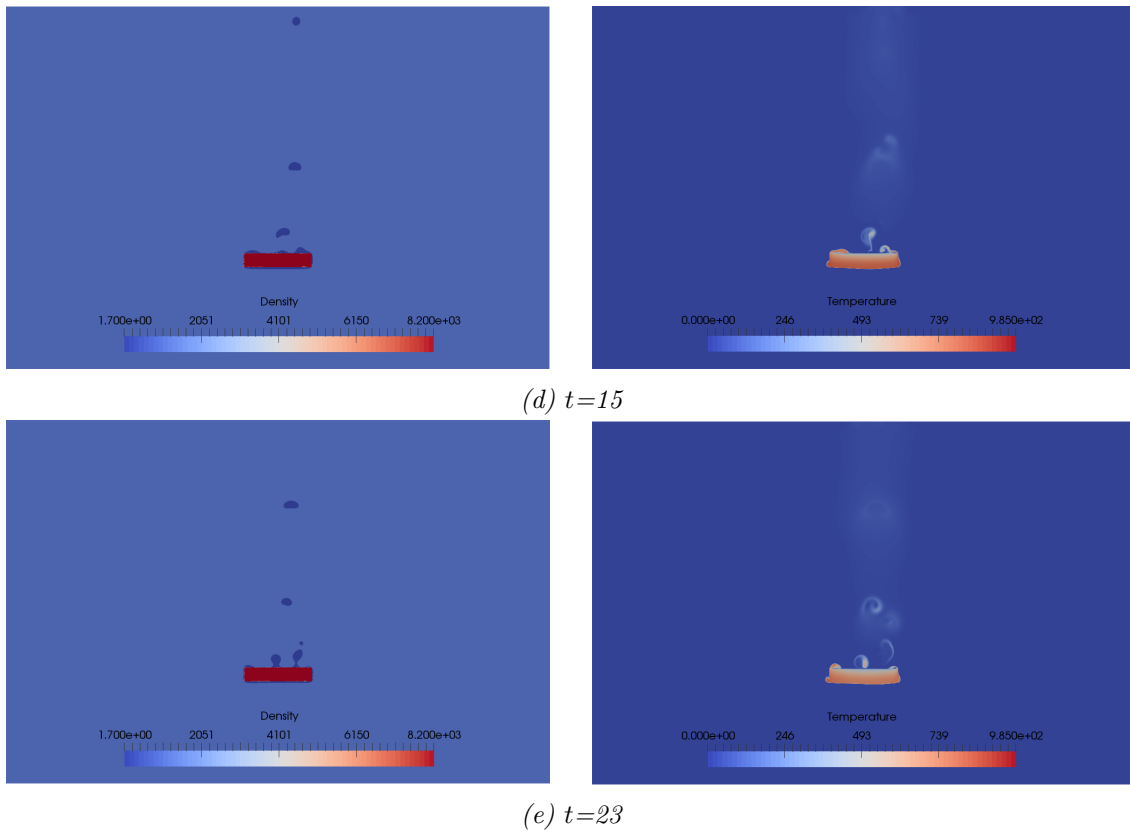


Figure 4.6: Dynamics (left) and temperature (right) evolution during the quenching duration (contin.)

The simulation has been performed in parallel with 4 cores and it took approximately 22 hours to be completed. In Figure 4.7, the temperature evolution at the solid center, the right side, and the left side is plotted.

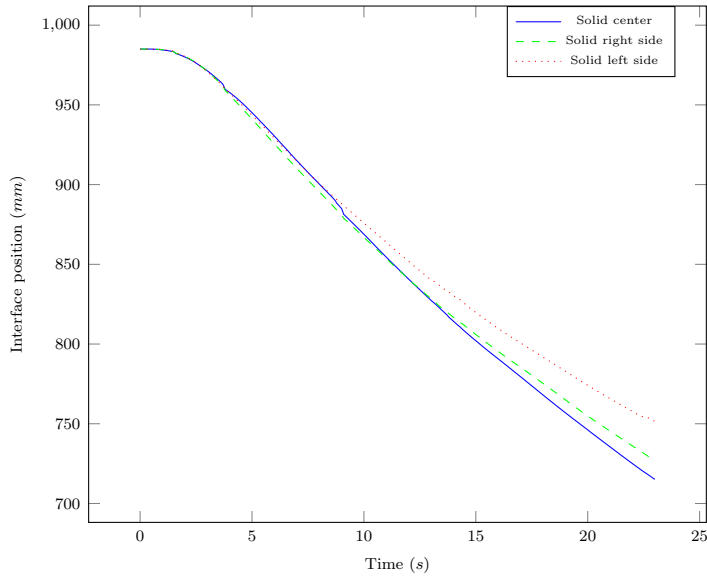


Figure 4.7: Evolution of the temperature at different region of the solid

The quantitative results show a solid cooling over the quenching simulation. The temperature in the solid center decreases from 985°C to 715°C in 23s. The temperature on the right side of the solid reaches 720°C and on the left side, it reaches almost 750°C . After 9s of quenching, the cooling of the solid left side is less quick than the solid center and right side. This can be explained by the region from which the bubbles start to rise. Indeed, by observing the dynamics of the multiphase flow in Figure 4.7, characterized by the density (left), the bubbles leave the solid region essentially from the middle and a bit less from the right side. Physically, when a bubble breaks away from the vapor film surrounding the solid, it gives way to the cooler water which comes into physical contact with the solid for a short time. This phenomenon provokes a quicker cooling of the solid region from where the bubble has split up.

4.5 Industrial applications

This section is an openness to industrial applications. The developments realized all over the present thesis will be applied to simulate 3D boiling and phase change of a quenching process. To do so, several test cases will be presented: first, a solid inside a quench water tank, second, two identical solids to the first case are quenched one below the other, and finally a quenching of a solid with a larger and more complex geometry. Due to confidentiality, these test cases presented here are like those encountered in the industry. As well, to keep a closer aspect to a real industrial quenching, physical properties similar to real cases are considered. The different simulations presented here are a proof of concept of the abilities of the solvers described within the present work. The aim is to have a glimpse of a more realistic industrial quenching for which cooling is observed. However, because of the assumptions established, like the non-evolution of the thermo-physical parameters, and not taking into account some phenomena involved in quenching, such as solid-phase transformation, wetting and contact angle, radiation, etc... no comparison with experimental data will be done.

In the next simulations, the solid is initially immersed in the water tank and surrounded by a thin vapor film. The density of the solid, vapor, and water is respectively denoted by ρ_s , ρ_v , and ρ_w [$\text{kg}\cdot\text{m}^{-3}$]. Idem, the viscosity of the solid, vapor, and water is respectively denoted by η_s , η_v , and η_w [$\text{Pa}\cdot\text{s}$]. The temperatures of the solid, vapor, and water are respectively initialized at T_s , T_v , and T_w [$^{\circ}\text{C}$]. The specific heat of the solid, vapor, and water is given by c_p^s , c_p^v , and c_p^w [$\text{J}\cdot\text{kg}^{-1}\cdot\text{K}^{-1}$]. The thermal conductivity of the solid, vapor, and water is given by k_s , k_v , and k_w [$\text{W}\cdot\text{m}^{-1}\cdot\text{K}^{-1}$]. The latent heat is denoted by \mathcal{L} [$\text{J}\cdot\text{kg}^{-1}$]. T_{sat} is the saturation temperature [$^{\circ}\text{C}$]. During boiling, the fluid flow takes into account the capillary action at the interface separating the water and vapor, with a surface tension coefficient σ [$\text{J}\cdot\text{m}^{-2}$]. The mobility M involved in the Cahn–Hilliard equations is a non-null constant. The time step of the simulations is given by Δt [s]. These parameters are fixed for all the next simulations with values given by Table 4.3.

| | | | |
|---------------|---------------------|------------|----------------------|
| ρ_w | 1000 | η_w | $5 \cdot 10^{-3}$ |
| ρ_v | 1.7 | η_v | $9.99 \cdot 10^{-4}$ |
| ρ_s | 8200 | η_s | 10^{-3} |
| c_p^s | 435 | c_p^v | 2010 |
| c_p^w | 4185 | k_s | 11.4 |
| k^v | $6 \cdot 10^{-1}$ | k_w | $2.5 \cdot 10^{-2}$ |
| T_s | 985 | T_v | 100 |
| T_w | 20 | T_{sat} | 100 |
| \mathcal{L} | $2.26 \cdot 10^6$ | M | 10^{-6} |
| σ | $7.3 \cdot 10^{-1}$ | Δt | $2.5 \cdot 10^{-3}$ |

Table 4.3: Fixed parameters of the 3D quenching test cases

4.5.1 3D quenching of a solid

This test case is about the quenching, within a water tank, of a solid with the shape of stacking of cylinders of different sizes as shown in Figure 4.8.

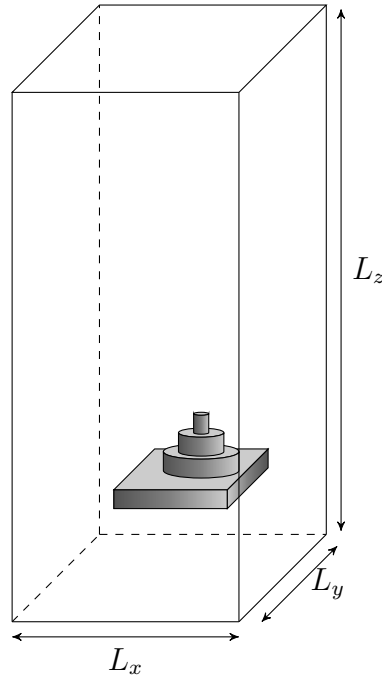


Figure 4.8: Quenching of a piece

The domain is a rectangular pave of dimension $[0, L_x] \times [0, L_y] \times [0, L_z] = [0, 1] \times [0, 1] \times [0, 2]$. The vapor film has an initial thickness $\varepsilon_{vap} = 5 \cdot 10^{-3}$ m from the solid surface. The interface separating the water and vapor has a thickness $\varepsilon = 6 \cdot 10^{-3}$ m.

The duration of the quenching is $t_f=7\text{s}$. The simulation has been performed on 32 cores with a visualization file created every 5-time increments. During the mesh adaptation, which happens every time step, the admissible minimum mesh size is $h_{min} = 10^{-4}\text{m}$. Figure 4.9 shows the temperature evolution at the solid surface, the dynamics of the interface separating water and vapor, and the evolution of the adapted mesh. The computations took 124h 41min to simulate this test case.

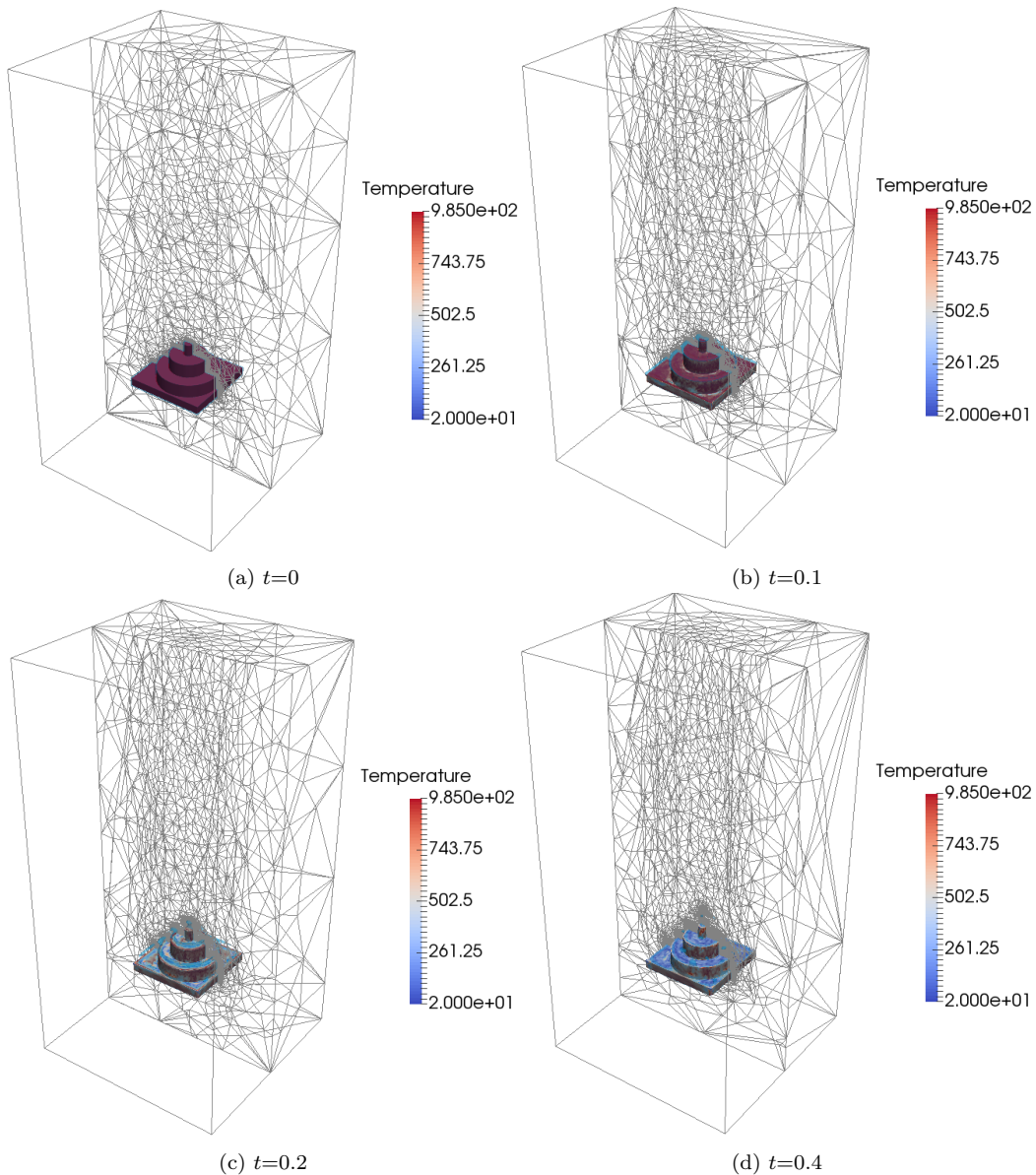


Figure 4.9: Dynamics, mesh, and temperature evolution during the quenching of a solid

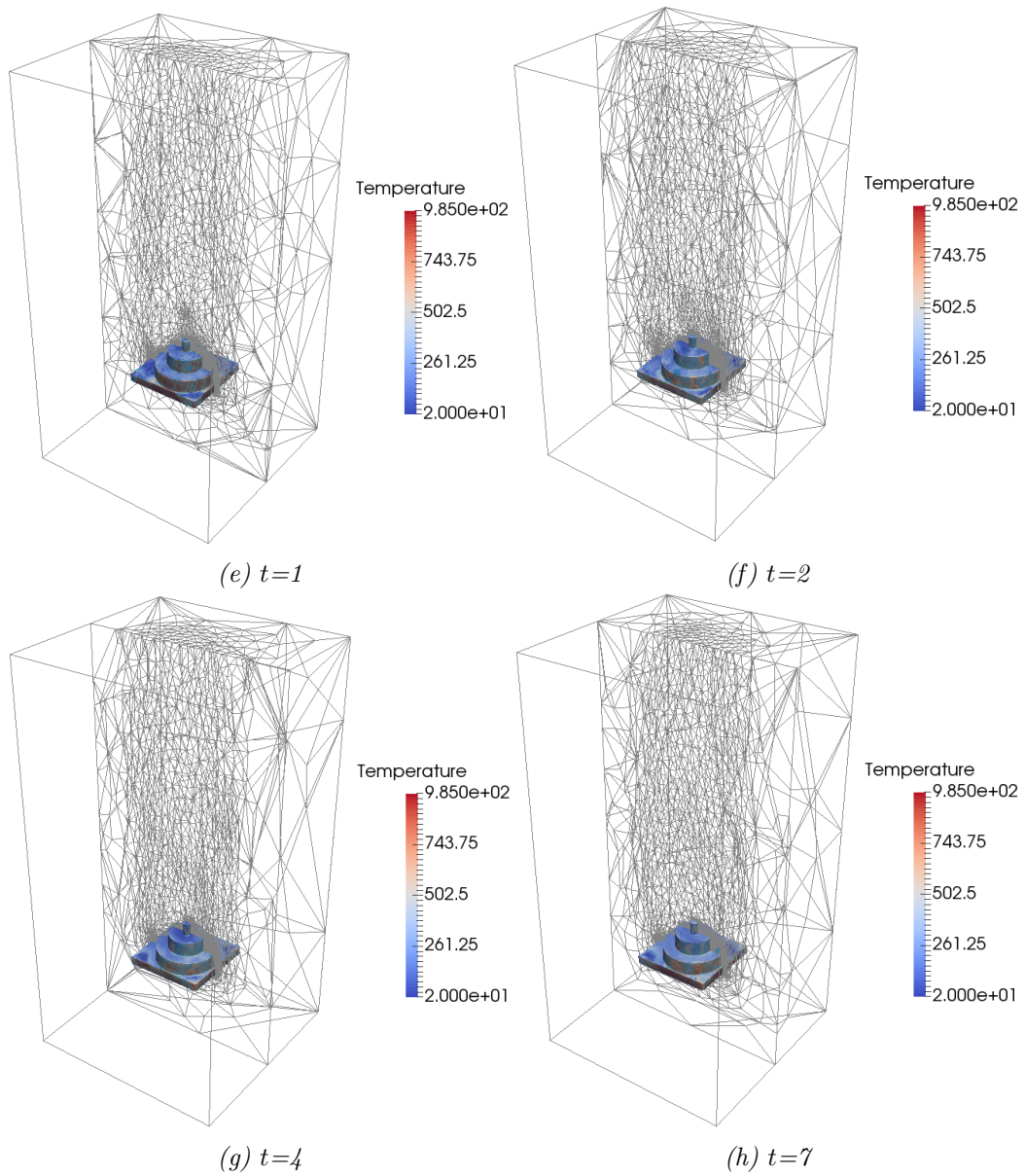


Figure 4.9: Dynamics, mesh, and temperature evolution during the quenching of a solid (contin.)

As expected, the solid is cooling over time. Some regions of the solid surface are close to the temperature of water T_w after a few seconds. However, it seems there are zones at the solid surface for which the temperature is still very hot and close to the initial temperature of the solid T_s . By focusing only on the solid, Figure 4.10 gives a clearer view of the temperature above and below the solid surface.

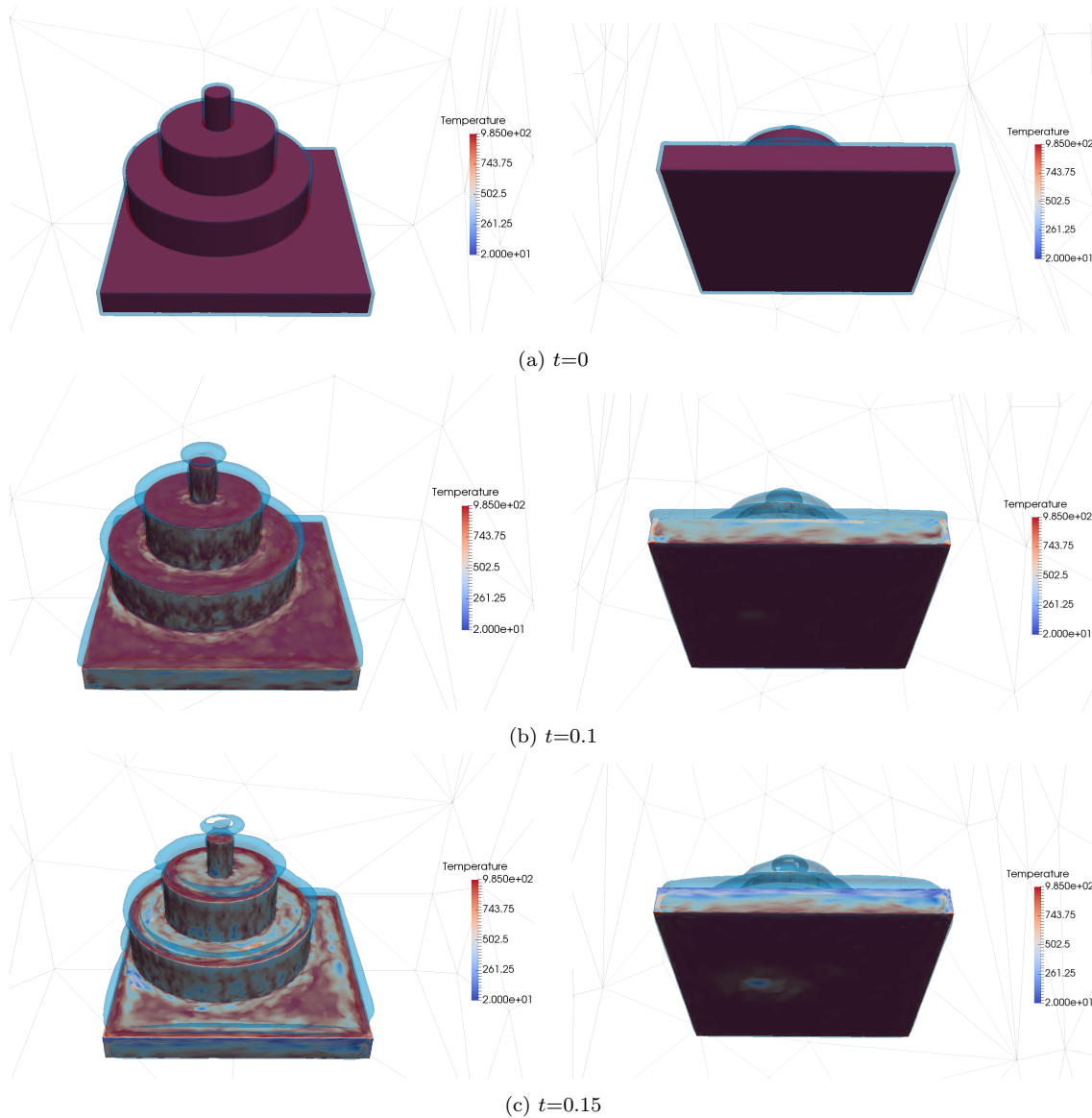


Figure 4.10: Evolution of the temperature at the solid interface and the dynamics of the interface separating water and vapor with a view from above (left) and below (right) at different time of the quenching of a solid

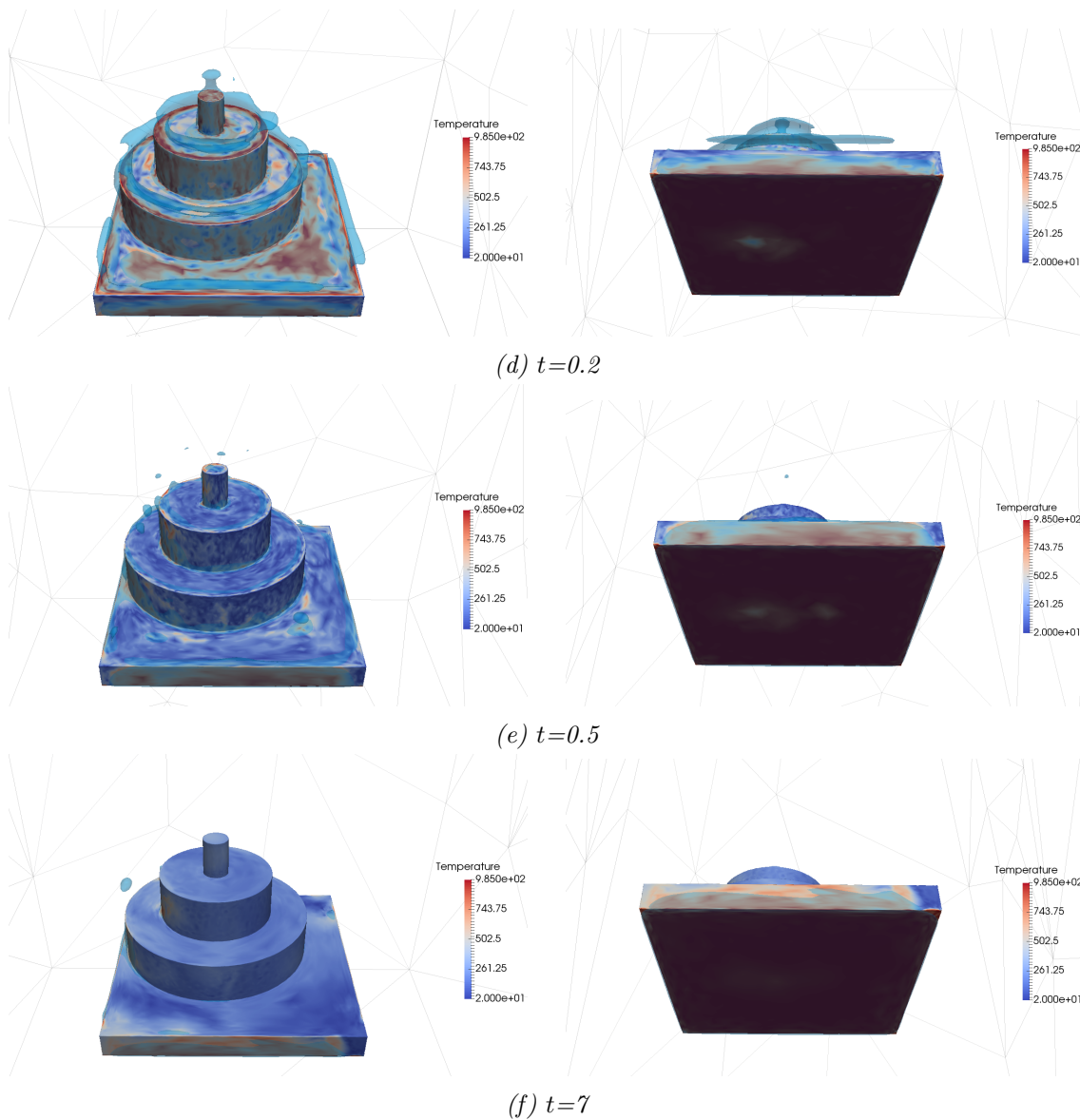


Figure 4.10: Evolution of the temperature at the solid interface and the dynamics of the interface separating water and vapor with a view from above (left) and below (right) at different time of the quenching of a solid (cont.)

From the visualizations, one observes that the above surface of the solid is cooled quicker than the below part. This can be explained by the film of vapor which is maintained below the solid and cannot escape. As remarked in the preceding paragraph, there are indeed zones, except below the solid, which are cooled quicker than others. In the more cooled regions of the solid surface, the film broke and

disappeared. This means that water can come into contact with the solid and cool it effectively. In the warmest zones, the vapor film still exists and covers them. Thus, the water doesn't come into contact with these regions of the solid surface which cool slower.

4.5.2 3D quenching of two identical solids

The present test case is similar to the previous one. The considered domain and solid are the same. In addition, there is an identical solid above the previous one from a distance $D=1\text{m}$ as represented in Figure 4.11.

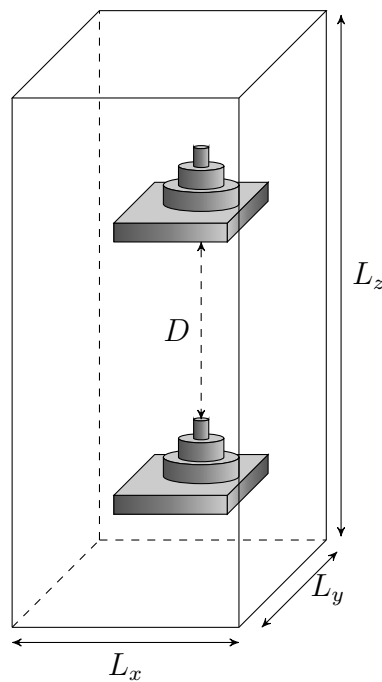


Figure 4.11: Quenching of 2 pieces

A simulation of this test case has been done for quenching with a duration $t_f=1.8\text{s}$. The rest parameters are the same as the previous case 4.5.1. In Figure 4.12, the evolution of the temperature at the solid surface, the dynamics of the interface separating water and vapor, and the adapted mesh, are represented at different instants. The simulation has been performed on 32 cores and took 145h 01min to be completed. A visualization file is created every 20-time increments.

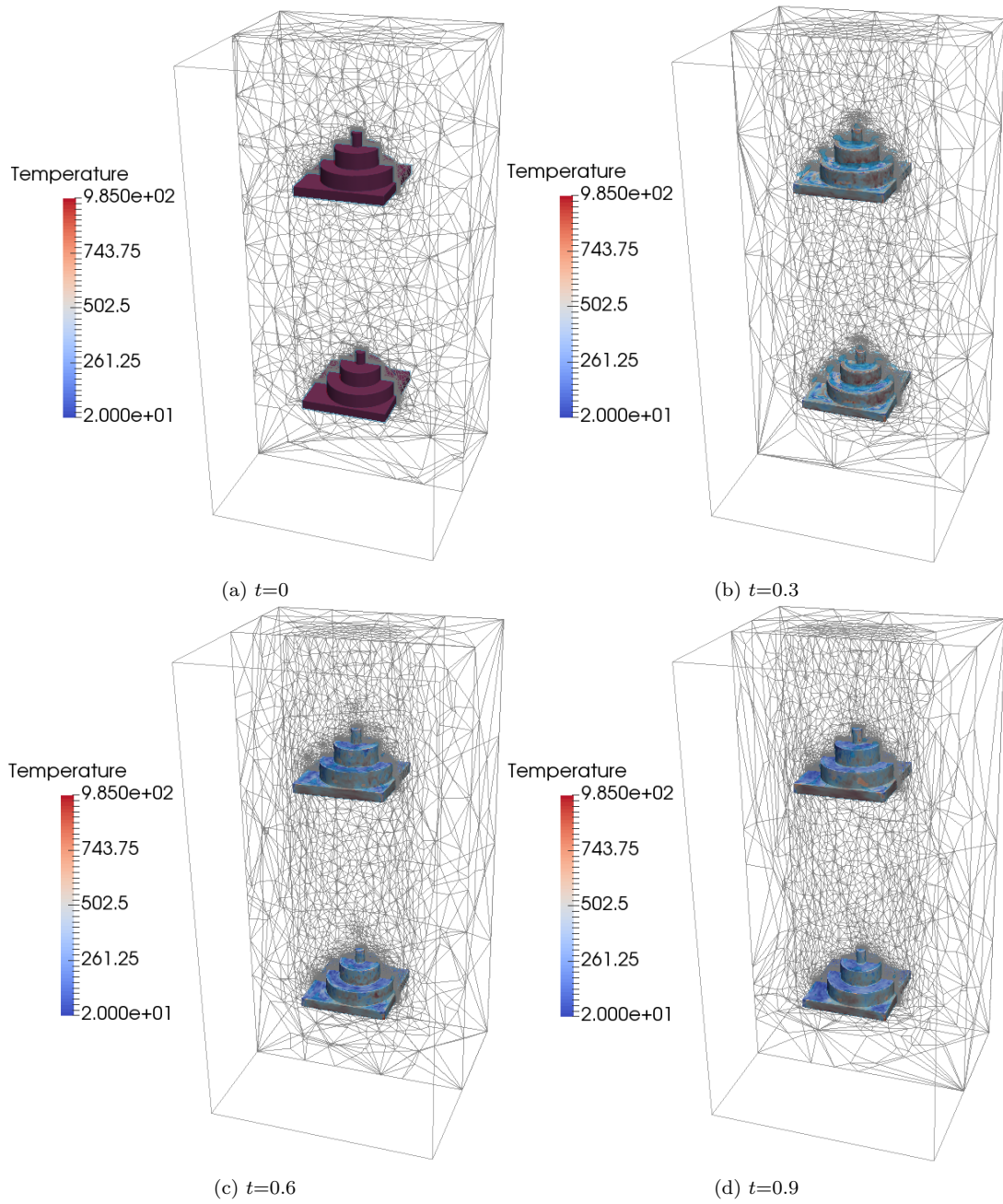


Figure 4.12: Dynamics, mesh, and temperature evolution during the quenching of two identical solids

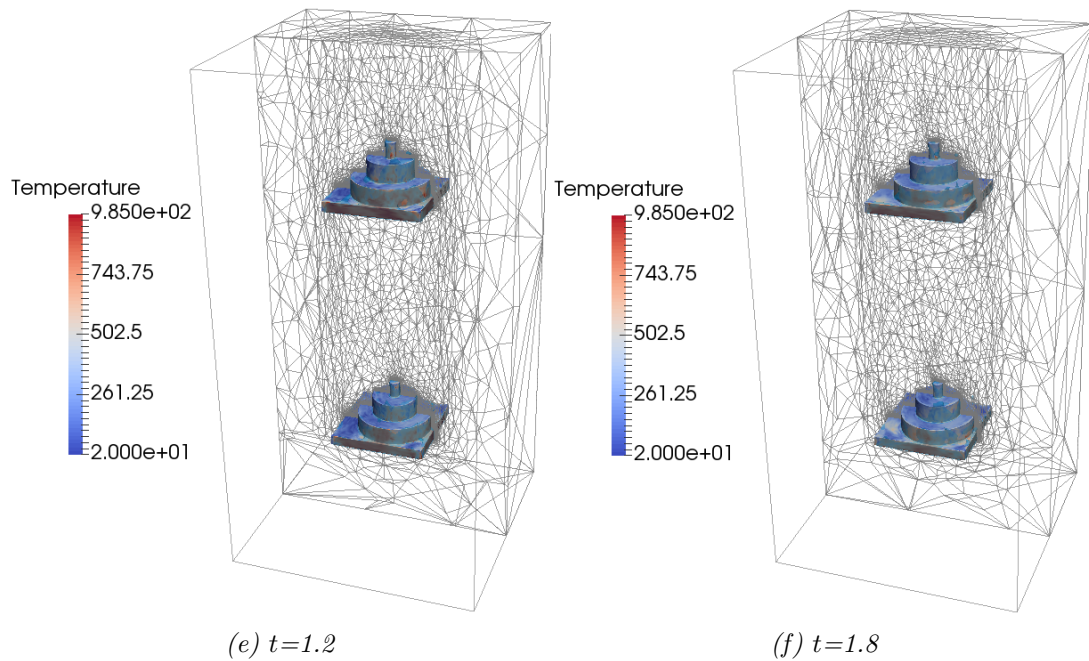


Figure 4.12: Dynamics, mesh, and temperature evolution during the quenching of two identical solids (contin.)

Similar behavior to the previous case is observed in this one. Both solids are cooling over time. As seen previously, there exist regions of the surface of the solids that are cooler than others. The adapted mesh is well refined in the interest zones, which means in the solids neighborhood. It is within this region that the main phenomena happen: boiling, rising bubble, fluid flow, phase change, and heat transfer,... Both solids seem not to be affected by each other. A view from above and below this both solid is shown in Figure 4.13 to have an accurate visualization of these pieces.

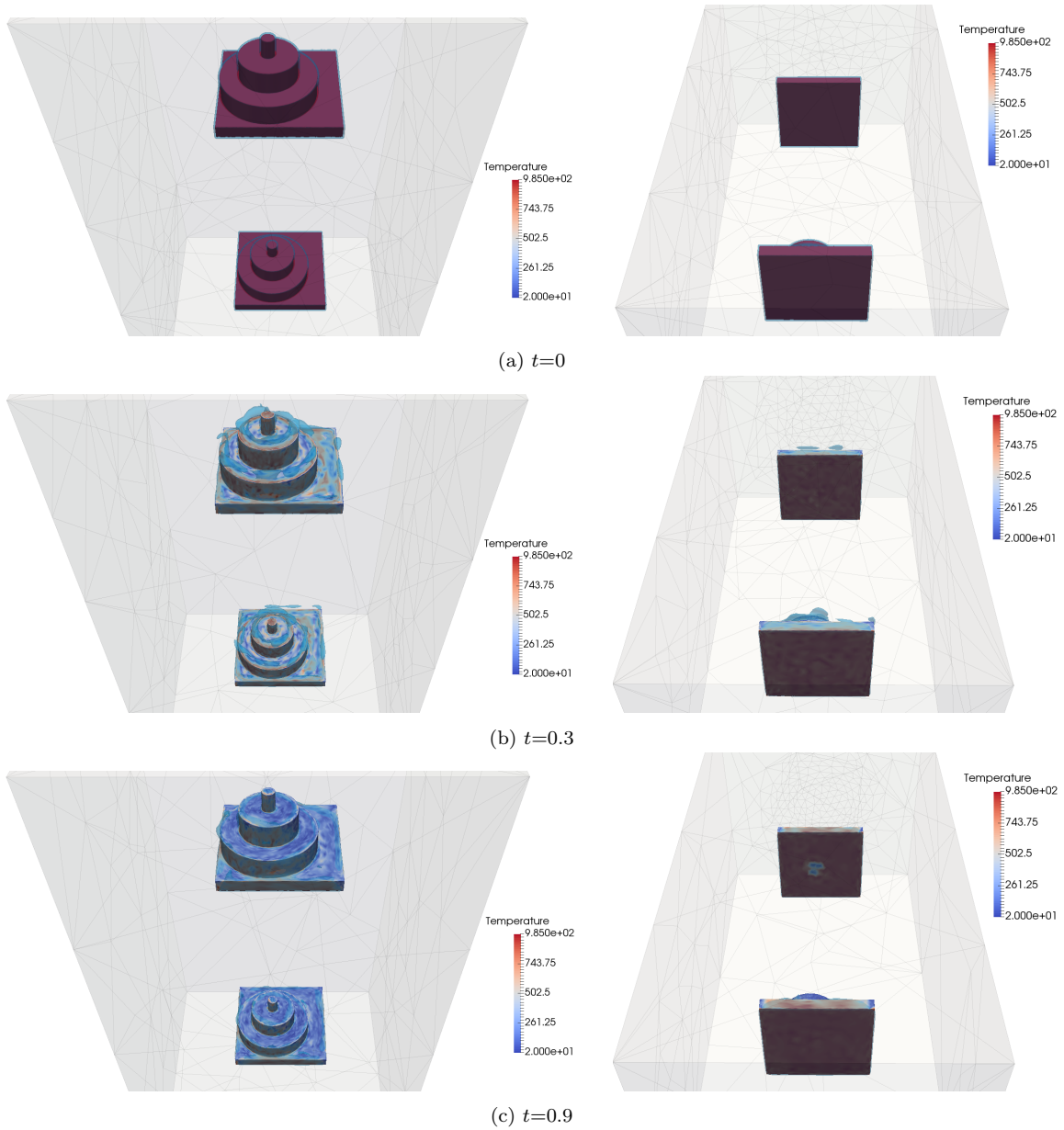


Figure 4.13: Evolution of the temperature at the solid interface and the dynamics of the interface separating water and vapor with a view from above (left) and below (right) at different time of the quenching of two identical solids

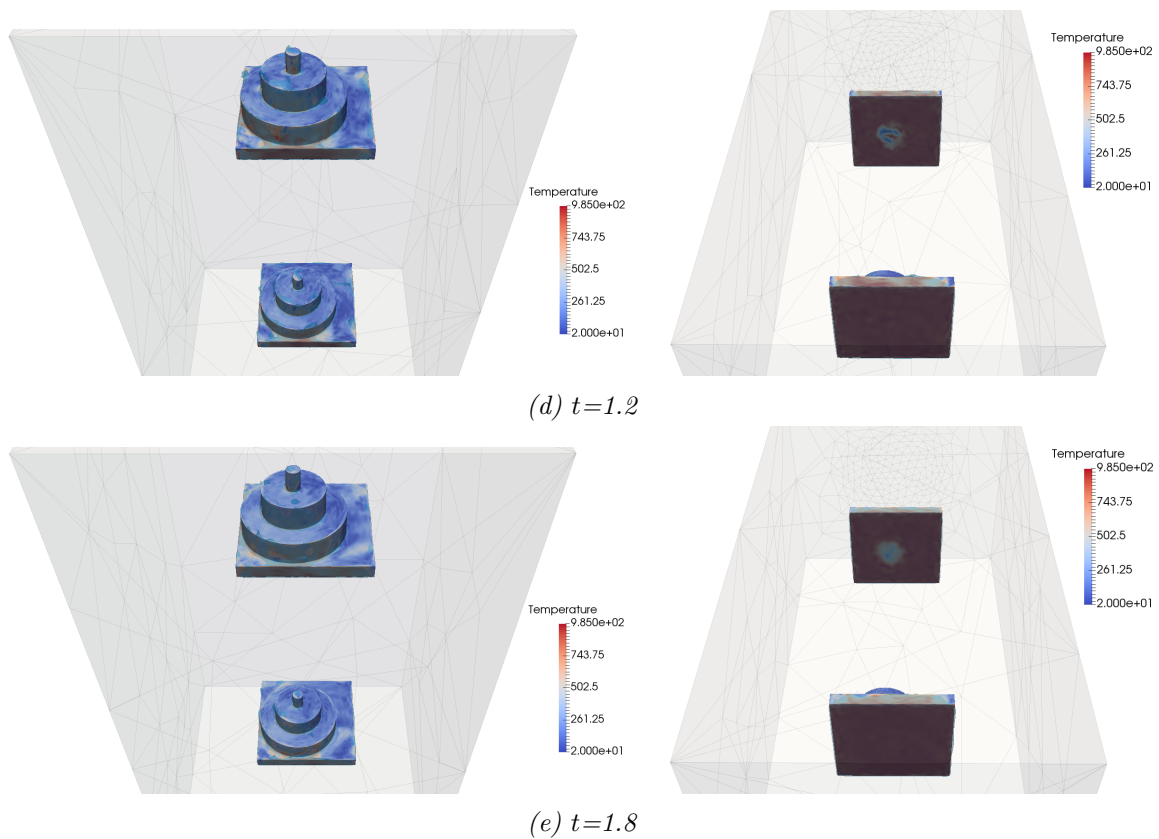


Figure 4.13: Evolution of the temperature at the solid interface and the dynamics of the interface separating water and vapor with a view from above (left) and below (right) at different time of the quenching of two identical solids (cont.)

By observing the visualizations of Figure 4.13, one can see a close behavior between the pieces' neighborhoods. The cooling and the boiling dynamics are similar even with 1m separating both solids. The vapor film moves from the bottom to the top. With the view from below, an interesting difference between the pieces appears and becomes clearer over quenching. Indeed, the solid at the bottom is in the same configuration as the case 4.5.2, whereas the solid at the top shows, in its below surface, a zone cooler than the rest of this surface. This zone is quickly created after $t=0.2s$ and located on the same vertical axis as the top of the below solid. This means that, within the same quenching bath, the quenching of a solid affects that of another one above it. This can be explained by the fact that the boiling of the below piece gives a vertical flow dynamics that weakens a zone of the vapor film stuck underneath the above solid. This zone corresponds to the closest zone from the below solid.

4.5.3 3D quenching of a large solid with a complex geometry

This final test case consists in quenching a solid larger than the previous ones and with more complex geometry. This solid is immersed in a domain of water with a rectangular pave shape of dimension $[0, L_x] \times [0, L_y] \times [0, L_z] = [0, 5] \times [0, 2] \times [0, 2.5]$. Figure 4.14 illustrates the initial configuration of the case.

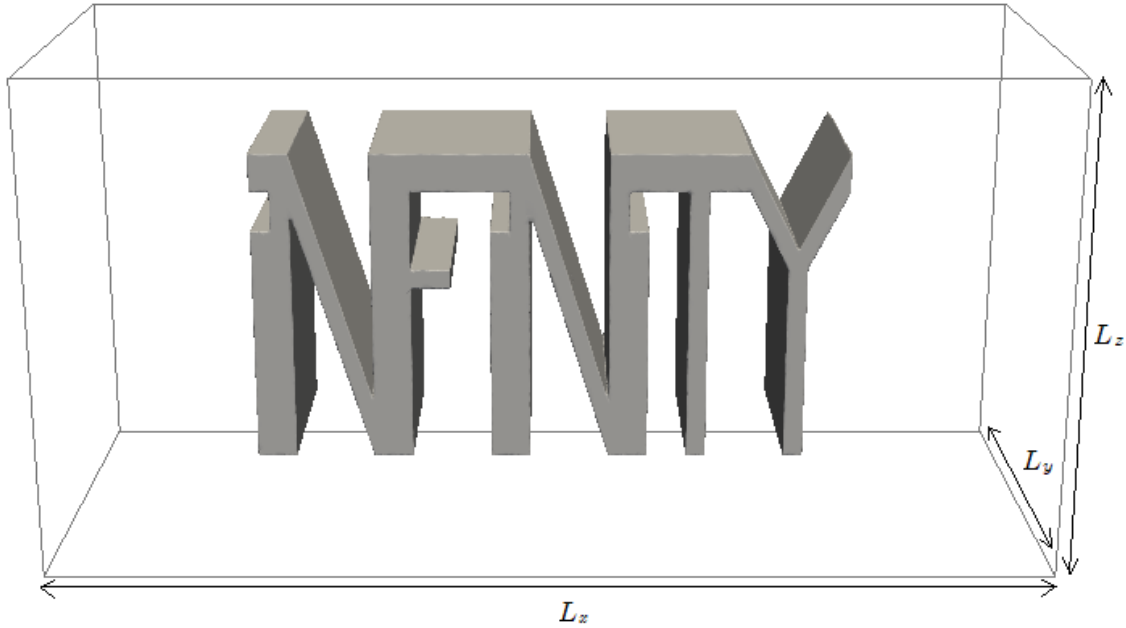
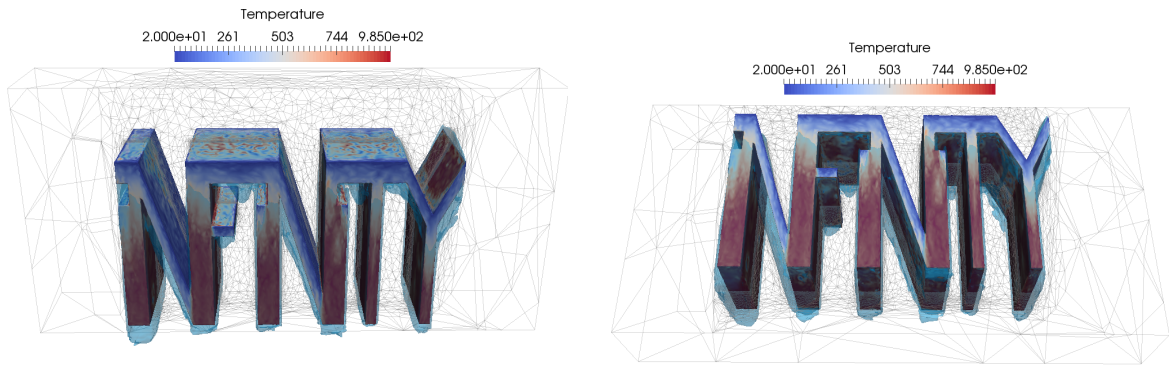


Figure 4.14: Quenching of a large solid with a complex geometry

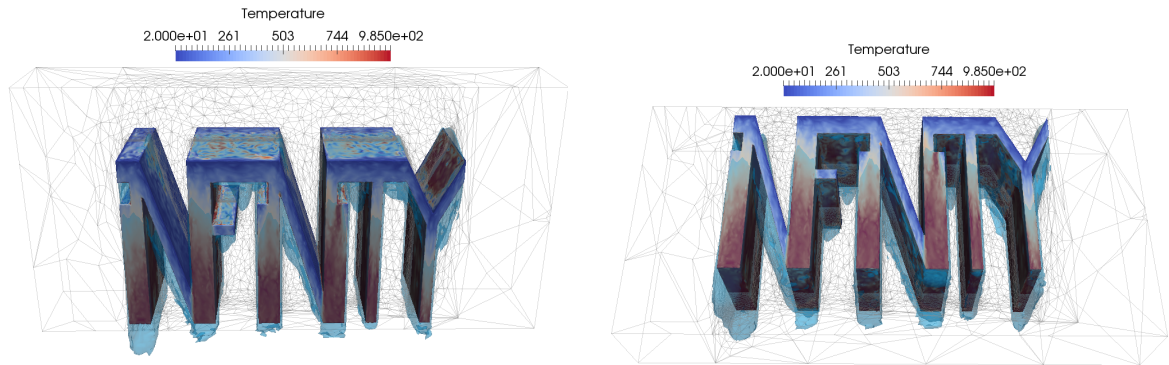
Pieces with complex geometries are common in industrial quenching. This part aims to challenge the framework developed in the present work for this kind of case as a proof of concept. Like the previous cases, the vapor film is assumed to exist and surround the solid at the initialization. The initial thickness of this vapor film from the solid surface is fixed at $\varepsilon_{vap} = 2 \cdot 10^{-2}$ m. Water and vapor are separated by an interface of thickness $\varepsilon = 1.6 \cdot 10^{-2}$ m. A simulation of quenching of $t_f = 0.7$ s has been performed on 64 cores with a visualization file created every 5-time step. The minimum mesh size encountered in the adapted mesh is fixed at $h_{min} = 10^{-4}$ m. The rest of the parameters are fixed according to Table 4.3. The duration of this simulation is 76h 46min. Figure 4.15 shows the evolution of the quenching every 0.1s until the final time t_f .



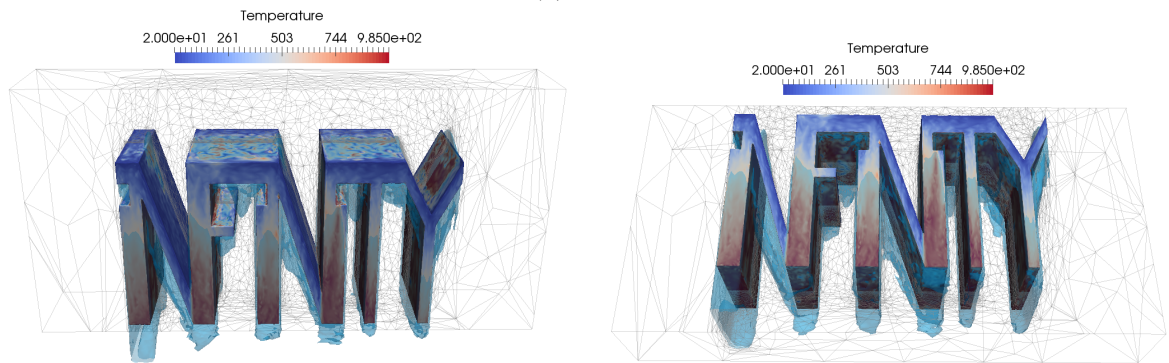
Figure 4.15: Evolution of the temperature at the solid interface and the dynamics of the interface separating water and vapor with a view from above (left) and below (right) at different time of the quenching of a complex geometrical solid



(d) $t=0.3$



(e) $t=0.4$



(f) $t=0.5$

Figure 4.15: Evolution of the temperature at the solid interface and the dynamics of the interface separating water and vapor with a view from above (left) and below (right) at different time of the quenching of a complex geometrical solid (cont.)

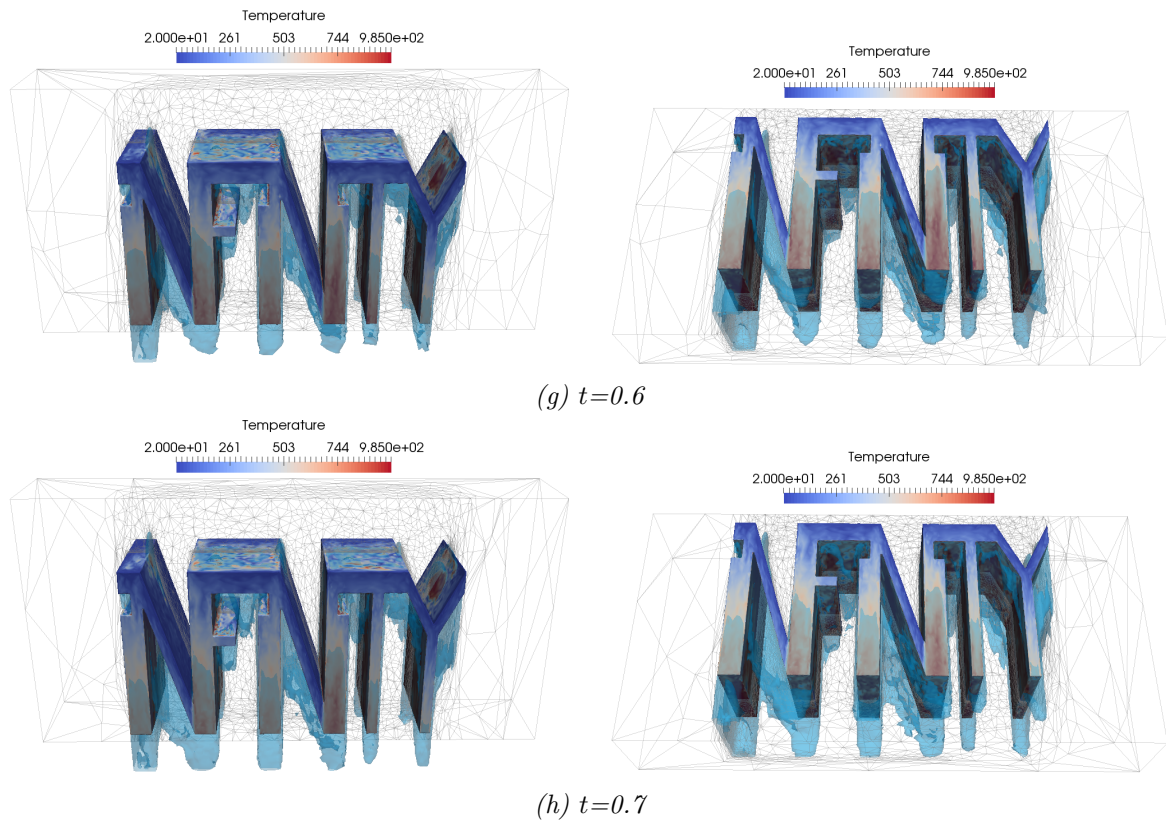


Figure 4.15: Evolution of the temperature at the solid interface and the dynamics of the interface separating water and vapor with a view from above (left) and below (right) at different time of the quenching of a complex geometrical solid (cont.)

In Figure 4.15, the cooling, as well as the vapor film disappearance, are visible a few times and progress from the top of the solid to the bottom. The hotter regions of the solid surface are still at the bottom. A particularity of this quenching, compared to the previous test cases, is the flow dynamics. Usually, the bubbles created during boiling rise towards the top of the domain. In the present case, the bubbles grew towards the bottom. This can be due to the particular geometry of the solid.

4.6 Conclusion

In the present chapter, the coupled model of phase-field and multiphase flow has been extended to a model that, in addition, takes into account the liquid-to-vapor phase change and heat transfer. The phase-field method has then been adopted for the liquid/vapor interface initially based on an existing level-set framework. The governing equations have been presented and numerical implementation of these equations has been done and tested on quenching cases. From 2D to 3D quenching of a complex geometrical solid, simulations have been performed to illustrate proof of concept about quenching simulations with phase-field. Some observations have been done from the different simulations. These observations are proof of concept and remain fairly qualitative.

Bibliography

- [1] F. Duval. *Modélisation du renoyage d'un lit de particules : contribution à l'estimation des propriétés de transport macroscopiques*. PhD thesis, Institut National Polytechnique de Toulouse, 2002. [130](#)
- [2] T. L. Bergman, A. S. Lavine, F.P. Incropera, and D. P. Dewitt. *Fundamentals of Heat and Mass Transfer*. John Wiley & Sons, 8th edition edition, 2017. [130](#)
- [3] M Khalloufi. *Multiphase flows with phase change and boiling in quenching process*. PhD thesis, Mines ParisTech - PSL Research University, 2017. [130](#)
- [4] H. W. Alt and I. Pawlow. A mathematical model of dynamics of non-isothermal phase separation. *Physica D: Nonlinear Phenomena*, 59(4):389–416, 1992. [131](#), [135](#)
- [5] J. W. Cahn and J. E. Hilliard. Free Energy of a Nonuniform System. I. Interfacial Free Energy. *Journal of Chemical Physics*, 28(2):258–267, 1958. [131](#)
- [6] M. I. M. Copetti and C. M. Elliott. Numerical analysis of the Cahn–Hilliard equation with a logarithmic free energy. *Numerische Mathematik*, 63(1):39–65, 1992.
- [7] A. Debussche and L. Dettori. On the Cahn–Hilliard equation with a logarithmic free energy. *Nonlinear Analysis: Theory, Methods & Applications*, 24(10):1491–1514, 1995. [131](#)
- [8] F. Boyer. *Ecoulements diphasiques de type Cahn–Hilliard*. PhD thesis, Bordeaux 1, 2001. [131](#)

- [9] F. De Anna, C. Liu, A. Schlömerkemper, and J.-E. Sulzbach. Temperature dependent extensions of the cahn-hilliard equation, 2021. [135](#)
- [10] M. E. Gurtin. Generalized Ginzburg–Landau and Cahn–Hilliard equations based on a microforce balance. *Physica D: Nonlinear Phenomena*, 92(3):178–192, 1996. [135](#)
- [11] A. Miranville and G. Schimperna. Nonisothermal phase separation based on a microforce balance. *Discrete and Continuous Dynamical Systems-series B*, 5(3):753–768, 08 2005. [135](#)
- [12] S.V. Patanka. *Numerical Heat Transfer And Fluid Flow*. Series In Computational And Physical Processes In Mechanics And Thermal Sciences. Taylor & Francis, 1980. [138](#)
- [13] S.W.J. Welch and J. Wilson. A volume of fluid based method for fluid flows with phase change. *Journal of Computational Physics*, 160(2):662 – 682, 2000. [142](#)
- [14] S. Hardt and F. Wondra. Evaporation model for interfacial flows based on a continuum-field representation of the source terms. *Journal of Computational Physics*, 227(11):5871 – 5895, 2008.
- [15] F. Gibou, L. Chen, D. Nguyen, and S. Banerjee. A level set based sharp interface method for the multiphase incompressible Navier—Stokes equations with phase change. *Journal of Computational Physics*, 222(2):536 – 555, 2007. [142](#)

Chapter 5

Conclusions and Perspectives

Contents

| | |
|-----------------------------------|------------|
| 5.1 Conclusion | 167 |
| 5.2 Perspectives | 167 |
| Bibliography | 168 |

Résumé en Français

Ce chapitre présente les conclusions générales de ces travaux de thèse, ainsi que les perspectives qui en découlent. La librairie élément fini CIMLIB-CFD préexistante, déjà munie de la méthode level-set, a été enrichie par une nouvelle méthode de capture d'interface : la méthode phase-field. Cette méthode permet de capturer l'interface séparant deux fluides en prenant en compte leur physique. Couplée à la dynamique des fluides et étendue à la thermique, diverses expériences numériques ont pu être réalisées pour valider les modèles étape par étape. À commencer par le modèle de Cahn–Hilliard pour la capture d'interface, puis le modèle de Cahn–Hilliard–Navier–Stokes incompressible pour la capture d'interface au sein d'un écoulement de deux fluides incompressibles, et enfin, ce dernier modèle a été étendu à la thermique pour prendre en compte les échanges de température et le changement de phase eau/vapeur. La simulation numérique en 3D d'une trempe industrielle a ainsi pu être réalisée comme preuve de concept, ce qui valide une première étape dans l'optique d'intégrer l'implémentation issue de ces travaux de thèse à l'outil numérique développé dans le cadre de la chaire INFINITY.

Toutefois, de nombreuses perspectives de recherche restent à explorer et exploiter afin de rendre robuste l'implémentation réalisée et favorable son intégration au logiciel. Parmi celles-ci se trouve l'importance de mettre en place une méthode permettant de borner le paramètre d'ordre de sorte à ce que le principe du maximum soit respecté pour les équations de Cahn–Hilliard. Ceci aidera à l'identification d'un schéma numérique stable même pour des simulations numériques en temps long. Il serait également intéressant de développer une nouvelle métrique pour l'adaptation de maillage qui soit spécifique à la méthode phase-field afin d'avoir une fine capture de l'interface avec un faible coût de calcul, en particulier pour les cas 3D. Afin d'avoir un modèle qui soit thermodynamiquement consistant, il serait pertinent de repartir des équations de la thermodynamique en considérant le cas non-isotherme de l'énergie libre et d'en obtenir les équations dérivées.

5.1 Conclusion

The work of the present thesis constitutes a first introduction of the phase-field method within the framework of the research group that, until today, had an interface capturing approach exclusively based on the level-set method. In the future, the aim is to make robust this new tool for realistic industrial applications. The phase-field model used here relies on the Cahn–Hilliard equations which have been presented and discretized within the CG1 finite element method to have a developed interface capturing solver. A review of theoretical results for the continuous and discrete equations has been done. Then, a series of numerical test cases have followed, including a verification of the solver by manufactured solutions. The framework has then been enriched to take into account multiphase flow. Thus, a coupled system of 4 equations based on Cahn–Hilliard and Navier–Stokes equations has been obtained. The goal is to be able to solve multiphase flow cases with an interface capturing based on the phase-field model and including capillary action. These equations have also been studied theoretically and numerically, especially by proving the continuous energy estimate. Test cases from the literature have been simulated with results in accordance with the references. In the optic to proceed to less time costly computations, and especially to be able to simulate 3D cases, an anisotropic mesh adaptation has been set up with an adaptation criterion based on a function of the order parameter. Finally, to hope for some industrial applications, these solvers have been enriched with a heat exchange evolution model and the liquid-to-vapor phase change due to vaporization. This allowed, as a promising proof of concept, to simulate 2D and 3D quenching of solids with different geometries inspired by those encountered in industry. A unified numerical solver capturing the interface within a multiphase flow and describing the heat transfers of the system has been designed as a promising - and subject to improvements - tool for complex industrial processes and beyond.

5.2 Perspectives

The numerical tool developed in the present work is far from perfect. It has its limitations at different scales. Improvements can be done to make robust this unified numerical framework, for example, by studying:

- The setup of a diffusive and anti-diffusive stabilization method coupled with the flux limiting strategy can help to bound the order parameter φ between -1 and 1 at any time to respect the maximum principle, which is not currently respected for Cahn–Hilliard equations.
- The development of a new metric for mesh adaptation that enables a finer capture of the interface with lower computational cost.

- The numerical scheme to identify how the mass flux contribution $(\mathbf{J} \cdot \nabla)\mathbf{u}$ in Navier–Stokes equations can be included in simulations, which is currently not the case due to stability issues in several simulations.
- The extension to the non-isotherm case and investigating the free energy $F(\varphi)$ to have a thermodynamically consistent model. To do this, it is necessary to start from the fundamental equation of thermodynamics.
- The current model in order to take into account all the main physics involved in the quenching process allowing, therefore, a better comparison between numerical and experimental results.
- The semi-discretization in time to drastically diminish the numerical diffusion for long time simulations.
- How the wetting of the wall can be taken into account in the phase-field model.
- The development of a good interpolate operator to have more regular solutions and boundary conditions that include contact angle

Bibliography

RÉSUMÉ

Cette thèse s'inscrit dans la volonté de développer un nouveau cadre numérique apte à traiter des cas industriels complexes. De cela est né le besoin de développer de nouveaux solveurs numériques qui viendront enrichir la bibliothèque des méthodes actuellement utilisées au sein de l'équipe. Cette volonté repose sur celle d'envisager une nouvelle approche de capture d'interface permettant d'obtenir de nouvelles informations sur la physique du système et apporter une robustesse numérique. La méthode phase-field est basée sur une approche énergétique de l'interface séparant les phases ce qui n'est pas le cas de la méthode de capture d'interface actuellement utilisée par l'équipe qui repose sur une approche géométrique. De plus, la méthode possède de bonnes propriétés pour modéliser l'action capillaire, impliquée dans le mouillage, et considérer les angles de contact. Orientée dans une perspective d'applications industrielles, cette interface de capture a pour objectif d'être unifiée à d'autres modèles physiques pour développer un outil multiphysique et une application multiple à la simulation numérique industrielle.

MOTS CLÉS

Mathématiques, Analyse numérique, Mécanique des Fluides Numérique, Calcul Haute Performance

ABSTRACT

This thesis is part of the desire to have a numerical framework dealing with complex industrial cases. For this reason, it is necessary to develop new solvers that enrich the library of methods currently used in the team. This desire relies on the will to consider a new approach of interface capturing enabling the obtaining of new information about the physics of the system and bringing numerical robustness. The phase-field method is based on an energetic approach of the interface separating the phases that which is not the case for the currently used interface capturing method. Furthermore, the method owns good properties to model the capillary action, involved in the wetting, and consider contact angles. Directed by a perspective of industrial applications, this interface capturing aims to be unified with other physical models for a multiphysics characteristic and a multiple applications to the industrial numerical simulation.

KEYWORDS

Mathematics, Numerical analysis, Computational Fluid Dynamics, High Performance Computing